Energy Island North Sea

Metocean Assessment

Part A: Data Basis – Measurements and Models
Establishment of bathymetry, measurements, and hindcast

Report
IO Number: 4500087261

Prepared for Energinet Eltransmission A/S

2023-06-28

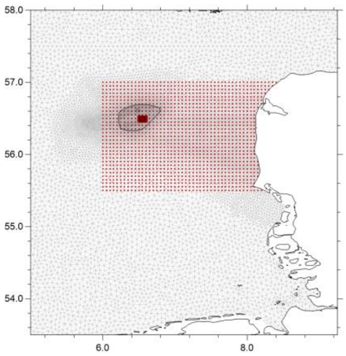

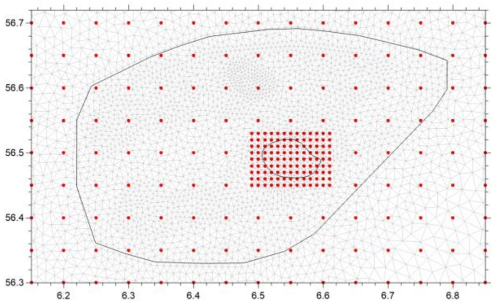

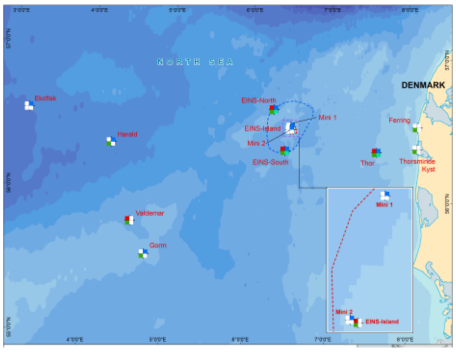

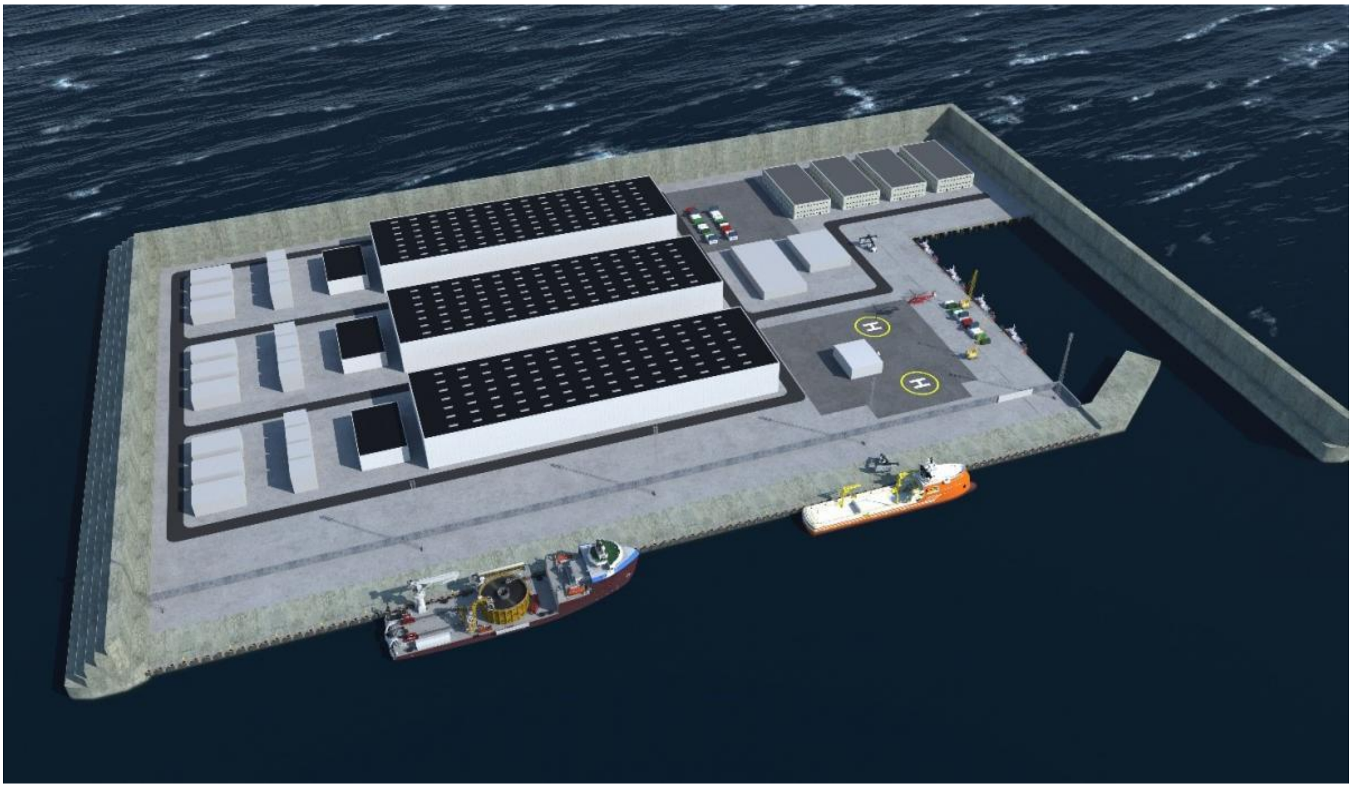

Energy Island North Sea

Metocean Assessment
Part A: Data Basis – Measurements and Models
Establishment of bathymetry, measurements, and hindcast

Report
IO Number: 4500087261

Prepared for:	Energinet Eltransmission A/S
Represented by	Mr Kim Parsberg Jakobsen

Contact person:	Patrick Dich Grode, pdg@dhihroup.com, +45 4516 9070
Project Manager:	Patrick Dich Grode
Quality Supervisor:	Patrick Dich Grode
Author:	Jose Rafael Meza Padilla, Eduardo Gonzalez - Gorbena Eisenmann
Project No.:	11828428
Approved by:	Jesper Ulrik Fuchs

Revision:	**Date:**	**Description:**
1.0	2023-06-28	Final report including final comments from client and certifier.
0.3	2023-06-09	Revised draft report including comments from client and certifier.
0.2	2023-04-21	New/revised sections 3.2.1, 3.2.2, 5.3.3, 5.3.4, and 5.4.
0.1	2023-03-29	Draft report issued for comments by client and certifier.

Classification:	Confidential
File name:	11828428_DHI_EINS_Metocean_Part_A_Data_Basis

DHI A/S • Agern Allé 5 • • DK-2970 Hørsholm • Denmark
Telephone: +45 4516 9200 • dhi@dhigroup.com • www.dhigroup.com • Company Reg. No.: 36466871

Contents

Nomenclature

Variable	Abbrev.	Unit
Atmosphere		
Wind speed @ 10 m height	WS_{10}	m/s
Wind direction @ 10 m height	WD_{10}	°N (clockwise from)
Air pressure @ mean sea level	P_{MSL}	hPa
Air temperature @ 2 m height	$T_{air,2m}$	°C
Relative humidity @ 2 m height	RH_{2m}	-
Downward solar radiation flux	SR	W/m^2
Ocean		
Water level	WL	mMSL
Current speed	CS	m/s
Current direction	CD	°N (clockwise to)
Water temperature	T_{water}	°C
Water Salinity	Salinity	-
Water density	ρ_{water}	Kg/m^3
Waves		
Significant wave height	H_{m0}	m
Peak wave period	T_p	s
Mean wave period	T_{01}	s
Zero-crossing wave period	T_{02}	s
Peak wave direction	PWD	°N (clockwise from)
Mean wave direction	MWD	°N (clockwise from)
Direction standard deviation	DSD	°

Executive Summary

Energinet Eltransmission A/S (Energinet) requested a metocean site conditions assessment to form part of the site conditions assessment and to serve as basis for the design of the Energy Island North Sea (EINS) artificial island and surrounding offshore wind farms.

This study provides detailed metocean conditions for EINS and establishes a metocean database for the artificial island and the surrounding offshore wind farm (OWF) development areas as shown in Figure 0.1.

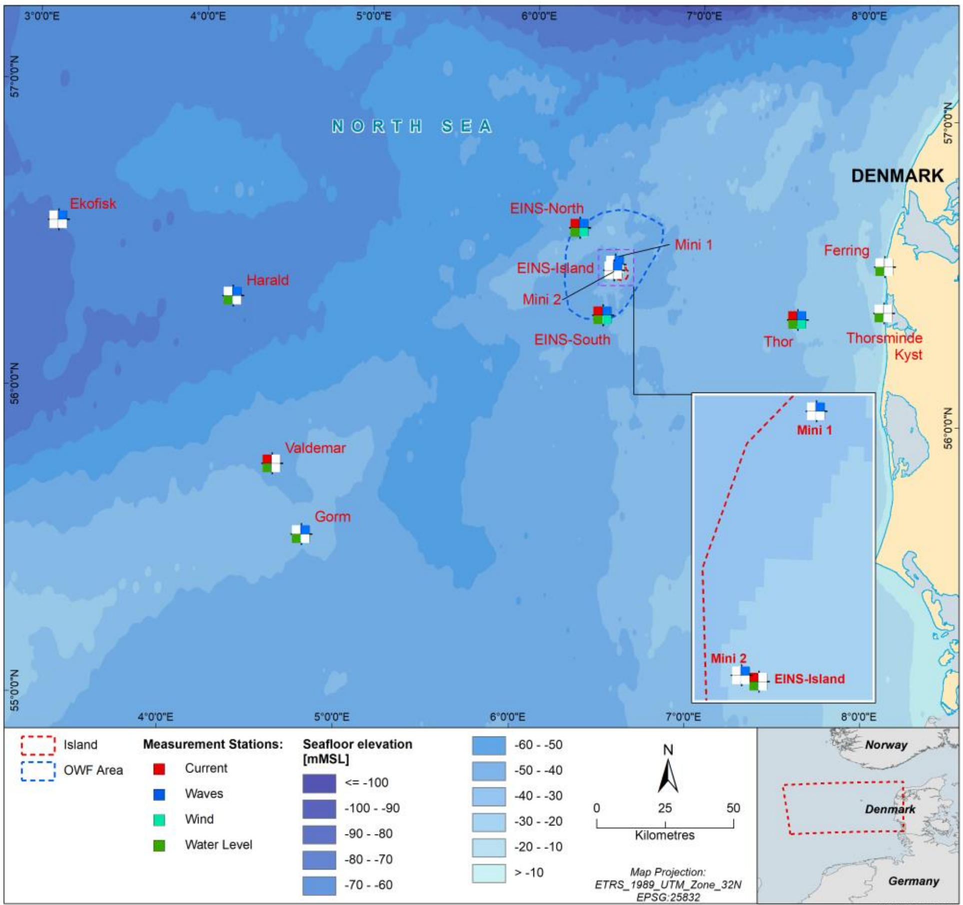

Figure 0.1 Location of the Energy Island North Sea, the related offshore wind farm development area, and measurement stations
The hindcast database (covering OWF area) entails: Waves: *EINS-SW-CFSR*, Ocean: *EINS-SW-CFSR*, Atmosphere: *Global-AT-CFSR*.

This report (Part A) concerns the establishment of metocean hindcast models and comparison of these against local and regional measurements, to arrive at a consistent, accurate, and validated metocean database applicable for assessment of normal, extreme, and joint metocean conditions.

Bathymetric basis

The bathymetric data basis was compiled from the local survey provided by Energinet and the EMODnet dataset, to jointly form a consistent and accurate bathymetric dataset applicable for hindcast hydrodynamic and wave modelling.

Measurements

A comprehensive set of wind, water level, current, wave, CTD (sea temperature and salinity) and visibility data were collected by FUGRO and provided to DHI by Energinet. The data was collected by floating (buoy) and bottom-mounted instruments from four stations within the EINS site during the period 2021-11-15 to 2022-11-15. Details are given in the survey campaign report [1, 2]. This dataset was supplemented by long-term measurements from other stations in the North Sea. Figure 0.1 shows a map of all stations.

Hindcast models

All hindcast model data of this study covered the period 1979-01-01 – 2022-09-30, ie. ~44 years (except 3D HD data which covered 2013 – 2022, ie. 10 years).

Wind data was adopted from CFSR due to its superior accuracy for extreme events, and to its successful use on certified projects in the North Sea and globally.

A local hindcast 2D hydrodynamic model was set up to simulate water levels and currents using the MIKE 21 HD model. The domain covered the EINS site only to take full advantage of boundary conditions adopted from the assimilated hydrodynamic model by DHI of North Europe, HD_{NE}. The data basis for currents was supplemented by data from the DHI United Kingdom and North Sea 3-dimensional (HD_{UKNS3D}) regional hydrodynamic model.

The waves were simulated using the MIKE 21 SW spectral wave model set up for the entire North Sea with high resolution and calibration targeted to the EINS site. The model used boundaries from the DHI global CFSR-forced wave model.

All hindcast data was compared extensively against local and regional measurements and found to be accurate and applicable for assessments of normal and extreme metocean conditions without any (bias) adjustment.

Time series data of air temperature, humidity, and solar radiation were adopted from CFSR. Rainfall time series data were extracted from the ERA5 reanalysis product. Lightning data was obtained from the LIS/OTD Gridded Climatology dataset [3] from NASA's Global Hydrology Resource Center (GHRC).

Water temperature and salinity at surface and seabed was adopted from the DHI HD_{UKNS3D} model. Water density was calculated, as a function of water temperature and salinity, using the international one-atmosphere equation of state of seawater, [4].

Climate change

The above introduced hindcast (wave and current) models were established and executed for the present-day scenario. A literature review on the possible impact of climate change demonstrated that the prediction of wind speed changes is very uncertain, and no conclusive statements on this have been made public. Therefore, the only climate change effect included in the modelling was sea level rise (SLR) estimated to +0.8 m by year 2113.

However, it is recommended that the designer consults the project owner and any given design requirements on climate change, to decide on the safety policy with respect to possible climate change effects. A (potentially conservative) guideline on climate change effects on wind and waves is suggested in NORSOK, [5].

Metocean Database

The metocean hindcast data developed in this study for EINS covers the entire light blue polygon in Figure 1.1. It entails all hindcast wave, ocean, and atmospheric variables, and was provided to Energinet on a hard disk in MIKE dfs file formats. The dfs files can be read using either the Python MikeIO[1] or the DHI-MATLAB-Toolbox[2] open source libraries available at GitHub.

Table 0.1 summarises the spatial and temporal data coverage and specifies the variables for each data category. Sections 3 – 8 provide details on the data establishment and documentation of representative averaging periods.

Table 0.1 Summary of the provided EINS metocean database

Spatial coverage: See Figure 1.1 (entire development area), Δx = 400 m. Temporal coverage: 1979-01-01 – 2022-09-30 (43.75 years), Δt = 30 min. Wave spectra: Stored on a ~1 km grid within the island and ~5 km elsewhere.

Category	Variable	Abbrev.	Unit
Atmosphere	**(0 – 10 m height)**		
Dataset: Global-AT-CFSR Rep. avg. period: 2 hours	Pressure @ mean sea level	P_{MSL}	hPa
	Wind speed @ 10 m height	WS10	m/s
	Wind direction @ 10 m height	WD10	°N (clockwise
	Air temperature @ 2 m height	$T_{air,2m}$	°C
	Sea Surface Temperature	SST	°C
	Relative humidity @ 2 m height	RH	-
Global-AT-CFSR (0.5°)	Downward solar radiation flux	SR	W/m^2
Ocean (HD)	**(Total, depth-average)**		
Dataset: EINS-HD-CFSR Rep. avg. period: 1 hour	Water level	WL	mMSL
	Current speed	CS	m/s
	Current direction	CD	°N (clockwise
Waves (SW)	**(Total, wind-sea, and swell)**		
Dataset: EINS-SW-CFSR Rep. avg. period: 3 hours	Significant wave height	H_{m0}	m
	Peak wave period	T_p	s
	Mean wave period	T_{01}	s
	Zero-crossing wave period	T_{02}	s
	Peak wave direction	PWD	°N (clockwise
	Mean wave direction	MWD	°N (clockwise
	Direction standard deviation	DSD	°

---

[1] https://github.com/DHI/mikeio
[2] https://github.com/DHI/DHI-MATLAB-Toolbox

1 Introduction

This study provides detailed metocean conditions for the Energy Island North Sea (EINS) and establishes a metocean database for the island and the adjacent offshore wind farm (OWF) development area (see Figure 1.1).

Energinet Eltransmission A/S (Energinet) was instructed by the Danish Energy Agency (DEA) to initiate site investigations, including a metocean conditions assessment, to form part of the site conditions assessment and to serve as basis for the design and construction of EINS and related OWFs. The study includes an assessment of climate changes considering an 80-year lifetime.

Energinet commissioned DHI A/S (DHI) to provide this study with Scope of Work (SoW) defined in [6]. Later, the work was extended to cover also FEED level metocean conditions for the offshore wind farm area cf. scope in [7]. The study refers to the following common practices and guidelines:

- DNV-RP-C205, [8]
- IEC 61400-3-1, [9]

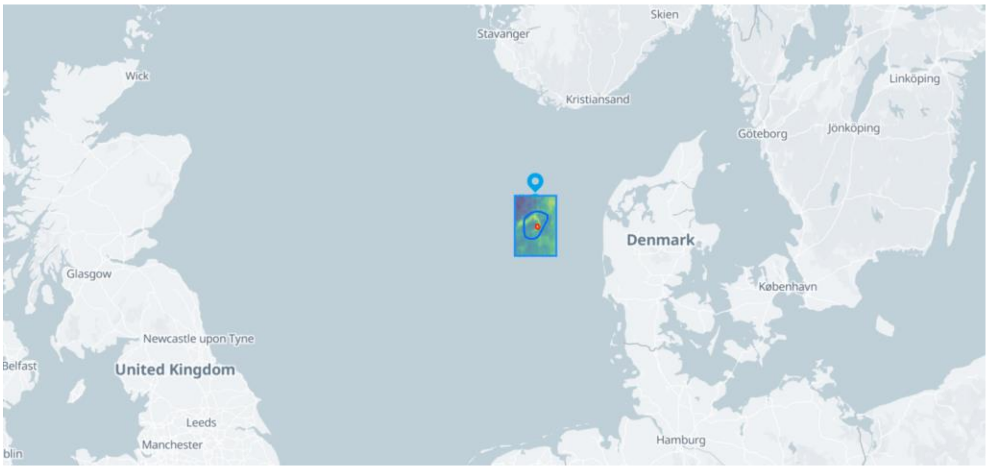

Figure 1.1 The location of the Energy Island North Sea (red), and related offshore wind farm development area (dark blue)
The hindcast database (light blue polygon) entails: Waves: *EINS-SW-CFSR*, Ocean: *EINS-SW-CFSR*, Atmosphere: *Global-AT-CFSR*.

The deliverables included time series data of hindcast metocean parameters, analyses of normal, extreme and joint metocean conditions at five (5) locations, a metocean database (see Figure 1.1), and four (4) separate reports:

- **Part A: Data Basis – Measurements and models (this report)**
  Establishment of bathymetry, measurements and hindcast metocean data.
- **Part B: Data Analyses – Energy Island**, [10]
  Metocean site conditions for detailed design of the energy island.
- **Part C: Data Analyses – Wind Farm Area, [11]**
  FEED level metocean site conditions for the offshore wind farm area.
- **Part D: Data Basis – Hindcast revalidation note**, [12]
  Revalidation of the hindcast metocean data vs. updated measurements.

2 Bathymetry

This section describes the general bathymetry, or seabed levels, in the North Sea and the EINS site followed by an evaluation of the relevant bathymetric data sources, their alignment and vertical datum, leading to a consistent and accurate bathymetric dataset applicable for the hydrodynamic and wave hindcast modelling activities of this project.

2.1 General seabed levels

The North Sea lies on the European continental shelf and is located between Britain and the continent of north-western Europe. It is connected to the Atlantic Ocean via the English Channel and the waters between Scotland and Norway.

Figure 2.1 shows the seabed levels in the North Sea. The seabed levels can be separated into three main areas: 1) The Norwegian Trench, up to about 1000 m deep; 2) the Dogger Bank, the shallowest region with water depths down to 15 m; and 3) the rest of the North Sea with offshore water depths generally within 30-100m.

The EINS site lies in the north-eastern North Sea with water depths of 25-50 m.

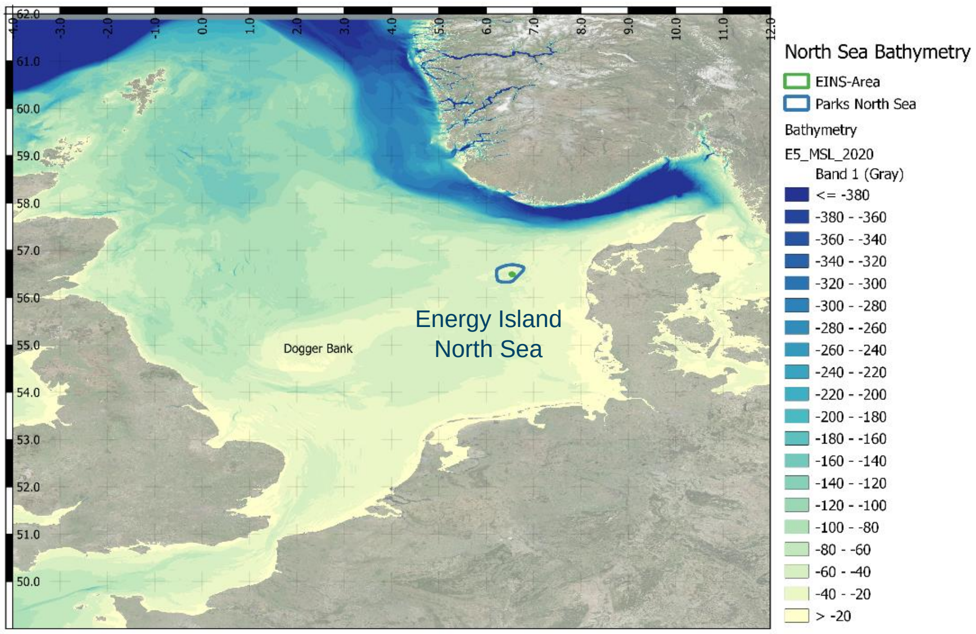

Figure 2.1 Seabed levels in the North Sea [Source: EMODnet 2020]
The Energy Island North Sea (EINS) lies in the north-eastern North Sea with water depth of 25-30 mMSL at the island and down to about 50 mMSL in the surrounding planned OWF area.

2.2 Bathymetric data sources

Energinet provided a local bathymetric survey covering the EINS site and the surrounding wind farm area. This dataset was supplemented by the regional EMODnet bathymetric dataset covering the entire North Sea. Table 2.1 presents an overview of the bathymetric data sources considered.

Table 2.1 Bathymetric data sources

Name	Coverage / relevance	Resolution [m]	Year / Version	Vertical datum	Provider
Survey	Project Site	5	2022	MSL	Energinet
EMODnet[1]	North Sea	115	2020	MSL	EU

[1] https://www.emodnet-bathymetry.eu/

Survey and datum

The local bathymetric survey was conducted by MMT and reported in [13]. The survey was done using a multi-beam high-resolution echosounder, and the data was resampled by Energinet to 5 m. The horizontal reference was World Geodetic System 1984 (WGS84), and the vertical datum was Mean Sea Level (MSL) via DTU21 MSL Reduction from WGS84-based ellipsoid heights.

The bathymetric survey recorded water depths across the EINS (~10x10 km) and the surrounding wind farm area. Figure 2.2 shows the seabed levels of the local bathymetric survey, while Figure 2.3 and Figure 2.4 shows the survey and depth profiles across the island adopted from [13]. Within the island area, the depths range mainly from 25 to 35 m MSL, while the park area is down to 50 m MSL.

The average height of DVR90 (Danish Vertical Reference 1990) is 0.28 m larger than that of DTU21, [13]. Thus, to convert absolute seabed levels from the local MSL herein to DVR90, one must add 0.28 m.

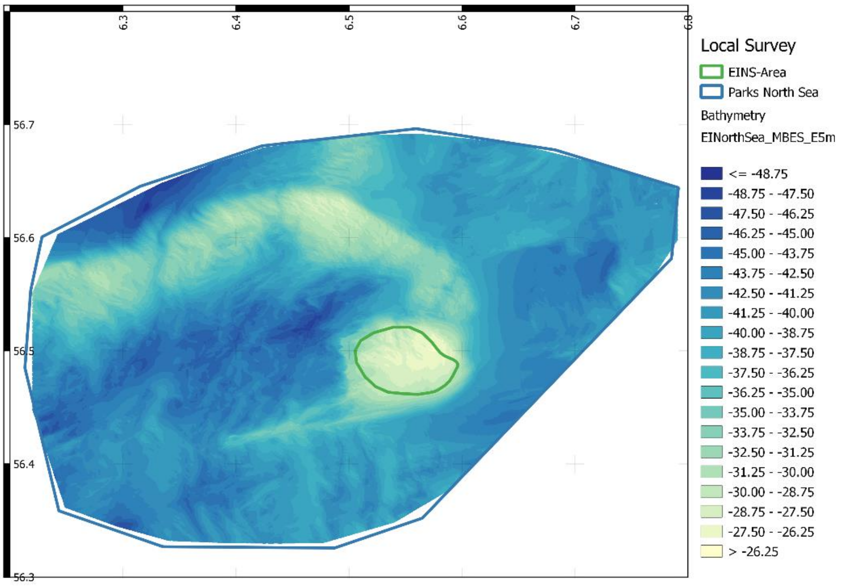

Figure 2.2 Seabed levels of the local bathymetric survey [m MSL]

Water depths at the EINS island area (green polygon) range from 25 to 35 m MSL, while the wind farm area (blue polygon) is down to 50 m MSL.

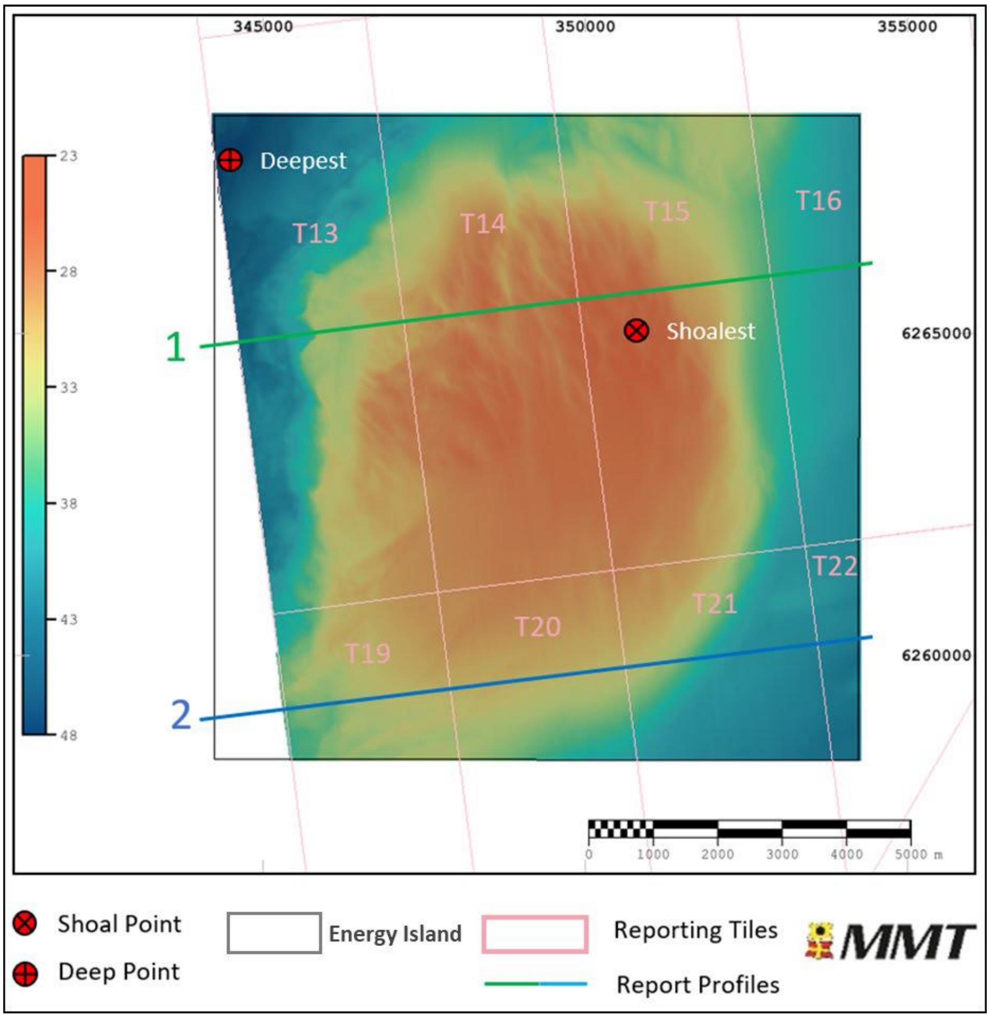

Figure 2.3 Survey and positions of profile lines in Figure 2.4, [13]

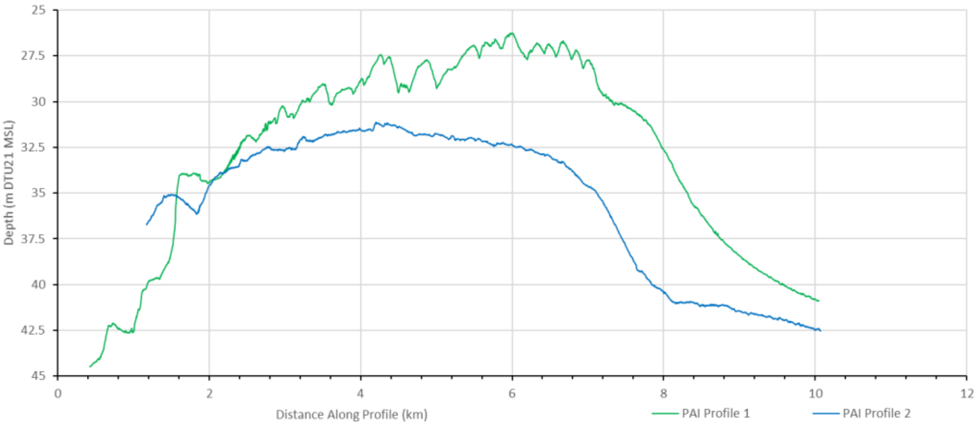

Figure 2.4 Depth profiles across the EINS island [m MSL DTU21], [13]

EMODnet 2020

Bathymetric data for areas of the North Sea not covered by the survey presented above was adopted from the EMODnet Bathymetry portal, see Figure 2.1 and Table 2.1. Data for this project was retrieved with a vertical datum of MSL from the 2020 version of EMODnet.

The EMODnet Bathymetry portal was initiated by the European Commission as part of developing the European Marine Observation and Data Network (EMODnet). The EMODnet digital bathymetry has been produced from bathymetric survey data and aggregates bathymetry datasets collated from public and private organisations. The data provided is pre-processed and quality-controlled) by EMODnet at a resolution of 1/16 arc minutes (~115 m.

In DHI's experience across several projects in the North Sea, the EMODnet bathymetry has shown good agreement with local survey data and is thus considered a useful and reliable data repository for metocean modelling and analyses.

Comparison between survey and recorded depth of in-situ stations

Table 2.2 compares the depth of survey and recorded depth of two in-situ measurement stations (LiDAR buoys). At both stations, the survey depth is about 0.5 m deeper than the station depth. This may be partially explained by the recordings being averaged over a winter season when mean sea level is relatively lower in the North Sea. Hence, overall, a very close agreement between the two independent sources is seen, thus providing confidence in the accuracy and vertical reference level of the survey.

Table 2.2 Depth of survey and recorded depth of in-situ stations

Station	Average recorded depth during Nov. 2021 – Mar. 2022 [m MSL][1]	Raster 50m averaged survey depth [m MSL]
EINS-North (pressure sensor)	45.8	46.4
EINS-South (pressure sensor)	39.3	39.8

[1] Increased by 1 m to account for the sensor position being 1 m above seabed.

Comparison between EMODnet and the survey

To validate and inter-compare the two bathymetry data sources, Figure 2.5 shows the difference between the EMODnet and the survey as well as two transects across the EINS island area and the wind farm area. The local survey has a higher degree of detail which may explain some of the deviations, but overall, the plot demonstrates a good agreement between the datasets with deviations predominantly less than +/-2-3 m (small regions outside the island area show differences up to 4-5 m).

On average, the survey depths were 0.3 m (~1%) deeper than EMODnet depths within the island area, and 1.0 m (~2%) deeper than EMODnet within the entire park area. Such differences may be due to discrepancies between the vertical reference level (MSL) of the two datasets, which for EMODnet is somewhat uncertain. Nevertheless, differences of the order of 1-2% of the total water depth is without significant effect for the (wave) modelling activities of this study.

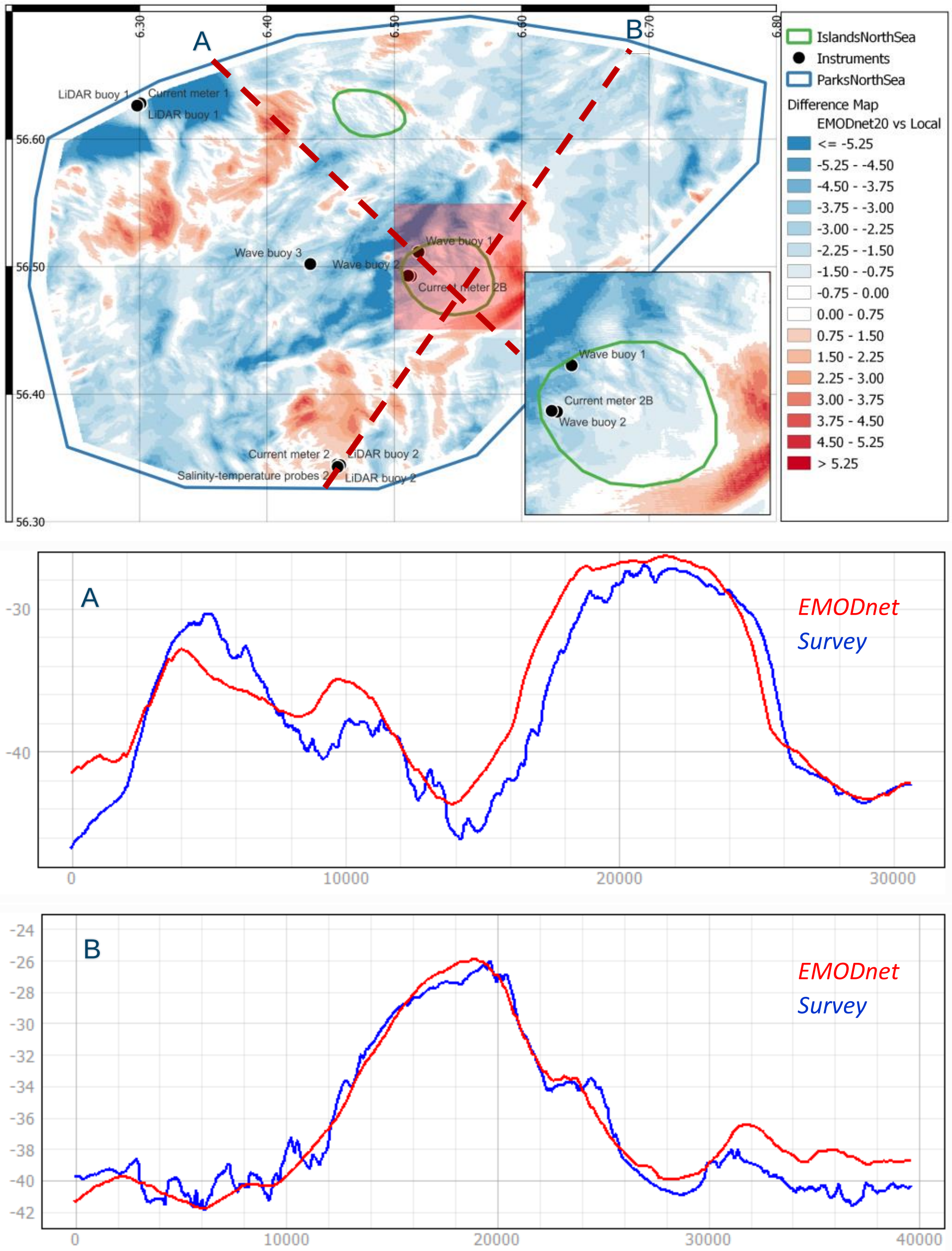

Figure 2.5 **Top: Difference between EMODnet and survey**
Bottom: Transects A and B across the island and park area.
Negative numbers (blue colours) mean that the survey is deeper.

2.3 Common uniform bathymetry

In conclusion, the considered bathymetric data sources are in reasonable agreement considering their origin and means of measure. Their vertical reference levels are acceptably close and validated against the recorded depth of local in-situ stations. Hence, the survey and EMODnet datasets are applied as received (i.e., without any modifications) to jointly form a consistent and accurate bathymetric dataset applicable for the hindcast hydrodynamic and wave modelling activities of this study and covering the North Sea and EINS site.

3 Wind

Atmospheric data used as forcing of the numerical hydrodynamic (HD) and spectral wave (SW) models, as well as for extreme values analysis, was adopted from the Climate Forecast System Reanalysis (CFSR) atmospheric model established by the National Centre for Environmental Prediction (NCEP).

The CFSR dataset is described and validated against measurements from the local EINS SeaWatch Wind LiDAR Buoys (i.e. EINS-North and EINS-South), [2] , and the Thor LiDAR Buoy (LB). CFSR dataset was chosen for this study due to its superior accuracy for extreme events, and due to its long record of successfully certified projects in the North Sea and globally.

3.1 General wind characteristics

The wind climate of the North Sea is affected by several weather phenomena. Among them, the North Atlantic Oscillation (NAO), which is described by the anomaly of pressure gradient between north-western (Iceland) and southwestern North Atlantic (Azores), has a significant influence on the wind conditions over the North Sea. During the winter months, the NAO has a larger effect than in the summer, when the surface heating generates disturbances weakening the large-scale circulation. Studies show that an increase in the NAO index results in higher wind speeds over northern Europe [14] in terms of monthly to interdecadal timescales. As extreme events are short period events (~hours), several authors associated them to other circulation patterns, see [15], [16].

At the current study region, winds predominantly blow from the third and fourth quadrant, i.e., from 180 – 360 °N, followed by winds coming from the second quadrant. Average wind speeds are around 9 m/s. Winds are stronger during the months of November to February, which are associated with directions coming from 240 – 330 °N and can reach speeds above 30 m/s.

Historic storms of the North Sea, British Isles and Northern Europe from 1509 to 1990 are reported by Huber Lamb in [17]. However, hindcast atmospheric data is generally available since 1979 only (see Section 3.3), and insufficient data (mainly pressure maps) is available in [17] to attempt to hindcast the historic storms described. Hence, conditions prior to 1979 are not considered. The storm on 24th November 1981, had a gust of 83 knots reported in Northern Jutland. This storm is one of the strongest in the hindcast data at EINS.

3.2 Wind measurements

Wind measurement data used for local validation of the CFSR data are listed in Table 3.1 and illustrated in Figure 3.1. Measurements were available at several elevations from 4 mMSL (anemometer) and 30 - 270 mMSL every 10 m (LiDAR) during 2021-11-15 to 2022-07-15 (8 months), see Figure 3.2.

The wind measurements at the EINS site measured by the SeaWatch Wind Lidar Buoys [2] (i.e., EINS-North and EINS-South) were quality controlled by the data surveyor (i.e., FUGRO) and checked by DHI before use. A similar process was done for the Thor data, recorded by Akrocean.

Table 3.1 Details of wind measurement stations

Station Name	Longitude [°E]	Latitude [°N]	Measurement Height [mMSL]	Data coverage	Instrument type	Model	Owner / Surveyor
EINS-North	6.3007	56.6280	4 30-270	2021-11-15 - 2022-07-15	Anemometer LiDAR	Gill Windsonic M ZephIR ZX300	Energinet / FUGRO
EINS-South	6.4574	56.3444	4 30-270	2021-11-15 - 2022-07-15	Anemometer LiDAR	Gill Windsonic M ZephIR ZX300	Energinet / FUGRO
Thor	7.605	56.347	43-200	2020-05-19 - 2021-05-19	LiDAR	Wind Cube WLS 866V2	Energinet / Akrocean

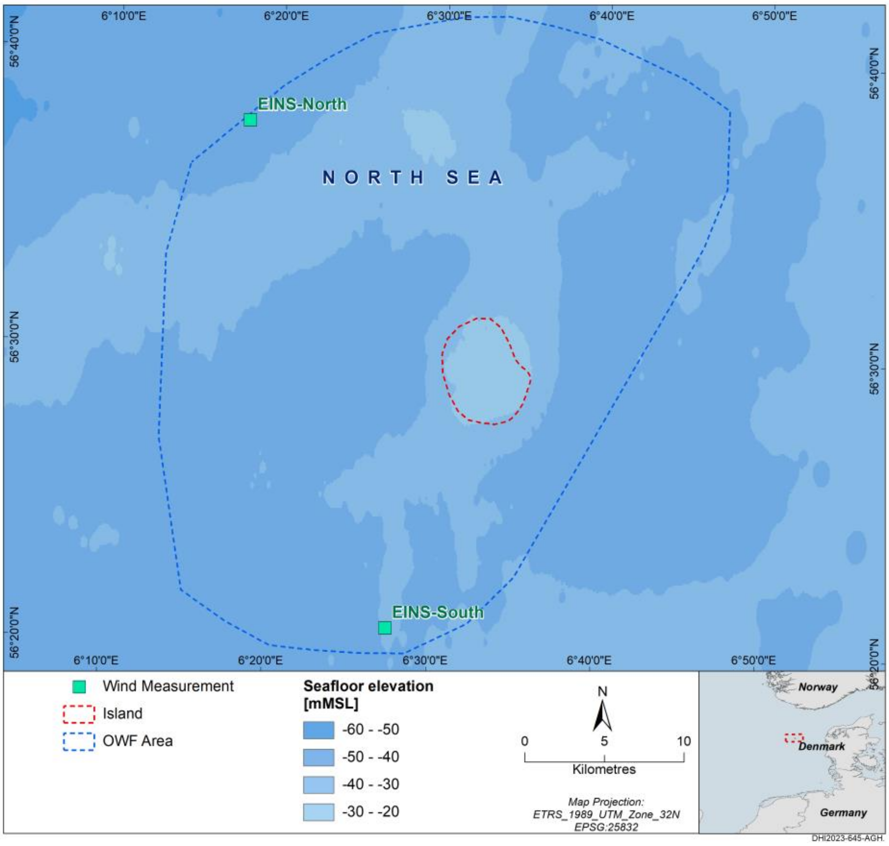

Figure 3.1 Location of local wind measurements
Location of regional measurements are shown in Figure 0.1.

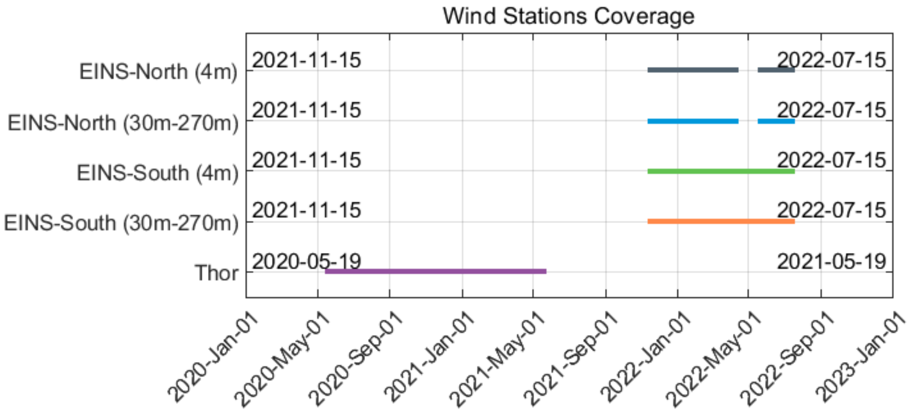

Figure 3.2 Temporal coverage of wind measurements

3.2.1 Wind profile (height conversion)

Wind speed at various heights above sea may be required for design purposes and for comparison of hindcast model data against measurements.

This section describes common wind profiles, and compares them to the local measurements to arrive at a recommended profile and height conversion factors for normal and extreme wind speeds.

The literature provides several guidelines for describing the vertical wind speed profile. The most common are Frøya, power and log profiles.

Frøya profile

Assuming neutrally stable atmospheric conditions, the vertical and temporal distribution of wind speed during storm conditions can be described by the Frøya profile. The Frøya profile is described as follows, in [8] and [18]:

$$U(\mathrm{T},\mathrm{z}) = U_0\left(1+\mathrm{C}\ \ln\frac{z}{H}\right).\left[1-0.41\cdot I_U(z)\cdot\ln\left({}^{T}\!/_{T_0}\right)\right]$$

- $U(\mathrm{T},\mathrm{z})$ is the mean wind speed [m/s} with averaging period T<T_0 = 3600 s at height z [mMSL}
- U_0 the 1-hour mean wind speed [m/s] at the reference elevation H = 10 m above sea level
- C a dimensionally dependent coefficient equal to $0.0573\ \cdot$ $(1+0.148U_0)^{1/2}$ for H = 10 m **(3.1)**
- I_U a dimensionally dependent value for the turbulence intensity of wind speed, given by

  $$I_U = 0.06\cdot(1+0.043\cdot U_0)\cdot\left({}^{z}\!/_{H}\right)^{-0.22}$$

- T_0 is the reference time averaging interval of 3600 s

Log profile

The wind profile of the atmospheric boundary layer (surface to around 2000 m) is generally logarithmic in nature and is often approximated using the log wind profile equation that accounts for surface roughness and atmospheric stability. However, for neutral conditions, the atmospheric stability term drops out and the profile simplifies to:

$$U_z = U_r\cdot log(z/z_0)/log(r/z_0) \tag{3.2}$$

where, U_z is the wind speed at height z, U_r is the wind speed at height r, and z_0 is the surface roughness length (in meters) (often in the range of 0.001 – 0.004 m at (rough) sea).

Power profile

The power law relationship is often used as a substitute for the log wind profile when surface roughness (and/or stability information) is not available. The power profile is defined as:

$$U_z = U_r\cdot(z/r)^{\alpha} \tag{3.3}$$

where, U_z is the wind speed at height z, U_r is the wind speed at height r, and α is the power law exponent (typically 0.100 - 0.146 for extreme wind speed).

Recommended wind profile

The vertical shear naturally fluctuates significantly over time due to the varying state and stability of the atmosphere, and thus the shear at individual profiles sometimes deviates substantially from the mean shear.

Figure 3.8 shows histograms of the measured wind shear at EINS-North for all wind speeds (top) and for $WS_{10,10\text{-min}}$ > 20 m/s (bottom) between the 30 and 40 m (left) and between 30 and 100 m (right).

It is noted that the measurements do not include very extreme wind speeds (highest recording is $WS_{10,10\text{-min}}$ = 26 m/s). The average measured value at each recoded level is indicated by a black dot.

For all wind speed, the shear from 30 to 40 m ranges from 0.85 – 1.15 with a mean value of 0.979, while the shear from 30 to 100 m ranges from 0.55 – 1.2 with a mean of 0.911. The mean shear corresponds to a power profile with α = 0.074 (30-40m) and α = 0.078 (30-100m). In conclusion, it is recommended to apply a power profile with α = 0.08 (representative of fully developed waves) to convert normal wind speeds from 10 to 30 m height (this corresponds to a factor of 1.09 going from 10 to 30 m).

For $WS_{10,10\text{-min}}$ > 20 m/s, the mean shear from 30 to 40 m is 0.98 (corresponding to α = 0.07), while the mean shear from 30 to 100 m is 0.911 (corresponding to α = 0.10). Hence, the measured mean shear is larger for stronger wind speed as expected due to increased wave action during strong wind and hence increased frictional effects leading to higher turbulence. In conclusion, it is recommended to apply a power profile with α = 0.10 to convert extreme wind speeds from 10 to 30 m height (this corresponds to a factor of 1.12 going from 10 to 30 m).

Figure 3.4 show comparisons of the theoretical wind profiles and the wind measurements up to a height of 120 m at EINS-North for all wind speeds (top) (using α = 0.08) and for $WS_{10,10\text{-min}}$ > 20 m/s (bottom) (using α = 0.10). The Frøya profile gives higher ratios for very extreme wind speeds, which may be because the Frøya profile was developed and validated for wind conditions off the Norwegian coast.

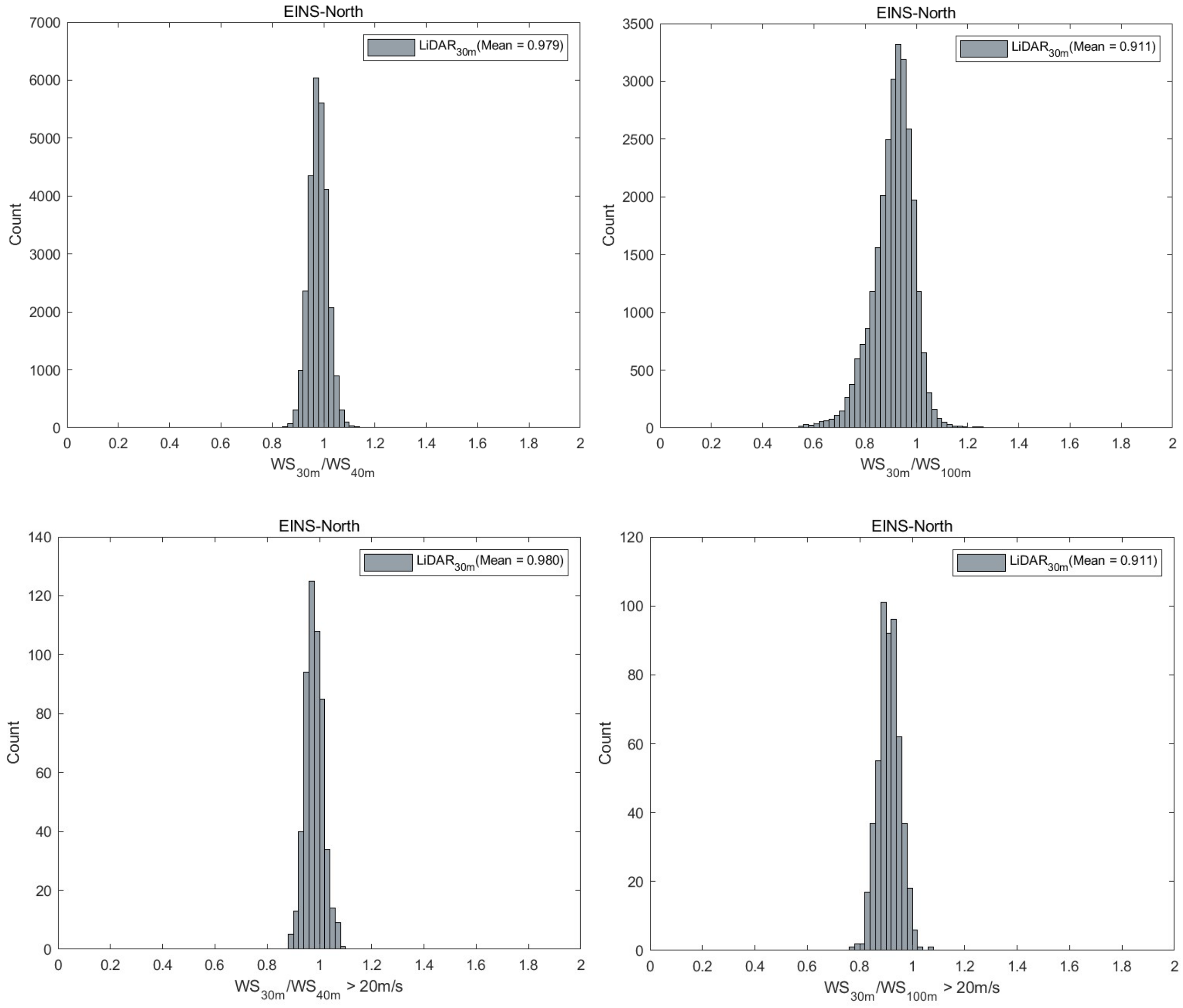

Figure 3.3 **Histograms of measured wind shear at EINS-North**
Top: All wind speeds; Bottom: $WS_{10,10\text{-}min}$ > 20 m/s; Left: WS_{30}/WS_{40}; Right: WS_{30}/WS_{100}

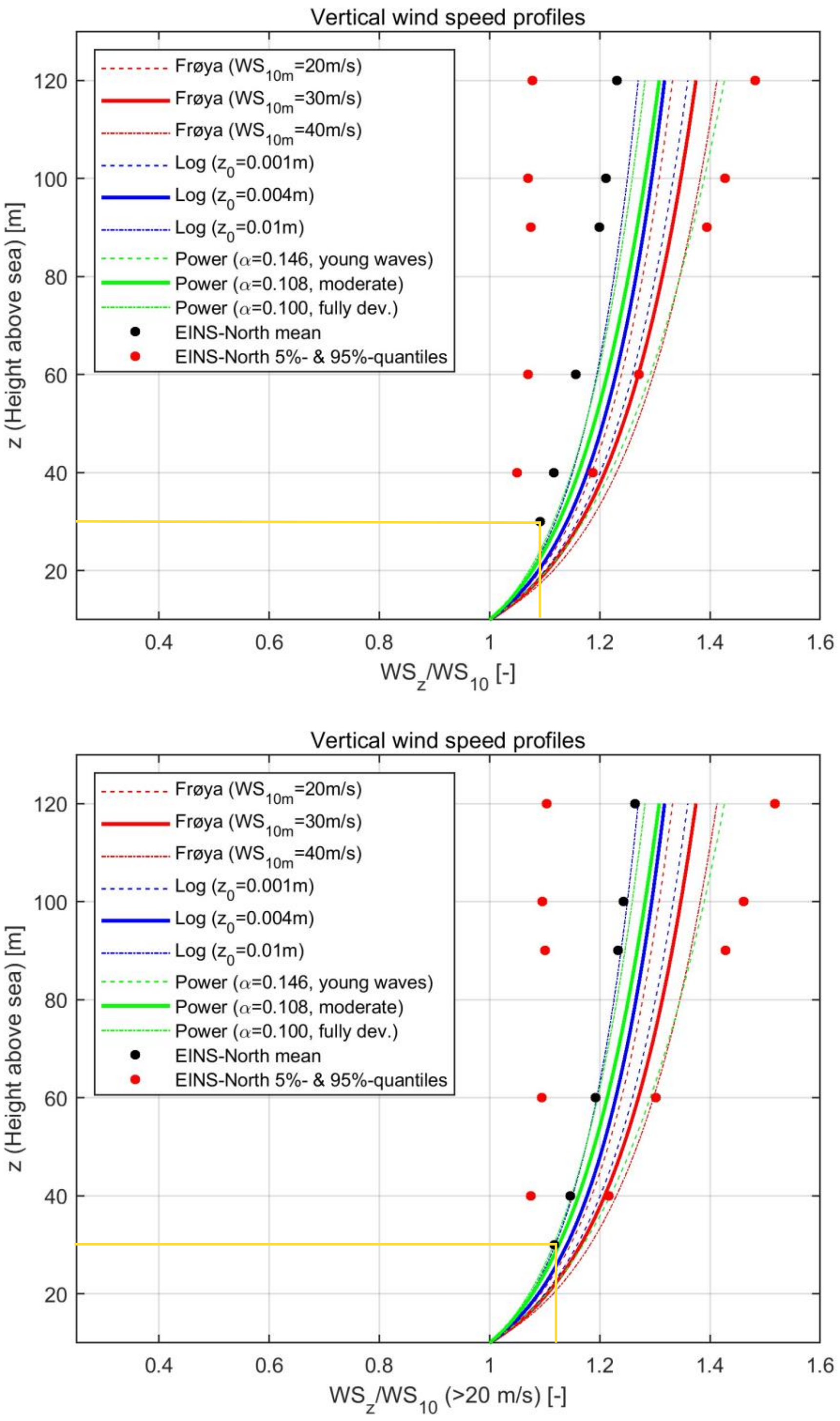

Figure 3.4 **Comparison of theoretical wind speed profiles and measurements at EINS-North**

Top: All measured wind speeds (using α = 0.08);

Bottom: Measured $WS_{10,10\text{-min}}$ >20 m/s (using α = 0.10).

3.2.2 Wind averaging (temporal conversion)

Wind speed of various averaging periods may be required for design purposes and for comparison of hindcast model data against measurements.

This section describes common factors for conversion between various wind averaging periods, and compares them to the local measurements, to arrive at recommended temporal conversion factors for <u>extreme</u> wind speeds.

Common temporal conversion factors

Table 3.2 lists common temporal conversion factors to convert between various averaging periods of <u>extreme</u> wind speeds. The factors are developed specifically for storm conditions, i.e., to represent the strongest sample wind speed (fx 10-min) within 1 hour. For example, if a 10-min extreme wind speed is 1.1 times the 1-h extreme wind speed, this means that the strongest wind speed in 6 samples of 10-min duration is expected to be 1.1 times the average for all 6 samples (= the 1-h mean). Thus, the factors are not applicable to convert time series of wind speeds (as this would increase the mean value).

The factors are adopted from IEC, CEM , WMO, and DNV/ISO (Frøya, see Eq. (3.1)). The CEM factors are given as equations relative to the 1-h mean, Eq. (3.4).

$$\begin{aligned} {}^{U_t}/_{U_{3600}} &= 1.277 + 0.296 \cdot tanh\left(0.9 \cdot \log10\left(\frac{45}{t}\right)\right), \underline{\text{for } 1 < t < 3{,}600} \\ {}^{U_t}/_{U_{3600}} &= 1.5334 - 0.15 \cdot \log10(t), \underline{\text{for } 3{,}600 < t < 36{,}000} \end{aligned} \qquad \mathbf{(3.4)}$$

The IEC, CEM, and WMO factors are independent of wind speed (fixed surface roughness). Hence, when using a wind speed independent vertical profile (such as the power profile), the factors become independent of height. The WMO factors are recommended specifically for tropical cyclones.

The DNV/ISO (Frøya) factors consider the variation in turbulence intensity as function of speed and height, and therefore, four examples using 20, 30, and 40 m/s wind speed at 10 and 30 m height respectively, are shown for Frøya.

The table shows that Frøya gives higher conversion factors than the other references, especially for the very extreme wind speeds and short temporal scales (note that Frøya is dependent on the wind speed and height above sea).

Table 3.2 **Common temporal conversion factors of extreme wind speed** (2 h is the averaging period of CFSR hindcast wind data).

Reference	Remark	3-h	2-h	1-h	10-min	1-min	3-s
DNV [8], ISO [18] (Frøya)	20m/s, 10m height	-	-	1.00	1.08	1.19	1.32
	30m/s, 10m height	-	-	1.00	1.10	1.23	1.40
	40m/s, 10m height	-	-	1.00	1.12	1.27	1.47
	40m/s, 30m height	-	-	1.00	1.09	1.22	1.37
IEC[1,3] [9]	All speeds/heights	0.95	0.97	1.00	1.05	-	-
CEM [19]	All speeds/heights	0.93	0.95	1.00	1.05	1.24	1.51
WMO[2] [20]	All speeds/heights	-	-	1.00	1.03	1.11	1.30

[1] Converted from being relative to the 10-min value to being relative to the 1-h value.
[2] WMO is recommended specifically for tropical cyclones.
[3] The 2 h factor was obtained by interpolating between 3 h and 1 h.

Recommended temporal conversion factors

Figure 3.5 presents the maximum 10-min average vs. the 1-h average wind speed measured at EINS-North together with the IEC and DNV/ISO (Frøya) temporal conversion factors. It is noted that the measurements do not include any very extreme wind speeds (highest recorded is $WS_{10,10\text{-min}}$ = 26 m/s).

The figure demonstrates that IEC provides a good fit to the measurements on average when considering the strongest wind speeds (> 20 m/s), while Frøya appears to overestimate the temporal conversion. Table 3.2 shows that the IEC factors are roughly in between the CEM and WMO factors when considering the range of 2-h to 10-min.

In conclusion, it is recommended to adopt the IEC factors for converting between averaging times of extreme wind speed within the range of 2-h and 10-min, i.e., a factor of 1.08 to convert from 2-h to 10-min average duration of extreme wind speeds. A more cautious/conservative approach would be to adopt the Frøya profile for temporal conversion of extreme wind speeds.

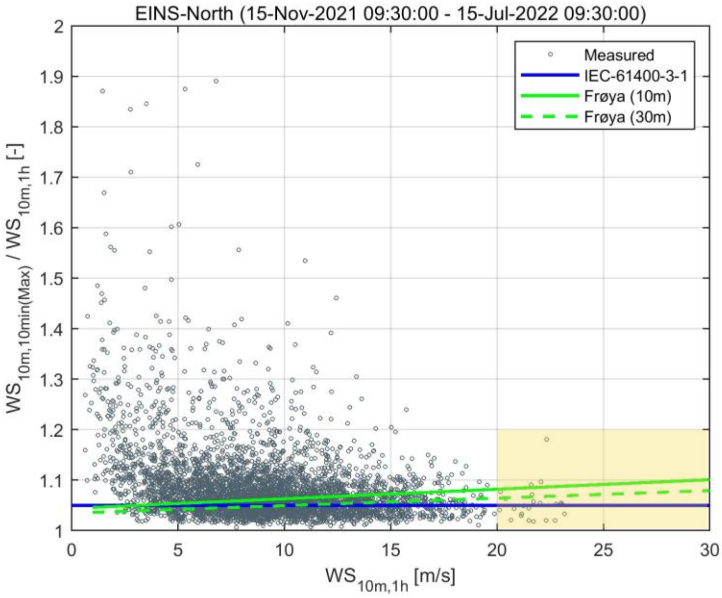

Figure 3.5 **Ratio of temporal average of wind speed at EINS-North**

3.3 Hindcast wind data

At the study site, there were two main atmospheric datasets available of appropriate data lengths (~44 years) to conduct normal and extreme analyses, namely:

- The **Climate Forecast System Reanalysis (CFSR)** dataset established by the National Centre for Environmental Prediction (NCEP), and

- The **ERA5** dataset from the European Centre for Medium-Range Weather Forecasts (ECMWF), provided by Copernicus, the European Union's Earth Observation Programme.

These datasets are briefly described below. However, the CFSR dataset was chosen for this study due to its superior accuracy for extreme events, and due to its long record of successfully certified projects in the North Sea and globally.

To support this decision, Section 3.3.3 presents a validation of CFSR against available measurements at the EINS site and at a regional level.

CFSR

The Climate Forecast System Reanalysis (CFSR) from the National Centers for Environmental Prediction (NCEP) is a coupled meteorological and oceanographic model system. The data has a resolution of 0.3° before 2011, and 0.2° after 2011, and covers the period from 1979-01-01 until today (~44 years) at hourly time steps.

Given that the location of the EINS project is relatively far offshore, the change in resolution after 2011 is not considered to be a major limitation as winds are not affected by land mask effects. Thus, yielding similar average wind speed for the two periods (see Section 3.3.1).

However, a limitation of CFSR is that it does not provide wind at 100 m height (but only wind at the 1000 mbar pressure level). While this is not a requirement for the Energy Island itself, it may be a requirement for any related studies such as, for example, for the offshore wind farm WTG's (in which case other methods or sources can be considered).

ERA5

ERA5 is a 30 km resolution reanalysis of meteorological conditions from 1979-01-01 until today (~44 years) at hourly time steps, established by ECMWF and provided by Copernicus, the European Union's Earth Observation Programme.

The ERA5 dataset has gained considerable acknowledgement for being of superior accuracy for normal conditions at many project sites globally, where DHI (and others) has gained experience. However, the ERA5 dataset tends to underestimate the strongest wind speeds in some regions including the North Sea.

ERA5 offers wind at 100 m height, however, it has a spatial resolution slightly coarser than that of CFSR, and thus the same limitations at the interfaces between land and sea as CFSR.

3.3.1 Climate Forecast System Reanalysis (CFSR)

CFSR was designed by the National Centers for Environmental Prediction (NCEP) from the National Oceanic and Atmospheric Administration (NOAA) as a global, high-resolution, coupled atmosphere-ocean-land-surface-sea ice system to provide the best estimate of the state of these coupled domains. This model system uses synoptic data for initialisation. GFS (Global Forecast System) is the atmospheric model included in the CFSR modelling complex. Further details are given in [21].

The data used for this study were available on an hourly basis from 1979-01-01 to 2022-09-30. Since CFSR is an operational dataset, it is possible later to update (expand) the database consistently. DHI's past experience using CFSR in the North Sea has shown very good performance in terms of both wind speed and direction.

The CFSR data covers the period from 1979 to 2010 (31 years), and since then, the operational re-forecast dataset (denoted CFSv2) has been applied. The underlying model in CFSv2 is the same as for CFSR; however, the spatial resolution of wind has been refined from 0.3° to 0.2° (see Figure 3.6), while the resolution of the atmospheric pressure is 0.5° for the entire period (interpolated to the same grid as the wind components in this project). Hereafter, 'CFSR' will refer to the combined CFSR and CFSv2 datasets.

Land sea mask

The land-sea mask of CFSR defines where the surface of the earth is interpreted as land and as sea, respectively. Whether an element is interpreted as land or sea affects, e.g., the estimated roughness of the surface, which in turn affects the wind profile. On land, the roughness is generally higher than at sea, hence, the wind speed on land is lower than at sea.

In some areas, the resolution of CFSR may be too coarse to resolve the land-sea boundary properly. In relation to this project, being well offshore, a very good performance was expected from CFSR and thus also from the hydrodynamic and wave models forced by CFSR.

Figure 3.6 shows the land-sea masks in CFSR and CFSv2, respectively, covering the North Sea and the Danish North Sea areas. An assessment of the effect of the change in land mask on the mean wind speed at the EINS site was made. The annual mean wind speed at 10 m height for the two periods is presented in Figure 3.7. The annual mean wind speed during the CFSR period (from 1979-2010) and for the period from 2011 (CFSv2 model) are almost identical with values slightly lower than 9 m/s. As EINS is reasonably far offshore, there is no effect of the land mask in the data.

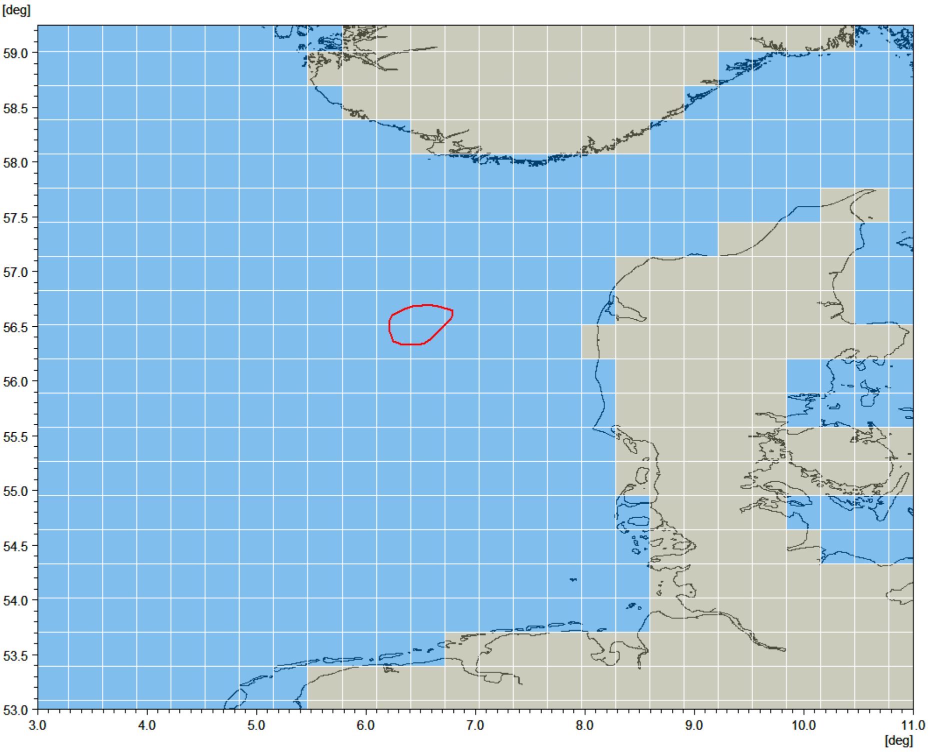

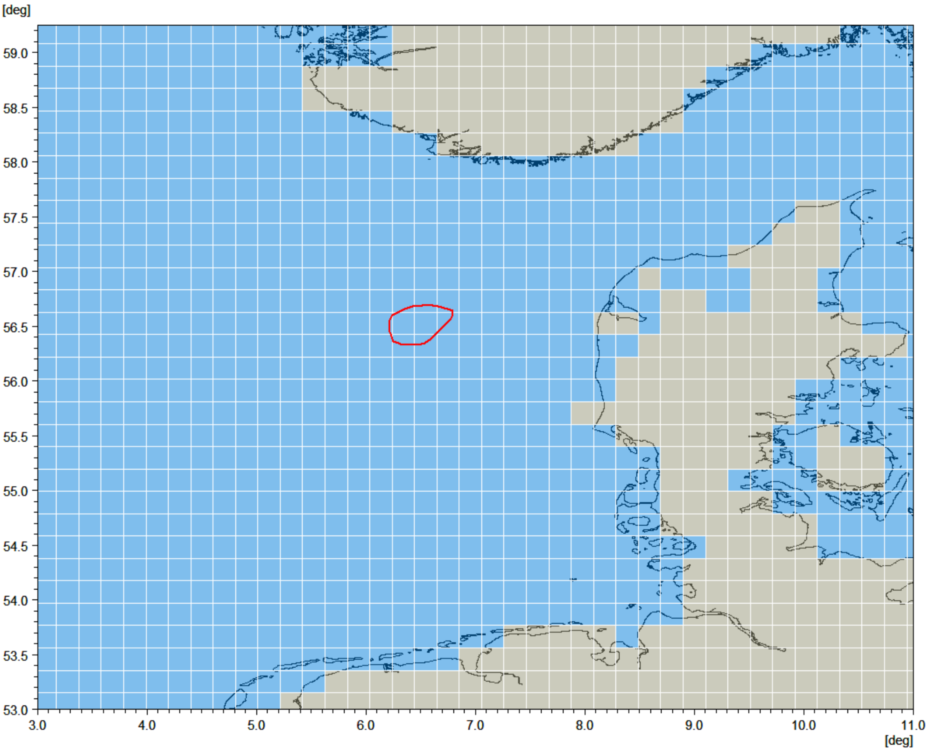

Figure 3.6 CFSR (upper) and CFSV2 (lower) land-sea mask in the North Sea (EINS OWF area is outlined in red)

The land cells are grey and water cells are blue.

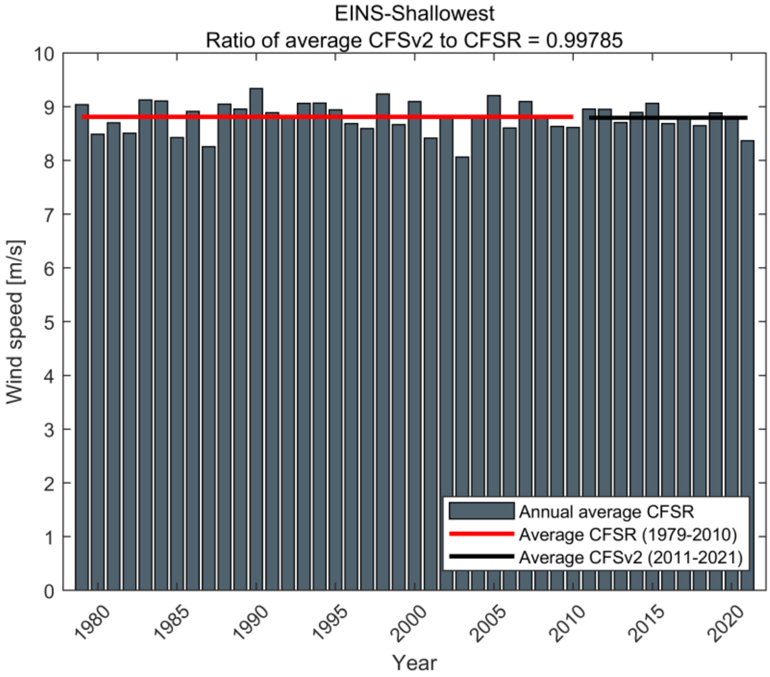

Figure 3.7 **Annual mean of 10 m wind speed from CFSR (1979-2021)**
Assessment of annual mean wind speed at EINS between CFSR (1979-2010) and CFSv2 (2011-2021) due to change in land mask.

3.3.2 Output specifications

The CFSR variables utilised for analyses in this study are summarised in Table 3.3. In CFSR, the wind speed at 10 mMSL (WS_{10}) is calculated from the lowest level model wind speed (~+20 mMSL) using the surface-layer similarity theory where the roughness length over water is updated at each time step using the Charnock relationship [21].

In addition to the 10 m wind, the 2 m air temperature, SST, air pressure and relative humidity are used in MIKE 21 SW to calculate the neutral wind fields. Those variables are also provided and analysed as part of this study (see Section 7.2).

Table 3.3 **Specifications of CFSR parameters used by this study**
[1] Spatial resolution for periods 1979-2010 and 2011-present
Wind is representative of 2-hour averages (see section below).

Parameter	Unit	Description	Spatial resolution [°][1]
WS_{10}	m/s	Wind Speed at height z [mMSL]	0.3/0.2
WD_{10}	°N-from	Wind Direction at height z [mMSL]	0.3/0.2
P_{air}	Pa	Air pressure	0.5
$T_{air,2m}$	°C	Air temperature at 2 mMSL	0.3/0.2
SST	°C	Sea Surface Temperature	0.3/0.2
RH	%	Relative Humidity	0.5
SR	W/m^2	Downward sun wave radiation flux	0.3/0.2

Averaging period

The averaging period is relevant when comparing various sources of data (e.g., models and measurements (peaks)), when considering operational conditions (weather windows), and for design purposes (extreme values).

For (in-situ) measurements, the averaging period is the duration of time across which each recording is averaged. For wind measurements, this is typically 10 min, while for currents and waves, it is usually the sampling duration (burst) of the instrument (typically 1-10 min for currents and 20-30 min for waves).

The output of numerical (hindcast/reanalysis) models represents an average of an area (grid cell) rather than a point, at a given point in time, and is not inherently associated with any averaging period. Further, there may be physical phenomena that the model does not describe or resolve adequately.

As such, one may expect the measurements to exhibit more variability (at high frequencies) compared to model data, or, reversibly, that the model data is somewhat ‘smoothed’ in time compared to measurements. The degree of ‘smoothing’ would depend on a combination of model type, forcing and grid.

To support validation of model data and application for operational and design purposes, a – representative – averaging period of the model data is assessed by comparing the magnitude and slope of a frequency power spectra of the model data to that of measurements averaged with various time windows. Such an analysis illustrates the energy density (variability) of the time series signals at frequencies up to the Nyquist frequency (two times the sampling frequency of the data, i.e., up to 2 h for model data saved 1-hourly).

Figure 3.8 shows a frequency power spectrum of wind speed from CFSR and measurements (LiDAR) at EINS-North. A reasonable agreement between CFSR data and measurements at the spectral tail is obtained when applying a 2 h averaging of the measurements, meaning that 2 h should be considered as a – representative – averaging period for CFSR (a better agreement might be obtained by using measurements closer to 10 mMSL in height than those recorded at about 100 mMSL applied here).

This finding is supported by other such comparisons of wind power spectra at different locations around the North Sea; see for example, the metocean study prepared for the Hollandse Kust (Zuid and Noord) Offshore Wind Farms [22].

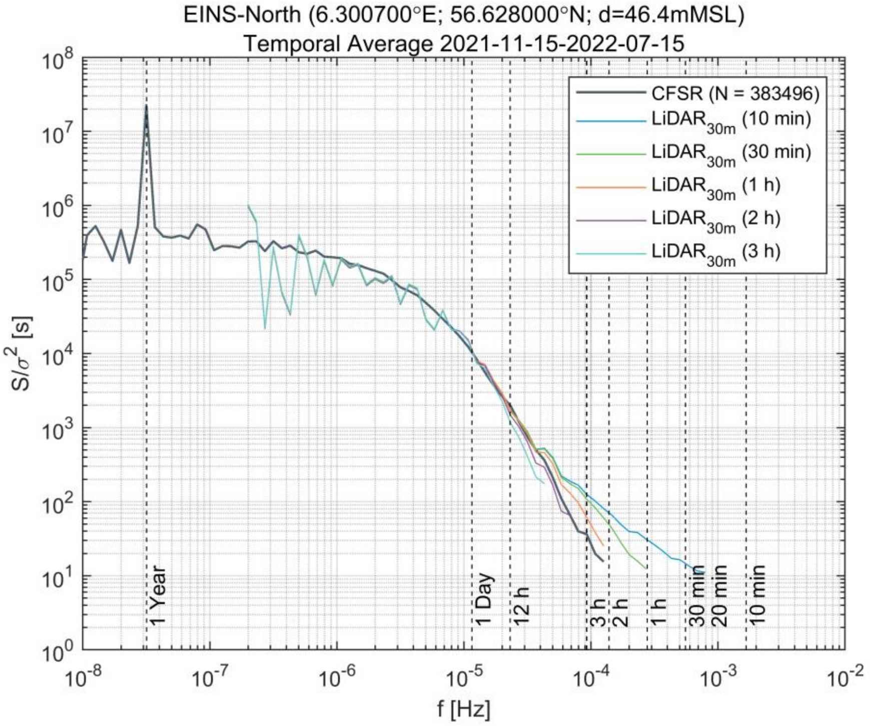

Figure 3.8 **Frequency power spectrum of wind speed at EINS-North**

3.3.3 Validation of wind

The CFSR dataset was validated against the measurements recorded by the Fugro floating LiDAR (EINS-North and EINS South), at the EINS site and by the Akrocean floating LiDAR at the Thor OWF site.

The measured wind speed of the local EINS LiDAR’s was converted from the recorded height of 30 m to 10 m following the approach in Section 3.2.1 (power profile with α = 0.08 as recommended for normal (average) wind conditions). The measured wind speed of the Thor LiDAR was already converted to 10 m prior to delivery to DHI.

Figure 3.9 to Figure 3.11 present comparisons of measured and CFSR data in terms of time series, scatter plots and wind roses. The figures demonstrate a very good agreement between the datasets of both wind speed and direction. Further validation of CFSR wind against measured data at other stations in the North Sea are available in [23].

In conclusion, the CFSR data compares very well to the local measurements and is considered excellent as wind forcing for the hindcast hydrodynamic and spectral wave models to produce accurate waves and current at the EINS site.

EINS-North

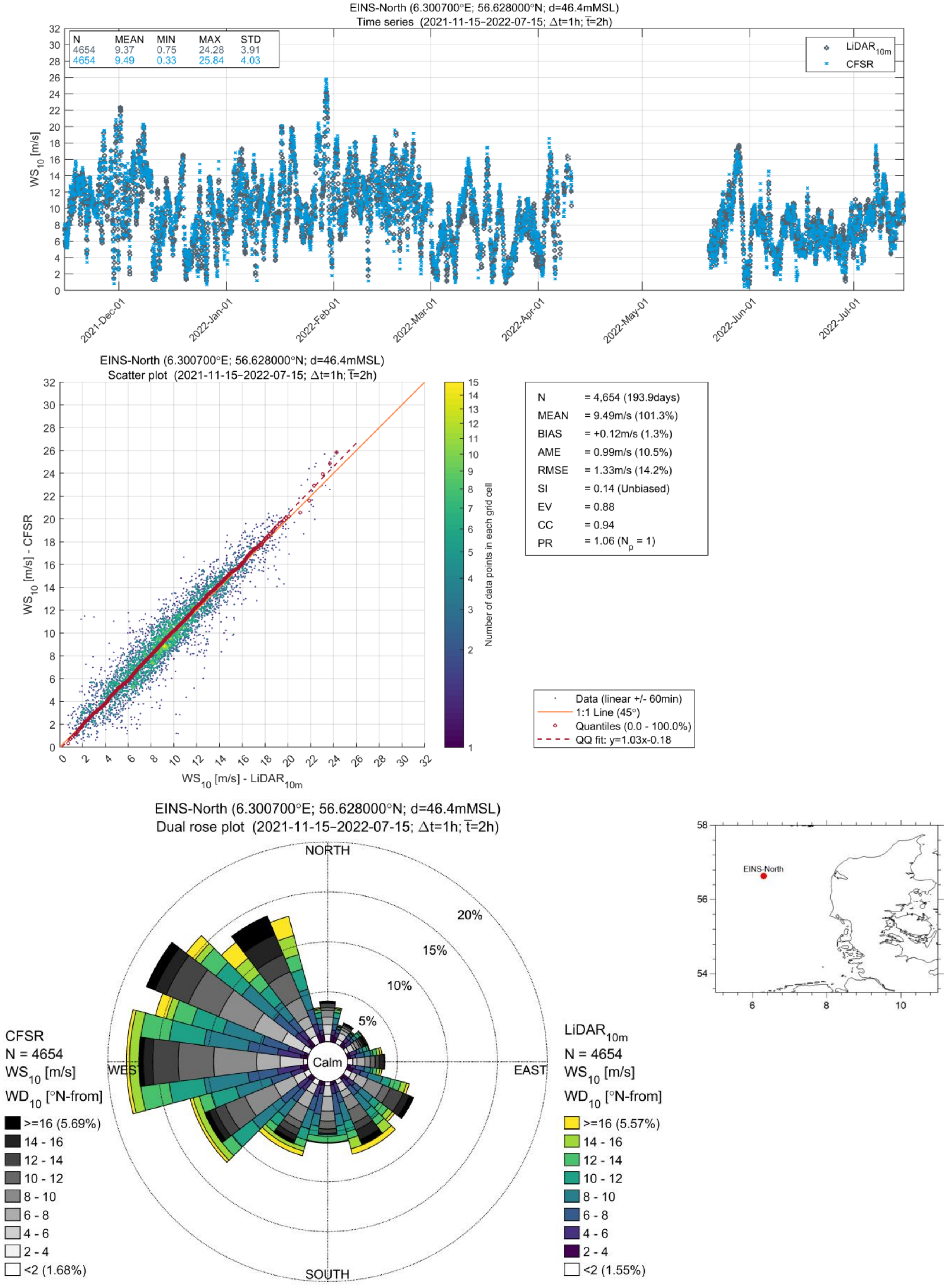

Figure 3.9 EINS-North: Comparison of CFSR and measured wind

EINS-South

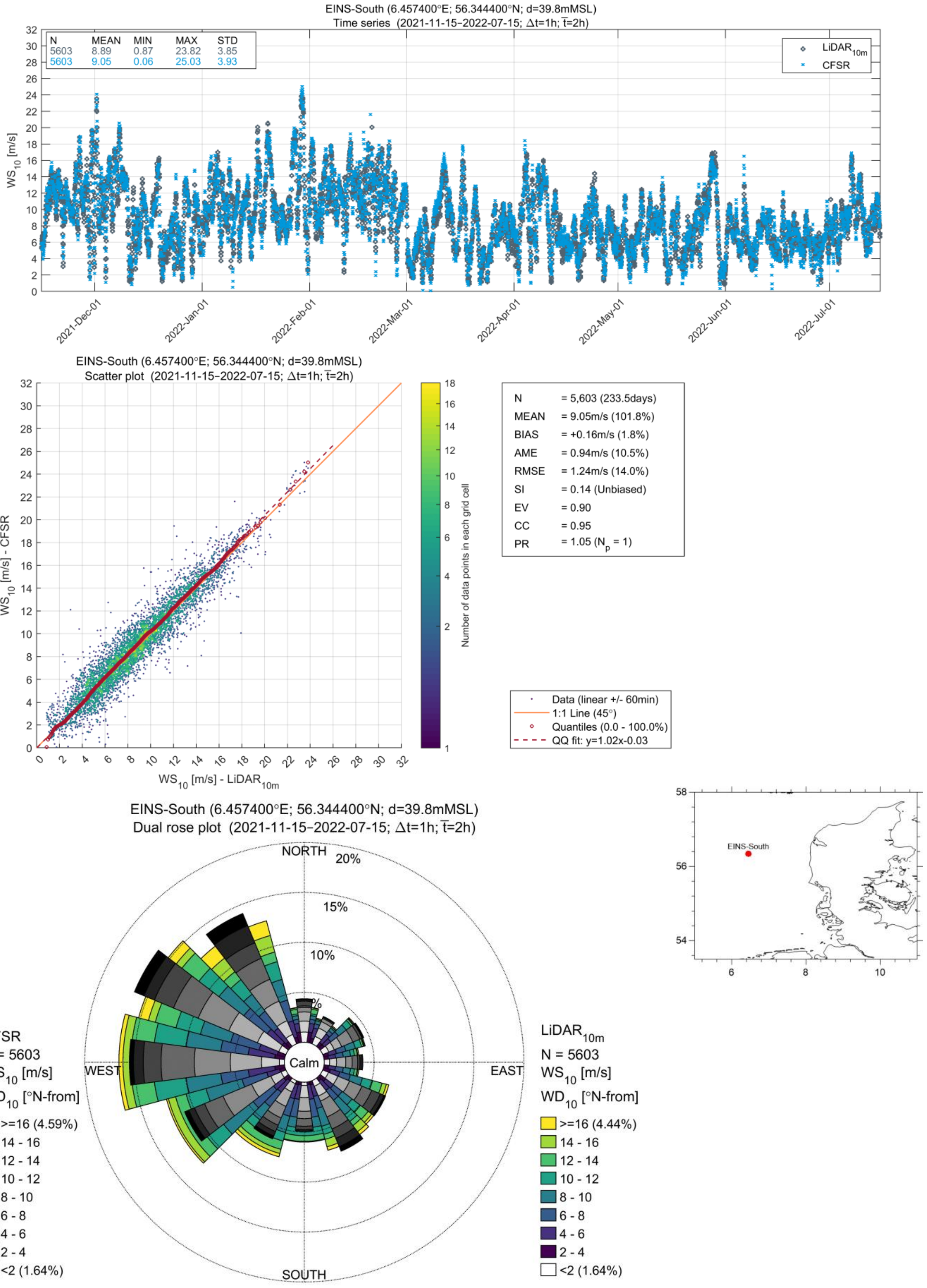

Figure 3.10 EINS-South: Comparison of CFSR and measured wind

Thor

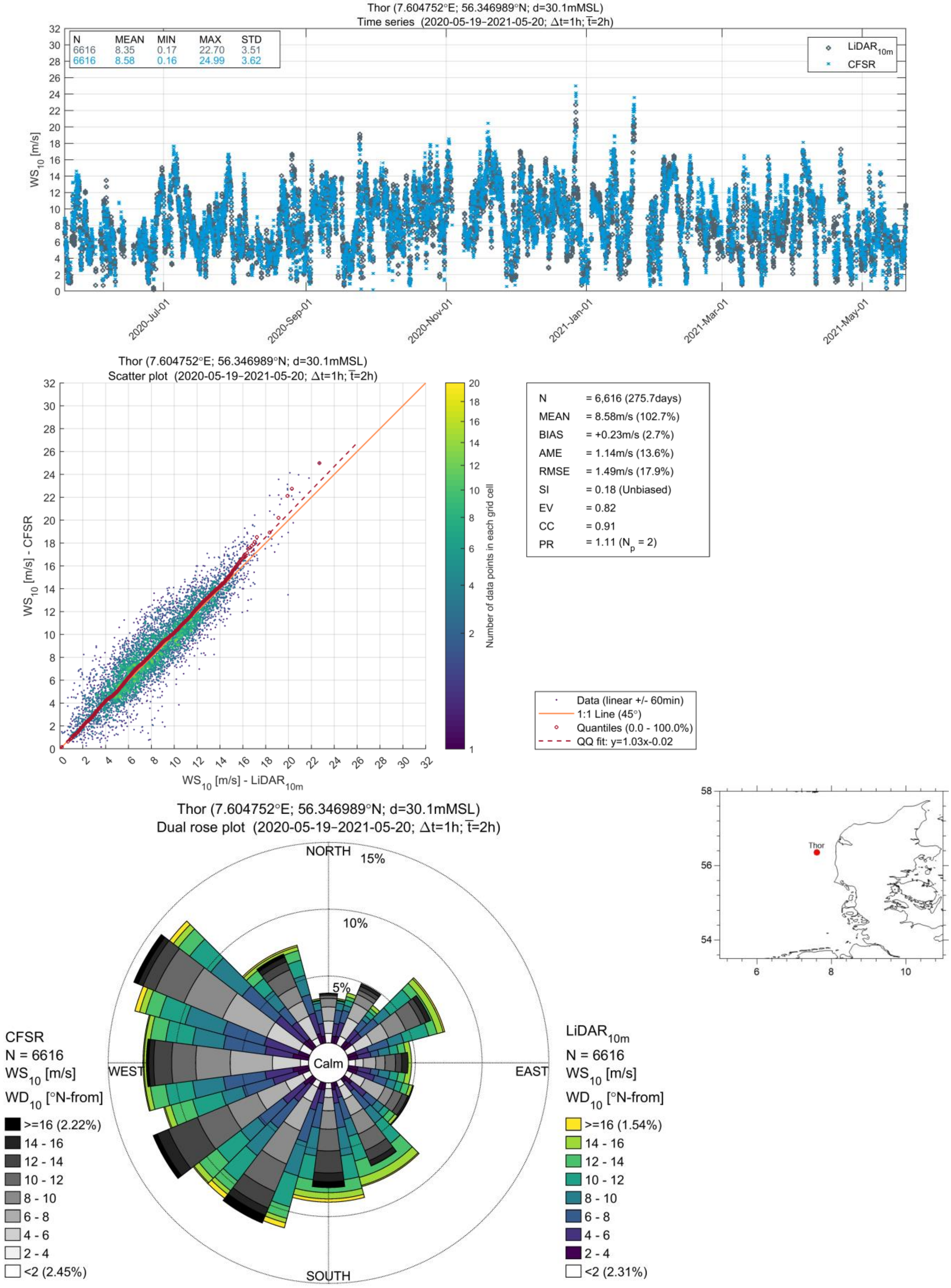

Figure 3.11 Thor: Comparison of CFSR and measured wind

4 Water Level

Hindcast water level data was established from a local high-resolution hydrodynamic (HD) model, HD_{EINS}, forced by boundary conditions extracted from the DHI North Europe regional model ($HD_{NE\text{-}DA}$) covering the northeast Europe. These data were established by numerical modelling using DHI's MIKE 21 Flow Model FM and validated against local and regional measurements.

4.1 General water level characteristics

Water levels in the North Sea are governed by astronomical tide and atmospheric conditions (wind and pressure). The tide has three amphidromic points (see Figure 4.1). One of them is located very close to the southwest coast of Norway. The second point is located at a distance >200 km offshore the west coast of Denmark. The third point is located between the coast of Norfolk (UK) and the Netherlands. The North Sea also receives energy form propagation of the Atlantic semi-diurnal Kelvin wave. Part of the energy leaks from the English Channel, as well as from diffraction around the north coast of Scotland.

From Figure 4.1, at the EINS site, due to its proximity to an amphidromic point, the tidal ranges are small with both neap and spring tides values below 0.5 m. However, the influence of large pressure systems combined with extreme winds can rise the total water level to values larger than 1.5 m.

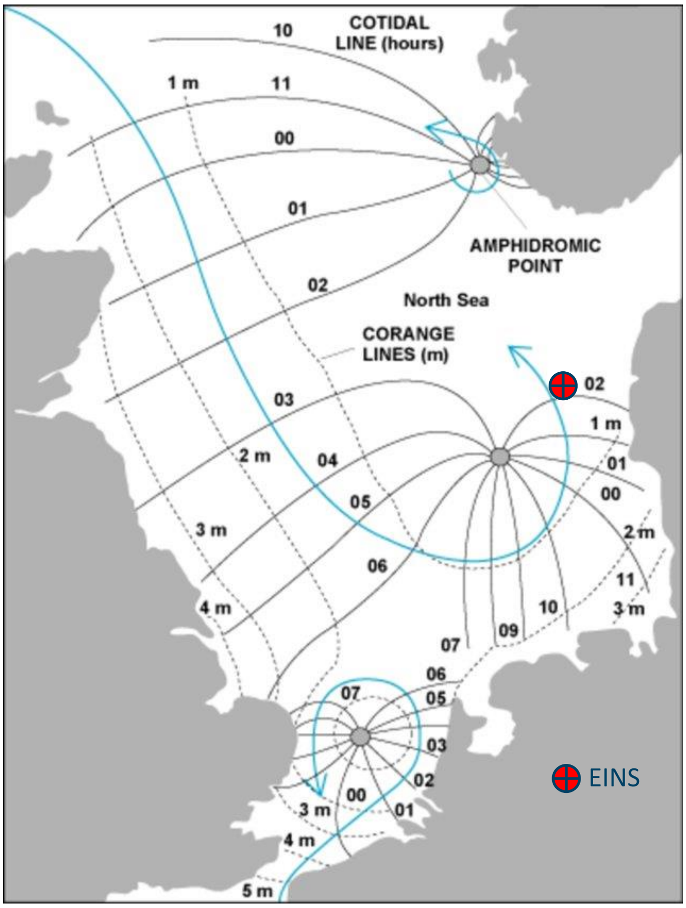

Figure 4.1 Tidal (amphidromic) systems in the North Sea (from [24])

4.2 Water level measurements

The locations and depths of the water level stations near or at the project location are summarised in Table 4.1 and shown on the map in Figure 4.2, while Figure 4.3 shows the temporal coverage of the water level measurements.

The quality of the measurements at the project location (EINS-North, EINS South and EINS-Island) was controlled by FUGRO [2], and checked by DHI before usage.

Water levels from the AWOS system, which collects and stores measurements from several sensors on Total E&P Denmark A/S (TEPDK) platforms in the North Sea, were retrieved for the Gorm, Harald and Valdemar platforms (see Figure 4.2). At these locations, Saab and Radac wave radars record the water surface elevation at a rate of ~10 times per second. From these measurements, water levels, wave heights and wave periods are determined. The quality of the measurements at these stations was checked by DHI before usage.

Water levels near the coastline (Ferring, Denmark) were obtained from the open-source data[3] of KDI (Kystdirektoratet), and quality controlled by DHI before usage. At this station, the 1-month moving average was subtracted from the data before comparison against model results, and outliers were removed, defined as data points more than ± 2.5 standard deviations from the mean. Also, some data was manually removed before comparison when irregularities were found, such as the following cases:

- Constant data over time
- Linearly connected data over time (instead of a tidal signal)

---

[3] https://confluence.govcloud.dk/display/FDAPI/Oceanographic+Observation

Table 4.1 **Metadata of applied water level measurements**
CP stands for current profiler and PS stands for pressure sensor

Station Name	Longitude [°E]	Latitude [°N]	Modelled seabed elevation [mMSL][1]	Surveyed seabed elevation [mMSL]	Data coverage	Instrument	Owner / Surveyor
EINS-North (CP)	6.3008	56.6272	-46.5	-46.0	15/11/2021 - 21/03/2022	Nortek Signature 500 current profiler	Energinet / FUGRO
EINS-South (CP)	6.4552	56.3442	-40.0	-40.0	15/11/2021 - 13/07/2022	Nortek Signature 500 current profiler	Energinet / FUGRO
EINS-North (PS)	6.3007	56.628	-46.5	-46.4	15/11/2021 - 12/02/2022	Thelma Biotel TBR700 pressure sensor	Energinet / FUGRO
EINS-South (PS)	6.4574	56.3444	-39.8	-39.8	15/11/2021 - 26/10/2022	Thelma Biotel TBR700 pressure sensor	Energinet / FUGRO
EINS-Island (Mini 2, CP)	6.5130	56.4925	-28.9	-28.0	15/11/2021 - 20/05/2022	Nortek Signature 500 current profiler	Energinet / FUGRO
Harald	4.2734	56.3448	-66.3	-67.0	15/09/2005 - 15/09/2015	Wave radar	TEPDK
Gorm	4.7601	55.5803	-36.7	-39.7	15/09/2005 - 15/09/2015	Wave radar	TEPDK
Valdemar[2]	4.5657	55.8048	-40.4	-41.9	28/12/2015 - 03/04/2016	Unknown	TEPDK
Thor[2]	7.605	56.347	-30.2	-30.1	2020-05-19 - 2021-05-19	AIRMAR EchoRange SS510	Energinet / Akrocean
Ferring	8.115	56.525	-3.1	-4.3[3]	1994-01-01-2022-04-25	Unknown	KDI

[1] Modelled seabed elevation based on the production mesh
[2] Data was discarded for the whole period due to irregularities
[3] Seabed elevation from EMODnet

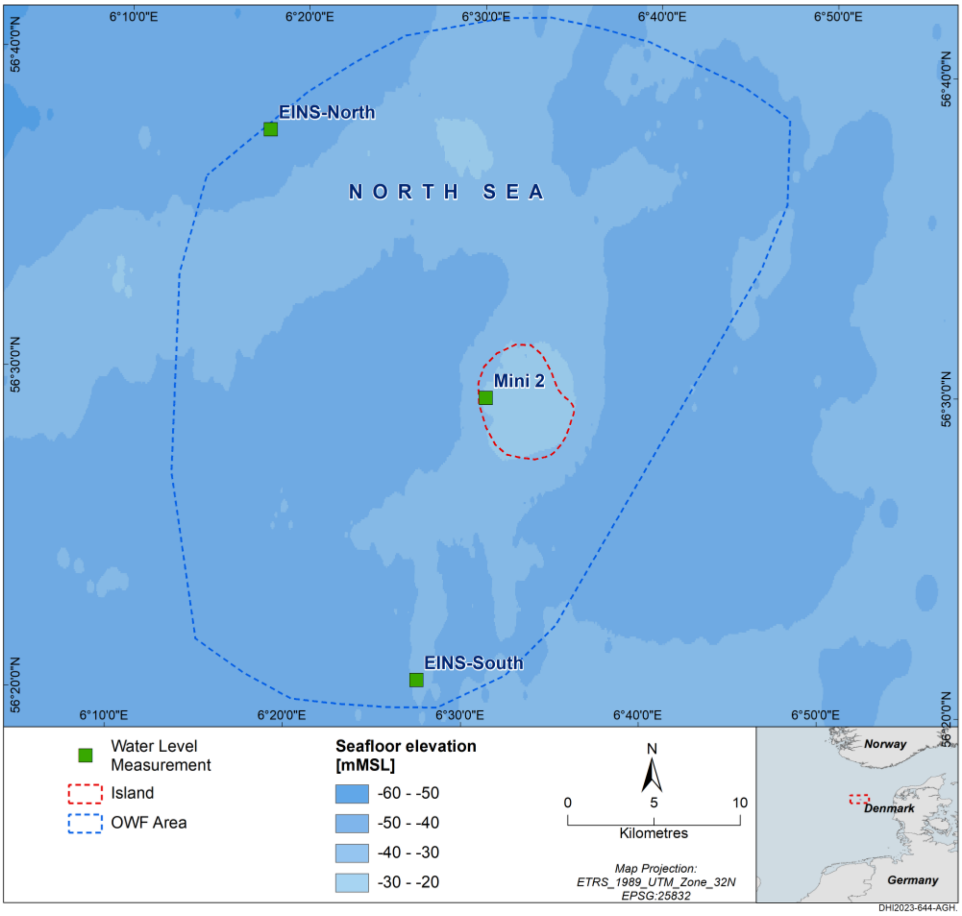

Figure 4.2 **Location of local water level measurements**
Location of regional measurements are shown in Figure 0.1.

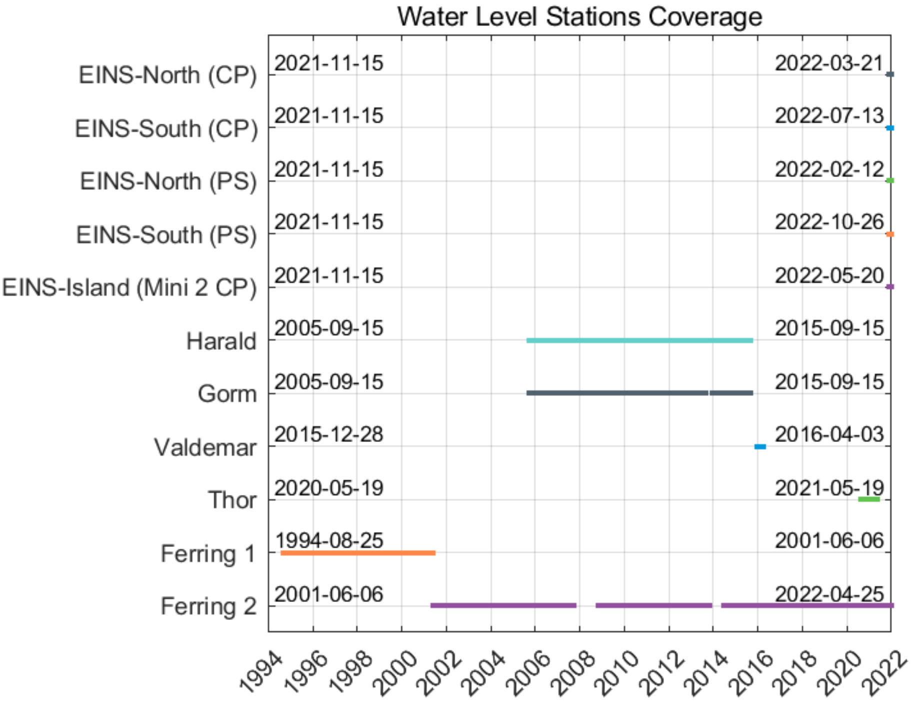

Figure 4.3 **Temporal coverage of water level measurements**

4.3 Hindcast water level data

Water level and current data for the metocean study were established from a local high-resolution hydrodynamic (HD) model developed by DHI for this study, named HD_{EINS}, see Section 4.3.3, which is forced by boundary conditions from a DHI regional model covering North Europe (HD_{NE-DA}), see Section 4.3.2. These data were established through numerical modelling using DHI's MIKE 21 Flow Model FM (see Section 4.3.1).

Flow modelling includes tide, forced from DHI's global tide model, and surge, forced by the meteorological data described in Section 3. Hydrodynamic model outputs were produced with a 30 min resolution and validated against local measurements (see Section 4.3.6). Described in this section are the following:

- Brief introduction to MIKE 21 Flow Model FM Release 2022
- General description of the Regional North Europe Model from which boundary conditions were used to force the local model, HD_{EINS}
- Details on the setup and calibration of the local EINS HD Model, HD_{EINS}
- Sensitivity studies; and
- Water level validation of the HD_{EINS} model

4.3.1 MIKE 21 Flow Model FM (HD)

The MIKE 21 Flow Model is a modelling system for 2D free-surface depth-integrated flows that is developed and maintained by DHI and offered as part of MIKE Powered by DHI [25]. The model system is based on the numerical solution of the two-dimensional (2D) incompressible Reynolds-averaged Navier-Stokes equations subject to the assumptions of Boussinesq and of hydrostatic pressure. The model is applicable for the simulation of hydraulic and environmental phenomena in lakes, estuaries, bays, coastal areas, and seas, wherever stratification can be neglected. The model can be used to simulate a wide range of hydraulic and related items, including tidal exchange and currents and storm surges [25].The hydrodynamic (HD) module is the basic module in the MIKE 21 Flow Model FM. The HD module simulates water level variations and flows in response to a variety of forcing functions in lakes, estuaries, and coastal regions. The effects and facilities include:

- Bottom shear stress
- Wind shear stress
- Barometric pressure gradients
- Sources and sinks (e.g. rivers, intake and outlets from power plants) (not applied here)
- Flooding and drying
- Momentum dispersion
- Tidal potential
- Coriolis force
- Precipitation/Evaporation (not applied in this study)
- Ice coverage (not applied in this study)
- Wave radiation stresses (not applied in this study)

The model uses a flexible mesh (FM) based on unstructured triangular or quadrangular elements and applies a finite volume numerical solution technique [25]. For HD_{EINS}, MIKE 21 HD Release 2022 was used.

4.3.2 North Europe HD Model ($\text{HD}_{\text{NE-DA}}$)

The North Europe hydrodynamic model previously developed by DHI, $\text{HD}_{\text{NE-DA}}$, was used to obtain boundary data for the local hydrodynamic model. Figure 4.4 shows the $\text{HD}_{\text{NE-DA}}$ domain along with the bathymetry. The $\text{HD}_{\text{NE-DA}}$ model includes tide (boundaries extracted from DHI's global tide model) and surge forced by wind and air pressure from the CFSR dataset. Furthermore, the model was optimised by using data assimilation of measured water levels. The assimilation was applied for the period from 1994-01-01 to 2017-12-31 when most of the stations had data were available. Figure 4.5 shows stations used for assimilation or validation of the $\text{HD}_{\text{NA-DA}}$ model in the North Sea area. The results of $\text{HD}_{\text{NE-DA}}$ have been successfully applied in many projects in the North Sea, the English Channel, the Baltic Sea, and the Inner Danish waters. Validation of water levels and currents are presented in Sections 4.3.6 and 5.3.2.

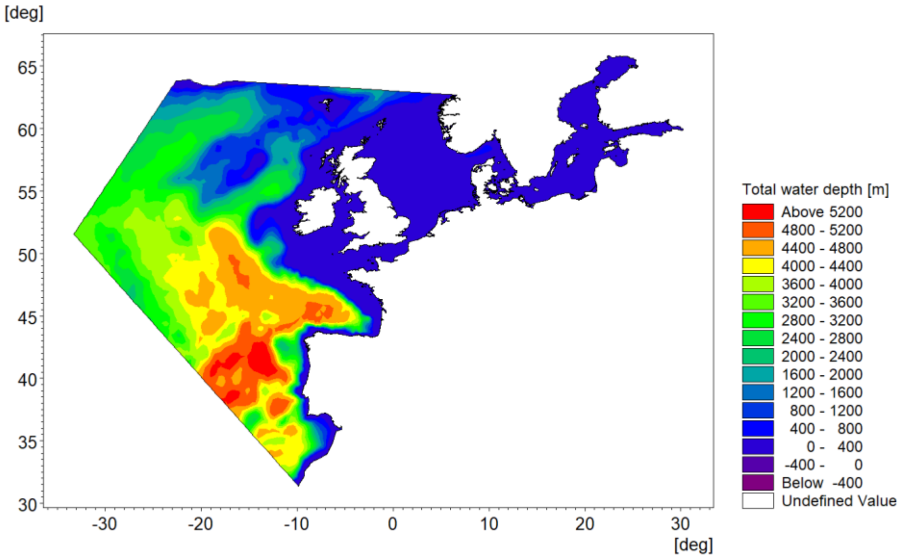

Figure 4.4 North Europe hydrodynamic model ($\text{HD}_{\text{NE-DA}}$) bathymetry

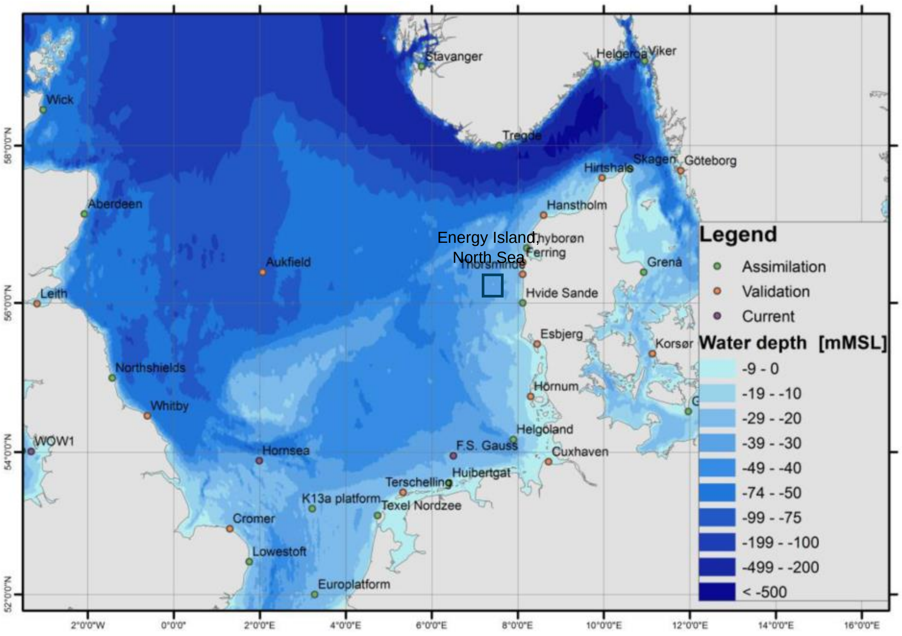

Figure 4.5 Water level and current measurement stations used for assimilation and validation of $\text{HD}_{\text{NE-DA}}$

4.3.3 Local EINS HD Model (HD$_{EINS}$)

This section describes the local hydrodynamic model for EINS (HD$_{EINS}$), which adopted boundary conditions and settings from the regional HD$_{NE\text{-}DA}$ model as described in Section 4.3.2, considering three key matters:

- Adoption of the local surveyed bathymetric data, cf. Section 2
- Application of a refined mesh resolution, and
- Local calibration of bed friction etc.

The boundary conditions for the HD$_{EINS}$ model were extracted from the regional model (HD$_{NE\text{-}DA}$). In this way, the local model was a high-resolution, down-scaled version of the regional model. Table 4.2 shows the settings of the hydrodynamic model set-ups, i.e., of HD$_{NE\text{-}DA}$ and HD$_{EINS}$. The impact or relevance of some of these parameters on the model results was assessed during the calibration phase and the sensitivity studies (e.g., mesh converge study, bed friction), and the final model setup of the HD$_{EINS}$ model is shown in Table 4.2 after calibration. During the calibration phase, model domain extent, as well as bed friction and mesh resolution were varied to achieve the best result. Initially, a non-uniform value of Manning's number was used, however, the best agreement was obtained using a constant value across the entire domain. The effect of the mesh resolution is discussed in Section 4.3.5.

The model extent, along with the bathymetry and the final mesh resolution, is shown in Figure 4.6.

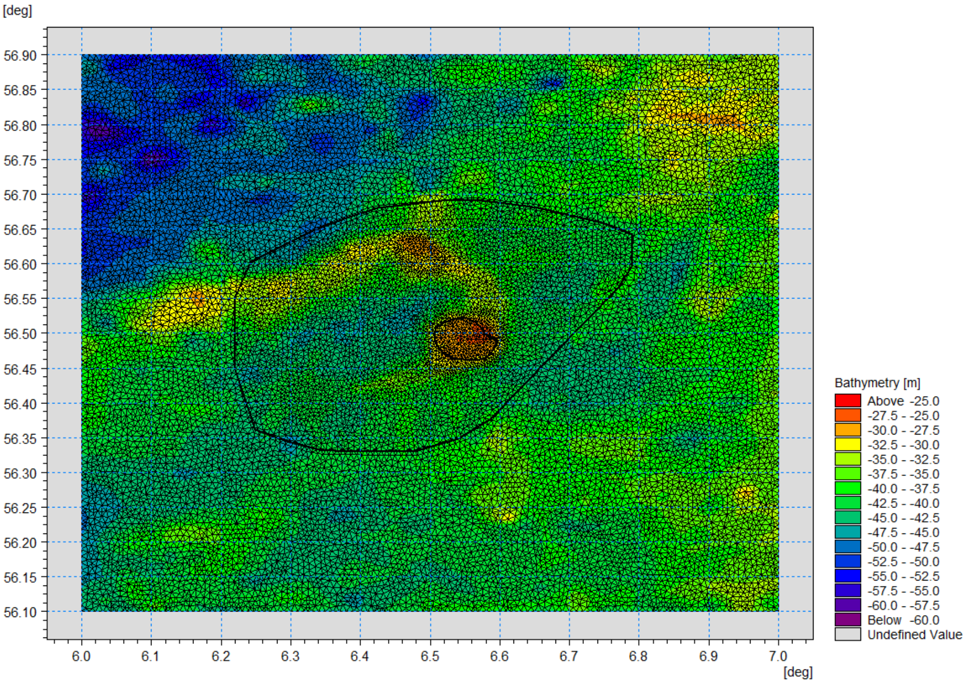

Figure 4.6 **Computational domain of the local hydrodynamic model, HD$_{EINS}$**
Flexible mesh is shown in dark lines; bathymetry/water depth is shown in colours.

Table 4.2 Summary of hydrodynamic model configurations

Setting	HD_{NE-DA} (see Section 4.3.2)	HD_{EINS} (after calibration)
Mesh resolution	Mainly 3-10 km.	Varying from 800 m at the OWF area to ~400 m at the Island
Simulation period	1979-01-01 – 2022-09-30	1979-01-01 – 2022-09-30
Output time step	30 minutes	30 minutes
Density	Barotropic	Barotropic
Eddy viscosity	Smagorinsky formulation with constant value of 0.28	Smagorinsky formulation with constant value of 0.28
Bed resistance	Manning number varies in domain ranging from 42 in the deepest areas to 39.6 $m^{1/3}/s$ at the northeast region of domain	A constant Manning number of 45 $m^{1/3}/s$ in the entire domain
Wind forcing	CFSR wind fields, see Section 3.2.1 Friction varying with wind speed: Linear variation from 0.001255 at 7m/s to 0.002425 at 25m/s wind speed	CFSR wind fields, see Section 3.2.1 Friction varying with wind speed: Linear variation from 0.001255 at 7m/s to 0.002425 at 25m/s wind speed
Tidal potential	Included	Included
Boundary conditions	Specified water level boundary conditions, extracted from DTU10 tide, varying in time and along the boundaries.	Flather boundary conditions, extracted from HD_{NE-DA} model, varying in time and along the boundaries: Current speed components Water level
Output specifications	WL, CS and CD saved at all grid elements with 1 hour interval.	WL, CS and CD saved at all grid elements with 30 min interval.

4.3.4 Output specifications

Table 4.3 presents the output specifications of HD_{EINS}.

Table 4.3 Output specifications of HD_{EINS}
Parameters saved at all grid elements at 30 min intervals.

Parameter	Abbreviation	Unit
Water level (total)	WL	mMSL
Current speed (depth-average)	CS	m/s
Current direction (depth-average)	CD	°N (going to)

4.3.5 Sensitivity studies

Mesh convergence

The mesh convergence study was undertaken to set a model resolution that allowed an accurate description of the conditions without model computation time being unreasonably impacted by the mesh size. The focus of this exercise was the extreme depth-averaged current speed events (see Section 5.3.1), however, water levels were also assessed.

The mesh convergence tests assessed the difference in results between the mesh resolutions for which three (3) different events were selected (i.e., Cases 01 to 03 from the previous section) with four different mesh resolutions: 200, 400 and 600 m at the island, and 600 m across entire area. The different mesh resolutions are shown in Figure 4.8. The extreme conditions were identified as the maximum depth-averaged current speeds (in HD_{NE-DA}) at three locations.

The mesh sensitivity assessment was done at the shallowest element of the model mesh, EINS-1 (shallowest): Lon.: 6.575°; Lat: 56.501°; model depth: 26.6 mMSL.

Results at EINS-1 (shallowest) location are shown in Figure 4.7. This figure shows time series of water levels for each of the four mesh resolutions. The results show practically no difference in water levels between the mesh resolutions. Section 5.3.1 presents the mesh sensitivity study for depth-averaged current speeds, as well as the reasoning behind the selecting the 400 m mesh resolution going forward.

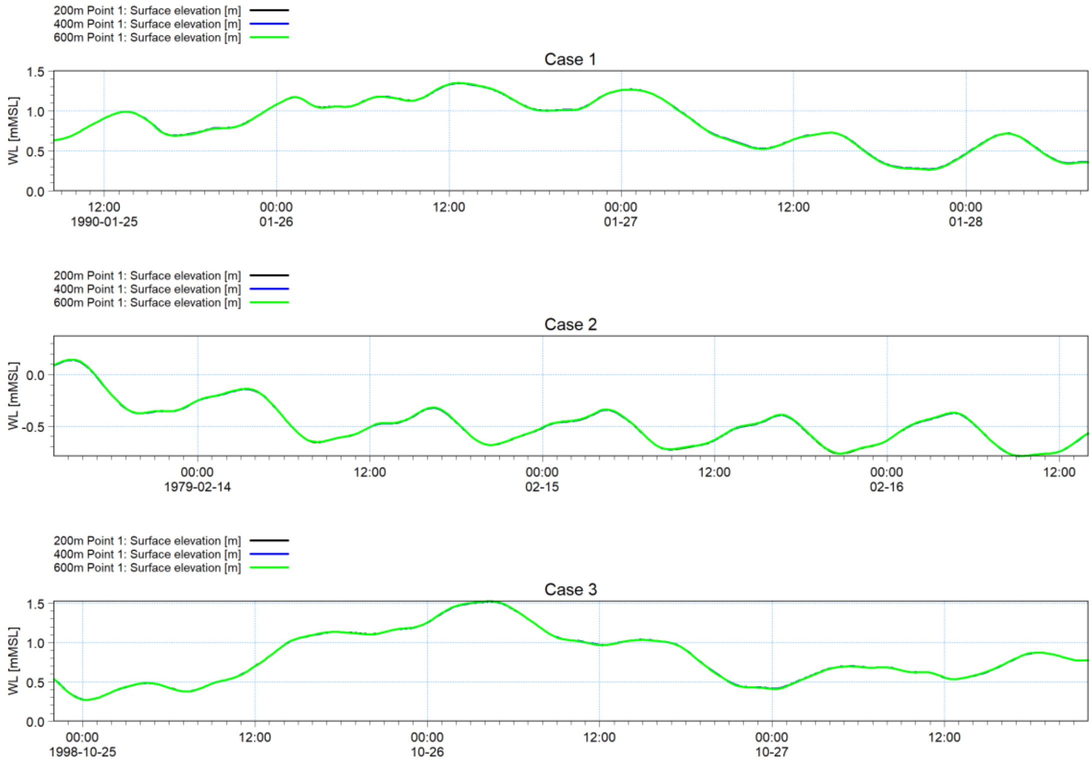

Figure 4.7 Comparison of water levels for the different mesh resolutions at EINS-1 (shallowest)
Case 01: 1990-01-26 (Top); Case 02: 1979-02-15 (Middle), and Case 03: 1998-10-25

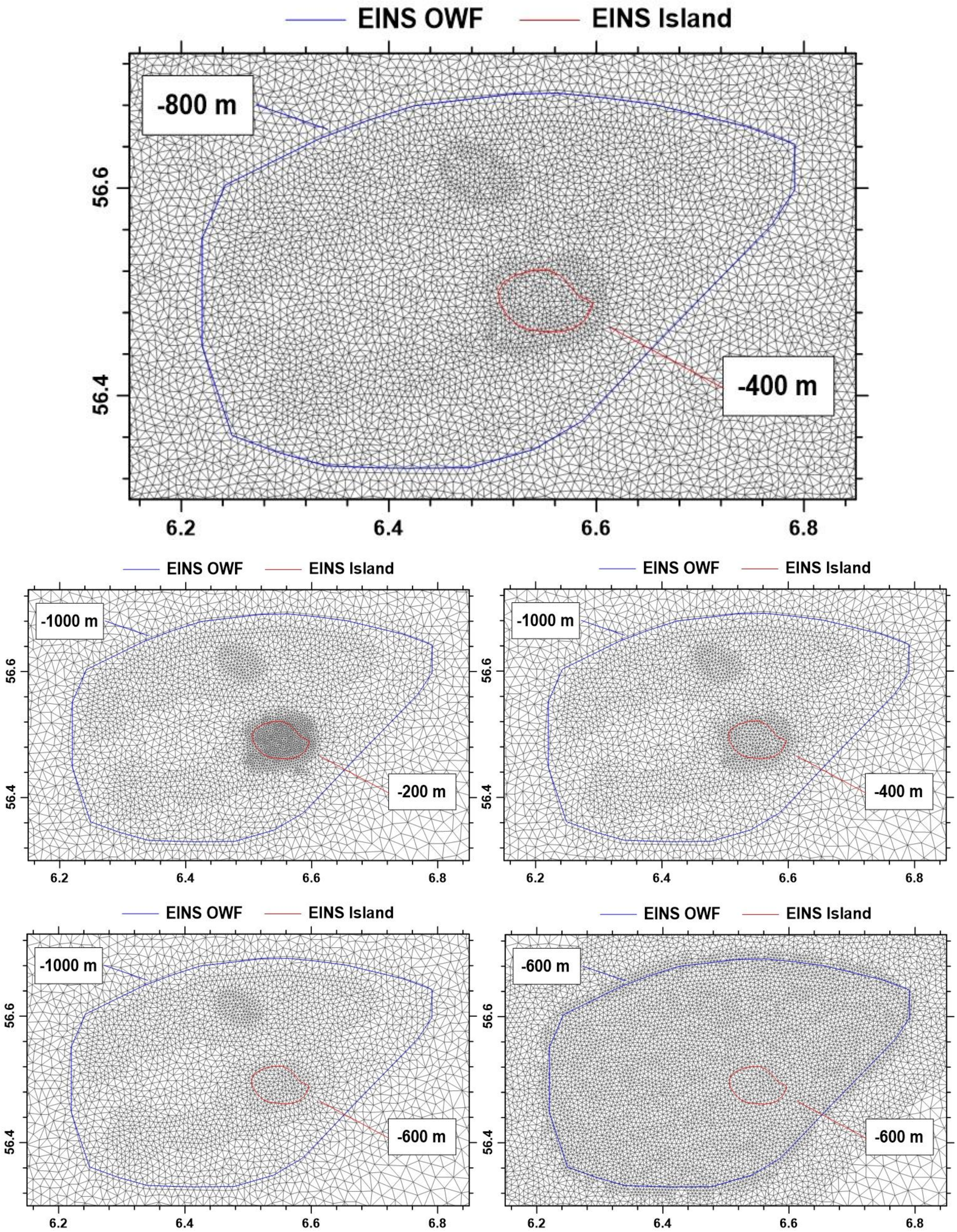

Figure 4.8 **Comparison of the different mesh resolutions for mesh convergence analysis**
Top panel shows the final mesh with resolution of 400 m at the island area
Middle left panel shows the 200 m resolution mesh at the island area
Middle right panel shows the 400 m resolution mesh at the island area
Bottom left panel shows the 600 m resolution mesh at the island area
Bottom right panel shows the 600 m resolution across the Island and OWF areas.

4.3.6 Validation of water level

The HD$_{EINS}$ model was validated against ~8 months of water levels measured at the LiDAR buoys and ADCPs deployed at the EINS site (see Figure 4.10 to Figure 4.14). The HD$_{NE-DA}$ model used to obtain the boundary conditions that forced HD$_{EINS}$ was also validated against longer term (up to ~31 years) records to show its validity (see Figure 4.15 to Figure 4.17). A summary of the stations used for the validation of both models is presented in Table 4.1 and Figure 4.2.

Overall, results show a skilful performance of the local HD$_{EINS}$ model at all the stations, with a BIAS close to zero, a correlation coefficient (CC) larger than 0.9, and a QQ alignment close to the 1:1 line. However, there is an extreme event (Storm Malik, 2022-01-30) that the model underestimates. Unfortunately, given the limited period of the measurements, only a single extreme event was captured, which is not sufficient to conclude whether the model consistently underestimates peak events. However, as shown in Figure 4.15 to Figure 4.17 (Harald, Gorm, Ferring) , the regional model, HD$_{NE-DA}$, providing boundaries to HD$_{EINS}$ has an overall high accuracy of extreme water level events with peak ratios in the range of 0.94 ≤ PR ≤ 1.05. Furthermore, a comparison of water levels between the HD$_{EINS}$ and HD$_{NE-DA}$ models was made to assess the performance of the former over a longer period. Results of this comparison (see Figure 4.9) show a similar performance during both, normal and extreme conditions. These assessments give confidence in the HD$_{EINS}$ model for normal and extreme events.

A comparison of the maximum water levels measured by the instruments closely deployed show a difference of 0.29 m between EINS-South (CP) and EINS-South (PS), and a difference of 0.03 m between EINS-North (CP) and EINS-South (PS). This indicates that the measurement uncertainty can be (at least) up to order of ~0.29 m.

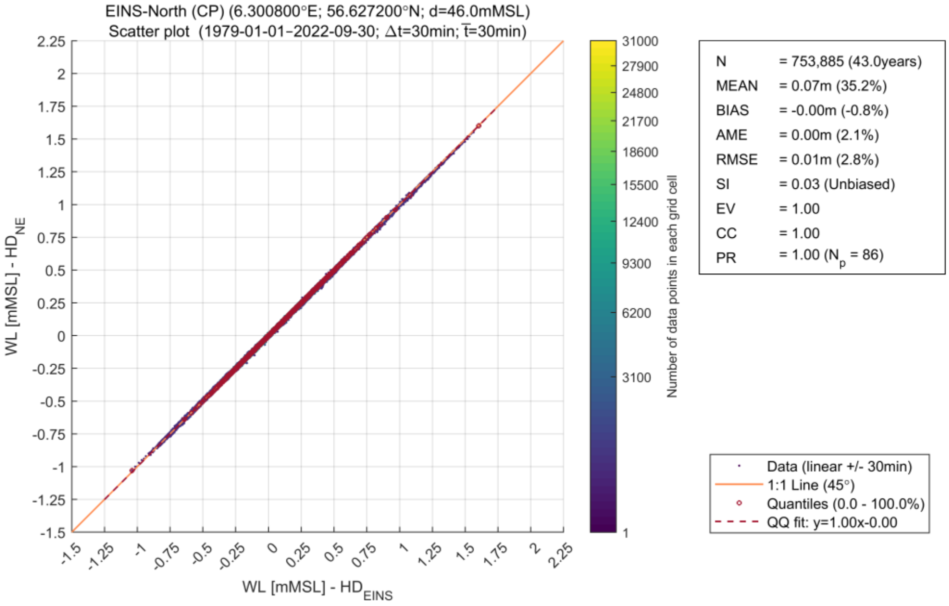

Figure 4.9 **Comparison of water levels between HD$_{EINS}$ and HD$_{NE-DA}$ at EINS-North (current profiler seabed)**

EINS-North (current profiler seabed)

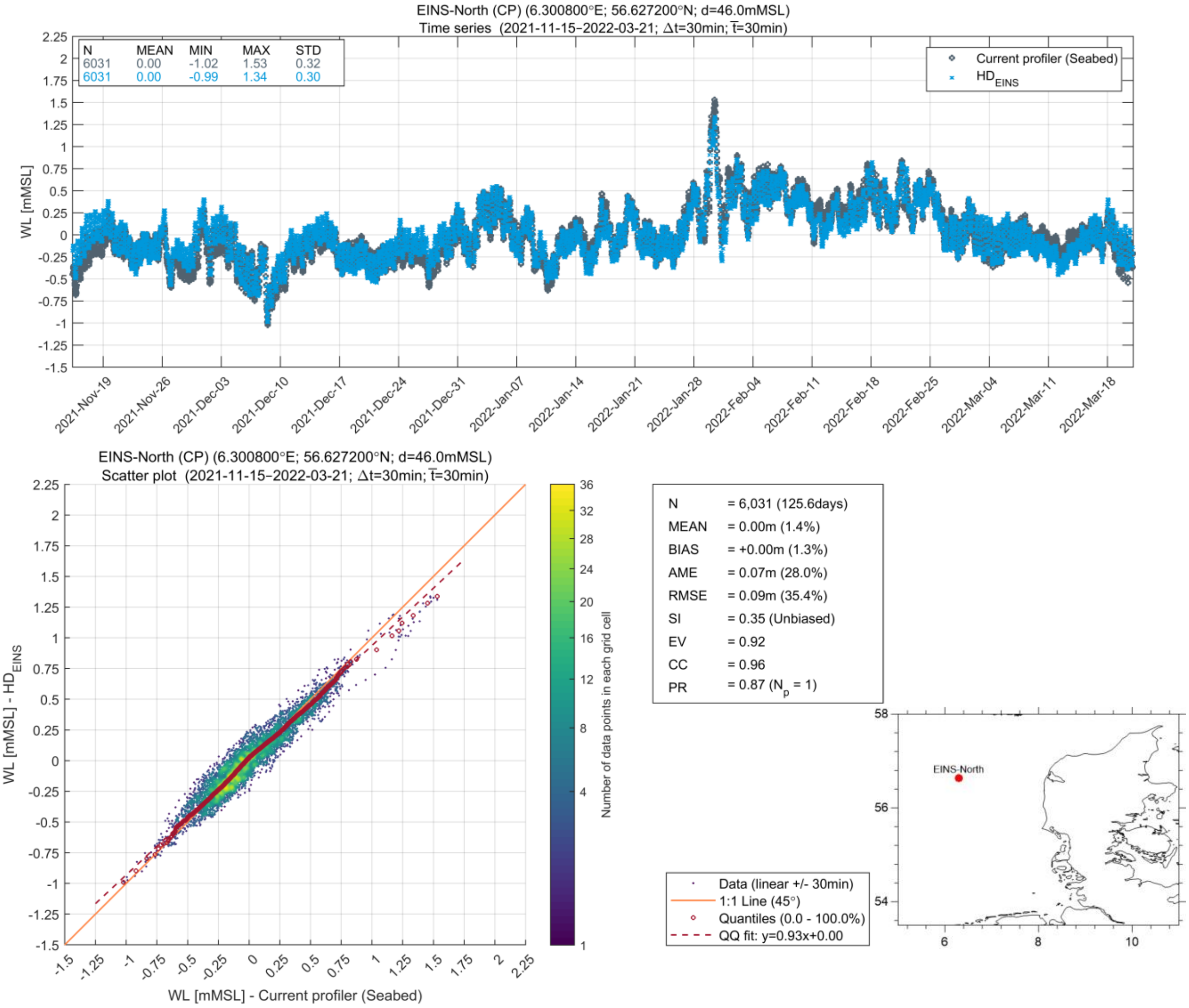

Figure 4.10 Comparison of water levels at EINS-North (current profiler seabed)

EINS-South (current profiler seabed)

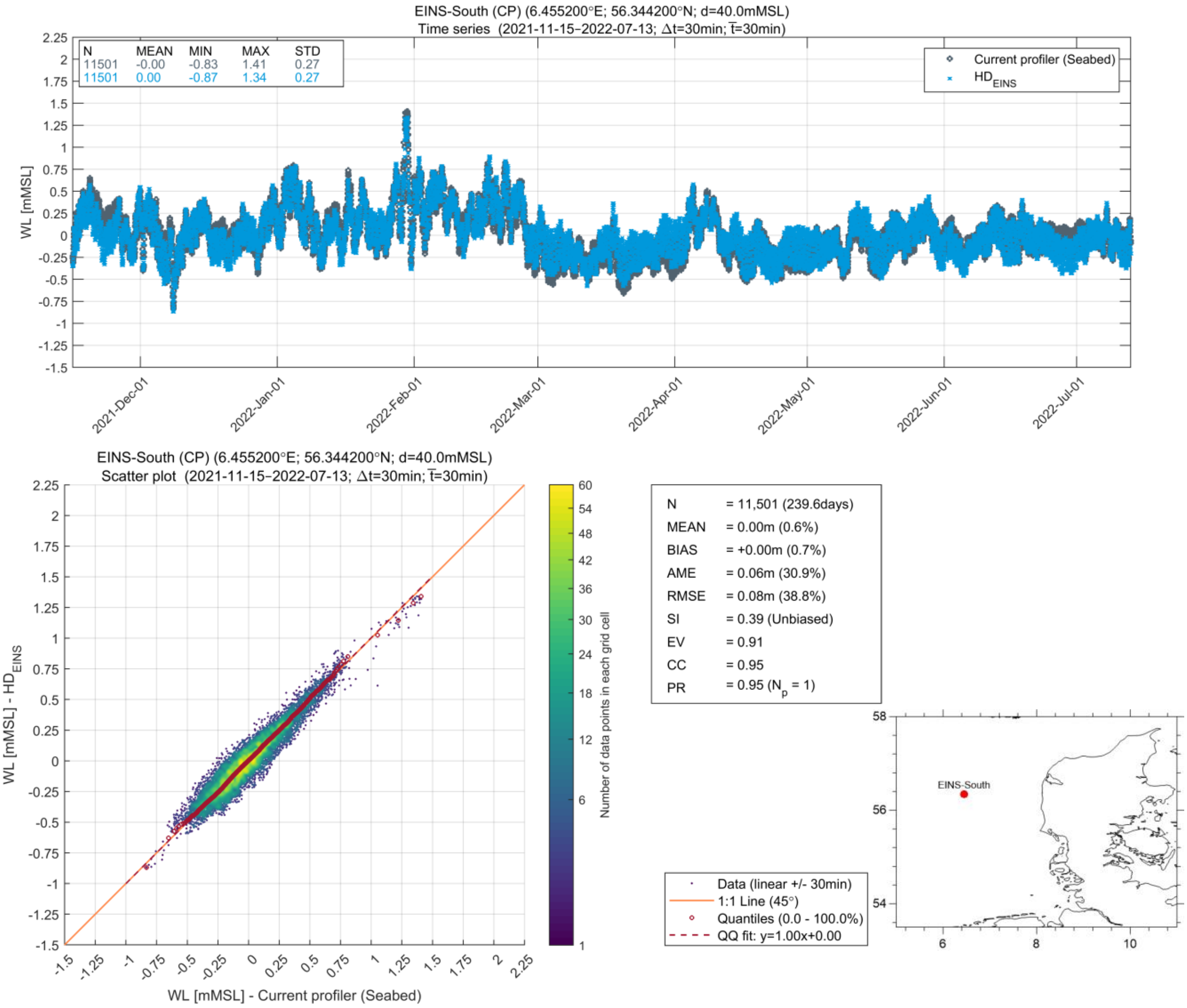

N	MEAN	MIN	MAX	STD
11501	-0.00	-0.83	1.41	0.27
11501	0.00	-0.87	1.34	0.27

N = 11,501 (239.6days)
MEAN = 0.00m (0.6%)
BIAS = +0.00m (0.7%)
AME = 0.06m (30.9%)
RMSE = 0.08m (38.8%)
SI = 0.39 (Unbiased)
EV = 0.91
CC = 0.95
PR = 0.95 (N_p = 1)

Figure 4.11 Comparison of water levels at EINS-South (current profiler seabed)

EINS-North (pressure sensor seabed)

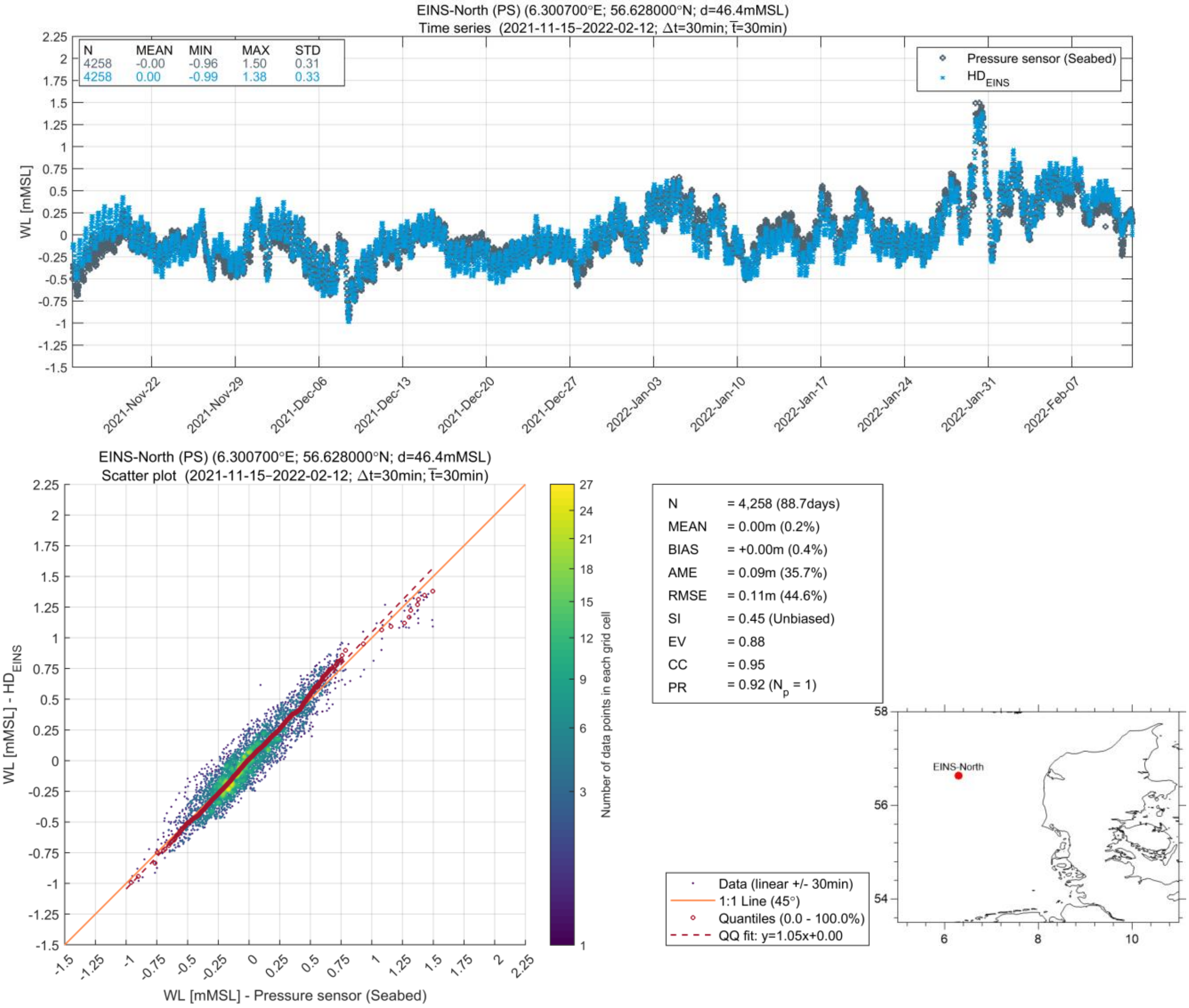

N	MEAN	MIN	MAX	STD
4258	-0.00	-0.96	1.50	0.31
4258	0.00	-0.99	1.38	0.33

N = 4,258 (88.7days)
MEAN = 0.00m (0.2%)
BIAS = +0.00m (0.4%)
AME = 0.09m (35.7%)
RMSE = 0.11m (44.6%)
SI = 0.45 (Unbiased)
EV = 0.88
CC = 0.95
PR = 0.92 (N_p = 1)

Figure 4.12 Comparison of water levels at EINS-North (pressure sensor seabed)

EINS-South (pressure sensor seabed)

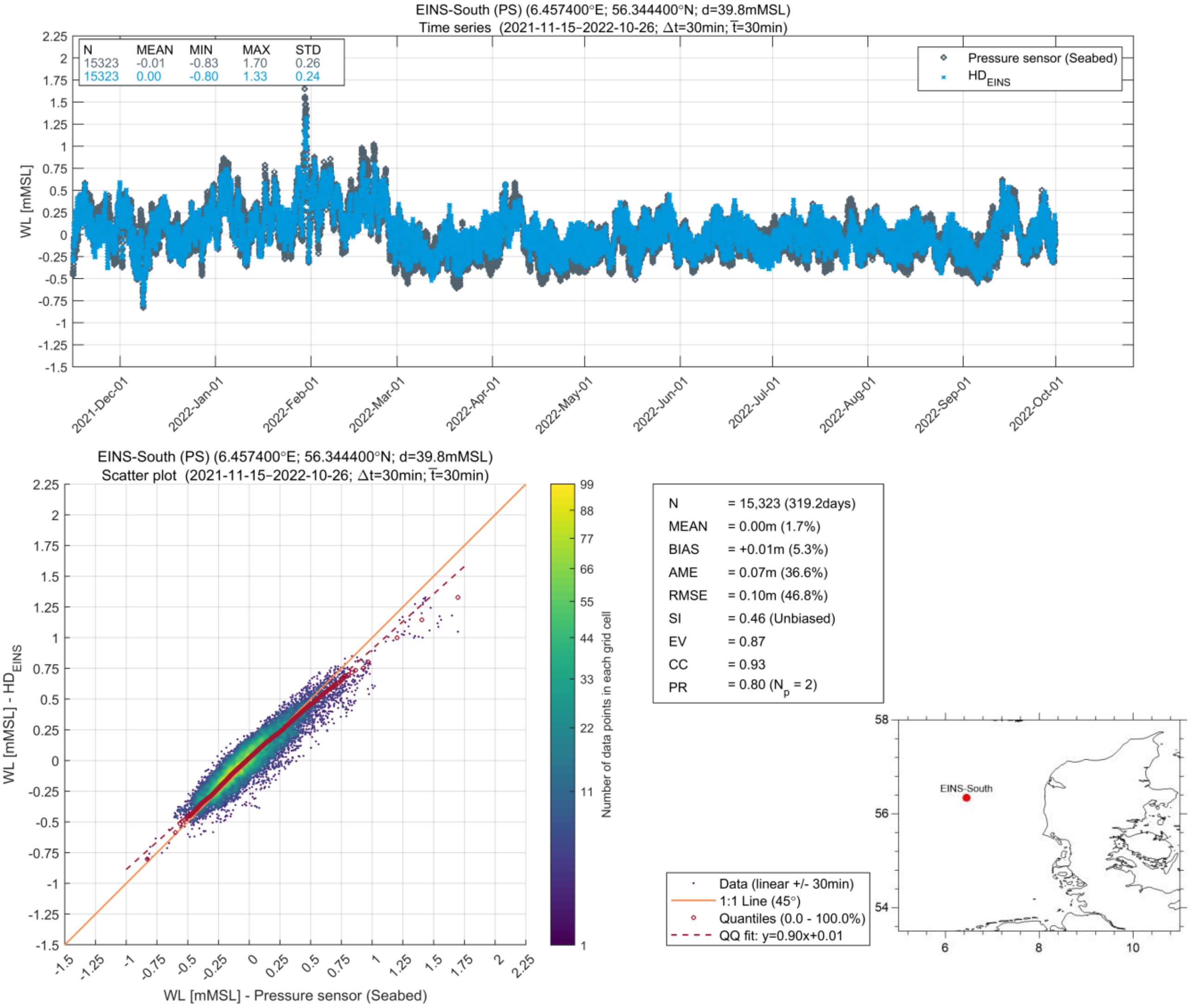

Figure 4.13 Comparison of water levels at EINS-South (pressure sensor seabed)

EINS-Island (Mini 2, current profiler seabed)

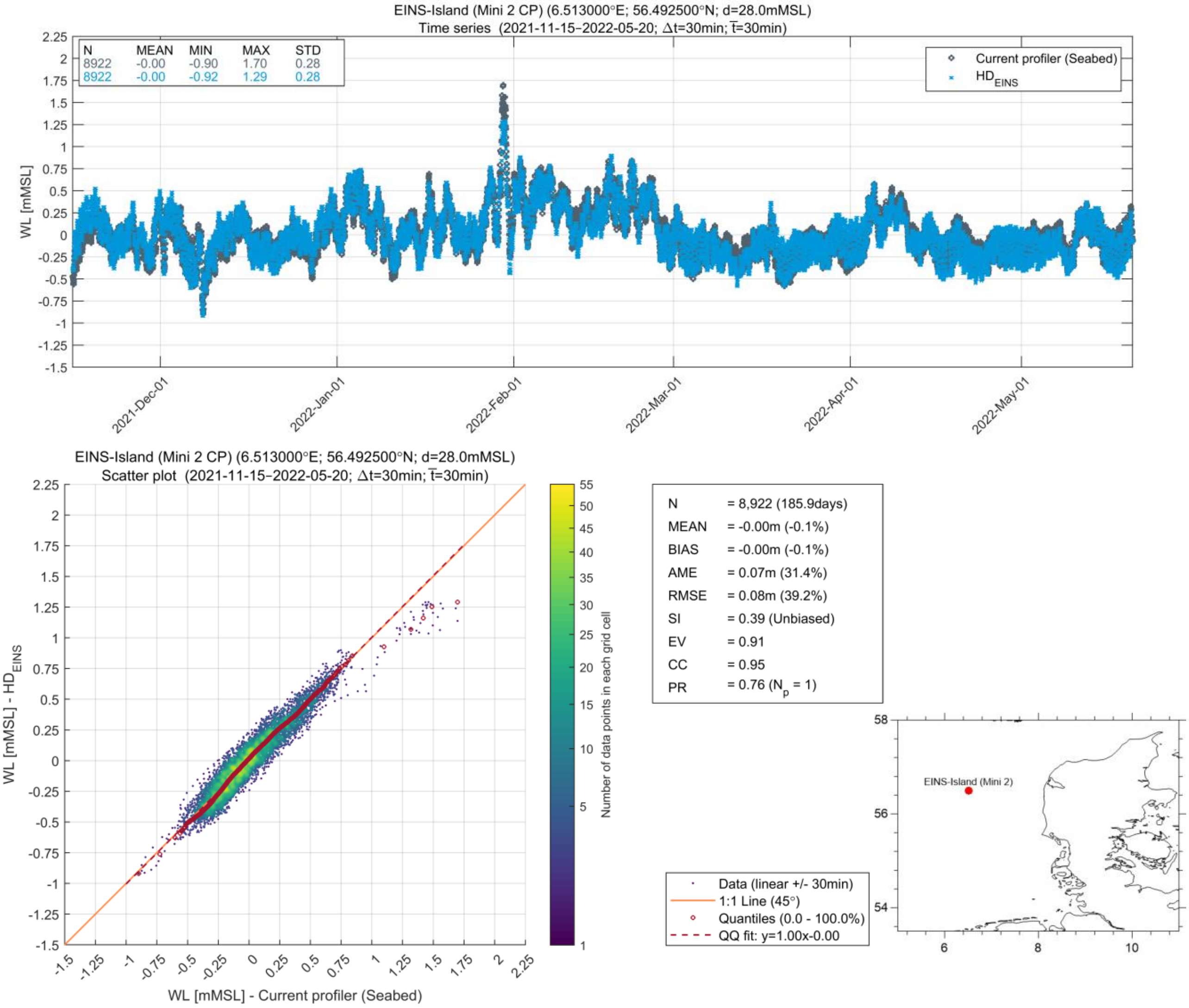

Figure 4.14 Comparison of water levels at EINS-Island (Mini 2, current profiler seabed)

Harald

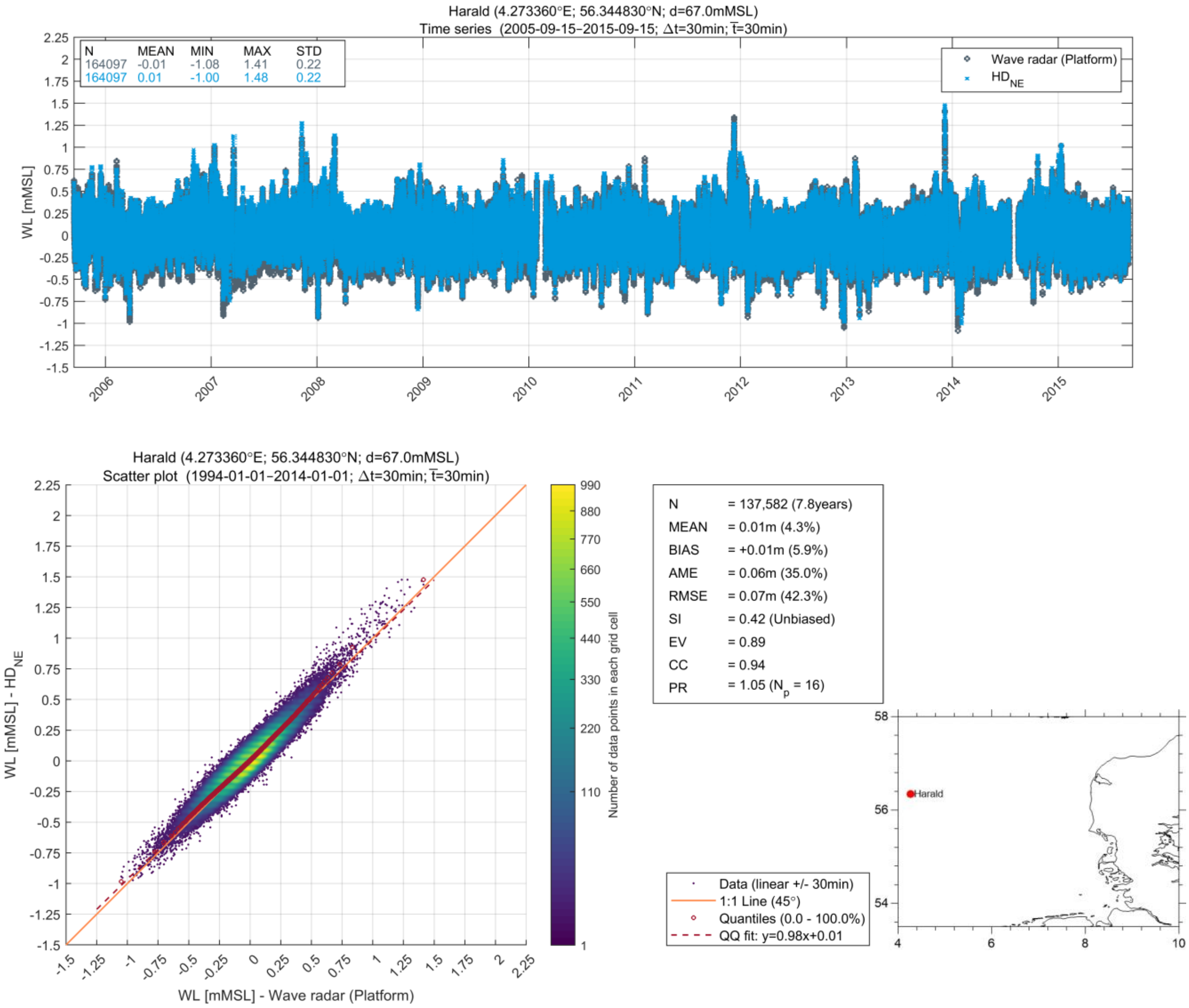

Figure 4.15 Comparison of water levels at Harald

Gorm

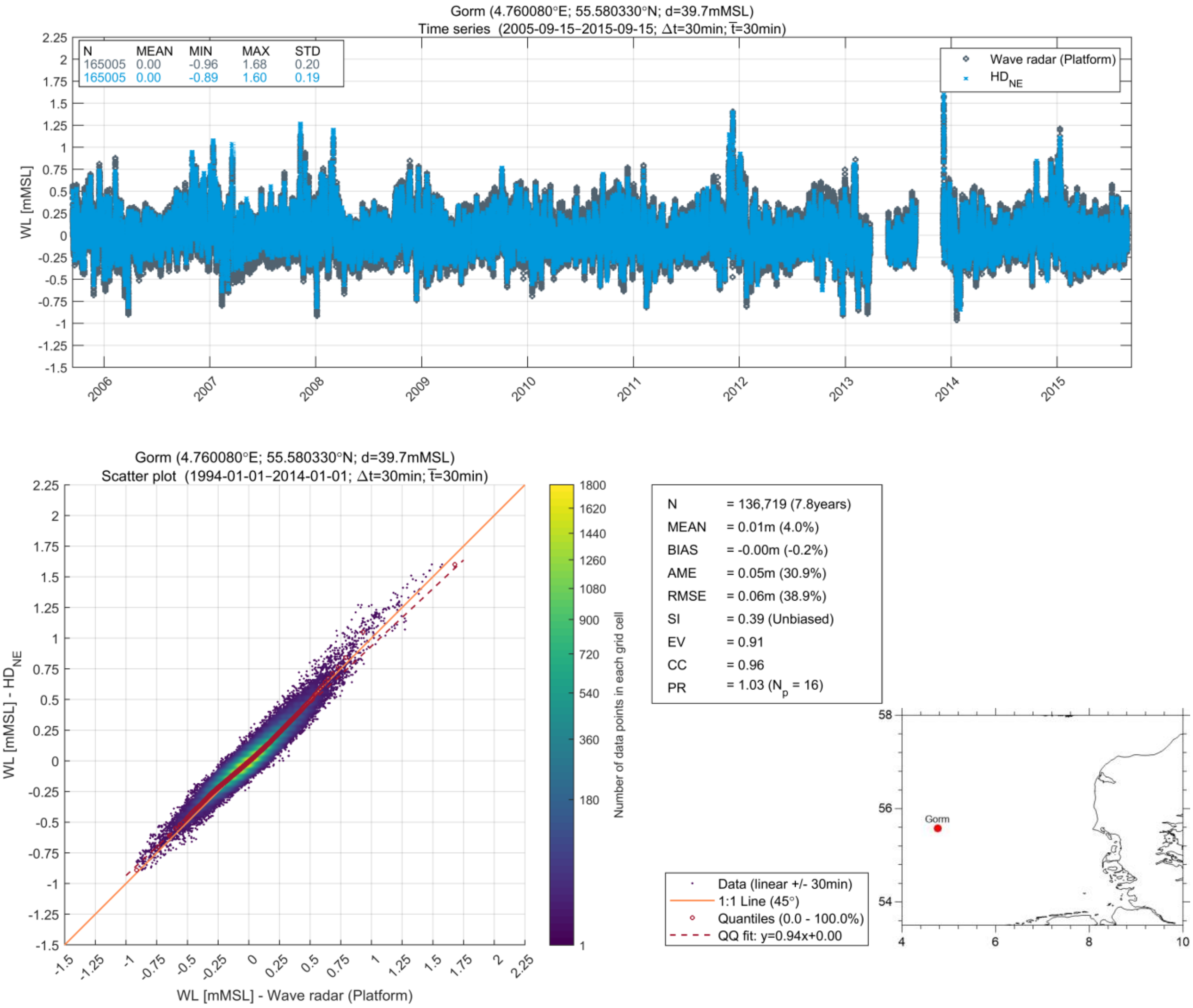

Figure 4.16 Comparison of water levels at Gorm

Ferring

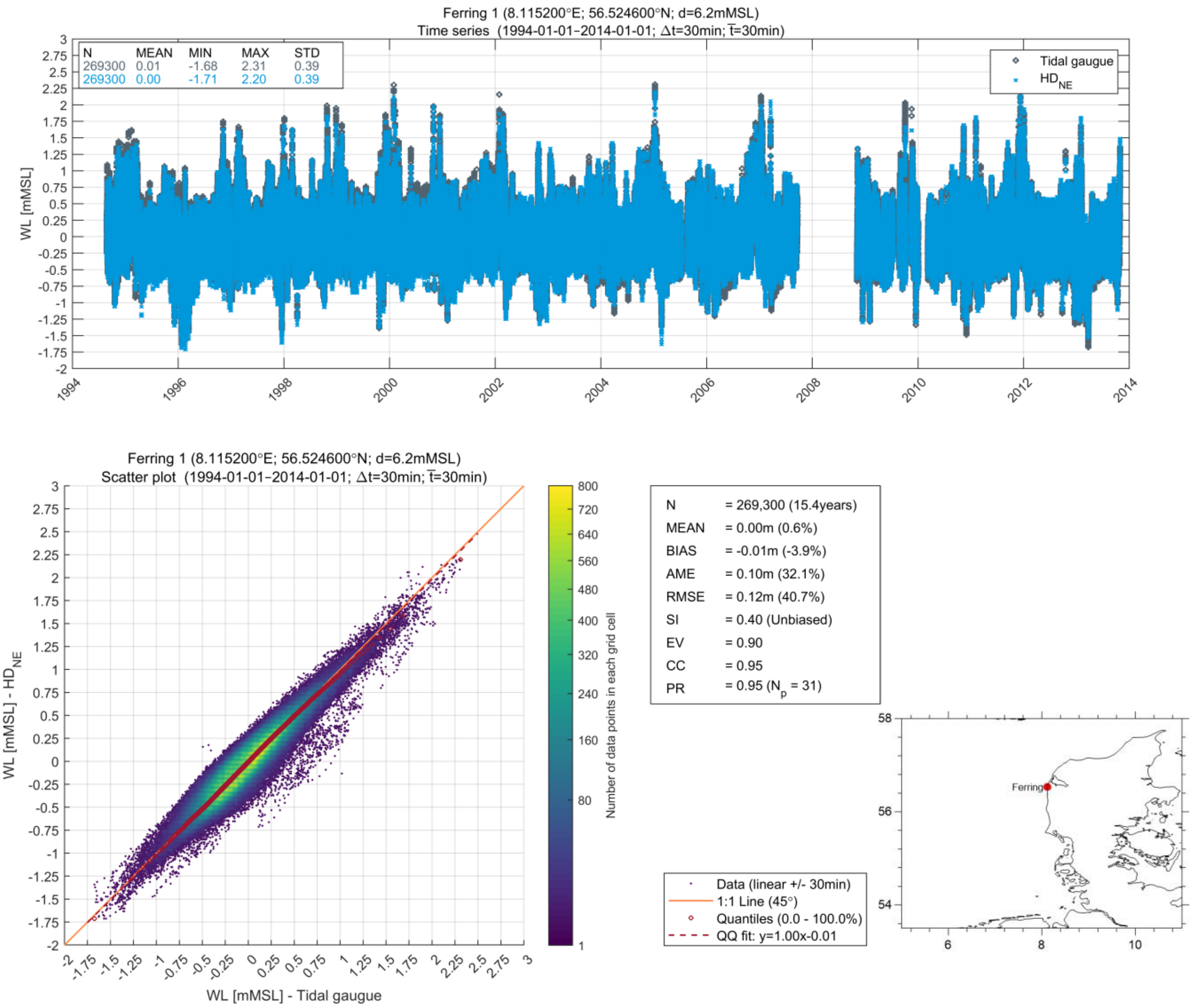

Figure 4.17 Comparison of water levels at Ferring

5 Current

This section presents a general overview of the current conditions at EINS and presents the measurements and the hindcast current data from HD$_{\mathrm{EINS}}$ (see Section 4.3.3). The data basis for currents was supplemented by data from the DHI United Kingdom and North Sea 3-dimensional (HD$_{\mathrm{UKNS3D}}$) regional hydrodynamic model. Finally, this section addresses appropriate current profiles for normal and extreme conditions.

5.1 General current characteristics

The general circulation of currents in the North Sea is a complex system, that involves a large warm oceanic current, like the Gulf Stream, as well as other regional currents coming from the Faroe Islands, the English Channel, and the Baltic Sea. All these currents meet at the North Sea where they form smaller circulation systems. This together with astronomically and meteorologically forced currents plus geological features, significantly affects the spatial variation of current intensities and directions across the North Sea, causing currents that flow mainly from southwest to northeast at the EINS site.

The EINS site is mainly affected by the tidal current that follows the tidal wave moving counter-clockwise around the North Sea, resulting in depth-averaged current speeds typically of ~0.2 m/s. However, extreme wind events have a significant impact on the direction and intensity of surface currents, which may be larger than 1.5 m/s.

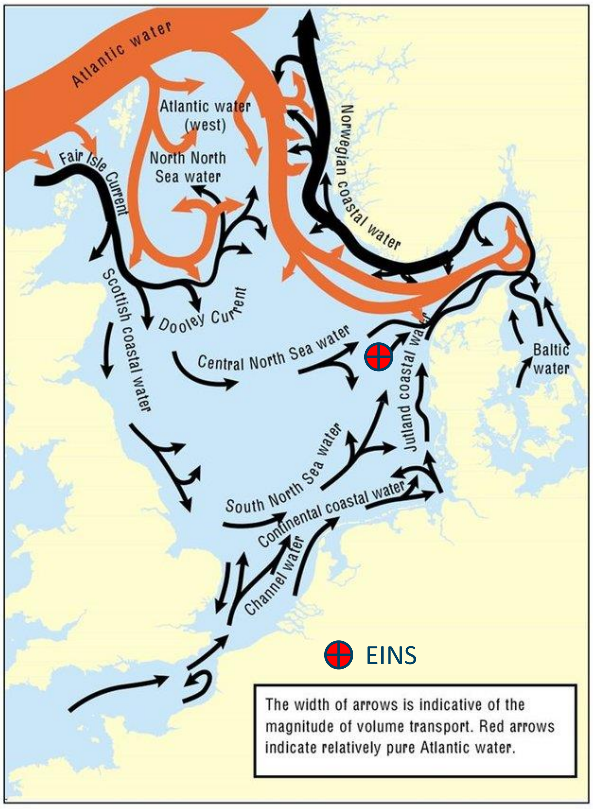

Figure 5.1 Schematic diagram of general water circulation in the North Sea
(Source: [26] after [27]). EINS is shown with red dot and black cross

5.2 Current measurements

The locations and depths of current measurements near or at the project location are summarised in Table 5.1 and shown in Figure 5.2, while Figure 5.3 shows the temporal coverage.

Current measurements at the project site (recorded by FUGRO, [2]) were gathered from several ADCPs [2]. Three bottom mounted upward-looking current profilers of type Nortek Signature 500, i.e. EINS-North (CP seabed), EINS-South (CP seabed) and EINS-Island (Mini 2 CP seabed), and two downward-looking current profilers of type Nortek Aquadopp 600 kHz, i.e. EINS-North (CP surface) and EINS-South (CP surface), mounted underneath the floating LiDAR's. The data was quality controlled by FUGRO and checked by DHI before usage.

Measured current speeds and directions from the bottom mounted upward-looking EINS-North (CP seabed), EINS-South (CP seabed) and EINS-Island (Mini 2 seabed) were available every 10 minutes at 1 m depth interval bins from 4 m above the seabed all the way to the surface (however, data near the surface is often disturbed by turbulence and not usable). Data from the downward-looking current profilers, EINS-North (CP surface) and EINS-South (CP surface), were available every 10 minutes at 1 m depth interval bins from 1 m depth all the way to the sea floor.

Two additional datasets from nearby stations (Valdemar and Thor) were used to show the predictive capabilities of the regional HD_{NE-DA} model, used to force the HD_{EINS} model. The characteristics of the instrument deployed at Valdemar were unknown, but current speed data is available every 60 minutes, and its quality was reviewed by DHI to check and remove irregularities and outliers in the data. The measurements from Thor OWF were also checked by DHI since its quality assessment was not reported in [28].

For the purpose of converting into depth-averaged values, and given the influence of the surface and seabed boundaries on the measurements, it was assumed that measurements at a distance from the seabed of 2/5th the water depth are representative of depth-averaged values [29]. An assessment of averaging current speeds over the entire water column was also done, however, a better agreement (i.e., less scatter) was found between model and measurements using the first approach.

Table 5.1 Metadata of current measurements

Station Name	Longitude [°E]	Latitude [°N]	Modelled seabed elevation [mMSL][1]	Surveyed seabed elevation [mMSL]	Availability period	Instrument	Owner / Surveyor
EINS-North (CP seabed)	6.3008	56.6272	-46.5	-46.0	15/11/2021 - 21/03/2022	Nortek Signature 500 current profiler at seabed	Energinet / FUGRO
EINS-South (CP seabed)	6.4552	56.3442	-40.0	-40.0	15/11/2021 - 22/07/2022	Nortek Signature 500 at seabed	Energinet / FUGRO
EINS-Island (Mini 2 CP seabed)	6.5130	56.4925	-28.9	-28.0	15/11/2021 - 20/05/2022	Nortek Signature 500 at seabed	Energinet / FUGRO
EINS-South (CP surface)[2]	6.3007	56.628	-46.5	-46.4	15/11/2021 - 15/03/2022	Nortek Aquadopp 600 at surface	Energinet / FUGRO
EINS-South (CP surface)[2]	6.4574	56.3444	-39.8	-39.8	15/11/2021 - 15/03/2022	Nortek Aquadopp 600 at surface	Energinet / FUGRO
Valdemar	4.5657	55.8048	-40.4	-41.9	28/12/2015 - 03/04/2016	Unknown	TEPDK
Thor	7.605	56.347	-30.2	-30.1	2020-05-19 - 2021-05-19	DCPS 5400 600 kHz	Energinet / Akrocean

[1] Modelled seabed elevation based on the production mesh

[2] Current direction data was discarded for the whole period due to irregularities

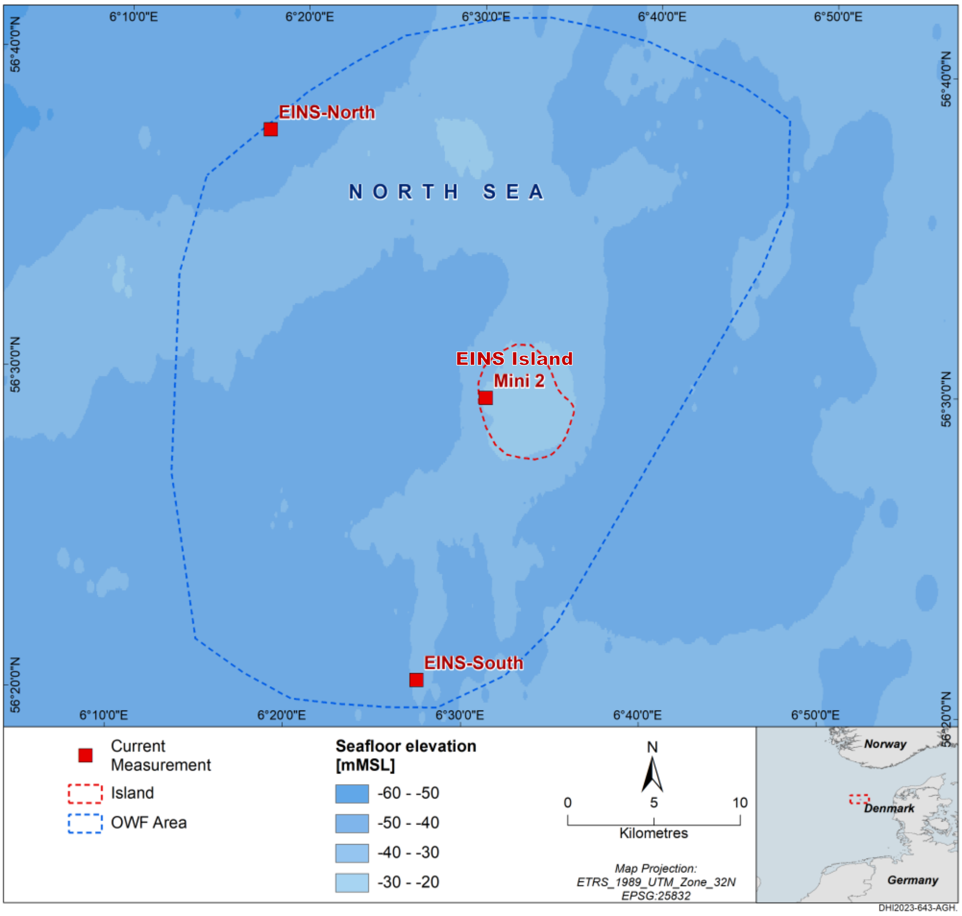

Figure 5.2 **Location of local current measurements**
Location of regional measurements are shown in Figure 0.1.

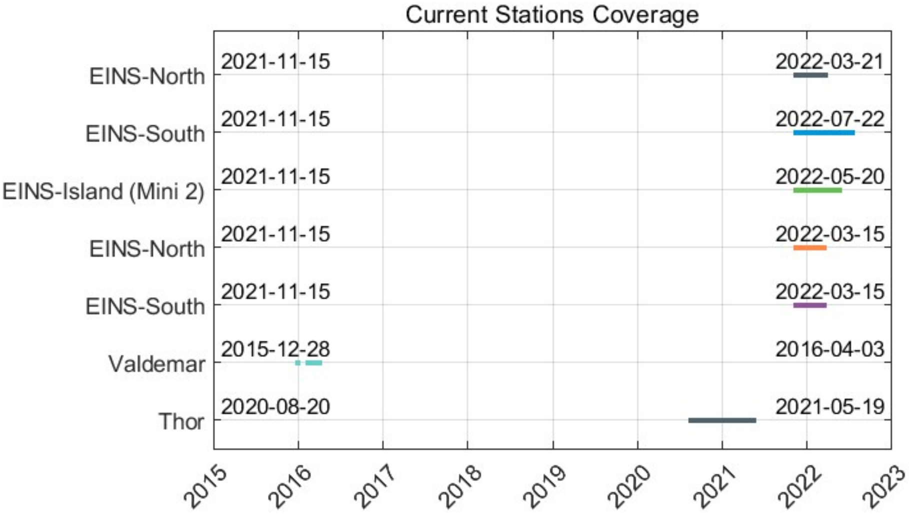

Figure 5.3 **Temporal coverage of local current measurements**

5.2.1 Current profile

The current profiles at EINS were initially assessed based on ~3 months of local measurements. Figure 5.4 shows the 5, 50, and 95%-tiles of the 1 m vertical interval measured data at the EINS-North (CP surface) (up to 5 m below the surface). This assessment indicated a uniform profile throughout the water column on average.

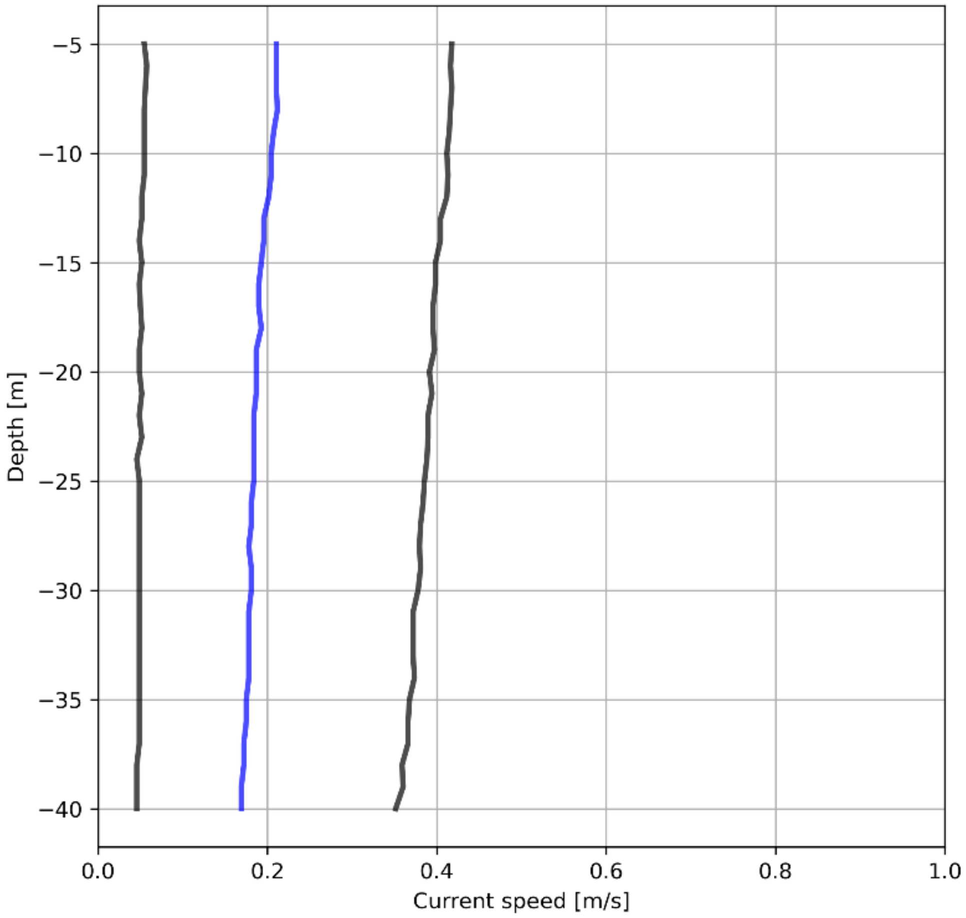

Figure 5.4 **5, 50, and 95%-tiles of measured current at EINS-North (CP surface)** Indicating a uniform profile throughout the water column on average.

However, inspection of the individual current profiles shows a high variation over the water column.

Figure 5.5 shows the measured 3D current profile at EINS-South (CP seabed) at 2021-11-20 07:41. The profile shows that the current speed at the surface layers (top ~5 m) are weaker than the current speed at the layers just below. This appears to be a general trend of the measurements which is suspicious. Thus, the top 5 m of the measurements are disregarded for further analysis.

Figure 5.6 shows the measured 3D current profile at EINS-South (CP seabed) at 2021-11-23 11:01. The profile shows large variation in current speed as well as current direction over depth, mainly since the current at the surface is flowing in the direction of the wind, while the current at the seabed is flowing in the direction of the tide.

Hence, overall, the individual current profiles are highly diverse, especially during strong wind.

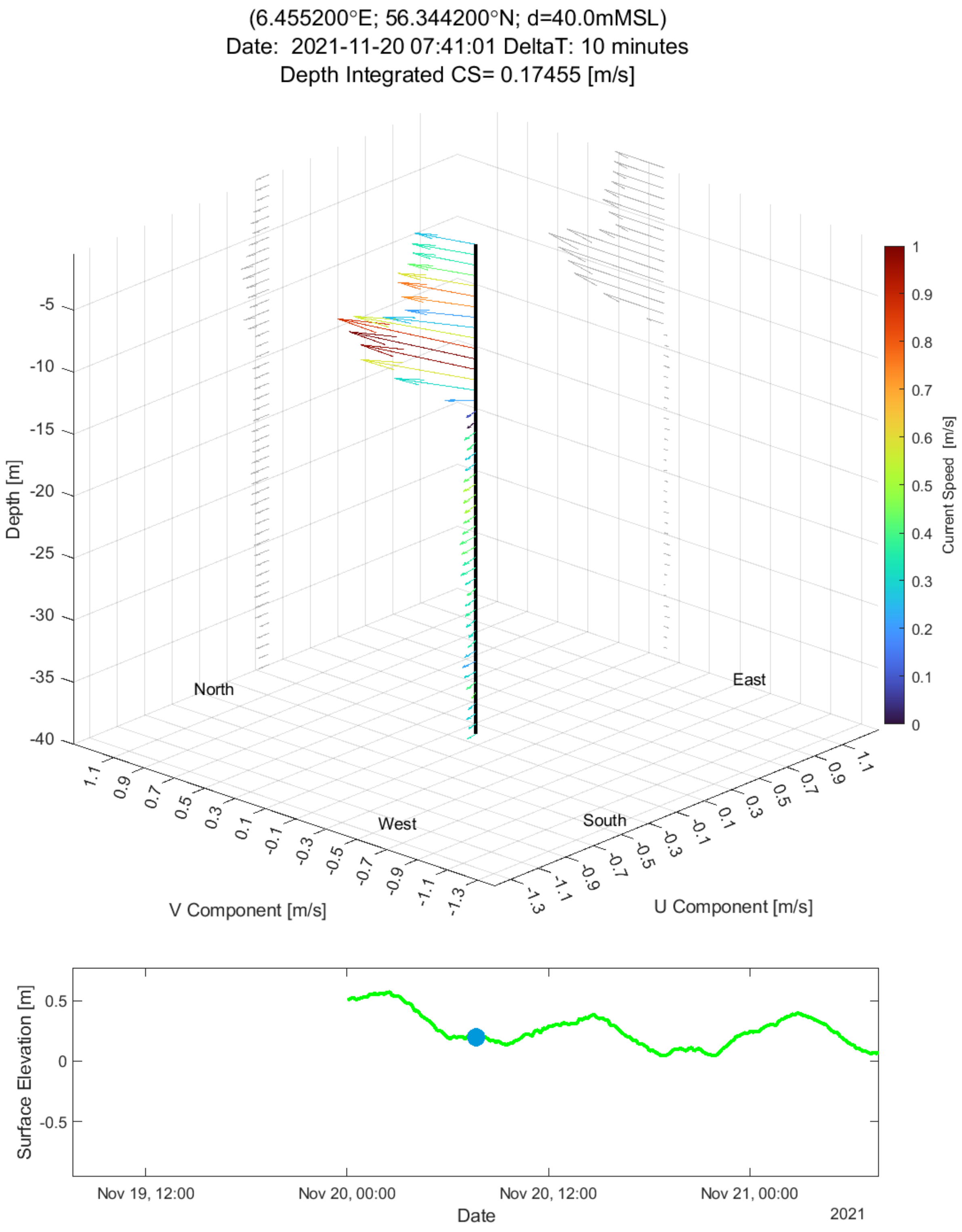

Figure 5.5 **Measured 3D current profile at EINS-South (CP seabed) at 2021-11-20 07:41**
The current speed at the surface layers (top 5 m) are weaker than the current speed at the layers just below.

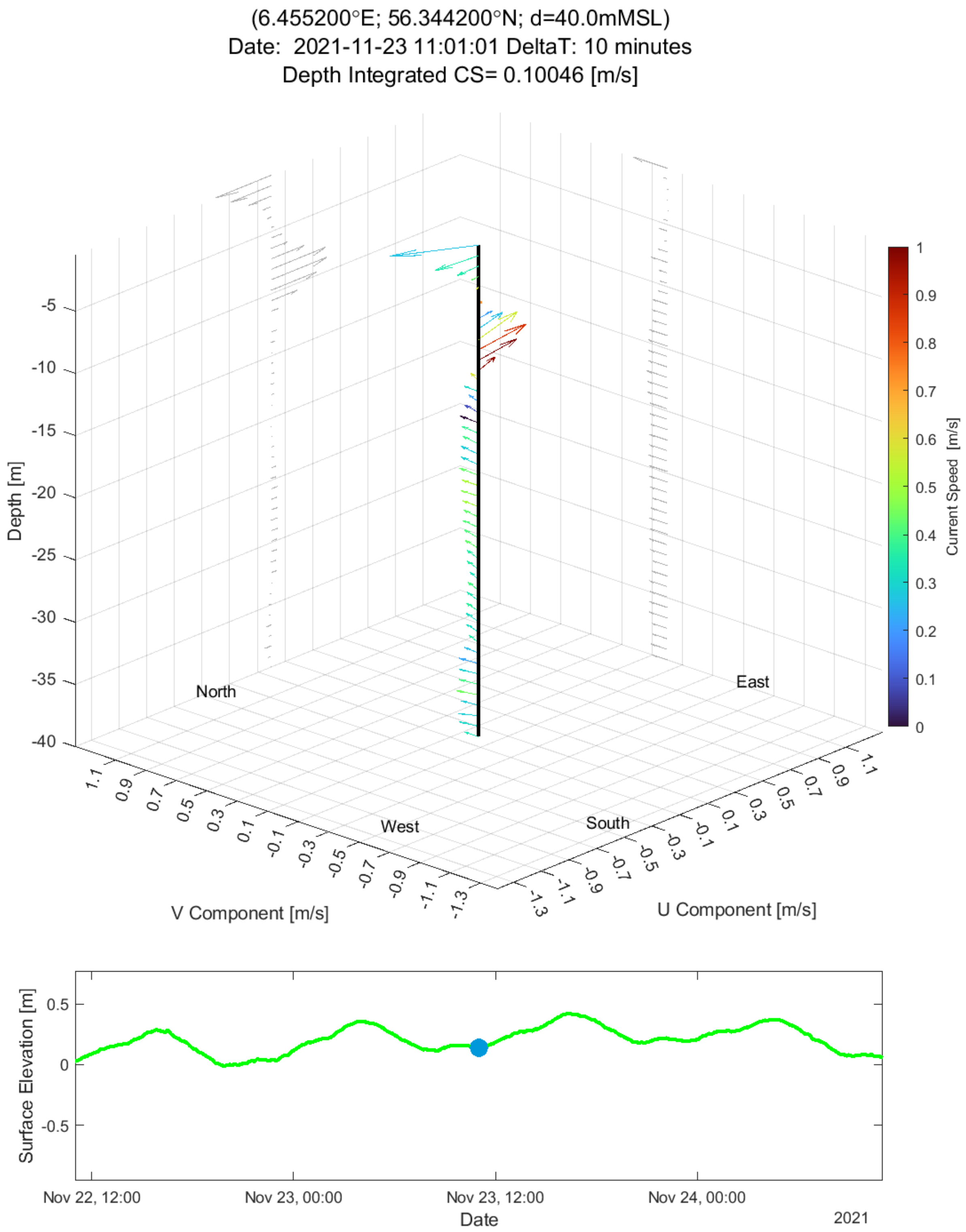

Figure 5.6 **Measured 3D current profile at EINS-South (CP seabed) at 2021-11-23 11:01**
The profile shows large variation in current speed as well as current direction over depth.

Another way to illustrate the variation in the current profiles is by plotting the current speed relative to the depth-averaged values.

Figure 5.7 displays such normalised current profiles during normal conditions (depth-averaged current speed > 50%-tile) and extreme conditions (depth-averaged current speed > 99%-tile) at EINS-South.

Figure 5.8 display the same only conditioned on near-surface (5 m below) current speeds instead of depth-averaged.

Both figures include the power profile using α = 1/7, see Eq. (5.1) shown as a black dashed line.

The following general set of characteristics can be inferred:

- The ratio between the 'bin level' current speed and the depth-averaged current speed shows a large variation (and is largest in the upper layers).
- In upper layers (> 24 m) it is more likely that the current speed is larger than the depth-average current speed (U/CS > 1), particularly for the 95%-tile, which shows occurrences of much stronger currents at the surface.
- In the lower levels (< 24 m) the current speed is more likely to be less than the depth-averaged current speed (U/CS < 1).
- The measured 50%-tile profile agrees reasonable with the power profile using α = 1/7, see Eq. (5.1), especially for the lower levels (<24 m).

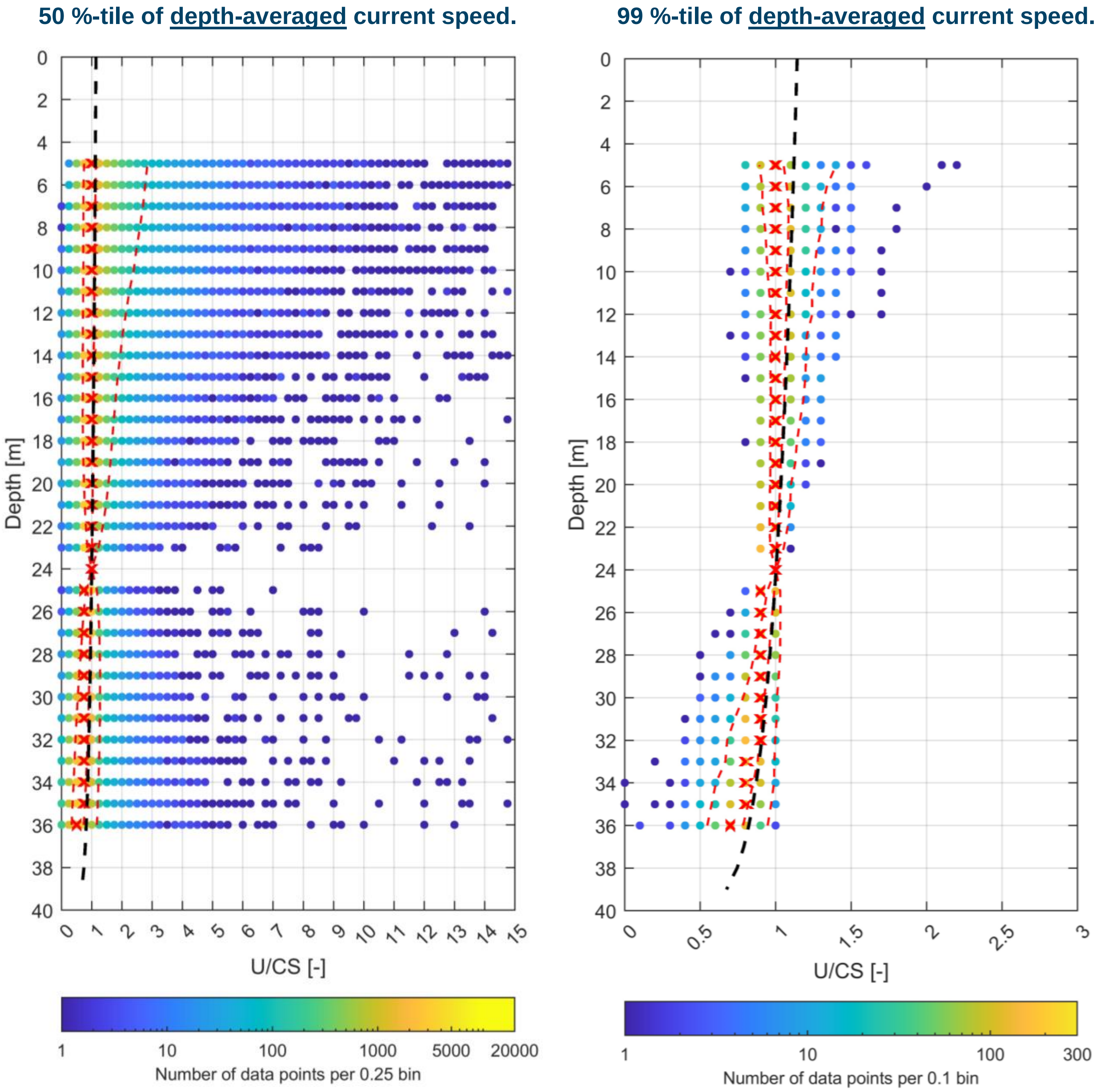

Figure 5.7 **Measured current profiles at EINS-South (CP seabed), filtered by depth-averaged current speed, and normalized by the current speed at 24 m (2/5th × depth above seabed).**
Red cross: Most probable value. Red dashed lines: 5%-, 50%-, and 95%-tiles.
Black dashed: Power profile using α = 1/7, see Eq. (5.1).

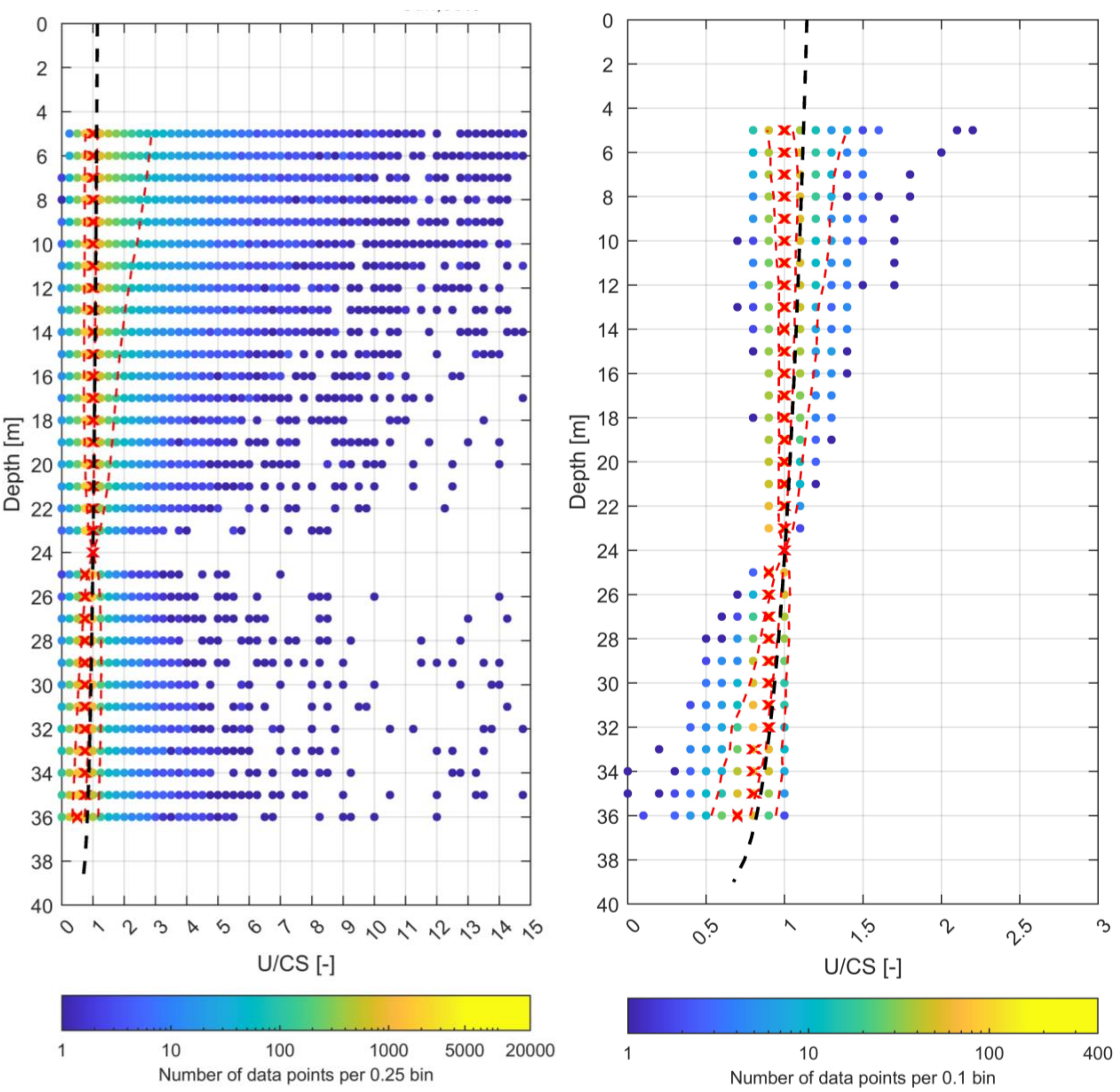

50 %-tile of near-surface current speed.

99 %-tile of near-surface current speed.

Figure 5.8 **Measured current profiles at EINS-South (CP seabed), filtered by near-surface (5 m below) current speed, and normalized by the current speed at 24 m (2/5th × depth above seabed).**

Red cross: Most probable value. Red dashed lines: 5%-, 50%-, and 95%-tiles.
Black dashed: Power profile using α = 1/7, see Eq. (5.1).

5.3 Hindcast current data – 2D

The setup of the local hydrodynamic model for the EINS site, HD_{EINS}, is described in Section 4.3 as the same model is used to obtain the hindcast water level and current data.

Like for the water levels, current speed outputs were saved with a 30 min interval. Sensitivity of extreme current speeds to mesh resolution and sea level rise were assessed as described below. Further, 3D model data was adopted.

The hindcast current dataset was validated using local and regional measurements. Described in this section are the following:

- Sensitivity studies mesh resolution and sea level rise (Section 5.3.1)
- Current validation of the HD_{EINS} model (Section 5.3.2)
- 3D hydrodynamic data and vertical current profiles (Section 5.4)

5.3.1 Sensitivity studies

Mesh convergence

Following the approach described in Section 4.3.5, a mesh convergence study was performed to assess the effect of mesh size on the extreme depth-averaged current speed events.

For the same events (i.e., Cases 01 to Case 03) and mesh resolutions (i.e., 200 m to 600 m) as described in Section 4.3.5, Figure 5.9 illustrates the results obtained for the shallowest point at the EINS site, EINS-1 (Shallowest).

The results show practically no difference in current speed and direction between the investigated mesh resolutions. Therefore, a 400 m mesh resolution at the shallowest areas of the EINS site (top panel of Figure 4.8) was used to produce the HD_{EINS} model data since this mesh size represents a reasonable trade-off between model accuracy and computational cost, while ensuring a correct characterisation of the bathymetric features of the model domain.

The maximum difference was found in Case 01 with a difference of 0.02 m/s (2% of the maximum current speed) between the 400 m resolution mesh and the 200 m resolution mesh (lowest and largest current speeds attained by each model, respectively).

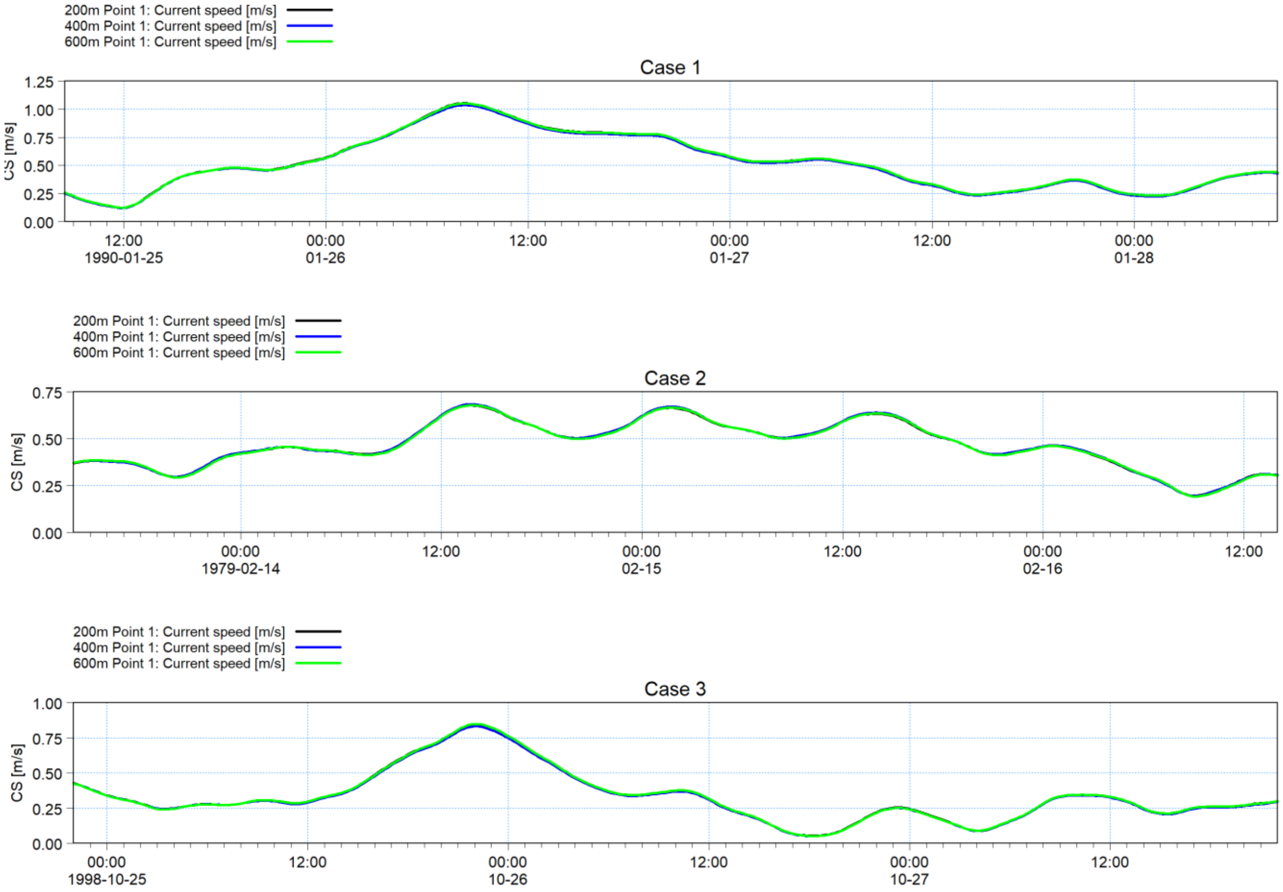

Figure 5.9 **Comparison of current speeds for the different mesh resolutions at EINS-1 (Shallowest)** Top: Case 01; Middle: Case 02, and Bottom: Case 03.

Sensitivity of currents to sea level rise (0.8m)

The effect of climate change, specifically, the effect of sea level rise (SLR) on depth-averaged current speeds was also assessed. Cf. Section 9.2, the sea level rise reach approximately (up to) 0.8 m by the year 2113. Therefore, this value was used to quantify the effect on current speeds during extreme events. For this purpose, water depths of the HD_{EINS} and $HD_{NE\text{-}DA}$ model were increased by 0.8 m, but forcings (i.e., wind, pressure, and boundary conditions of water level and current) were unchanged. As the boundaries for the HD_{EINS} come from the $HD_{NE\text{-}DA}$, if SLR assessment doesn't produce any significant change on currents speeds from the HD_{NE}, it is unlikely as well that currents speeds from the HD_{EINS} will be affected.

The sensitivity of currents to sea level rise was assessed for the set of extreme events presented in Table 6.3. Extreme events were selected based on the largest current speed events estimated by the $HD_{NE\text{-}DA}$ model at the EINS site. Results of current speeds during the entire event obtained from this sensitivity analysis for both models were unnoticeable as shown in Figure 5.10 and Figure 5.11 for the largest event selected.

Table 5.2 **Extreme events used to assess the effect of SLR on current**

Storm ID	Start Time	End Time	Approx. max. modelled CS at EINS-South (Mini 2) [m/s]
#1	1985-11-05	1985-11-07	1.04
#2	2000-01-20	2000-01-22	0.91
#3	1990-12-25	1990-12-27	0.75

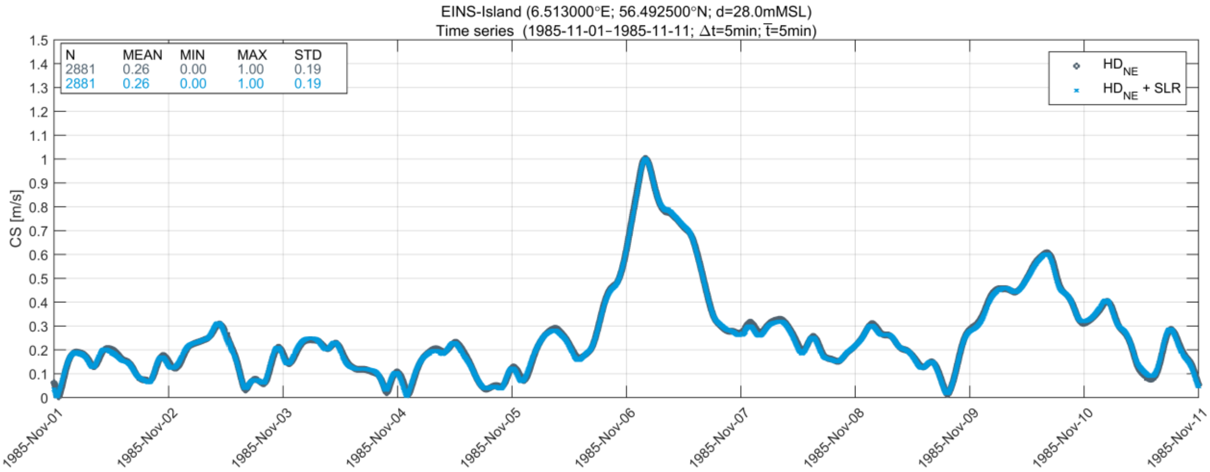

Figure 5.10 **Comparison of modelled current speeds from HD_{NE-DA} at EINS-Island (Mini 2) considering the present situation (grey line) and the scenario with a sea level rise of 0.8 m (blue line)**

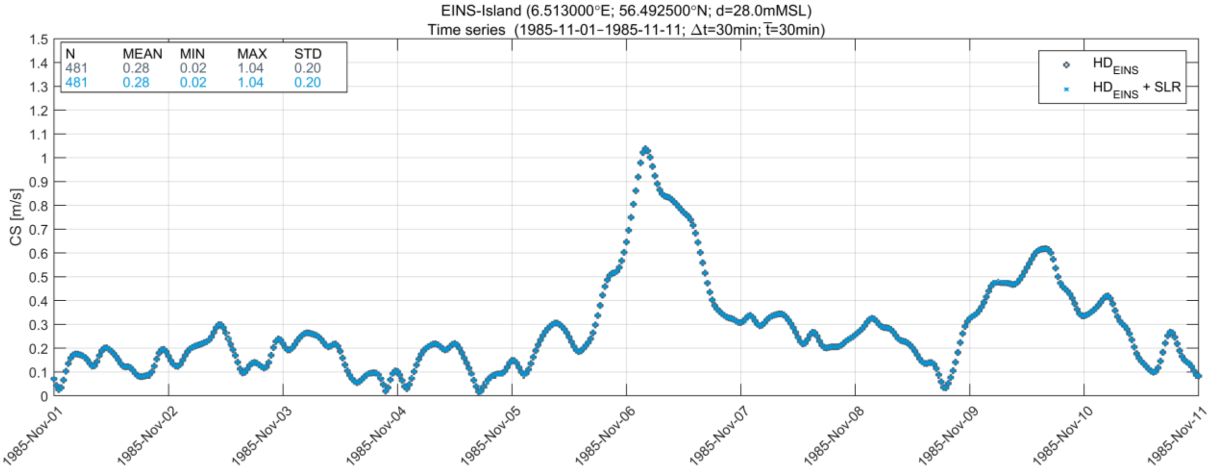

Figure 5.11 **Comparison of modelled current speeds from HD_{EINS} at EINS-Island (Mini 2) considering the present situation (grey line) and the scenario with a sea level rise of 0.8 m (blue line)**

5.3.2 Validation of 2D current

The HD_{EINS} model was validated against ~8 months of currents measured at the LiDAR buoys and ADCPs deployed at the EINS site (see Figure 5.12 to Figure 5.16). The $HD_{NE\text{-}DA}$ model used to obtain the boundary conditions that forced HD_{EINS} was also compared with records (~4 months) from Valdemar and Thor to show its validity (see Figure 5.17 and Figure 5.18). A summary of the stations used for the validation of both models is presented in Table 5.1, their locations in Figure 5.2 and their time coverage in Figure 5.3. Table 12.3 presents validation statistics for all measurements.

Overall, results show a good performance of the local HD_{EINS} model in all the stations, with a BIAS close to 0, a correlation coefficient (CC) greater than 0.66, and a QQ alignment close to the 1:1 line.

Current directions in terms of both frequency and intensities, are also well characterised, as shown by the rose plot comparisons. Current directions from the LiDAR buoys, i.e., EINS-North (CP surface) and EINS-South (CP surface) were discarded as they seemed to be wrong when comparing them against the upward-looking measurement devices and the model.

EINS-North (CP seabed)

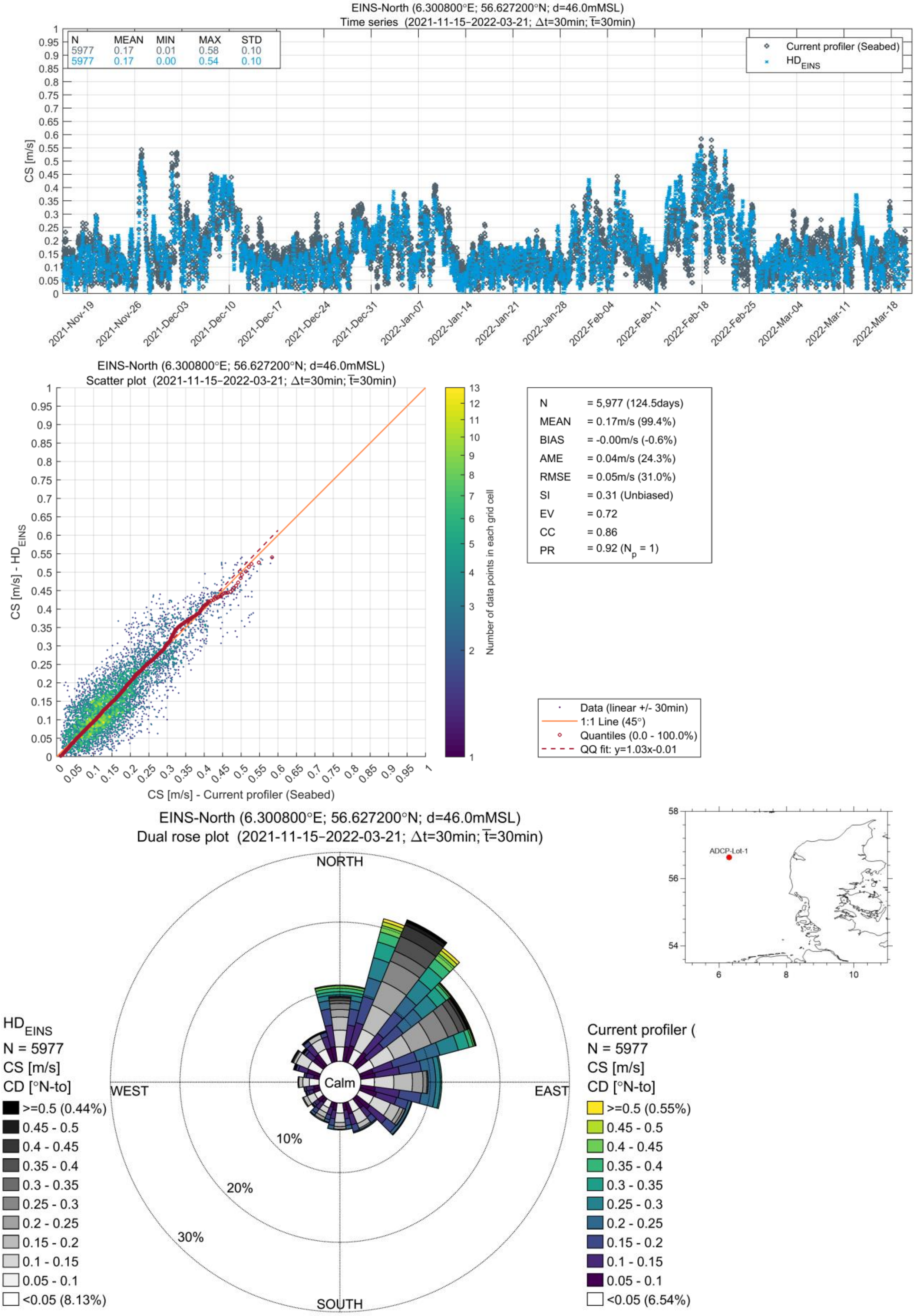

N	MEAN	MIN	MAX	STD
5977	0.17	0.01	0.58	0.10
5977	0.17	0.00	0.54	0.10

N = 5,977 (124.5days)
MEAN = 0.17m/s (99.4%)
BIAS = -0.00m/s (-0.6%)
AME = 0.04m/s (24.3%)
RMSE = 0.05m/s (31.0%)
SI = 0.31 (Unbiased)
EV = 0.72
CC = 0.86
PR = 0.92 (N_p = 1)

Figure 5.12 Comparison of currents at EINS-North (CP seabed)

EINS-South (CP seabed)

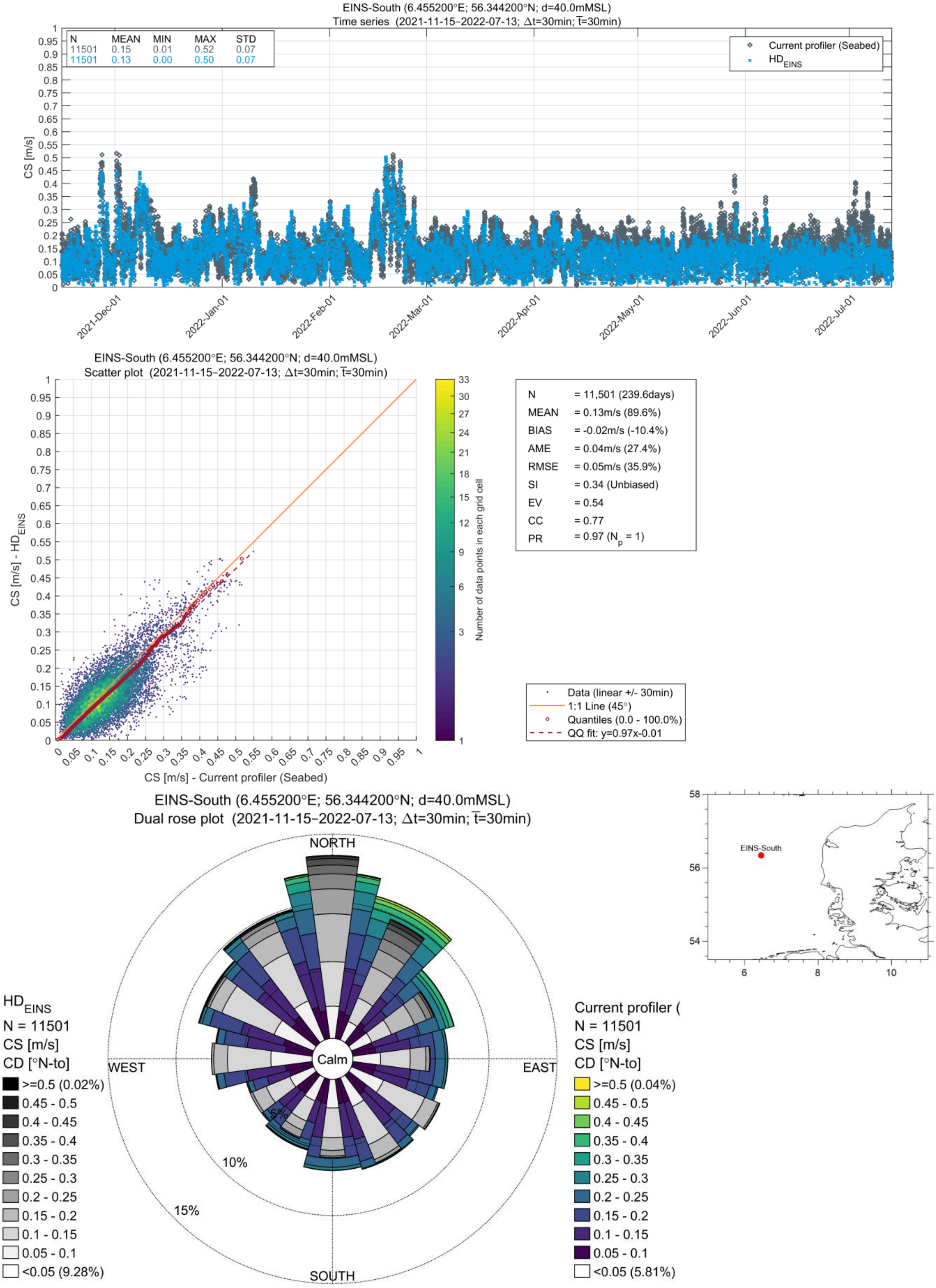

Figure 5.13 Comparison of current at EINS-South (CP seabed)

EINS-South (Mini 2, CP seabed)

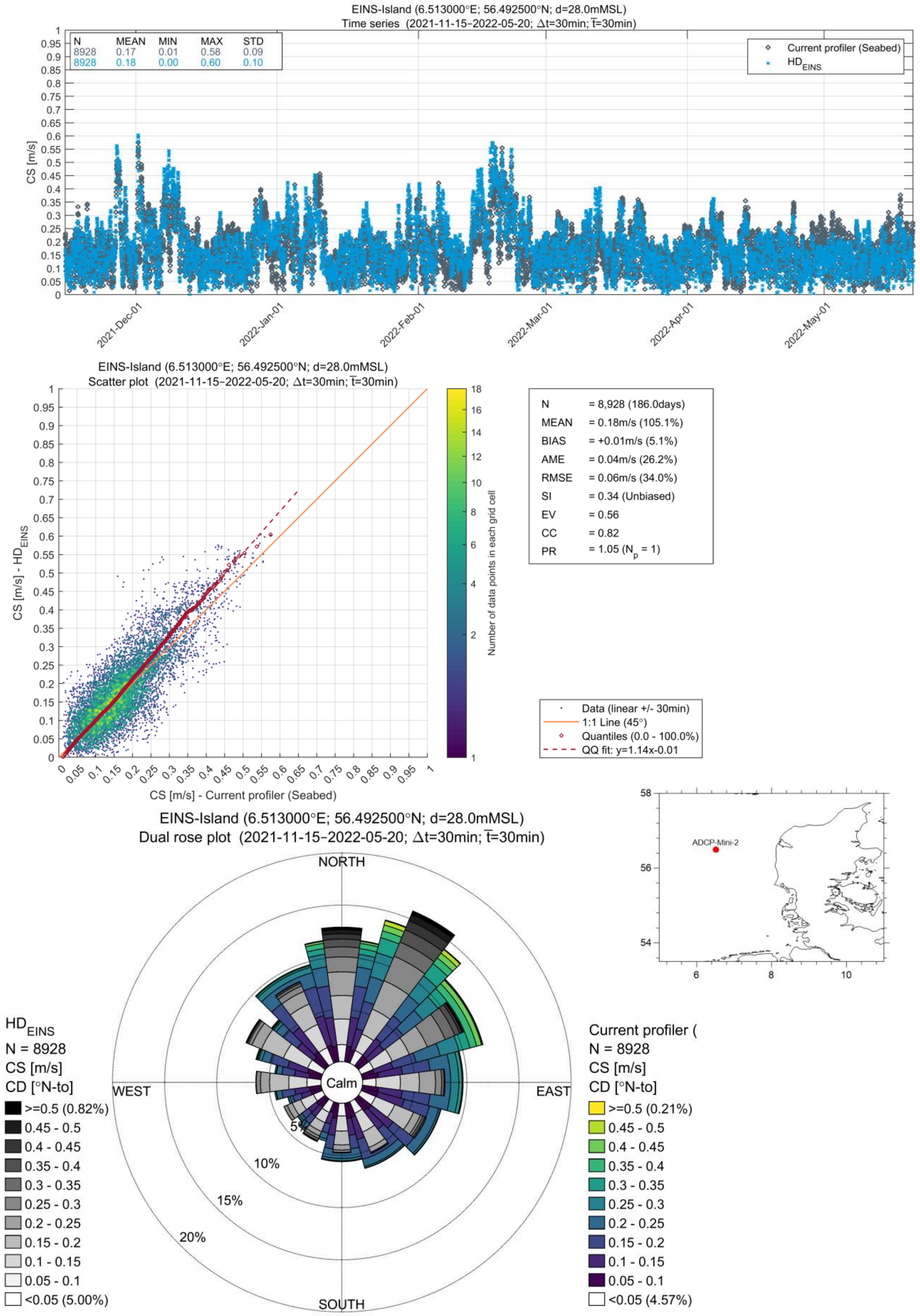

Figure 5.14 Comparison of currents at EINS-South (Mini 2, CP seabed)

EINS-North (CP surface)

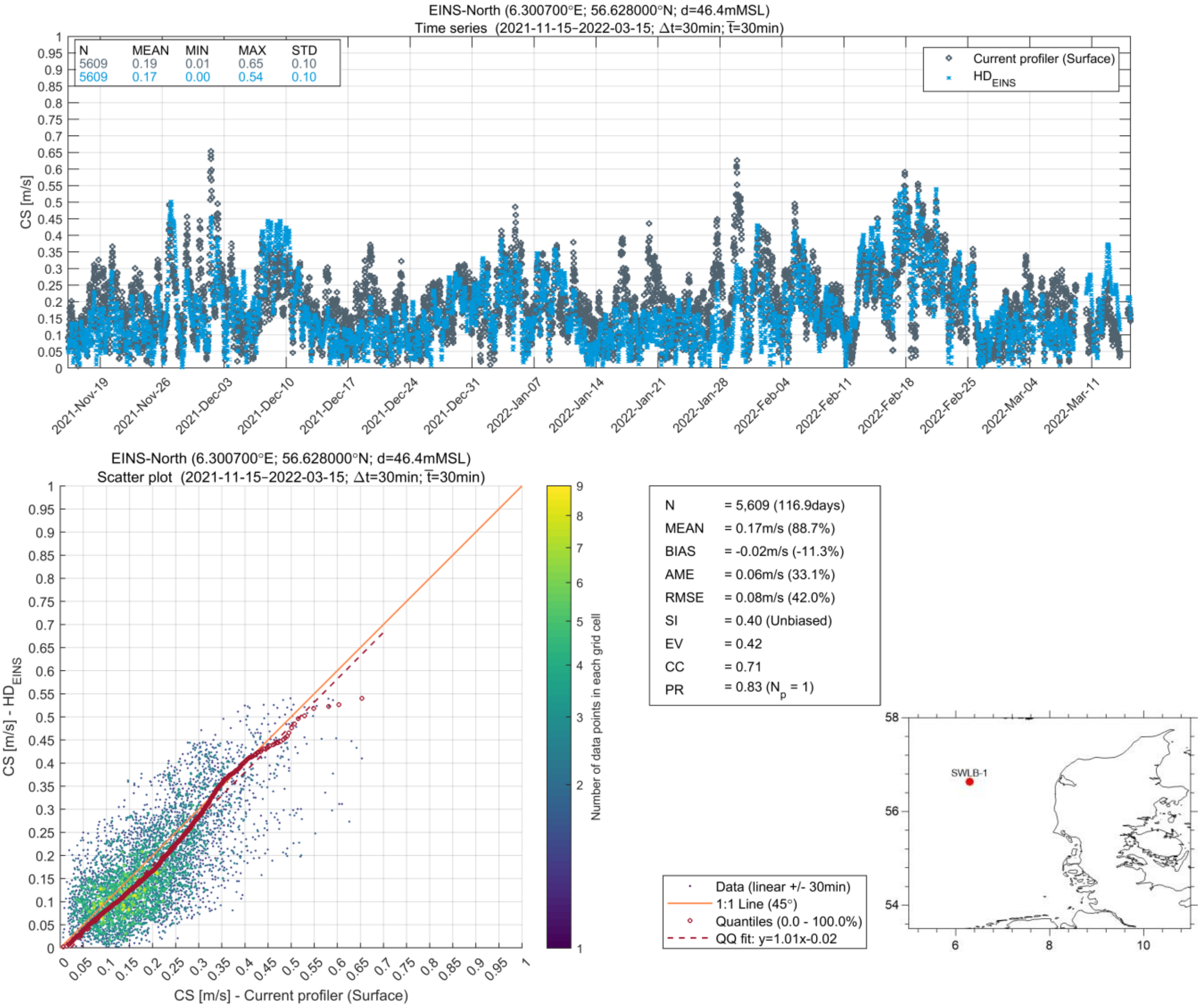

Figure 5.15 Comparison of currents at EINS-North (CP surface)

EINS-South (CP surface)

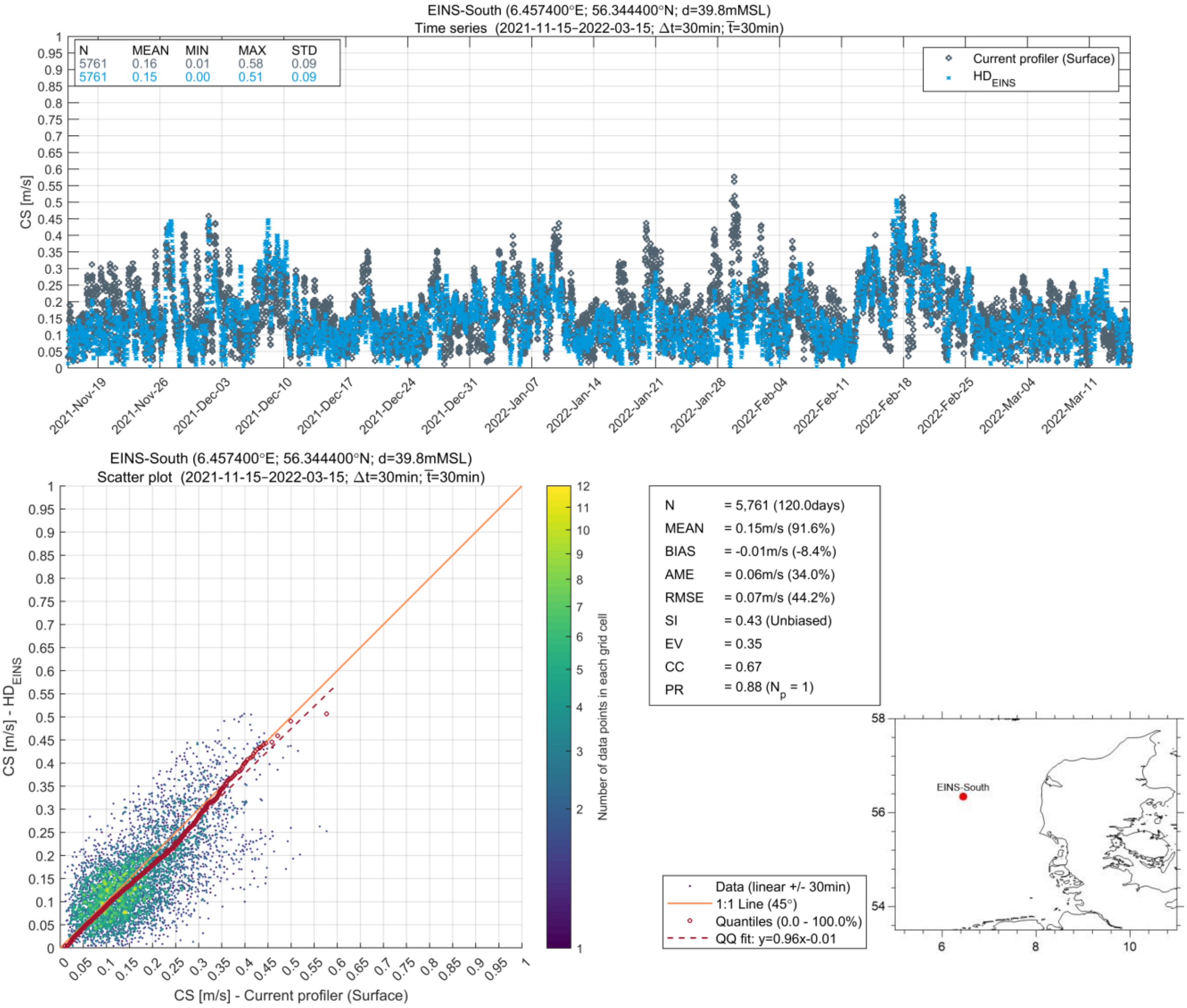

Figure 5.16 Comparison of currents at EINS-South (CP surface)

Valdemar

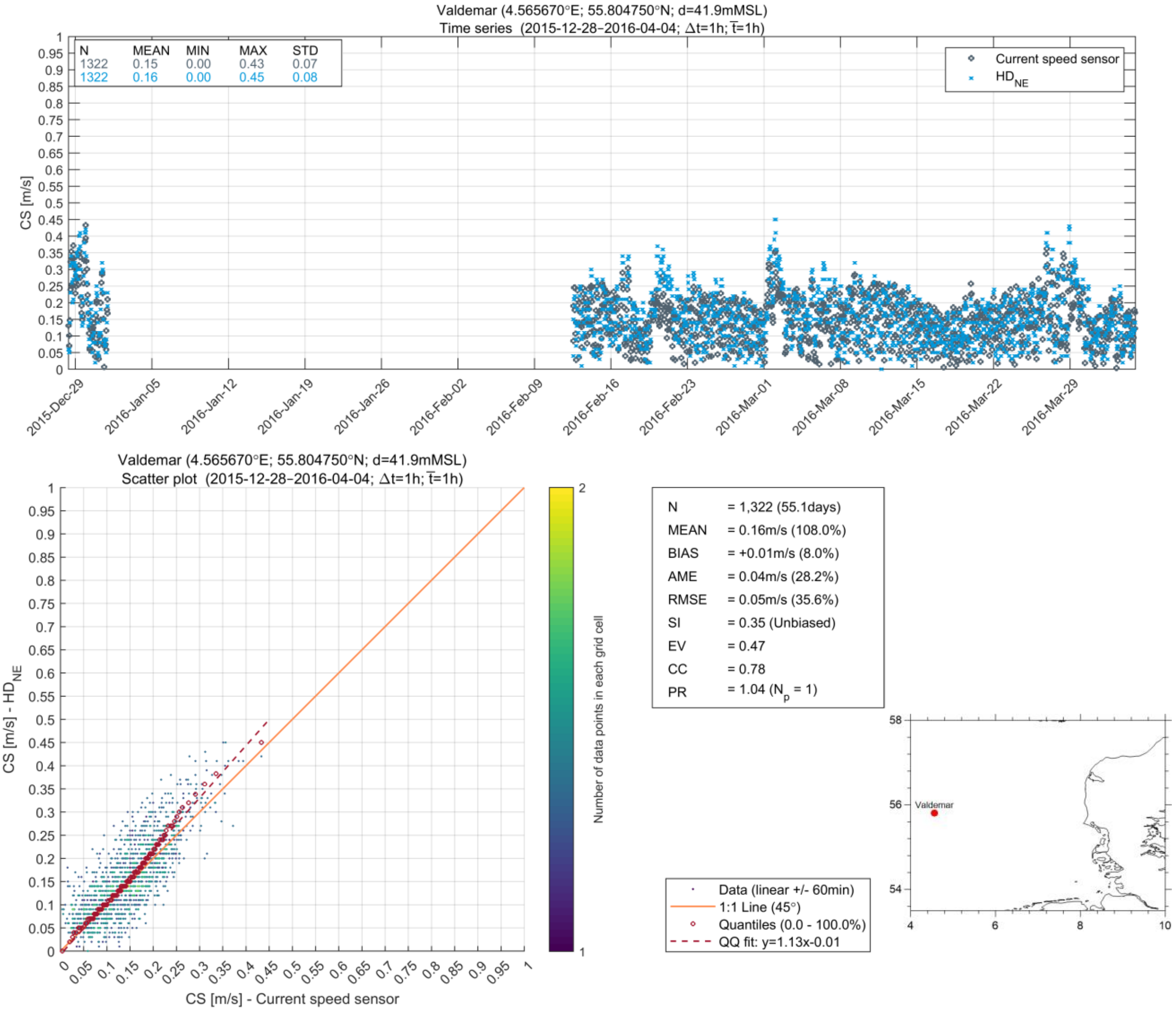

Figure 5.17 Comparison of currents at Valdemar

Thor

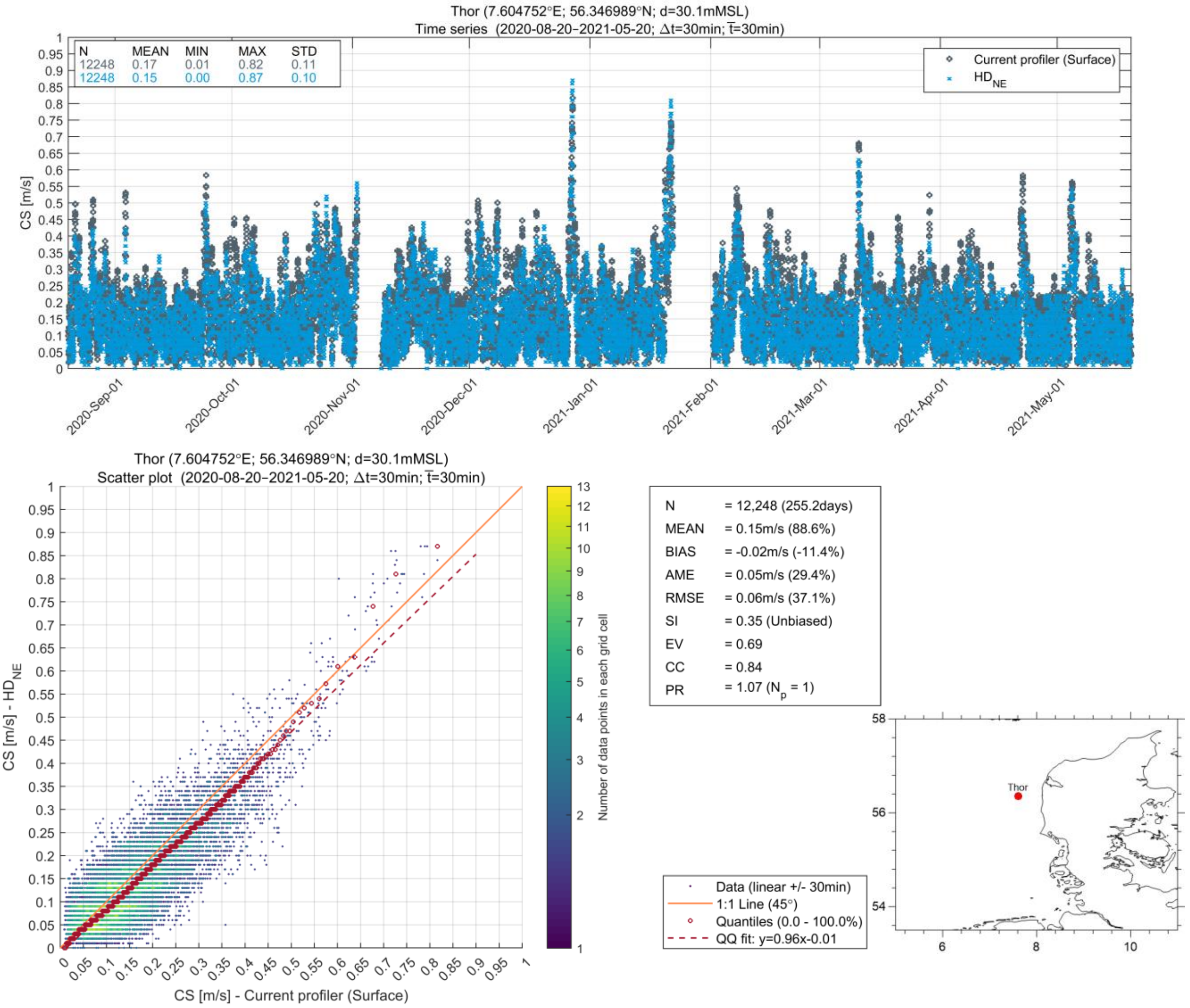

Figure 5.18 Comparison of currents at Thor

5.3.3 Validation of extreme events

A validation of modelled current speeds during peak events was conducted to assess the predictive capabilities of the HD_{EINS} model during extreme conditions. Measurements from the bottom mounted upward looking current profilers, EINS-North (CP seabed), EINS-South (CP seabed) and EINS-Island (Mini 2, CP seabed), were used to for this validation exercise. Figure 5.19 shows the three events used for the validation.

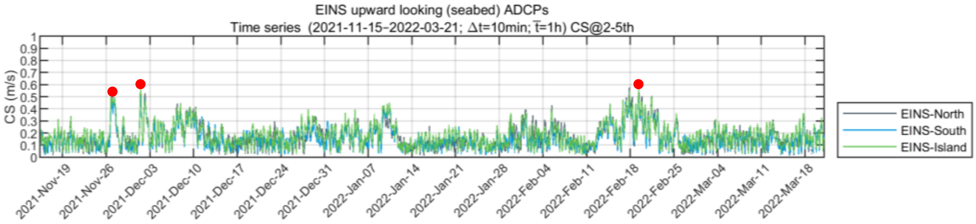

Figure 5.19 Time series of current speed from EINS upward looking ADCPs
Red dots show those occurrences used for peak event validation

Measurements from upward looking sensors are affected by reflections from the surface boundary reducing their quality. Therefore, measurements at the surface (top 5 m) were discarded, implying there is no information on surface currents. This is important during extreme events, where the wind shear over the sea-surface transfers energy to the water column modifying the shape of the vertical profile.

For currents following a logarithmic or power profile, the 2/5th approximation holds true to estimate depth-averaged currents, while for highly distorted profiles, as shown in Figure 5.20, this assumption is invalid or unprecise.

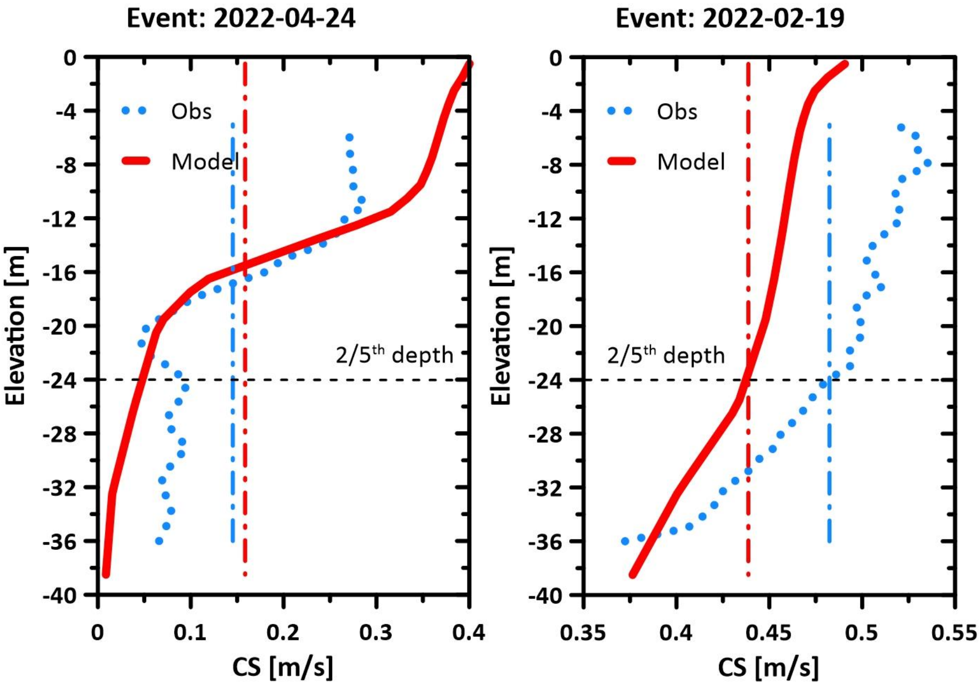

Figure 5.20 Comparison of measured and modelled current profiles during two events at EINS-South
Solid red lines represent profiles of HD_{UKNS3D} (see Section 5.4); Dashed lines represent the depth-averaged currents (averaged over the entire water column).

Figure 5.21 to Figure 5.23 presents time series comparison of measured and modelled depth averaged current speeds for each event and device, and Table 5.3 summarises the peak depth-averaged current speeds from measurements and HD_{EINS} model for each event and each device.

The results indicate a slight underestimation of modelled peak currents at EINS-North and EINS-South, but a slight overestimation at EINS-Island (Mini 2). On average, HD_{EINS} is 0.01 – 0.03 m/s less than the measurements, which is considered well within the uncertainties of estimating the depth-average measurements during extremes.

Discrepancies between different measurements devices and model could be attributed, in part, to the difficulty of averaging incomplete measurements throughout the water column as well as to the complexity of the vertical structure of the measured current profiles during peak events. Longer time series will be required to assess the capabilities of the HD_{EINS} to estimate current speeds during more severe peak events.

Table 5.3 Summary of the maximum measured and modelled current speeds for each of the peak events assessed

Peak event	Date	Device	Measured $CS_{2/5th}$ [m/s][1]	Measured CS_{da} [m/s][2]	HD_{EINS} CS [m/s][3]
#1	2021-11-27	EINS-North	0.53	0.53	0.50
		EINS-South	0.51	0.50	0.44
		EINS-Island (Mini 2)	0.49	0.50	0.56
		Avg.	**0.51**	**0.51**	**0.50**
#2	2021-12-01	EINS-North	0.53	0.51	0.45
		EINS-South	0.48	0.49	0.44
		EINS-Island (Mini 2)	0.56	0.56	0.60
		Avg.	**0.52**	**0.52**	**0.50**
#3	2022-02-19	EINS-North	0.58	0.54	0.54
		EINS-South	0.51	0.52	0.44
		EINS-Island (Mini 2)	0.55	0.56	0.55
		Avg.	**0.55**	**0.54**	**0.51**

[1] Measurements at a distance from the seabed of 2/5th the water (see Section 5.2).
[2] Depth-averaged CS of combined profile from measurements and parametric estimation
[3] Depth-averaged CS from HD_{EINS} model

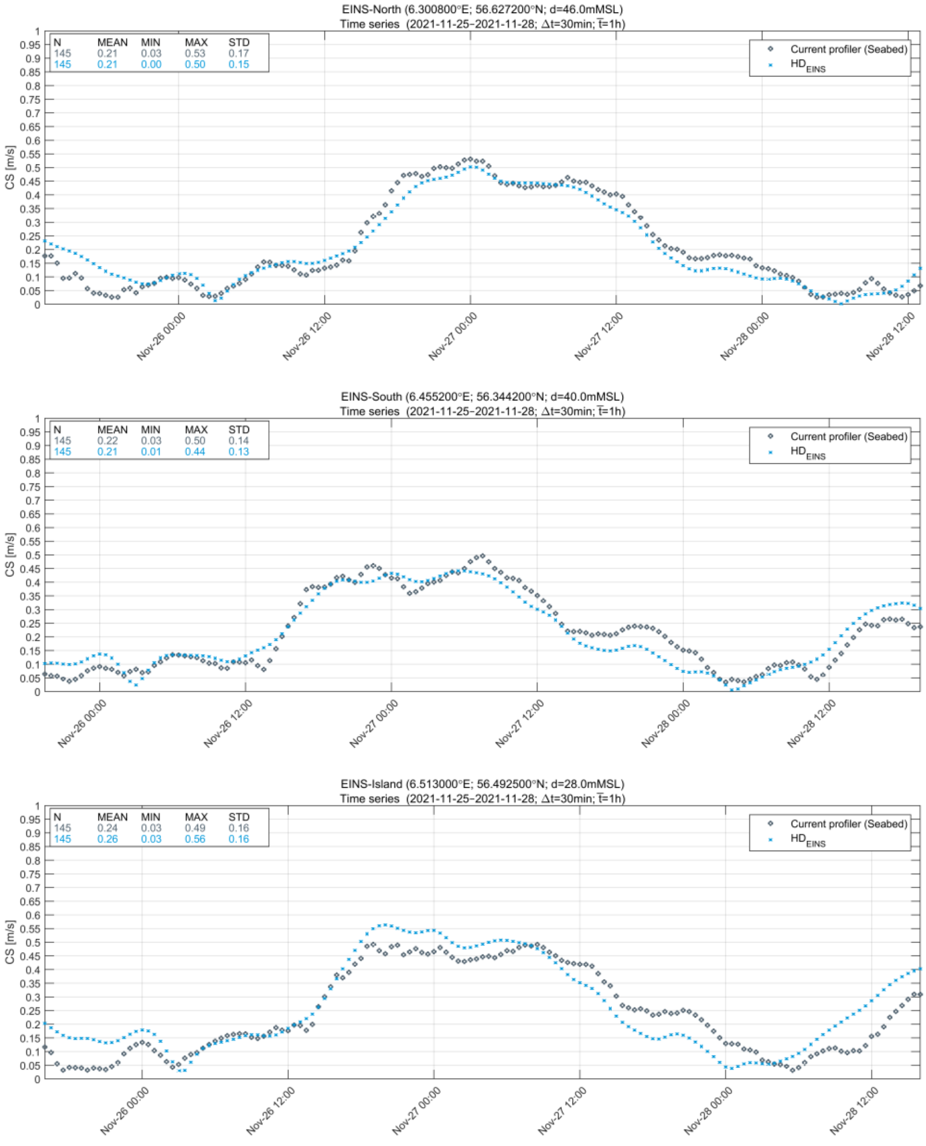

Figure 5.21 Comparison of measured and modelled depth-averaged current speeds during the peak event on 27th Nov 2021

Top panel: EINS-North (CP seabed). Middle panel: EINS-South (CP seabed). Bottom panel: EINS-Island (Mini 2, CP seabed)

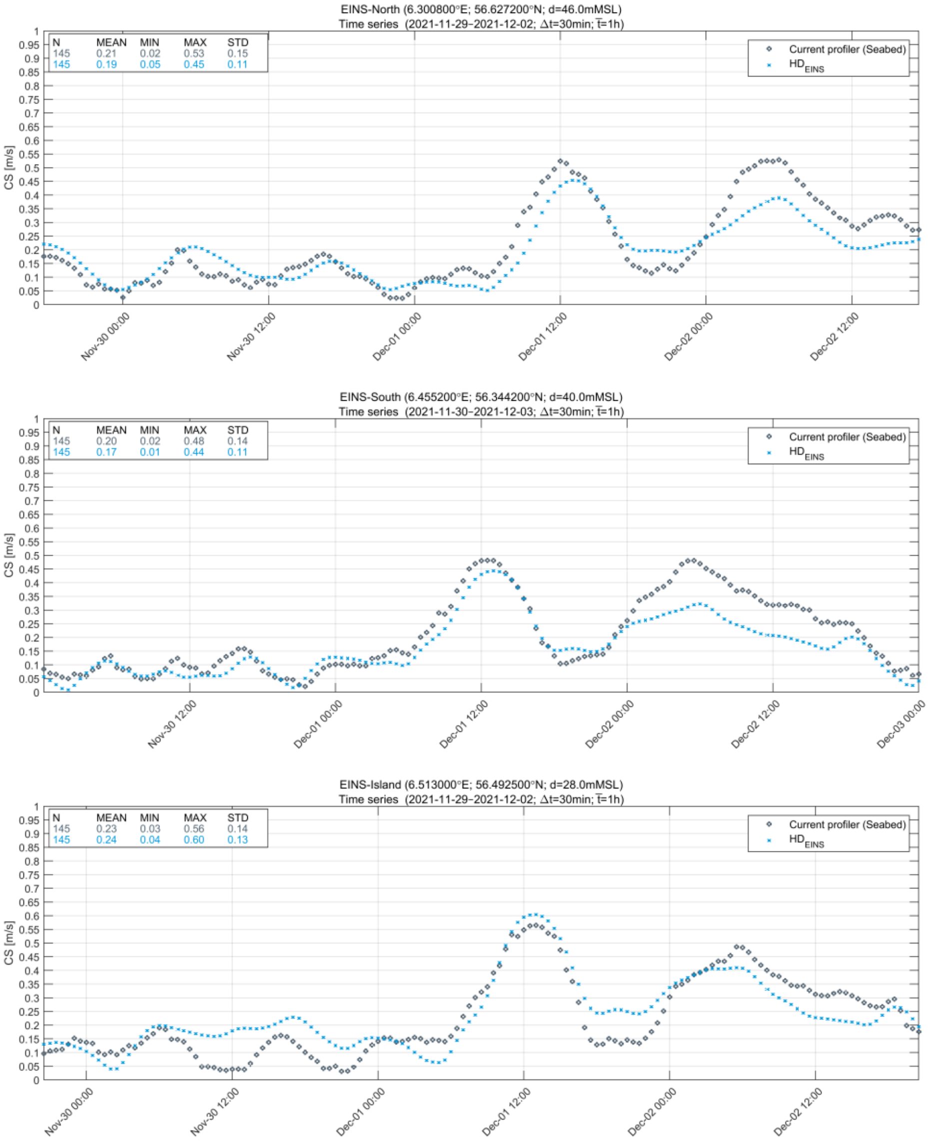

Figure 5.22 **Comparison of measured and modelled depth-averaged current speeds during the peak event on 1st Dec 2021**

Top panel: EINS-North (CP seabed). Middle panel: EINS-South (CP seabed). Bottom panel: EINS-Island (Mini 2, CP seabed)

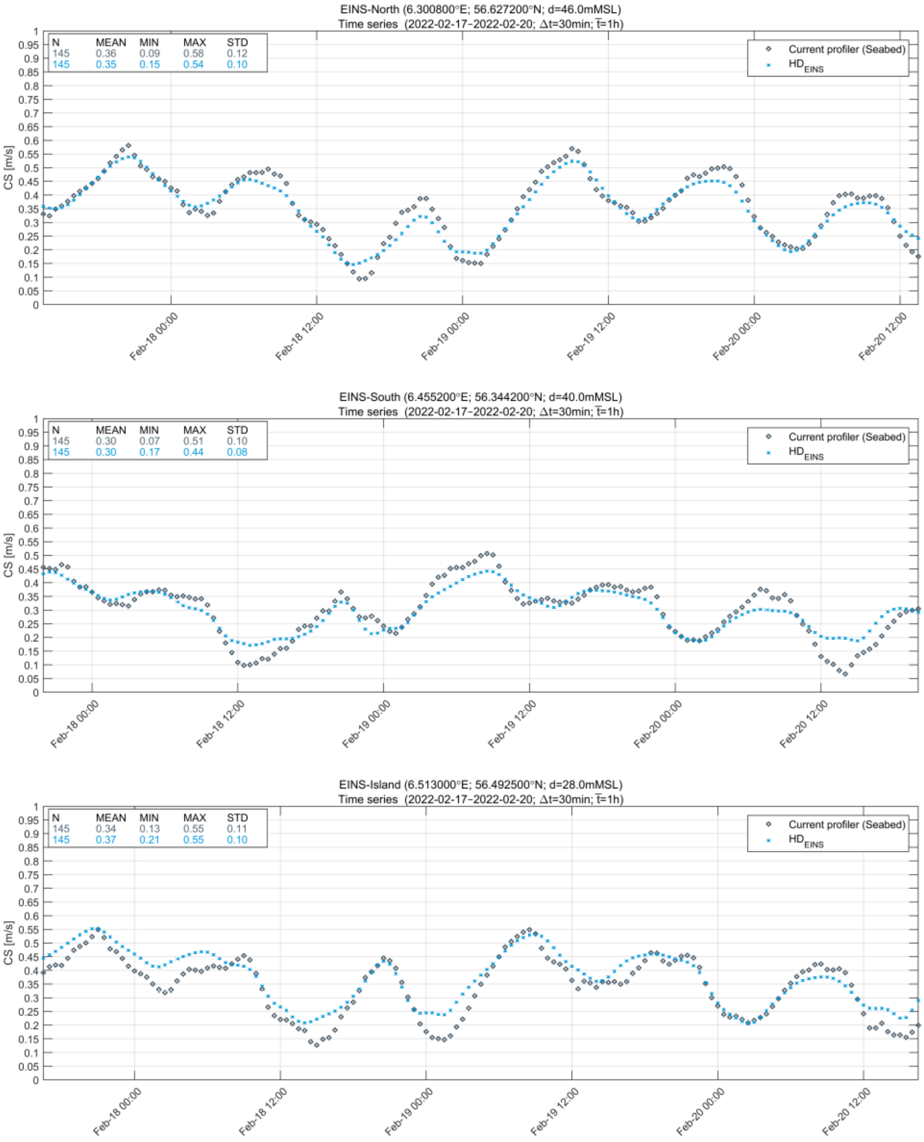

Figure 5.23 Comparison of measured and modelled depth-averaged current speeds during the peak event on 18th Feb 2022

Top panel: EINS-North (CP seabed). Middle panel: EINS-South (CP seabed). Bottom panel: EINS-Island (Mini 2, CP seabed)

5.4 Hindcast current data – 3D

DHI's United Kingdom and North Sea 3-dimensional ($\text{HD}_{\text{UKNS3D}}$) regional hydrodynamic model dataset (covering 2001-2022) served as input for the assessment of current profiles, including surface and seabed currents (see Section 5.5), and for the assessment of sea temperature, salinity, and density (see Section 8.1). Time series of the most recent 10 years (2013 – 2022) at four locations (see Table 8.1) were adopted for this study.

5.4.1 UK and North Sea 3D hydrodynamic model ($\text{HD}_{\text{UKNS3D}}$)

The $\text{HD}_{\text{UKNS3D}}$ model is run with the modelling software MIKE 3 FM (M3FM) developed by DHI. M3FM uses a flexible mesh, and it is developed for applications within oceanographic, coastal, and estuarine environments.

The model is based on the numerical solution of the three-dimensional (3D) incompressible Reynolds averaged Navier-Stokes equations invoking the assumptions of Boussinesq and of hydrostatic pressure. Thus, the model consists of continuity, momentum, temperature, salinity and density equations and it is closed by a turbulent closure scheme. The free surface is considered using a sigma-coordinate transformation approach. Scientific documentation of M3FM is given in [30]. The $\text{HD}_{\text{UKNS3D}}$ model domain (see Figure 5.24) covers the waters around the UK and the North Sea, and has open boundaries towards the North Atlantic, the English Channel, and in Kattegat.

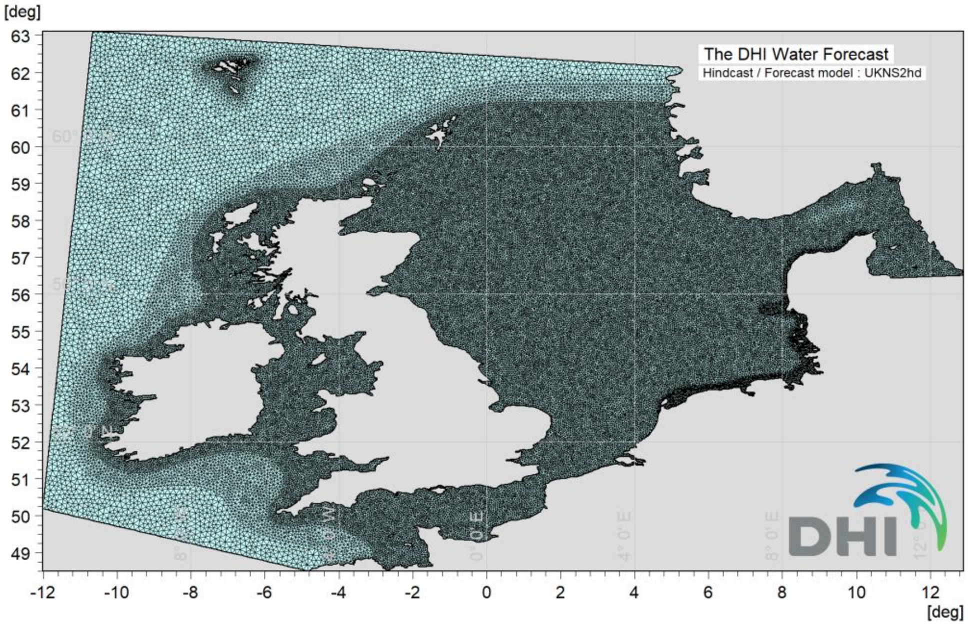

Figure 5.24 Domain and mesh of the $\text{HD}_{\text{UKNS3D}}$ model

The model resolution varies from 3-6 km in the main part of the model domain to 8- 12 km near the ocean boundaries. In a band along the west coast of Netherlands, Germany, and Denmark the resolution is as fine as 2-3 km. At EINS, the model resolution is 3-6 km.

The vertical model discretisation consists of 13 σ-layers down to -61 m level, and 33 z-level layers from -61 m level and below. The thickness of the σ-layers varies from approximately 1.5 m at the surface to approximately 10 m at the -61m level (and proportionally less at water depths less than 61 m). The thickness of the z-layers is 10 m down to -200 m level. Below the -200 m level, the thickness increases gradually from 20m to several hundred meters in the deepest parts.

At EINS, the thickness of the near seabed σ-layer varies between ~5 m (at the shallowest point) and ~8 m (at the deepest point). HD_{UKNS3D} is forcing by atmospheric data provided by StormGeo in terms of temporally and spatially varying fields of wind (WRF model), air pressure (WRF model), precipitation, air temperature, and cloud cover. The HD_{UKNS3D} model includes several sources representing freshwater run-off, and the open boundaries use water level and currents combined from:

- DTU10 global tide [31]
- CMEMS global ocean model (http://marine.copernicus.eu/)

Full details of the HD_{UKNS3D} model as well as model calibration and validation is given in [32]. The bathymetry and metadata can be viewed on MOOD[4]

5.4.2 Validation of 3D current

Figure 5.25 shows a comparison of the measured and the HD_{UKNS3D} depth-averaged current speed. Here, like the approach followed in Section 5.3.2, current speeds at 2/5th the water depth above the seabed are representative of depth-averaged currents speeds.

The figure shows that the HD_{UKNS3D} depth-averaged current speeds and directions accurately represent the measurements (bias = -0.00 m/s and RMSE = 0.03 m/s), however, it seems to slightly underestimate the largest extreme event (on depth-average) (PR = 0.96), as well as some of the less intense events.

Figure 5.26 and Figure 5.27 presents comparisons of near-surface (5 m below) and near-seabed (4 m above) current speed. The comparisons show an overall excellent agreement between the model and the measurements (Surface: bias = +0.01 m/s and RMSE = 0.07 m/s; Seabed: bias = +0.01 m/s and RMSE = 0.03 m/s).

The extreme near-surface currents appear slightly overestimated by the model, however, that may relate to measurement uncertainties during extreme events when the top layers are severely affected by wave action and turbulence. The extreme near-seabed currents also match the measurements well on average, albeit one event is underestimated.

---

[4] https://www.metocean-on-demand.com/metadata/waterdata-dataset-UKNS_HD3D_SGEO

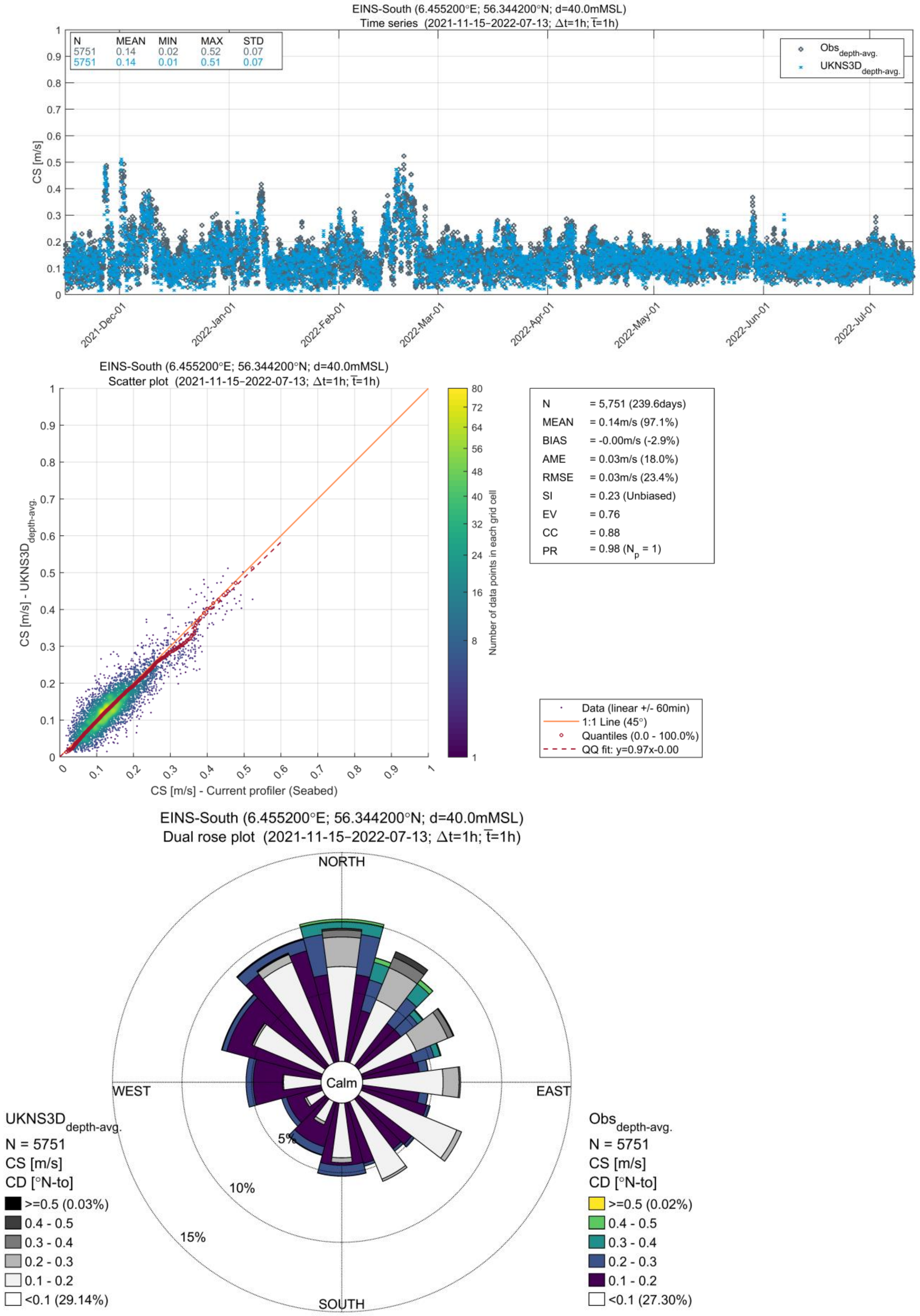

Figure 5.25 Comparison of measured and HD$_{UKNS3D}$ depth-averaged current speeds and directions at EINS-South (CP seabed)

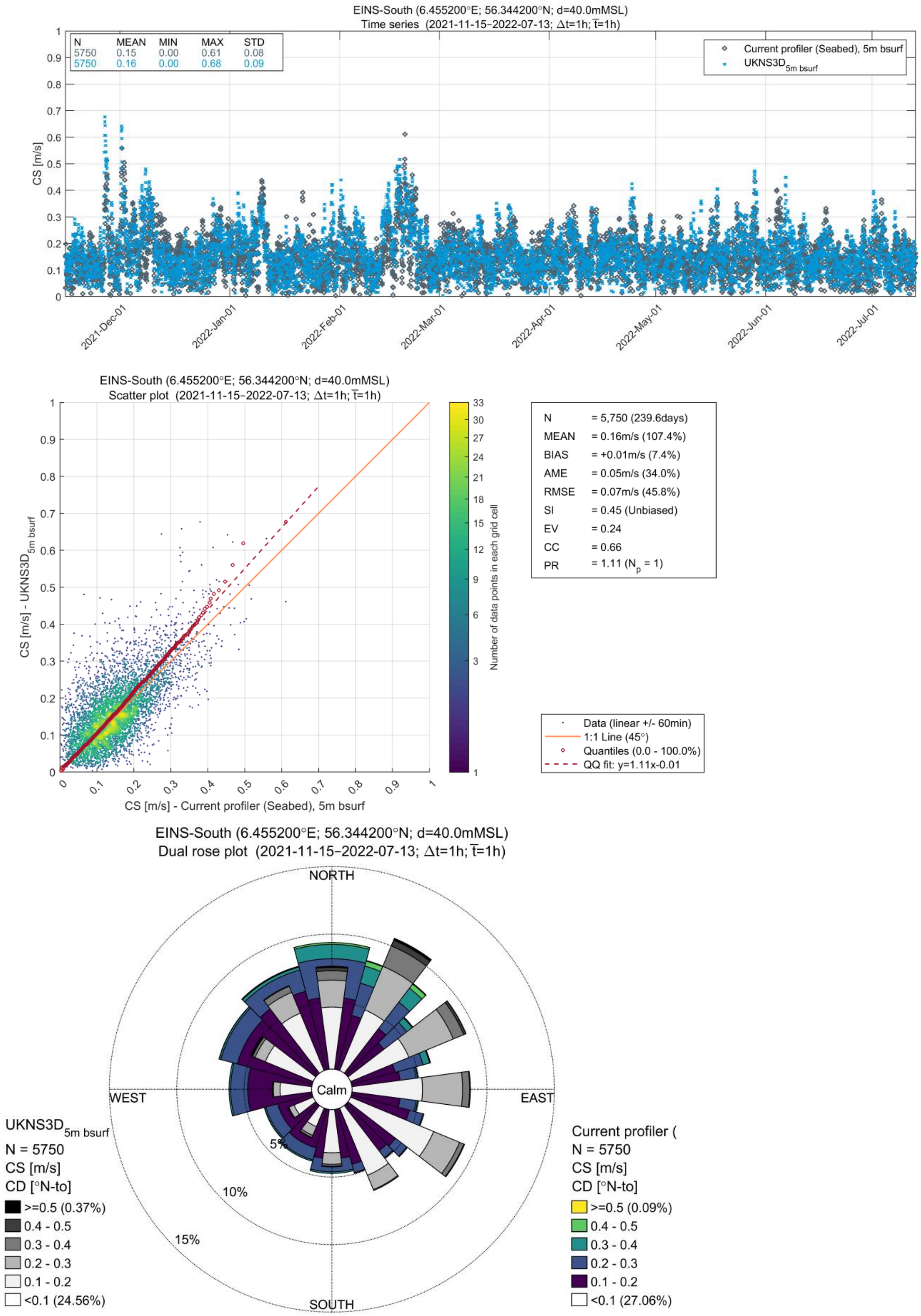

Figure 5.26 Comparison of measured and HD_{UKNS3D} near-surface (5 m below) current speeds and directions at EINS-South (CP seabed)

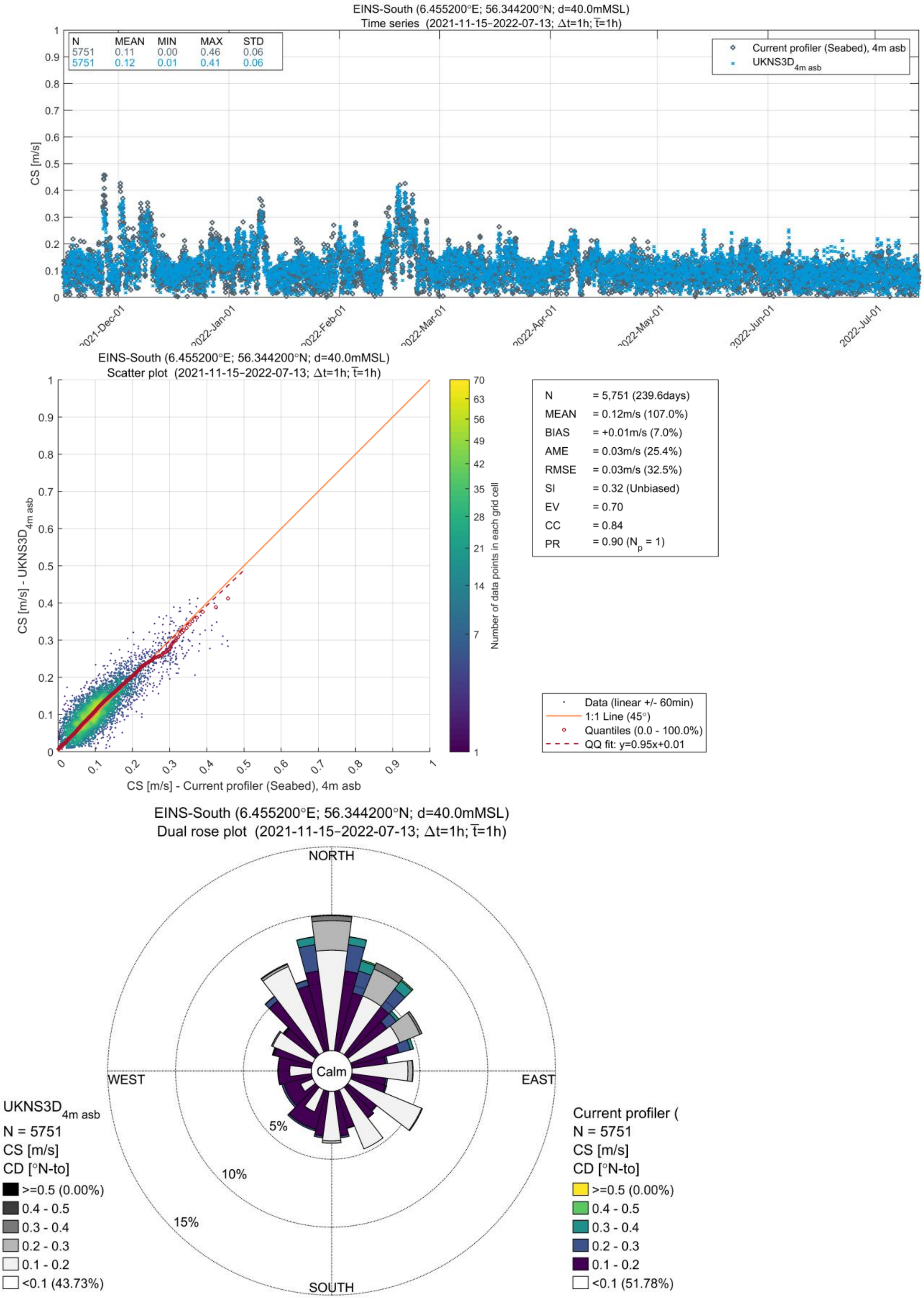

Figure 5.27 Comparison of measured and HD_{UKNS3D} near-seabed (4 m above) current speeds and directions at EINS-South (CP seabed)

5.4.1 Validation of current profiles

Figure 5.28 illustrates 16 timesteps of current profiles at EINS-South (CP seabed) (up to 5 m below the surface) compared to the HD_{UKNS3D} model.

The measurements show somewhat more fluctuations than the model over the water column (partially due to the up to 5-8 m layer thickness of the model), but overall, HD_{UKNS3D} describes the trends and magnitudes well.

The surface currents speed is up to ~0.5 m/s in these examples, and there is a clear influence of wind drag at the surface, resulting in stronger currents at the surface, either in line with or against the tidal current. It is evident that the individual profiles may deviate rather significantly from the mean profiles (see Figure 5.4).

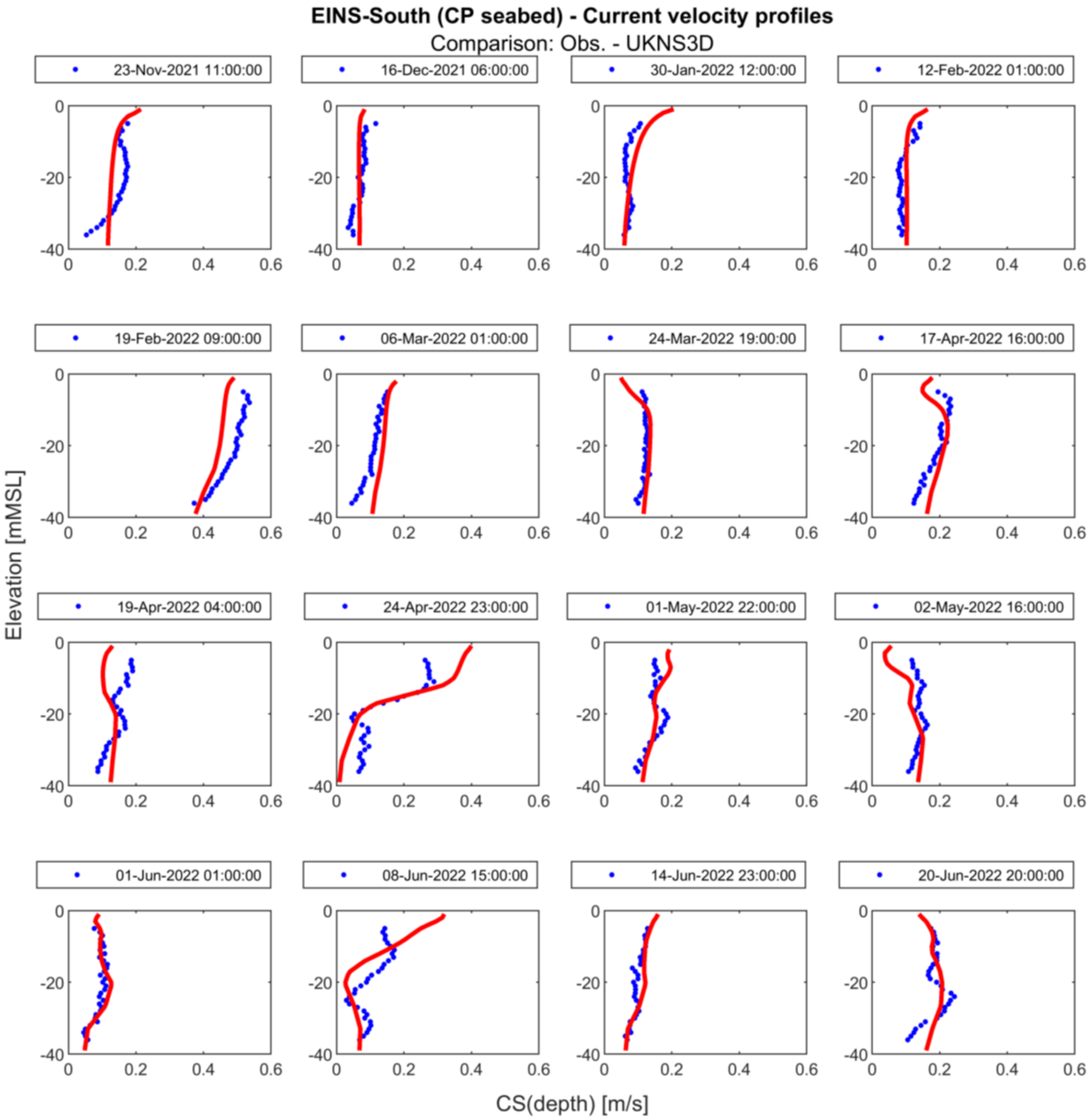

Figure 5.28 Comparison of current profiles at 16 timesteps at EINS-South (CP seabed), blue lines: measured) and red lines: HD_{UKNS3D} model

The profile for the 30th of Jan 2022 (3rd profile) corresponds to storm Malik, however, there were events with larger current speeds like the event on 19th Feb 2022 (5th profile).

5.5 Assessment of current profile

At EINS, the tide is weak, and the current is dominated by residual effects, especially during extreme events. Considering the relatively shallow water depths and the offshore location, density-driven currents are considered minor, and hence, the residual is ascribed mainly to wind.

Design current profile

It is common practice to use standard guidelines (DNV RP-C205, [8], and IEC 61400-3-1, [9]) for characterising the current profile of the tidal and the residual components separately and then (vector-) summing the two components.

When detailed measurements are not available, the variation of tidal current speed with depth in shallow water may be modelled as a simple power profile, cf. Section 4.1.4.2 in [8], see Eq. (5.1). The wind-generated current profile may be described by a linear profile, cf. Section 4.1.4.3 in [8], see Eq. (5.2).

$$\mathrm{CS_{tide}}(z) = \mathrm{CS_{tide}}(0)\times\left(\frac{d+z}{d}\right)^{\alpha} \quad for\ z\ \leq 0 \qquad \textbf{(5.1)}$$

$$\mathrm{CS_{wind}}(z) = \mathrm{CS_{wind}}(0)\times\left(\frac{\mathrm{d_0}+\mathrm{z}}{\mathrm{d_0}}\right) \qquad \textbf{(5.2)}$$

$$z =\ distance\ from\ still\ water\ level, positive\ upwards$$

$$d =\ water\ depth\ to\ still\ water\ level\ (taken\ positive)$$

$$d_0 =\ reference\ depth, IEC: d_0 = 20m, DNV: d_0 = 50m$$

$$\alpha\ typically = \frac{1}{7}$$

Using α = 1/7 means that the tidal current speed at the surface, $\mathrm{CS_{tide}}(0)$, equals 8/7 (= 1.14) times the depth-averaged current speed (and that the current speed at 2/5th (= 0.4) times the water depth above the seabed equals the depth-averaged current speed).

If attributing the entire residual to the wind component, then the wind-driven current at the surface, $\mathrm{CS_{wind}}(0)$, becomes a factor *2 x d/d₀* times the depth-average. For large water depth (d), then this factor becomes quite large. For example, for $d = d_0$, the factor becomes 2, which is considered quite excessive.

Alternatively, in deep water along an open coastline, the wind-generated current speed at the surface may, if statistical data are not available, be taken as a percentage of the wind speed (in the direction of the wind) cf. Section 4.1.4.5 of [8], or Section 6.3.3.3.3 of [9], see Eq. (5.3).

Using the upper limit of k = 0.03, then an extreme wind speed of 40 m/s (corresponding to the ~10,000-year event at EINS) would give surface current of only 1.2 m/s. This magnitude is almost on par with the maximum modelled surface current over just 10 years in $\mathrm{HD_{UKNS3D}}$, see Figure 5.30, and hence considered quite low and unconservative.

$$CS_{wind}(0) = \mathrm{k}\cdot WS_{1h,10m}$$

$$WS_{1h,10m}\ is\ the\ 1\ hour\ sustained\ wind\ speed\ at\ 10\ m\ above\ sea\ level. \qquad \textbf{(5.3)}$$

$$IEC: k\ =\ 0.01$$

$$DNV: k\ =\ 0.015 - 0.03$$

Recommended current profile – Normal

The individual current profiles are highly diverse, as demonstrated in Figure 5.5, Figure 5.6 and Figure 5.28, especially during strong wind. Therefore, each individual current profile cannot be adequately described a by a general/simple profile (e.g. the power (Eq. (5.1)) or linear (Eq. (5.2)) relations).

However, on average, the current profile is uniform, as demonstrated in Figure 5.4, and it can be well represented by a simple profile, for which it is recommended to adopt the power profile, Eq. (5.1) (with $\alpha = 1/7$, and $CS(0) = 1.14 \times CS_{depth\text{-}averaged}$). This profile is shown in Figure 5.7 and Figure 5.8.

For further information on individual current profiles for normal conditions, it is recommended to adopt and analyze 3D model data.

Recommended current profile – Extremes

Considering that one of the key purposes of assessing the current profile is to inform about surface and seabed current speed during extreme conditions, a closer assessment of the measurements and the 3D model data is taken.

The model data is available all the way to surface, and not only from ~5 m below the surface as the measurements. Further, the model has 10 years of data, while the measurements cover 8 months only, which includes very few strong current events.

The drawback of the 3D model is that it does not have the local bathymetry embedded nor the high spatial resolution of the local 2D model. Further, the layer thickness of the lowest layer of the 3D model is about 6 m at EINS, hence, it does not inform about the profile in the lowest 6 m.

Consequently, two different approaches for extreme surface and extreme seabed currents are adopted.

Extreme surface currents

For extreme surface currents the following approach is followed:

1. Compare the surface and depth-averaged current speed at the depth closest to surface (5 m below) available in the measurements
2. Establish the ratio between surface and depth-averaged current speed at the very surface ($z = 0$ m) based on the 10 years of 3D model.

Figure 5.29 show scatter plots of near-surface (5 m below) vs. depth-average current speed at EINS-South. The figure shows a large scatter for the bulk of data but also demonstrate a clear correlation for strong currents. The correlation is evident for the measurements as well as for the model data. The measurements show a lower slope compared to the model, which may possibly be related to measurement uncertainties during extreme events where the surface layers are strongly affected by waves and turbulence (cf. Section 5.2.1). Further, as noted earlier, the measurements cover very few strong currents events.

Hence, for extreme surface currents it is feasible to establish a ratio between surface and depth-average current speed based on the HD_{UKNS3D} model.

Figure 5.30 shows the surface ($z = 0$ m) vs. depth-average current speed from HD_{UKNS3D} (10 years) at four stations across EINS. These stations cover the general water depths (27 – 40 mMSL) across EINS and are thus considered representative of the site conditions. All stations show a clear (linear) correlation with a ratio of 1.2 – 1.3.

As described above, applying standard (design) profiles for wind-induced current is a very crude simplification and it may impose rather significant conservatism. In conclusion, for extreme surface currents, it is recommended to apply a factor of 1.3, based on the 3D model data, to convert the depth-average current speed to surface (z = 0 m).

Extreme near-seabed currents

For extreme seabed currents the following approach is followed:

1. Compare the seabed and depth-averaged current speed at the depth closest to seabed (4 m above) available in the measurements.
2. Adopt a simple profile reflecting that boundary layer (frictional) dynamics are governing for the profile near the seabed.

Figure 5.31 shows scatter plots of near-seabed (4 m above) vs. depth-average current speed at EINS-South. The plots demonstrate a high degree of correlation between near-seabed (4 m above) and depth-average current speed with a ratio of ~0.87. This ratio is very similar to the ratio obtained if using the power profile with $\alpha = 1/7$ at near-seabed (4 m above).

Hence, for extreme near-seabed current it appears feasible to rely on a fixed relation between seabed and depth-average current speed. Unfortunately, neither the measurements nor the 3D model informs about the seabed currents at the very lowest levels. The lowest layer of the 3D model is ~6 m thick, and the bottom-mounted (upward looking) measurements do not record below ~4 m above the seabed, while the buoy mounted (downward looking) measurements do not record below ~2 m above the seabed.

In conclusion, for extreme near-seabed currents, it is recommended to apply the power profile, Eq. (5.1) (with $\alpha = 1/7$, and $CS(0) = 1.14 \times CS_{\text{depth-averaged}}$), to convert the depth-average current speeds to seabed (1 m above). This corresponds to a factor ranging from 0.65 at 25 m depth to a factor of 0.72 at 50 m depth.

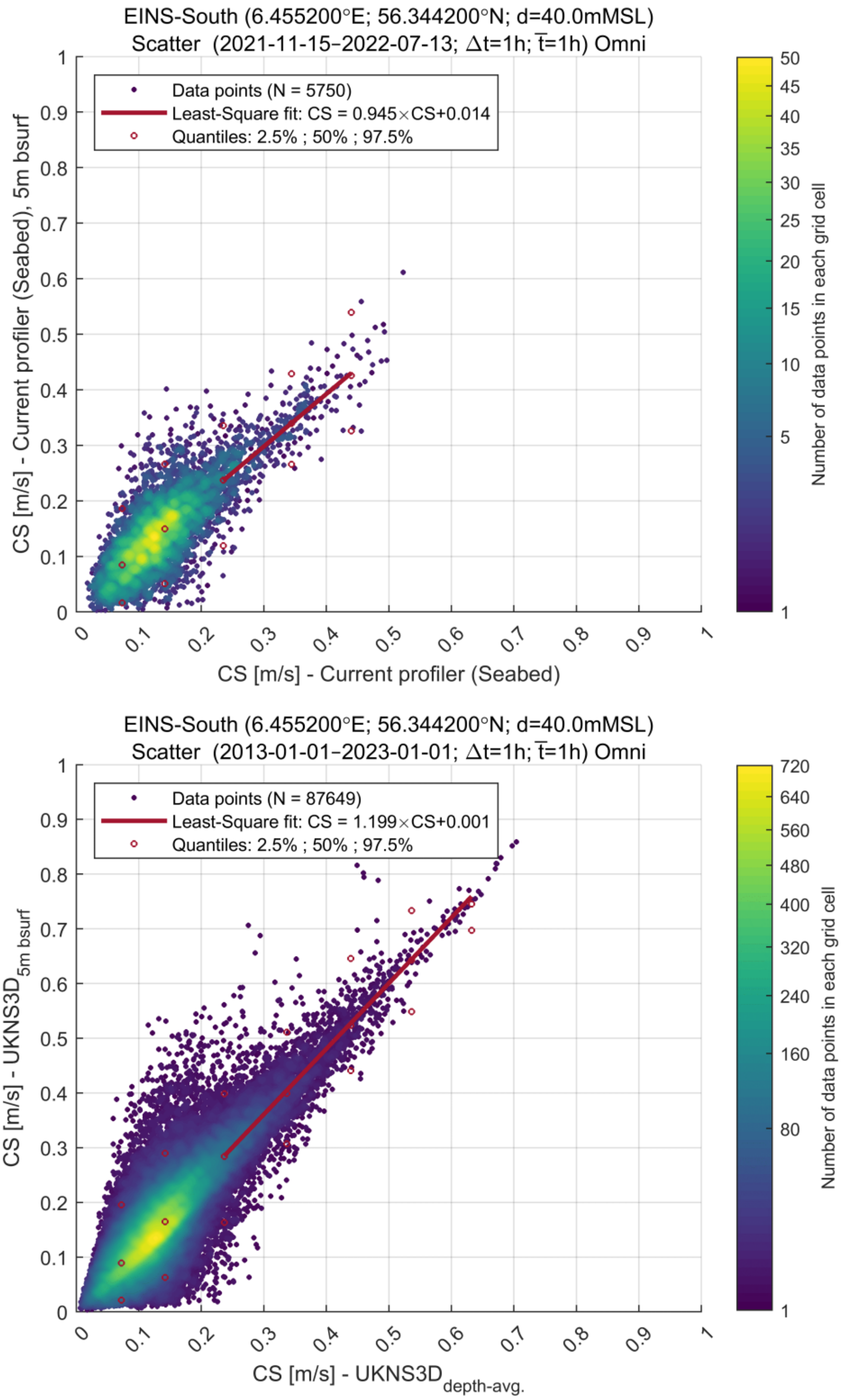

Figure 5.29 **Near-surface (5 m below) vs. depth-average CS at EINS-South**
Top: Measurements (8 months), Bottom: $\text{HD}_{\text{UKNS3D}}$ (10 years).

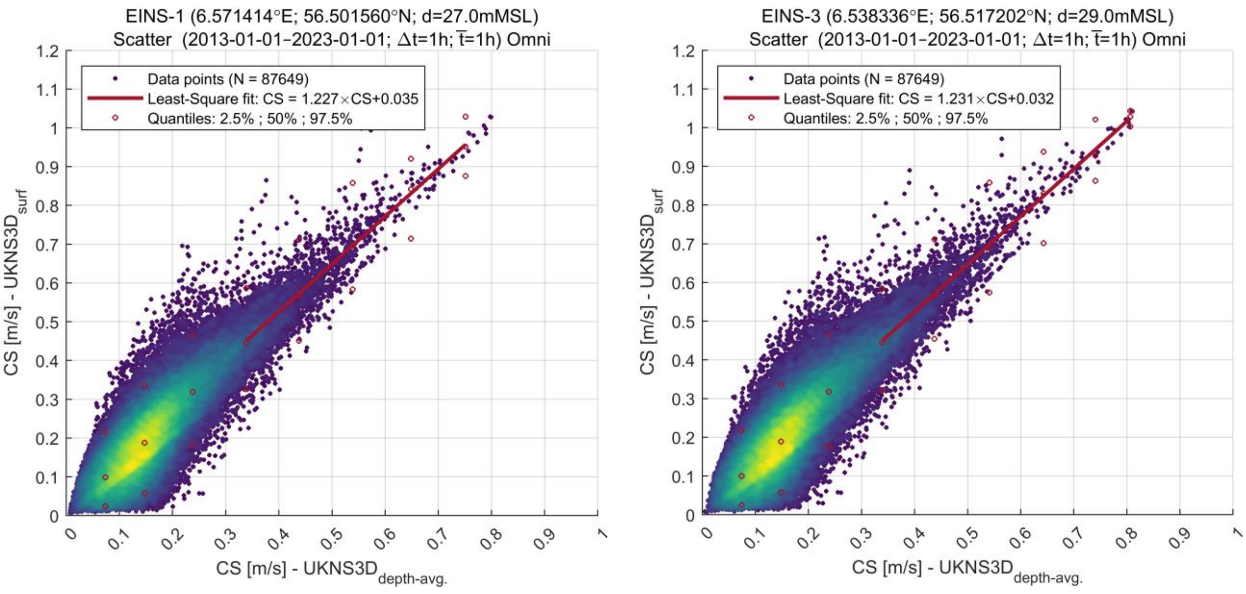

EINS-1 (d = 27 mMSL)

EINS-3 (d = 29 mMSL)

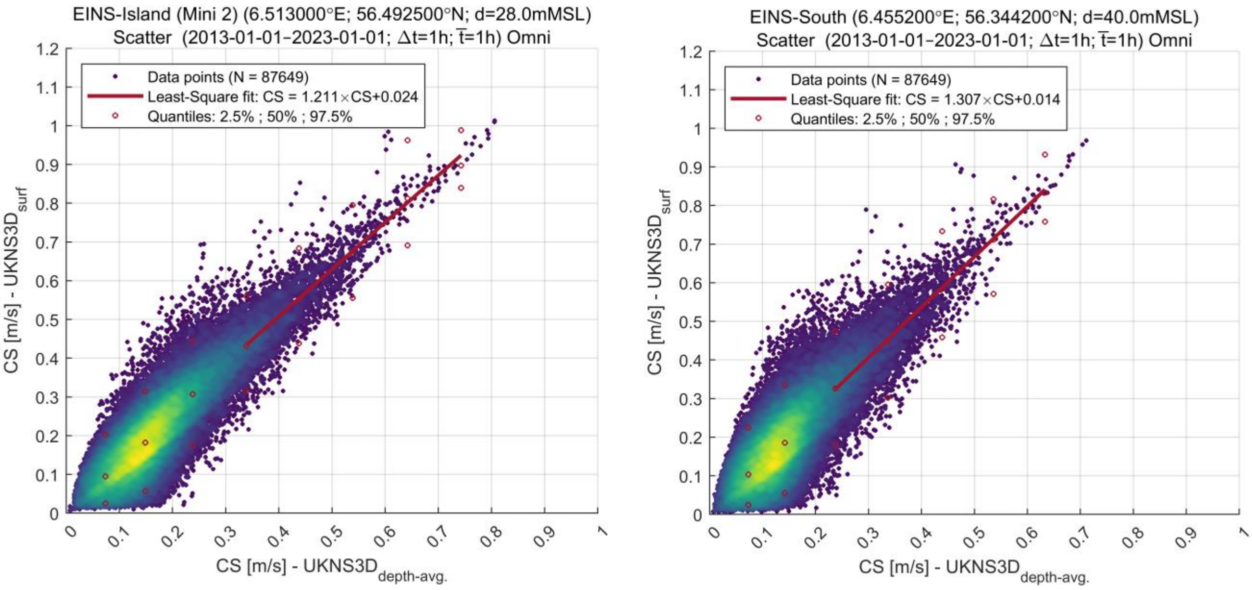

EINS-Island (d = 28 mMSL)

EINS-South (d = 40 mMSL)

Figure 5.30 Surface (z = 0 m) vs. depth-average current speed from HD_{UKNS3D} (10 years)
All four stations show a clear (linear) correlation with a ratio of 1.2 – 1.3.

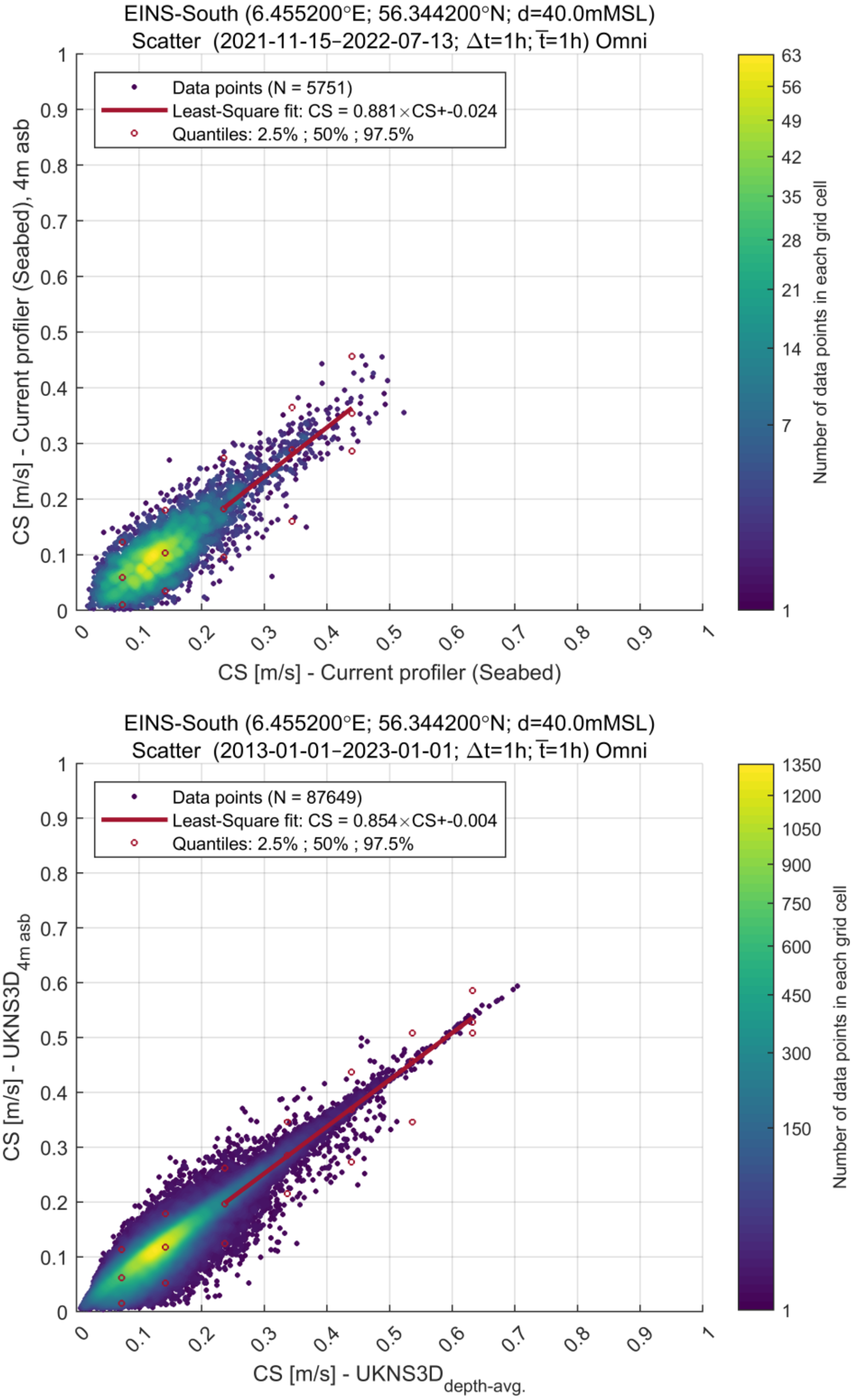

Figure 5.31 **Near-seabed (4 m above) vs. depth-average CS at EINS-South**
Top: Measurements (8 months), Bottom: HD_{UKNS3D} (10 years).

6 Waves

This section presents a general overview of the North Sea wave conditions and presents the wave measurements used to calibrate and validate the local spectral wave model (SW_{EINS}) established to obtain a validated and long-term wave data basis at the EINS site applicable for the assessment of normal and extreme wave conditions. Finally, an assessment of frequency wave spectra is given.

6.1 General wave characteristics

Wave conditions in the North Sea vary seasonally due to the influence of large-scale weather systems. During the autumn and winter months, large storms develop in or cross the North Sea generating rough sea conditions. During the summer months, weather conditions tend to be milder and constant wind patterns are predominant, affecting wave condition patterns. Given its natural boundaries, the North Sea is not exposed to large swells from the Atlantic Ocean, however, powerful low-pressure systems can generate significant waves.

The EINS site is exposed to waves from multiple directions, as it is more than 100 km offshore the west coast of Denmark. On average, at the EINS site, significant wave heights and peak wave periods are of the order of ~2 m and 8 s, while during extreme events, waves can be (much) larger than 10 m. The largest waves often come from the northwest.

6.2 Wave measurements

The locations, depths, etc of measured wave parameters near or at the project site are summarised in Table 6.1 and shown on map in Figure 6.1, while Figure 6.2 shows the temporal coverage.

The quality of the measurements at the project location recorded by the EINS-North, EINS-South, and EINS-Island buoys [2] were quality controlled by FUGRO and checked by DHI to remove any potential outlier or any irregularities in the data. The data from these have an averaging period of 1,024 s, however, data was provided at a running average of 10 min interval.

Measurements outside of the project area were (assumed to be) quality checked by the different providers. Nevertheless, DHI investigated the measurement data to remove any spurious measurements (outliers or unexpected spikes). This is particularly important for the purpose of comparing the model results with the measurement data. Harald and Gorm wave data were retrieved from the AWOS system, which collects and stores measurements from several sensors on Total E&P Denmark A/S (TEPDK) platforms in the North Sea. Data was already processed with time averaging and interval of 10,800s and 3,600 s, respectively. Ekofisk data was provided by Met Norway with a time interval period of 3600 s but unknown time averaging, which was assumed to be similar as the sampling interval. Finally, Thor data was provided by Energinet with a time averaging and interval period of 600 s.

Table 6.1 Metadata of wave measurements

Station Name	Longitude [°E]	Latitude [°N]	Modelled seabed elevation [mMSL][1]	Surveyed seabed elevation [mMSL]	Availability period	Parameters	Averaging period [s]	Sampling interval [s]	Instrument	Owner / Surveyor
EINS-North	6.3007	56.628	-45.5	-46.4	2021-11-15 - 2022-07-15	H_{m0} [m], T_P [s], T_z [s], T_{m01} [s], T_{m02} [s], MWD [°], PWD [°], DSD [°], Spectra	1,024	600	Wavesense 3	Energinet / FUGRO
EINS-South	6.4574	56.3444	-41.3	-39.8	2021-11-15 - 2022-07-15	H_{m0} [m], T_P [s], T_z [s], T_{m01} [s], T_{m02} [s], MWD [°], PWD [°], DSD [°], Spectra	1,024	600	Wavesense 3	Energinet / FUGRO
EINS-Island (Mini 1)	6.519	56.5114	-30.9	-27.0	2021-11-15 - 2022-07-15	H_{m0} [m], T_P [s], T_z [s], T_{m01} [s], T_{m02} [s], MWD [°], PWD [°], DSD [°], Spectra	1,024	1,800	Wavesense 3	Energinet / FUGRO
EINS-Island (Mini 2)	6.5108	56.4929	-29.9	-28.7	2021-11-15 - 2022-07-15	H_{m0} [m], T_P [s], T_z [s], T_{m01} [s], T_{m02} [s], MWD [°], PWD [°], DSD [°], Spectra	1,024	1,800	Wavesense 3	Energinet / FUGRO
Harald	4.273	56.345	-46.5	-46.4	15/09/2005 - 15/09/2015	H_{m0} [m], T_P [s], T_{m01} [s], T_{m02} [s]	10,800	1,800	Not known	TOTAL
Gorm	4.760	55.580	-39.8	-39.8	15/09/2005 - 15/09/2015	H_{m0} [m], T_P [s], T_{m01} [s], T_{m02} [s]	10,800	1,800	Not known	TOTAL
Ekofisk	3.211	56.550	-68.5	-70.5[2]	1980-01-06 - 2021-10-25	H_{m0} [m], T_P [s], T_z [s]	~3,600[3]	3,600	Wave rider	MET Norway
Thor	7.605	56.347	-30.2	-30.1	2020-05-19 - 2021-05-19	H_{m0} [m], T_P [s][4], T_{m02} [s], MWD [°], PWD [°][4], DSD [°][4]	~600	600	Aandera MOTUS	Energinet / Akrocean

[1] Modelled seabed elevation based on the production mesh.
[2] Seabed elevation from EMODnet.
[3] Averaging period is not known but assumed to be the same as the sampling interval.
[4] Parameters available only from 2021-02-01 onwards.

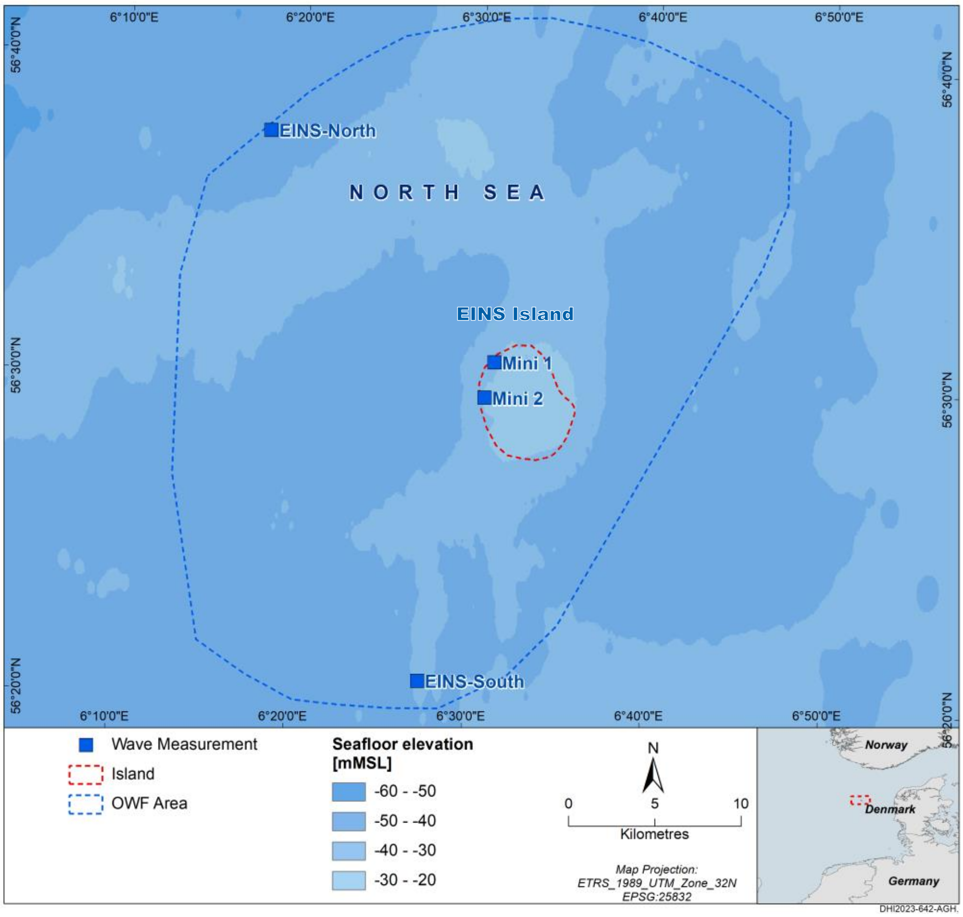

Figure 6.1 **Location of local wave measurements**
Location of regional measurements are shown in Figure 0.1.

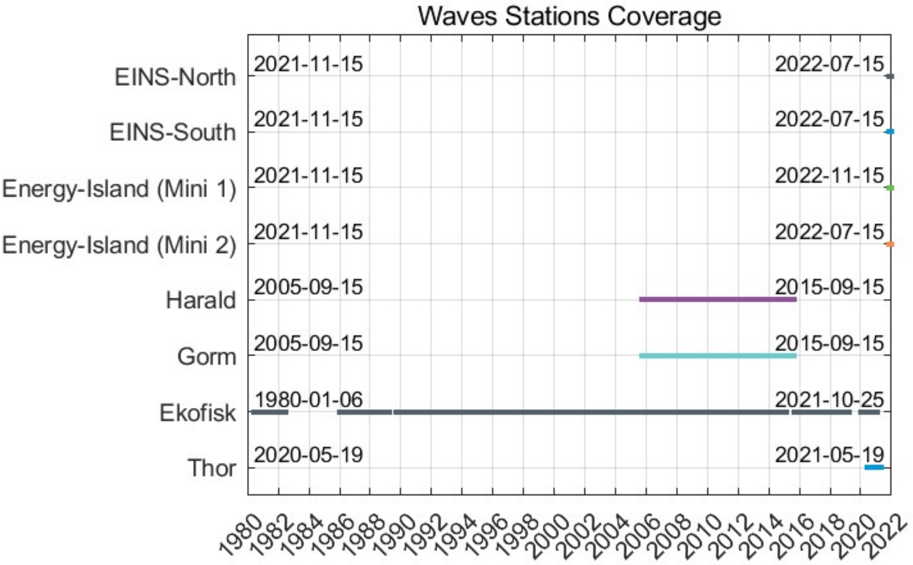

Figure 6.2 **Temporal coverage of wave measurements**

6.2.1 Evaluation of short-term wave and crest distributions

The wind and fetch conditions during storms in the North Sea produce sea states of moderate to high steepness. At EINS, the waves are furthermore affected by the relatively small water depths, and the result is moderate to highly non-linear sea states and wave breaking during severe storms.

A calibrated and validated hindcast spectral wave model is usually our best prediction of the wave spectra in these sea states. It does, however, not inform about the statistical distribution of the individual waves and crests, which must therefore come from published short-term distributions and/or high-quality measurements during relevant (severe storm) sea states. The latter is generally rare, the local buoy data is available for less than one year, and buoy data is often less suitable compared to e.g. mast-mounted radar recordings. Thus, this study must rely on published short-term distributions to assess the individual waves and crests. Numerous distributions exist, Karmpadakis, [33], gives a thorough evaluation of commonly applied distributions as well as suggested new short-term distributions as recently published in [34].

Commonly used short-term distributions

The applicability of, and appropriate choice between, well-known and widely applied short-term distributions, such as the Glukhovskiy (wave height only), [35], and Forristall (wave and crest), [36], is of relevance to estimate the extreme maximum wave height, H_{max} and maximum wave crest, C_{max}. The Rayleigh wave height distribution is often too conservative for extreme sea states but often included for reference. The Rayleigh crest distribution is well-known to be non-conservative. Other distributions exist but are less commonly used. The variation of water depth across EINS (25 - 50 mMSL) combined with the severe storm sea states induces a high likelihood of wave breaking, especially in the shallow regions, which challenges the validity of (any) such published short-term distribution.

For H_{max}, in deep water depth, the Glukhovskiy and Forristall wave height distributions yield similar results of H_{max}, but in intermediate water depth, Glukhovskiy yields lower H_{max} compared to Forristall, because Glukhovskiy accounts for the effect of water depth, which Forristall does not. The Glukhovskiy distribution is a Weibull distribution with a shape parameter increasing with increasing H_{RMS}/d ratio, and therefore a shorter-tailed distribution for increasing H_{RMS}/d ratio. Popular speaking, the distribution predicts that individual waves become more alike and the likelihood of a large H/H_{m0} ratio reduces, as the H_{m0}/d ratio increases.

For C_{max}, there is no distribution by Glukhovskiy, however, the Forristall crest distribution does account for the effect of water depth. The Forristall crest distribution comes in a 2D (long-crested) and 3D (short-crested) version. The 3D distribution is applied herein. The Forristall crest distribution is based on second-order irregular wave theory and does, therefore, not account for non-linear effects beyond second-order, nor for breaking. The former is known to lead to higher crests, while the latter is known to reduce the crests. Hence, at deep/intermediate water depths, the Forristall wave crest distribution is well documented, but for very non-linear waves it may underestimate C_{max}, while during wave breaking it may overestimate C_{max}. The most extreme sea states at EINS are very non-linear (Ursell number > 100), and subject to breaking.

Comparison with measurements

Figure 6.3 shows time series of measured H_{m0}, H_{max} , T_p, and T_{Hmax} at EINS-Island (Mini 1). The average ratio of H_{max}/H_{m0} is 1.51, which is reasonable considering that the measured sea state duration is 17 min, hence, the ratios should be lower than for a 3 h sea state. The average ratio of T_{Hmax}/T_p is 0.81.

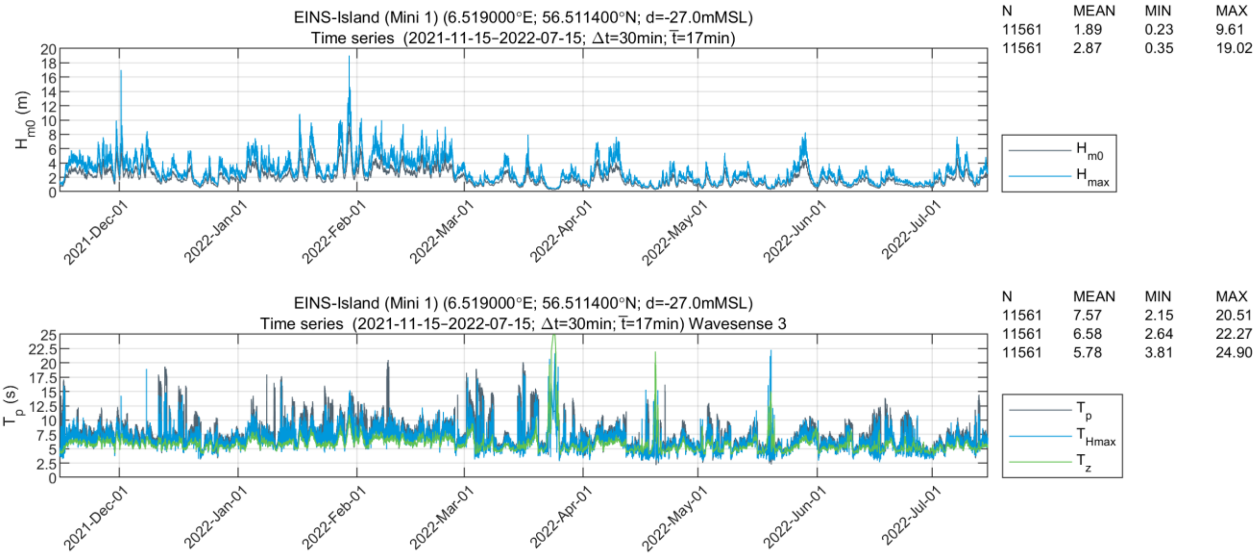

Figure 6.3 **Time series of measured H_{m0}, T_p, T_z, H_{max}, and T_{Hmax} at EINS-Island (Mini 1)**

Figure 6.4 shows the distributions of measured and published (Rayleigh and Forristall) H_{max}/H_{m0} at EINS-Island (Mini 1), the shallowest station, and at EINS-North, the deepest station, for $H_{m0} > 5$ m. The Glukhovskiy distribution is a function of H_{m0} and water level and can therefore not be presented in the normalized format.

The figures show that the measured wave height distributions compare well to that of Forristall, which is expected for the recorded measurements covering H_{m0} up to 9.6 m at a depth of 27 – 46 mMSL. However, the expected extreme 50 – 10.000-year H_{m0} at EINS are in the order of 11 – 15 m, and such large sea states are much more prone to wave breaking at the water depths of the EINS island (25-30 mMSL). In such conditions, the Forristall wave height distribution is likely to be conservative since it does not account for breaking.

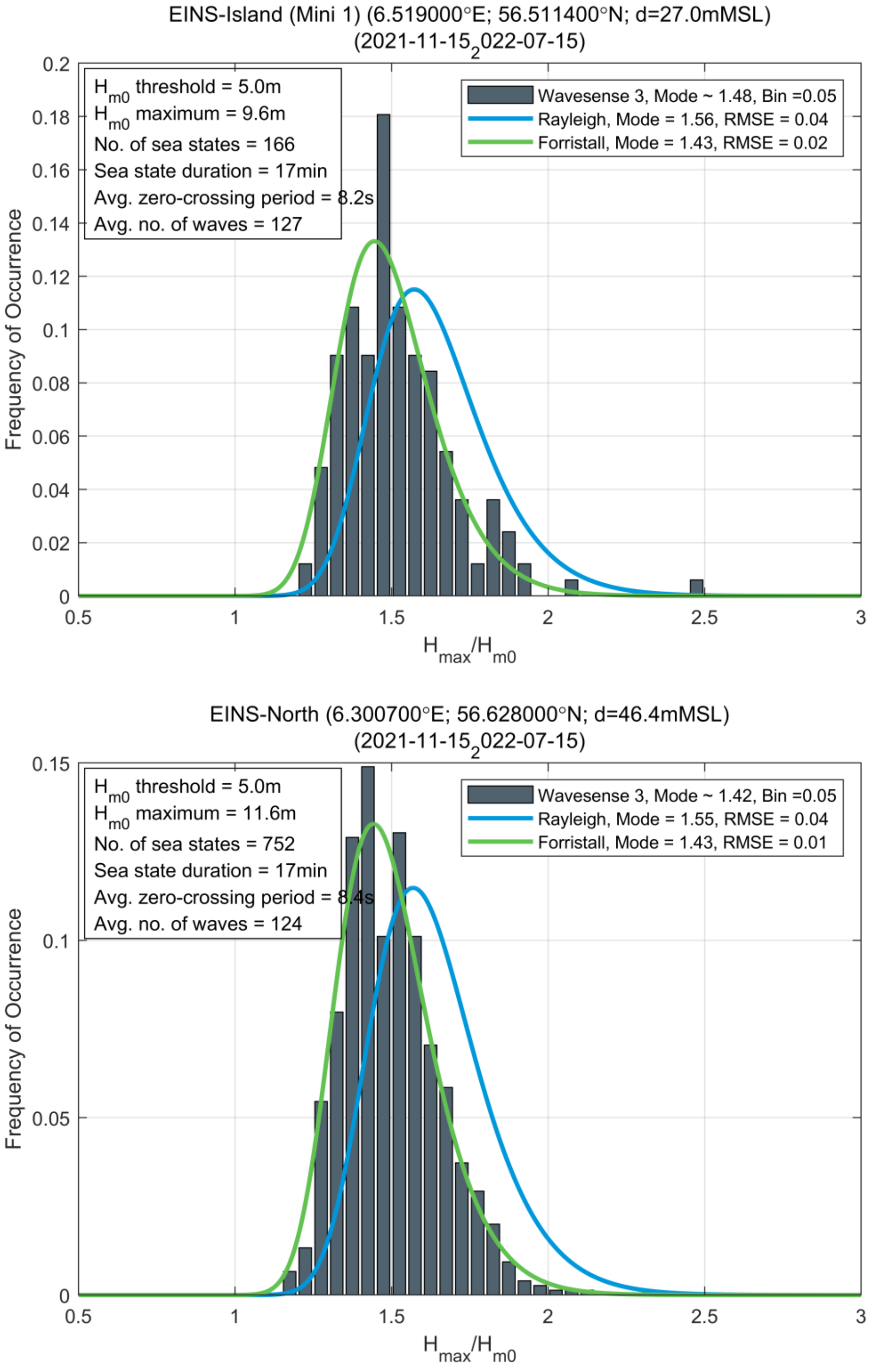

Figure 6.4 Distribution of measured and theoretical H_{max}/H_{m0} at EINS-Island (Mini 1), d = 27 mMSL, and EINS-North, d = 46 mMSL

Conclusion from other studies

Several studies of crest distributions based on laboratory-generated random waves have been made in recent years, primarily in the oil and gas industry, but unfortunately most of this work is not in the public domain. However, generally, the studies have shown that amplifications of crests beyond second order (i.e. above Forristall) are present in many sea states, but that wave breaking may reduce the extreme crests, such that the empirical distribution drops back to the Forristall distribution or even below. Directional spreading has been shown to ‘postpone’ both the non-linear amplifications and the wave breaking, [33], such that crest distributions in directionally spread sea states resembles the Forristall distribution more than the long-crested sea states.

Figure 6.5 shows a typical example of the crest distribution resulting from long random wave simulations in the DHI 3D wave basin of a relatively steep sea state. The measured crests are shown in blue and compared to the Rayleigh and Forristall 3D distribution. The highest elevation over a 72x72 m area has also been plotted for all crests exceeding 13 meters anywhere over the 72x72 m area. This illustrates that the largest crest over an area comparable to the deck-size of many offshore structures is considerably higher than the maximum elevation at a point. This is a result of the 3D and transient nature of an irregular sea state, but it is of course less relevant for offshore wind turbines whose waterplane area is small. The subject of point-to-area crest height ratio has been dealt with by Forristall in [37].

It has also been assessed (visually, by inspection of videos from the model tests) whether the crests with an area-maximum exceeding 13 meters were breaking. The breaking classification is shown in Figure 6.5 with different colour markers for the different types of breaking waves. More than half the waves were assessed to be breaking somewhere within the point of view of the camera, and more than 25% of these were assessed to be plunging. The proportion of waves that were breaking was found by [38] to be highly dependent on the wave steepness.

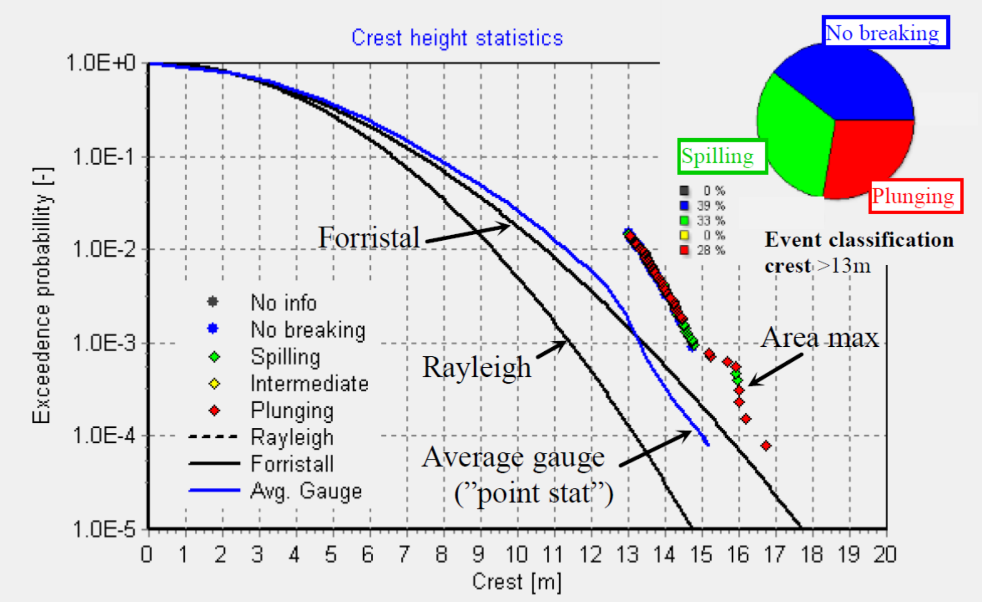

Figure 6.5 Crest distribution resulting from long random wave generation in the DHI 3D shallow water wave basin, Full scale depth 45m, $H_{m0} = 12$m, $T_p = 12.5$s and medium directional spreading, [38]

Recommendations on short-term distributions

Based on the observations from the cited studies above and DHI's experience in these matters, we expect the following effects of short-term distributions:

- The most extreme sea states at EINS are in the region of steepness-induced breaking (of regular waves) and the wave height to water depth ratio is relatively high, especially in the shallowest region at the island area. This means that wave breaking is widespread and thus that the wave and crest distributions are relatively short-tailed.
- The Glukhovskiy wave height distribution is not extremely short-tailed, and its shape parameter depends on the H_{rms}/d ratio, but is not changing with wave height, nor does it consider effects of steepness. The Battjes and Groenendijk and the Wu, et al. distributions, see e.g. [33], have a tail that decays more rapidly. We therefore believe that it is more likely that the Glukhovskiy wave height estimates are on the conservative side than not.
- The Forristall crest distribution does not consider effects beyond second order or wave breaking. Recent studies have shown that both effects are important for the crest distribution, [33]. As higher-order effects and wave breaking have opposite effects on the crests, it is not possible to say with certainty whether the crests at EINS are higher or lower than those based on Forristall. It is possible that the crests in the deeper regions of EINS would increase if higher than second-order effects were included, but it is also possible that wave breaking would counteract the higher-order effects. It is likely that the most severe crests (long return periods) in the shallow regions of EINS would decrease due to intensive wave breaking.

In conclusion, it is recommended to apply the Glukhovskiy wave height distribution to derive extreme H_{max}, and the Forristall wave crest distribution to derive extreme C_{max}, as these distributions consider the local water depth, and since they are commonly recognized and have long history of usage in similar conditions. For future studies, it may be considered to evaluate the applicability of the recently published distributions by Karmpadakis, [34].

6.3 Hindcast wave data

To produce high-resolution modelled wave conditions to be used as input to analysis for design at the EINS site, a dedicated spectral wave model, SW_{EINS}, was established.

This dedicated model incorporated the site bathymetry survey data (see Section 2.2). It was calibration based on in-situ measurements at the site as well as in the greater North Sea. Atmospheric forcing was provided by the global CFSR model for 43+ years (1979-2022), see Section 3.3.1.

SW_{EINS} was established using MIKE 21 SW Spectral Wave FM by MIKE Powered by DHI. The model includes the effects of water levels and currents both of which were provided from the regional hydrodynamic model, HD_{NE}, as described in Section 4.3.2. Described in this section are the following:

- Brief introduction to MIKE 21 SW Spectral Wave FM Release 2022
- Description of the boundary conditions
- Sensitivity studies
- Calibration of the SW_{EINS} model
- Final model setup of the SW_{EINS} model
- Averaging period of waves; and
- Validation of the SW_{EINS} model (integral parameters and spectra)

6.3.1 MIKE 21 Spectral Wave FM (SW)

MIKE 21 SW is a state-of-the-art third-generation spectral wind-wave model developed by DHI. The model simulates growth, decay and transformation of wind-generated waves and swells in offshore and coastal areas. For more information on the MIKE 21 SW model, see [39].

The latest available MIKE 21 SW release was used in this project: MIKE 21 SW 2022 Update 1. The MIKE 2022 release included a comprehensive scientific update including:

- The fully spectral formulation “Modified WAM Cycle 4” and “Ardhuin et al”
- New options for wind sea and swell separation
- Possibility to use neutral wind speed calculated within MIKE 21 SW

The release notes[5] for MIKE 2022 Update 1 are available for more details.

---

[5] https://manuals.mikepoweredbydhi.help/latest/Release_Notes/MIKE%2021%20Release%20Notes.pdf

6.3.2 Boundary conditions

DHI runs a Global Wave Model (GWM) and several regional wave models. The GWM model provided full spectral boundary conditions to DHI's existing regional spectral wave model of North Europe (SW_{NE}), which subsequently provided full spectral boundary conditions to the local model established for the EINS project (SW_{EINS}). Provided in the following sections is a brief introduction to DHI's models used as boundary conditions.

Global Wave Model (GWM)

The DHI Global Wave Model (GWM) is forced by CFSR wind and ice coverage data. The model has been validated against wave observations and has proven successful also when applied as boundary conditions for numerous regional models around the globe. The GWMv3 uses a computational mesh with a varying element size resulting in a resolution of ~100km (snapshot of the mesh in Figure 6.6). The GWM was established with MIKE SW Release 2021 or earlier. The GWM model hindcast was run, including the following:

- Cap on wind friction
- Stability corrected wind fields
- Temporal and spatially varying ratio of air/sea density (based on CFSR)
- Correction of wave celerity for surface current speeds

The GWM provided boundaries for the regional DHI North Europe regional wave model (SW_{NE}), which in turn provided boundaries for the local spectral wave model for EINS (SW_{EINS}).

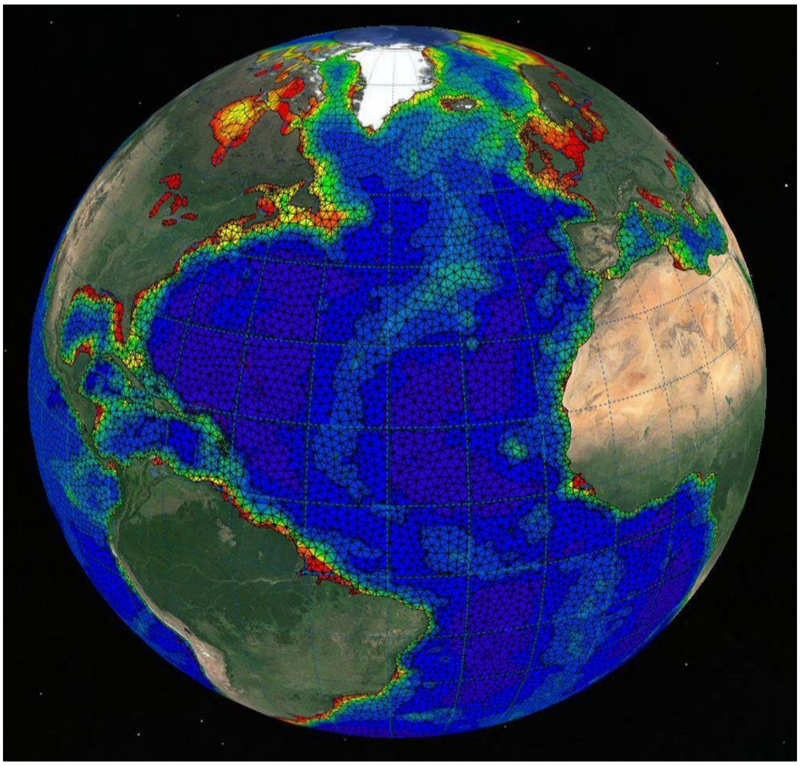

Figure 6.6 Domain of the DHI Global Spectral wave model GWMv3
View centred on the Atlantic Ocean.

North Europe Regional Spectral Wave Model (SW_{NE})

The EINS wave model, SW_{EINS}, was forced by high-accuracy data from the existing DHI North Europe regional spectral wave model, SW_{NE}. Figure 4.4 shows the model domain, going from a resolution of ~16 km (in the North Atlantic) to about 5 km in the southern North Sea and the English Channel. SW_{NE} was established with MIKE SW Release 2021 or earlier. The open boundaries of the regional wave model were forced by directional wave spectra (2D spectra) from GWM presented in the previous section.

The SW_{NE} has been widely used with success in various projects in the North Sea, including major offshore wind farm projects as well as coastal infrastructure and oil and gas industry projects. It takes advantage of some of the latest developments also implemented in the GWM, such as:

- Accounting for the atmospheric stability effects
- Accounting for air-sea density ratio (varying in time and domain)
- Accounting for wind-induced current effect on the wave growth

Validation of modelled significant wave height from SW_{NE} against available altimeter data in the central North Sea is presented in Figure 6.7. The validation shows a good model performance indicated by the low scatter index (SI) and high correlation coefficient (CC). A general validation is available on MOOD (‘*North Europe Spectral Wave Model Validation.pdf*’)[6].

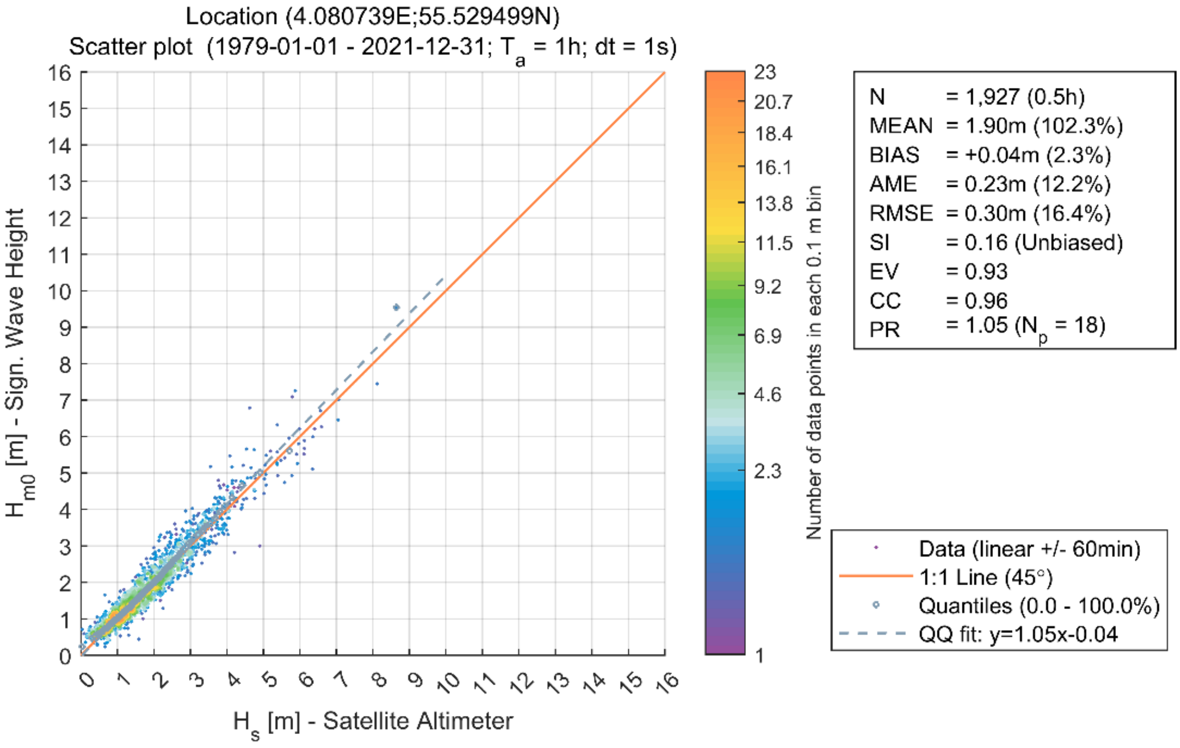

Figure 6.7 Validation of significant wave height (H_{m0}) from DHI’s Regional North Europe spectral wave model (SW_{NE}) in the North Sea against satellite altimeter data

Validation from the DHI Metocean-on-demand portal[7]

---

[6] https://www.metocean-on-demand.com/metadata/waterdata-dataset-Nordic_SW

[7] https://www.metocean-on-demand.com/

6.3.3 Sensitivity studies

Model calibration

During the calibration phase of SW_{EINS}, the sensitivity of model outputs to several model parameters was assessed (e.g., bed friction, wave breaking parameter). Table 6.2 presents all parameters tested. In Section 6.3.4, Table 6.5 summarises the SW_{EINS} model setup used for production of 43+ years (1979-2022) of data.

Table 6.2 Parameters of SW_{EINS} model tunned during calibration

Parameter	Value
Air-sea interaction	Background Charnock 0.062 (Coupled)
Correction of friction velocity	Cap value of: [0.06, 0.14]
Wave breaking	Included, Specified Gamma γ= [0.8, 0.9]
Bottom friction	Nikuradse, k_n = [variable, 0.02, 0.01 m
Air-sea interaction	Background Charnock: [0.0185, 0.062] (Coupled)
Wave age tunning parameter	[0.008 – 0.011]
Non-linear growth parameter	[1.35 – 1.42]

Mesh convergence

Sensitivity studies were carried out to optimise the model computational time without impacting the quality of the modelling. The aim was to find a balance between a model mesh resolution, i.e., a finer mesh is more computationally expensive, and the quality of the model results.

At the EINS site, the sea floor elevation from the site survey was used as input in the model mesh. From the site survey (see Section 2.2), it was known that there are morphological features, that could impact wave propagation and transformation.

Three variations of the mesh resolution at the island were tested: 600, 400, and 200 m (see Figure 4.8), and the survey data was averaged to the same resolution.

The impact of the mesh resolution was assessed at the shallowest point of the EINS site based on 3 of the highest storm events from various directions within the hindcast period, see Table 6.3.

Table 6.3 Storms used for SW_{EINS} model mesh convergence tests at EINS-1 (shallowest)

Case	Start Time	End Time	Approx. max. modelled H_{m0} [m]
#1	2000-01-28	2000-02-02	10.0
#2	2005-01-06	2005-01-10	9.0
#3	2000-10-29	2000-11-01	8.2

The effect of the mesh resolution at the EINS site was almost unnoticeable in the results. For example, the differences in the modelled wave parameters (i.e. H_{m0}, T_{02} and MWD) in the Jan 2000 storm (which was the largest of the 3 storms investigated and therefore expected to demonstrate any difference) are shown in Figure 6.8 to Figure 6.10. The differences are of less than 2 cm in the maximum H_{m0}.

It was therefore concluded that the highest resolution of 200 m was not required and was too computationally expensive with no added value. As a compromise, the model mesh with 400 m resolution was applied. Additionally, the 400 m resolution was chosen to alignment with the HD model (HD_{EINS}) resolution.

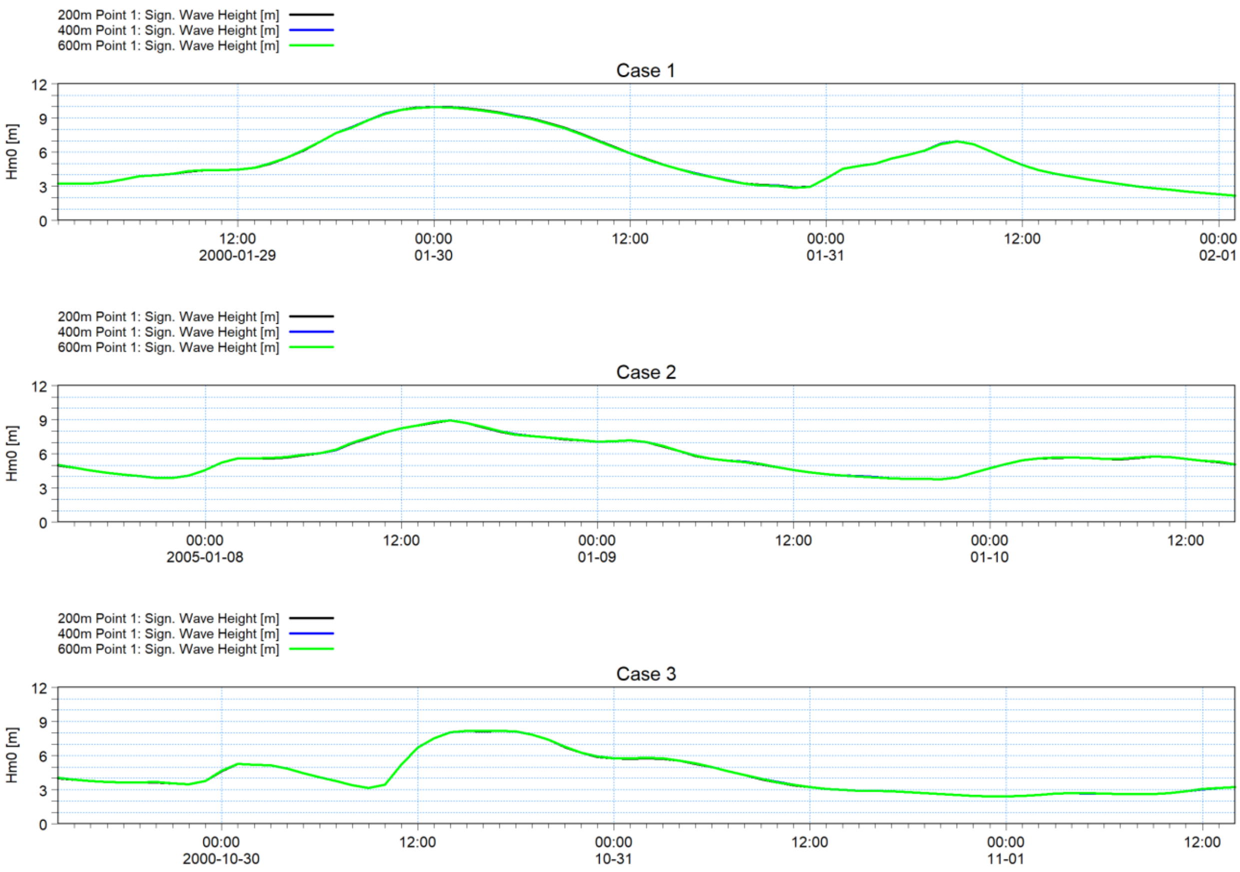

Figure 6.8 Comparison of H_{m0} for three mesh resolutions at EINS-1 (shallowest)

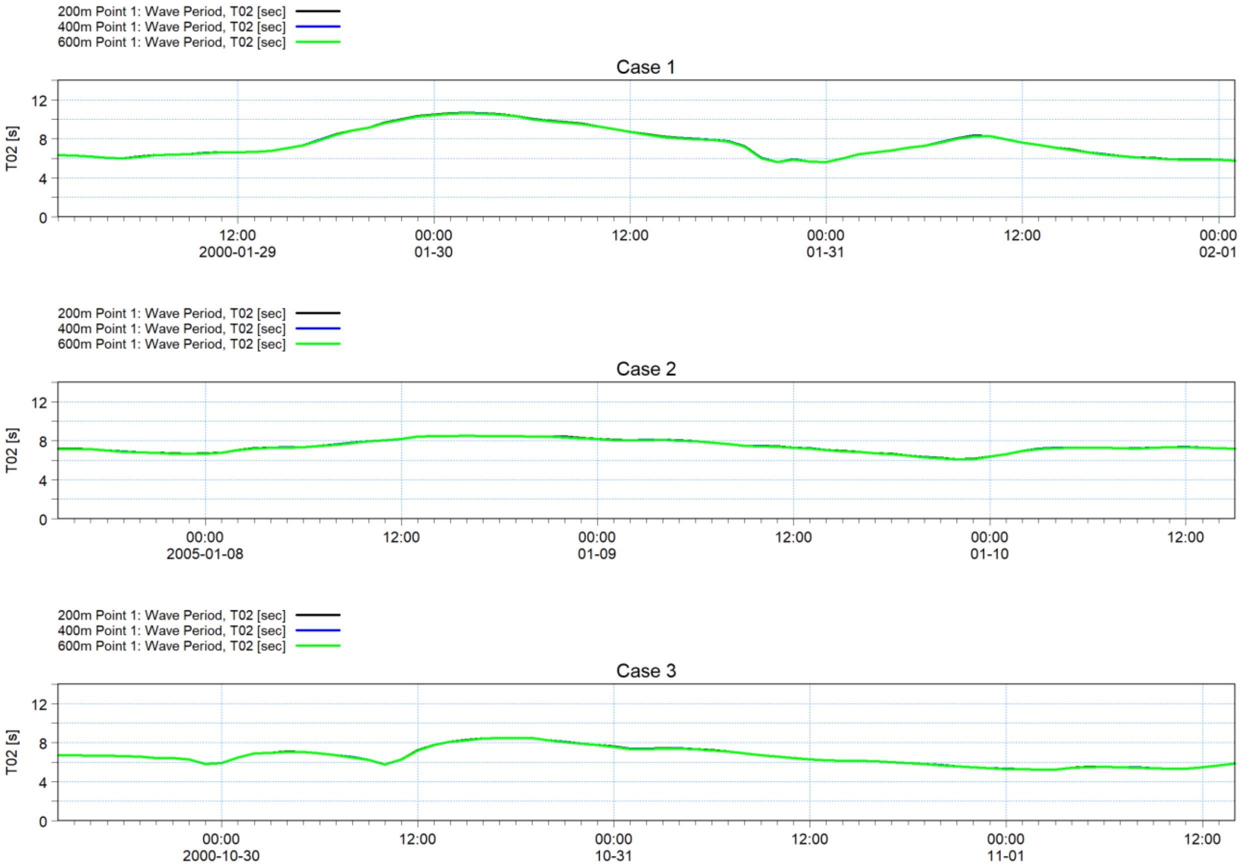

Figure 6.9 Comparison of T_{02} for three mesh resolutions at EINS-1 (shallowest)

Figure 6.10 Comparison of MWD for three mesh resolutions at EINS-1 (Shallowest).

Sensitivity of waves to sea level rise (0.8m)

To assess the impact of SLR on the wave climate, the conservative SLR projection of 0.8 m by 2113 (see Section 9.2) was adopted for adaption of the SW_{EINS}. For this purpose, a set of storms, based on the storms with the highest waves, was modelled using a modified version of the SW_{EINS} model (i.e., $SW_{EINS+SLR}$) that included this sea level rise. A summary of the storm events selected and modelled are presented in Table 6.4. The assessment was conducted at EINS-South location, which is the station within the EINS site where the largest wave height difference was obtained between $SW_{EINS+SLR}$ and SW_{EINS}.

Table 6.4 Extreme events at EINS-South for SLR sensitivity on modelled H_{m0}

Storm ID	Storm date	H_{m0} from SW_{EINS} [m]	H_{m0} from $SW_{EINS+SLR}$ [m]	Diff [%]
#1	1981-11-24	9.99	10.11	1.2
#2	1985-11-05	10.75	10.83	0.7
#3	1990-12-12	7.64	7.72	1.0
#4	2000-01-30	9.96	10.07	1.1
#5	2006-10-31	7.89	7.97	1.0

It was expected that the effect of SLR would be greatest during the largest storm, as the increase in water level would allow for this wave to increase by the largest increment. The largest peak at EINS-South was 10.75 m on 1985-11-06-11-06 06:00.

Changes in maximum significant wave height across the EINS site, from the +0.8 m SLR model scenario relative to hindcast model, were relatively small. The SLR simulation resulted in a mean increase (over the 5 simulated events) of H_{m0} of 0.09 m (0.9%) and a maximum increase of 0.12 m (1.2%). The comparison of the SLR simulations at the location with the largest difference (EINS-South) at the EINS site is shown in Figure 6.11.

Given the very minor impact of SLR on the modelled waves, and that it is an order of magnitude smaller than other uncertainties related to climate change effects on waves (wind), no further action was taken in terms of estimating extreme wave conditions due to climate change for a future scenario, as agreed with Energinet, cf. Section 9.

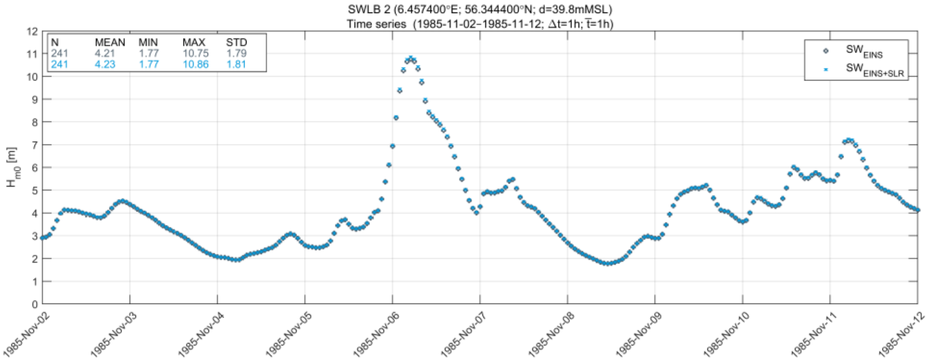

Figure 6.11 Comparison at EINS-South of modelled H_{m0} between SW_{EINS} and $SW_{EINS+SLR}$ during storm event of 1985-11-05

Practically no difference (9 cm = <1 %) in modelled H_{m0}.

6.3.4 Model setup (SW_{EINS})

The SW_{EINS} model setup used for production of the 43+ years (1979-2022) is summarized in Table 6.5.

The HD model used as part of the forcing of the SW_{EINS} model was HD_{NE} (see Section 4.3.2). This was due to the domain of the SW_{EINS} model being larger than the local HD_{EINS}. Modelled water level and current at the site were compared between HD_{NE} and HD_{EINS}, and the results of the two model were mostly similar, such that the derived effect on the waves was negligible. To force the SW_{EINS}, the use of HD_{NE} was therefore considered of adequate quality. For any analyses or provision of HD time series data from this study, it is noted that the data is from the HD_{EINS} model.

Table 6.5 Specifications of SW_{EINS} model settings
Final model setting of the local spectral wave model, SW_{EINS}.

Setting	Value
Engine (version)	MIKE 21 Spectral Wave (SW) model (2022, Update 1)
Mesh resolution	Element size at EINS OWF ~ 400m
Simulation period	1979-01-01 – 2022-09-30 (43+ years), 0.5-hourly output
Basic equations	Fully spectral in-stationary
Discretisation	35 frequencies (0.78–30.3 s (0.033-1.273 Hz), 36 directions
Time step (adaptive)	0.01-120 s with a maximum time-step factor of 16
Water level	HD_{NE} and $HD_{NE\text{-}DA}$ (temporally and spatially varying)
Current conditions	HD_{NE} and $HD_{NE\text{-}DA}$ (temporally and spatially varying)
Wind forcing	CFSR
Air-sea interaction	Background Charnock 0.062 (Coupled)
Neutral winds	True (Varying in time and domain calculated from CFSR)
Correction of friction vel.	Cap value of 0.06
Air/water density ratio	Varying in time and domain calculated from CFSR
Energy transfer	Included, quadruplet-wave interaction (no triads)
Wave breaking	Included, Specified Gamma, γ=0.9, α= 1 [40]
Bottom friction	Nikuradse, k_n = 0.01 m
Boundary conditions	2D spectra varying in time and along line; from SW_{NE}
Growth parameter	0.02
Wave age tunning param.	0.008
Output specifications	Integral wave parameters saved at all grid elements with a 30 min interval. Spectra saved on a 1 -5 km grid, see Section 6.3.5.

6.3.5 Output specifications

Output was saved with a 30 min interval and included the integral wave parameters listed in Table 6.6 at every mesh element in the model domain.

Each integral parameter was saved for the total sea state and for swell and wind-sea components, respectively. The wind-sea/swell partitioning was based on a wave-age criterion (see section 5.1 of [41]), where the swell components are defined as those components fulfilling:

$$\frac{U_{10}}{c}\cos(\theta - \theta_w) < 0.83$$

where U_{10} is the wind speed at 10m above MSL, c is the phase speed, and θ and θ_w are the wave propagation and wind direction, respectively.

Table 6.6 Output specifications of $\mathrm{SW_{EINS}}$
Parameters saved at all grid elements with 30 min interval.

Parameter (**total, wind-sea, and swell)**	Abbreviation	Unit
Spectral significant wave height	H_{m0}	m
Peak wave period	T_p	s
Spectral mean wave period	T_{01}	s
Spectral zero-crossing wave period	T_{02}	s
Peak wave direction	PWD	°N (clockwise from)
Mean wave direction	MWD	°N (clockwise from)
Direction standard deviation	DSD	°

Full (directional-frequency) wave spectra were saved on a 0.1° (~10 km) grid within the island area and on a 0.5° (~50 km) grid within the OWF area and surrounding region, see Figure 6.12.

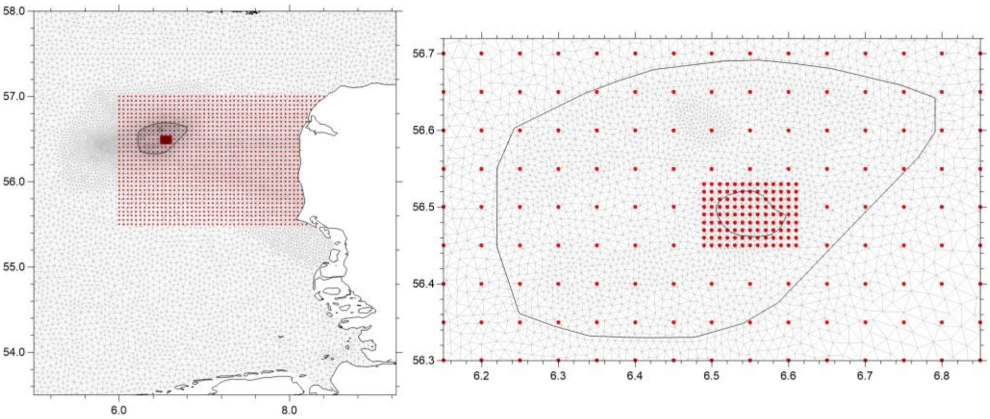

Figure 6.12 Locations of wave spectra saved from $\mathrm{SW_{EINS}}$
Left: Surrounding region (0.5°). Right: Island (0.1°) and OWF area (0.5°).

Averaging period of waves

The significant wave heights, H_{m0}, from the SW_{EINS} model are essentially instantaneous ’snapshots’ of the wave field that are saved at ½-hour time intervals from the model. The time scales resolved in the numerical models underpinning the hindcast data are affected by the spatial resolution and the wind forcing, and hence the data represents wave heights that are implicitly averaged over some time averaging period, T_{avg}. One may therefore expect measurements to exhibit higher variability compared to model data. Correspondingly, the model data may be regarded as somewhat ‘smoothed’ (in space and time) compared to the observations. For practical applications such as for example extreme value assessment or load calculations (e.g., wave heights associated with extreme sea-states), appropriate accounting for the smoothed nature of the model data must be considered.

A simple and frequently used approach for assessing the representative temporal scale (or smoothing) of the wave models is by comparing the power spectra of modelled wave heights with the power spectra of measurements that have been smoothed using various averaging windows (10-minutes, 60-minutes, 120-minutes, and 180-minutes). The spectral analysis was performed to the measured data sets from one of the LiDAR buoys (EINS-North) at the EINS site and from the Ekofisk station (see Figure 6.1) as well as to their corresponding data sets from the SW_{EINS}. The resulting frequency power spectra for H_{m0} are shown in Figure 6.13 and Figure 6.14, where the frequency power spectra follow the 180-minutes line the most closely. Therefore, for the purposes of this study, we have adopted 180-minutes as the representative temporal averaging period of H_{m0} of the SW_{EINS} model, i.e., T_{avg} = 180 minutes.

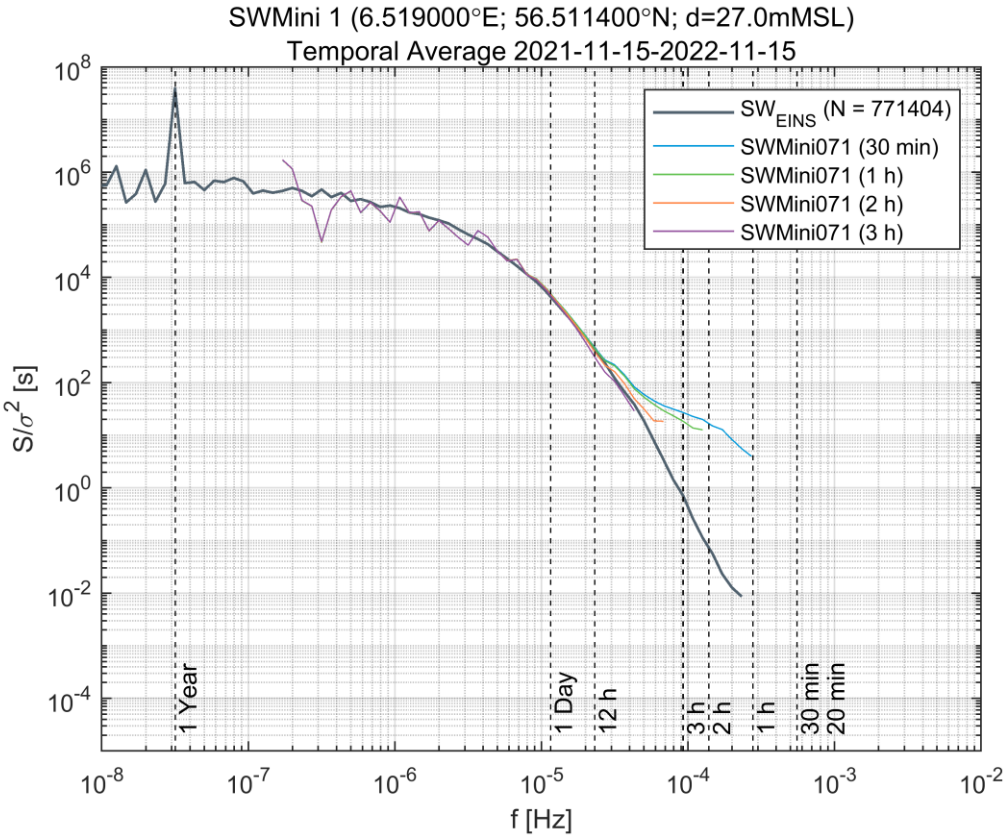

Figure 6.13 Frequency power spectra of H_{m0} at SWMini1

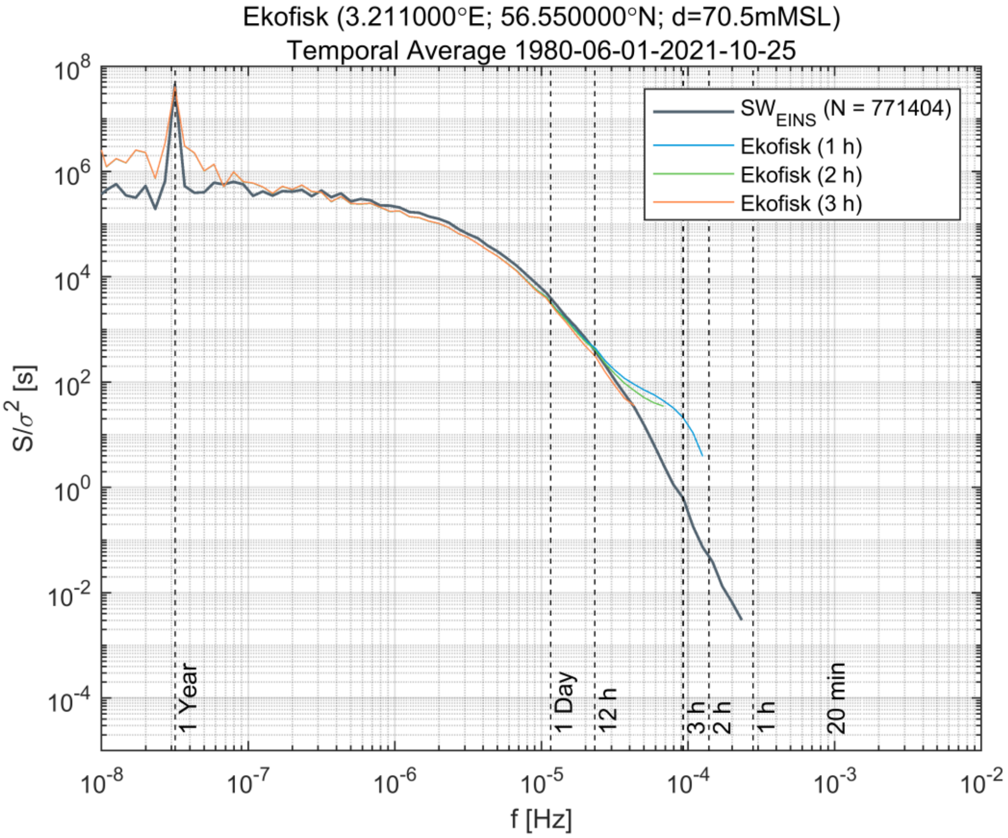

Figure 6.14 Frequency power spectra of H_{m0} at Ekofisk

6.3.6 Validation of integral wave parameters

Presented in this section are the validation results of the SW_{EINS} model against available measurement data, previously introduced in Section 6.2. A summary of the model validation statistics at the measurement stations of significant wave height (H_{m0}) data is presented in Table 12.4. Additionally, summaries of the model validation statistics at the measurement stations of peak wave period (T_p) and mean zero-crossing wave period (T_{02}) data are presented in Table 12.5 and Table 12.6.

The validation plots (time series, scatter plots, wave roses etc.) highlighting the performance of the model at the EINS site and its proximities are presented in Figure 6.15 to Figure 6.38. These include the plots for EINS buoys (EINS-North, EINS-South and EINS-Island), Harald, Gorm, Ekofisk and Thor LiDAR Buoy.

The SW_{EINS} model shows an excellent comparison with measurements of H_{m0}. This is shown through the bias being + 10 cm, RMSE < 27 cm, SI < 0.13, and CC > 0.98 across all measurement stations. The performance at the EINS site is excellent, as shown in Figure 6.15 to Figure 6.26. Slightly further away from the site, the performance of the model is backed up with an excellent representation of the wave conditions measured at four locations, three long-term measurements to the west (Ekofisk, Harald, and Gorm) and one short term measurement to the east (Thor) of the project site. The modelled MWD shows to follow the measured directional pattern very well.

In general, there is a tendency by SW_{EINS} to slightly overestimate T_p, but this may be partly due to scatter in the measured data. T_{02} is shown to compare reasonably with measurements, albeit it appears to slightly underestimate T_{02} by ~0.2-0.4 s. However, such slight underestimation may well be caused by differences in the definition of T_{02} from model and measurements respectively. T_{02} being dependent on the second order moment of the wave spectra and thus very sensitive to the shape of the spectral tail (high frequencies, short waves) which may not be well recorded by a large instrument. A closer agreement between measurements and model may be obtained by cropping the model spectra accordingly and reprocess T_{02}.

EINS-North

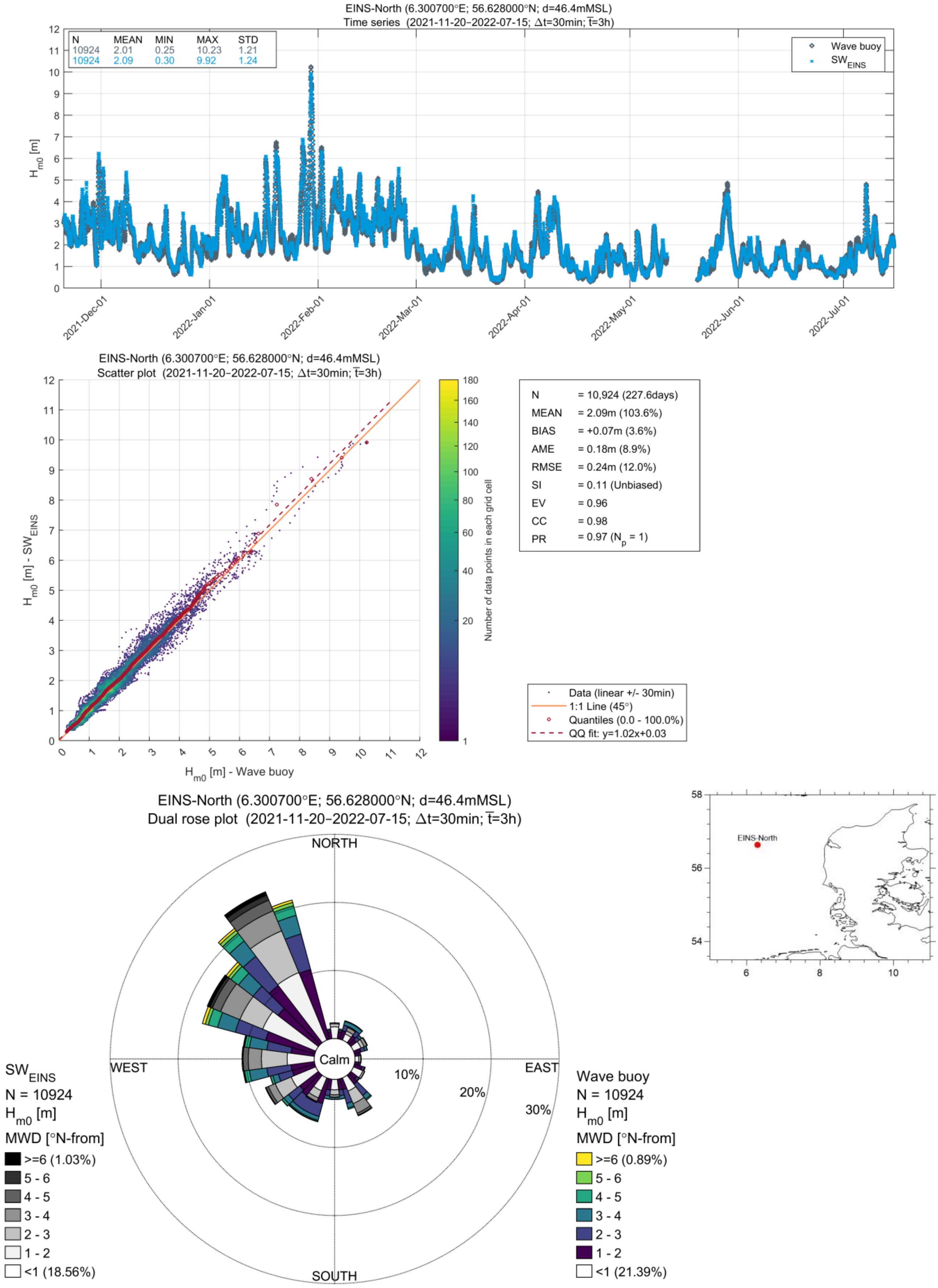

Figure 6.15 EINS-North: Comparison of measured and modelled H_{m0}

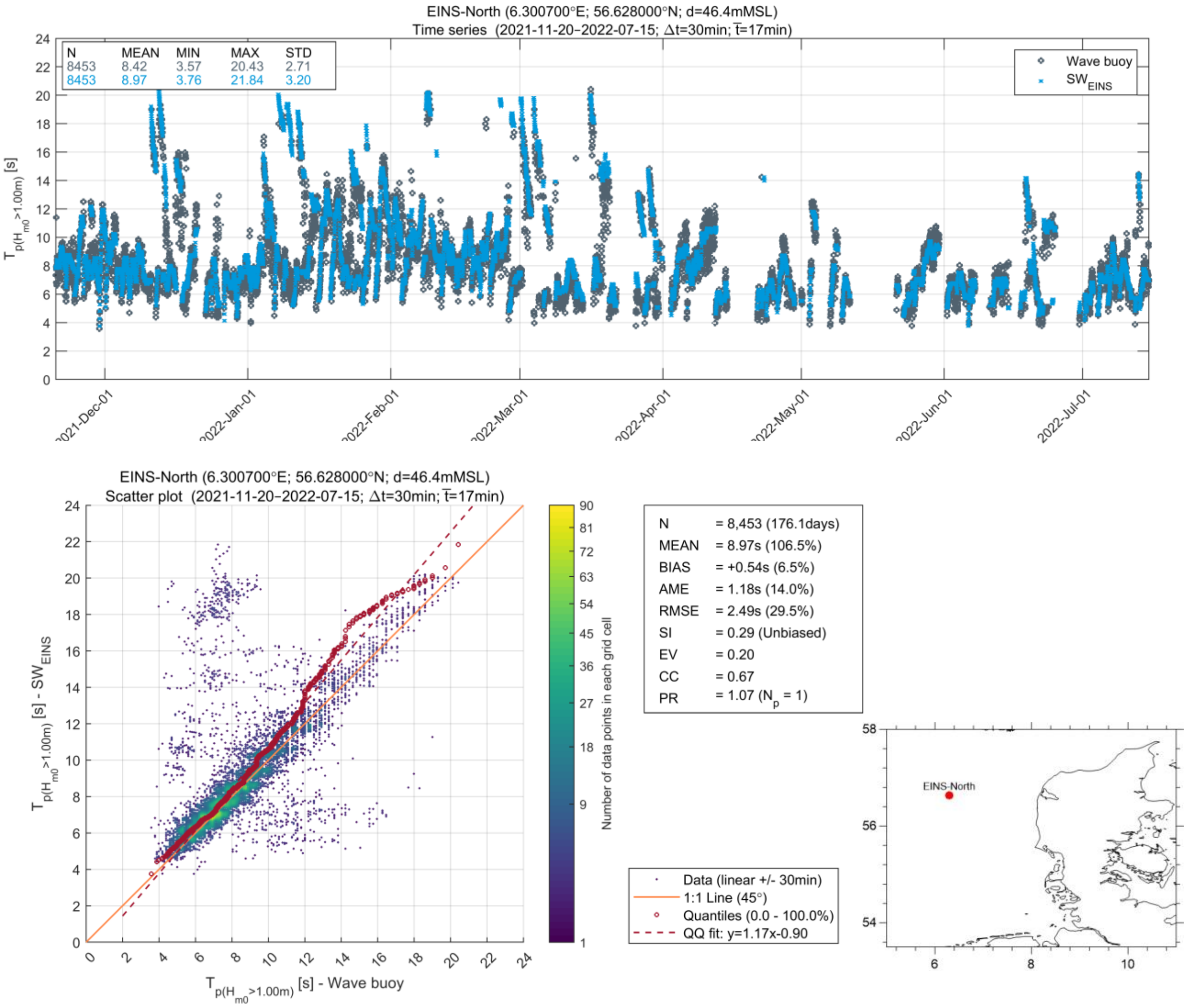

Figure 6.16 EINS-North: Comparison of measured and modelled T_p

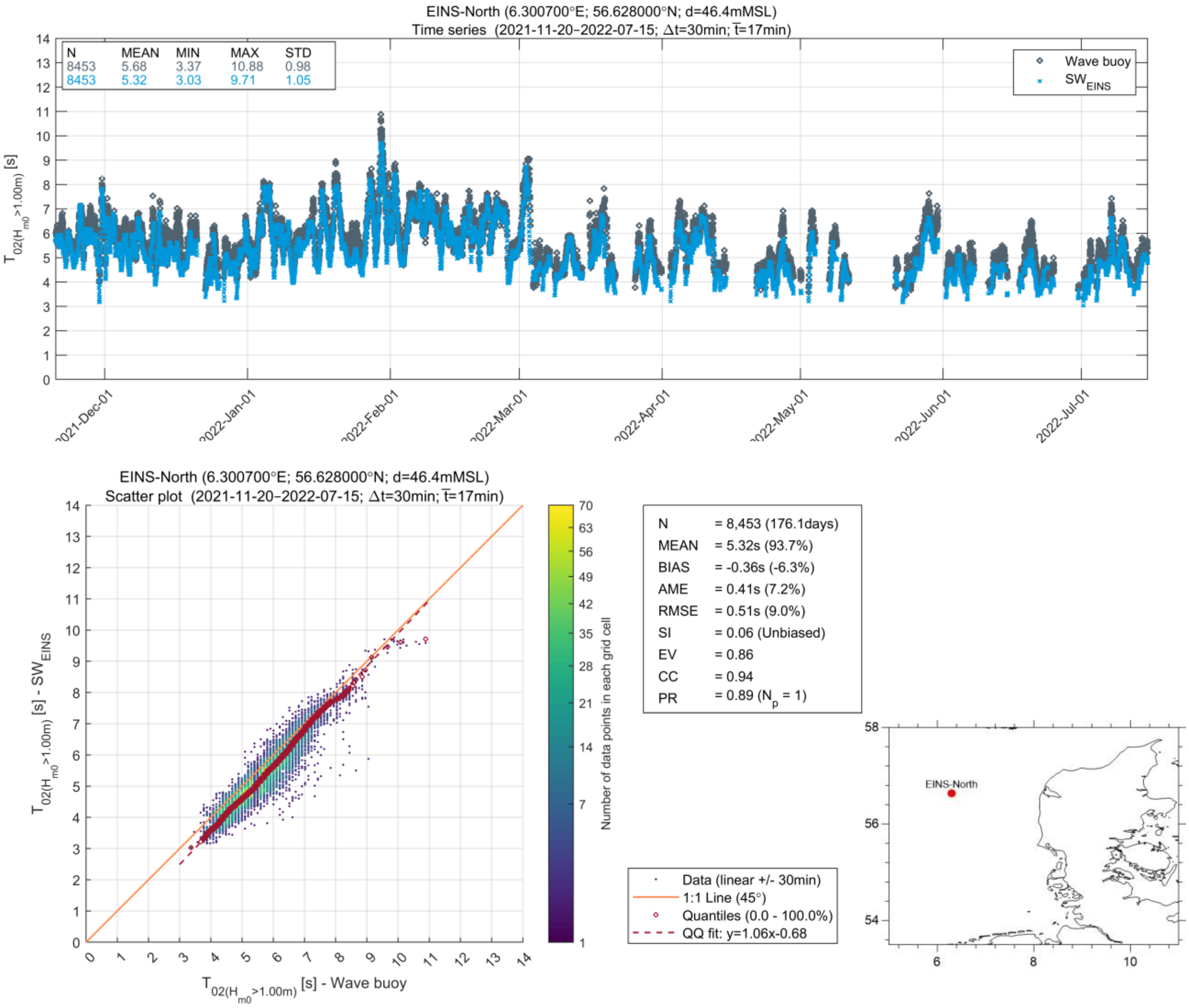

Figure 6.17 EINS-North: Comparison of measured and modelled T_{02}

EINS-South

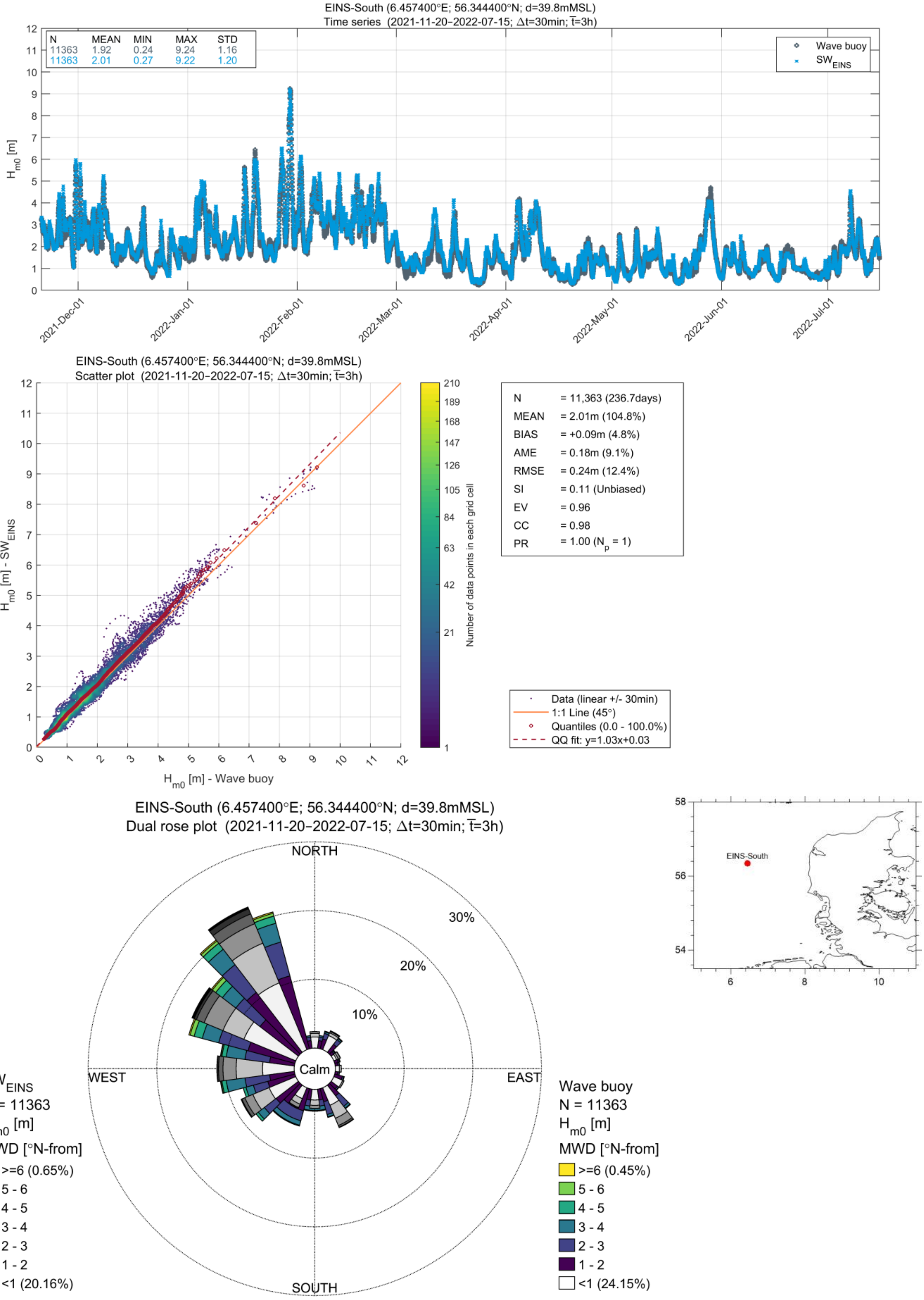

Figure 6.18 EINS-South: Comparison of measured and modelled H_{m0}

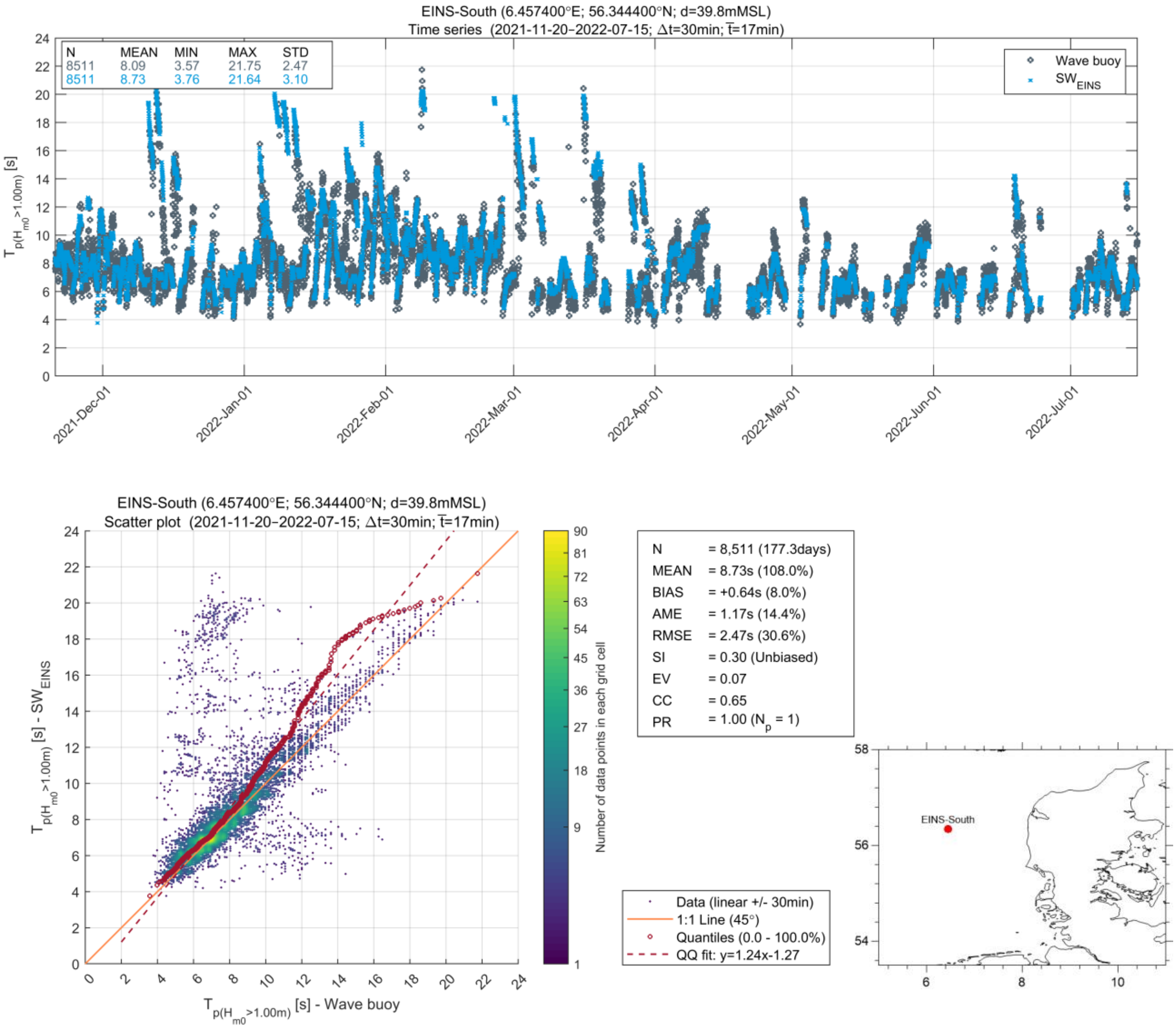

Figure 6.19 EINS-South: Comparison of measured and modelled T_p

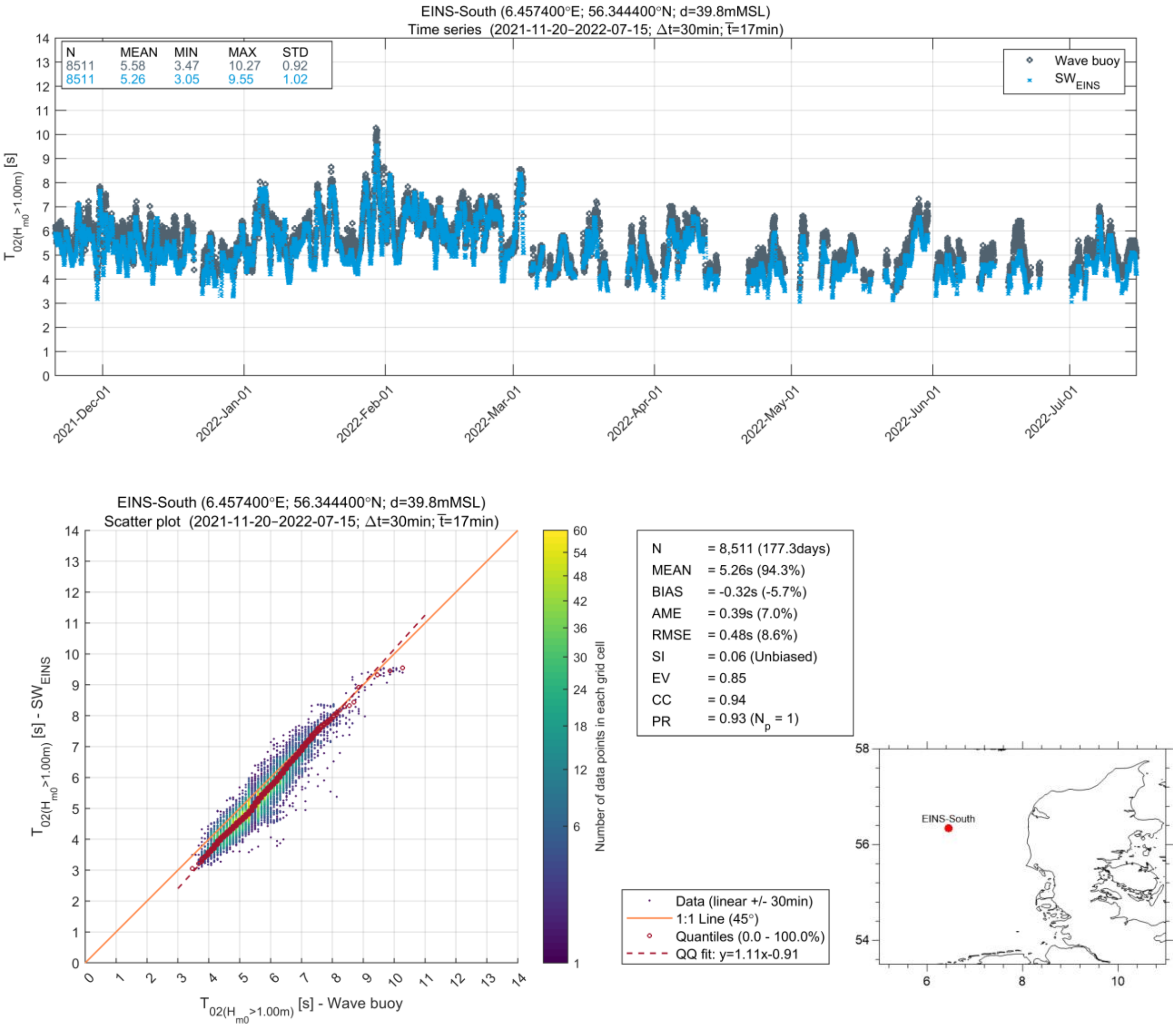

Figure 6.20 EINS-South: Comparison of measured and modelled T_{02}

EINS-Island (Mini 1)

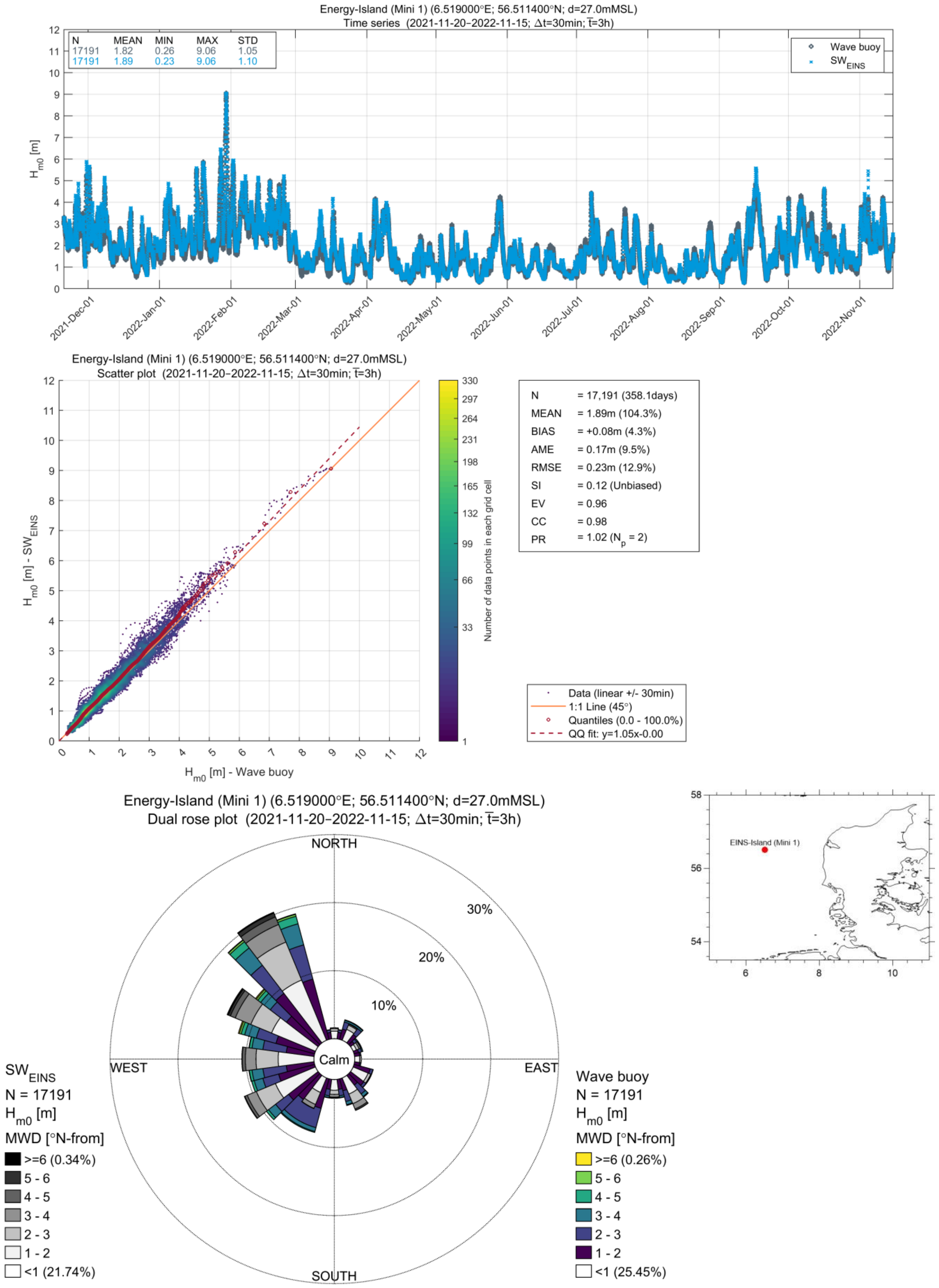

Figure 6.21 EINS-Island (Mini 1): Comparison of measured and modelled H_{m0}

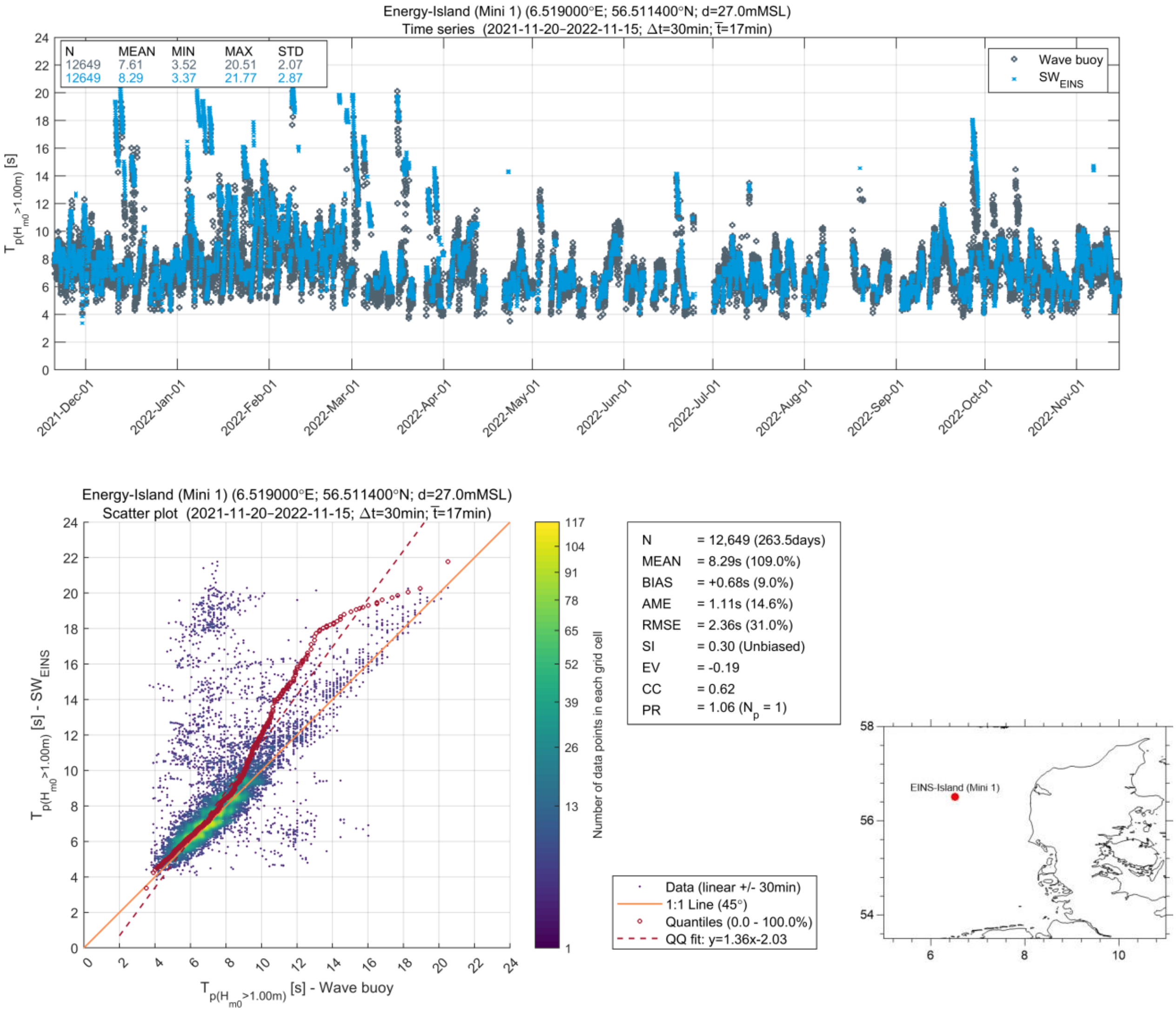

Figure 6.22 EINS-Island (Mini 1): Comparison of measured and modelled T_p

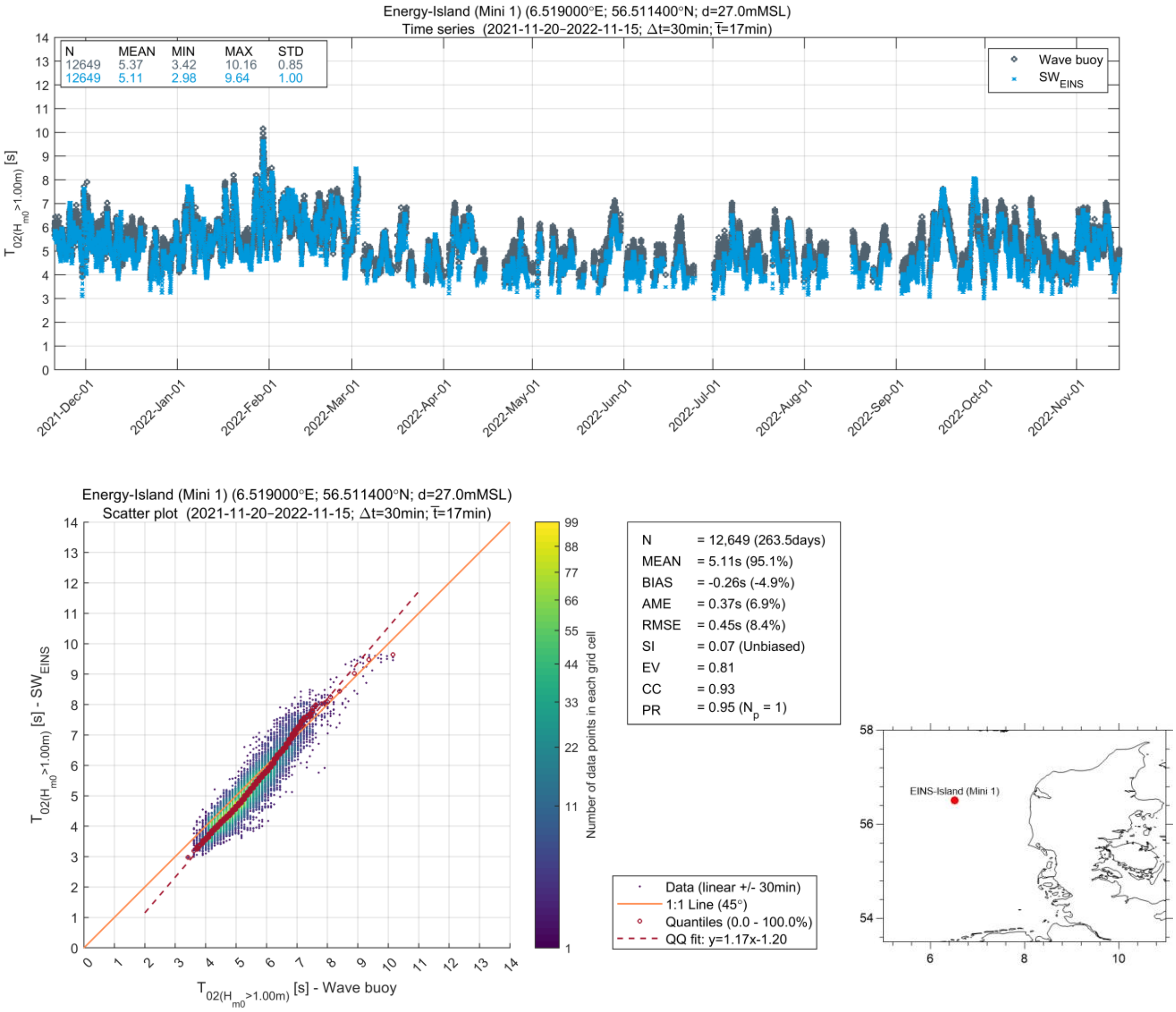

Figure 6.23 EINS-Island (Mini 1): Comparison of measured and modelled T_{02}

EINS-Island (Mini 2)

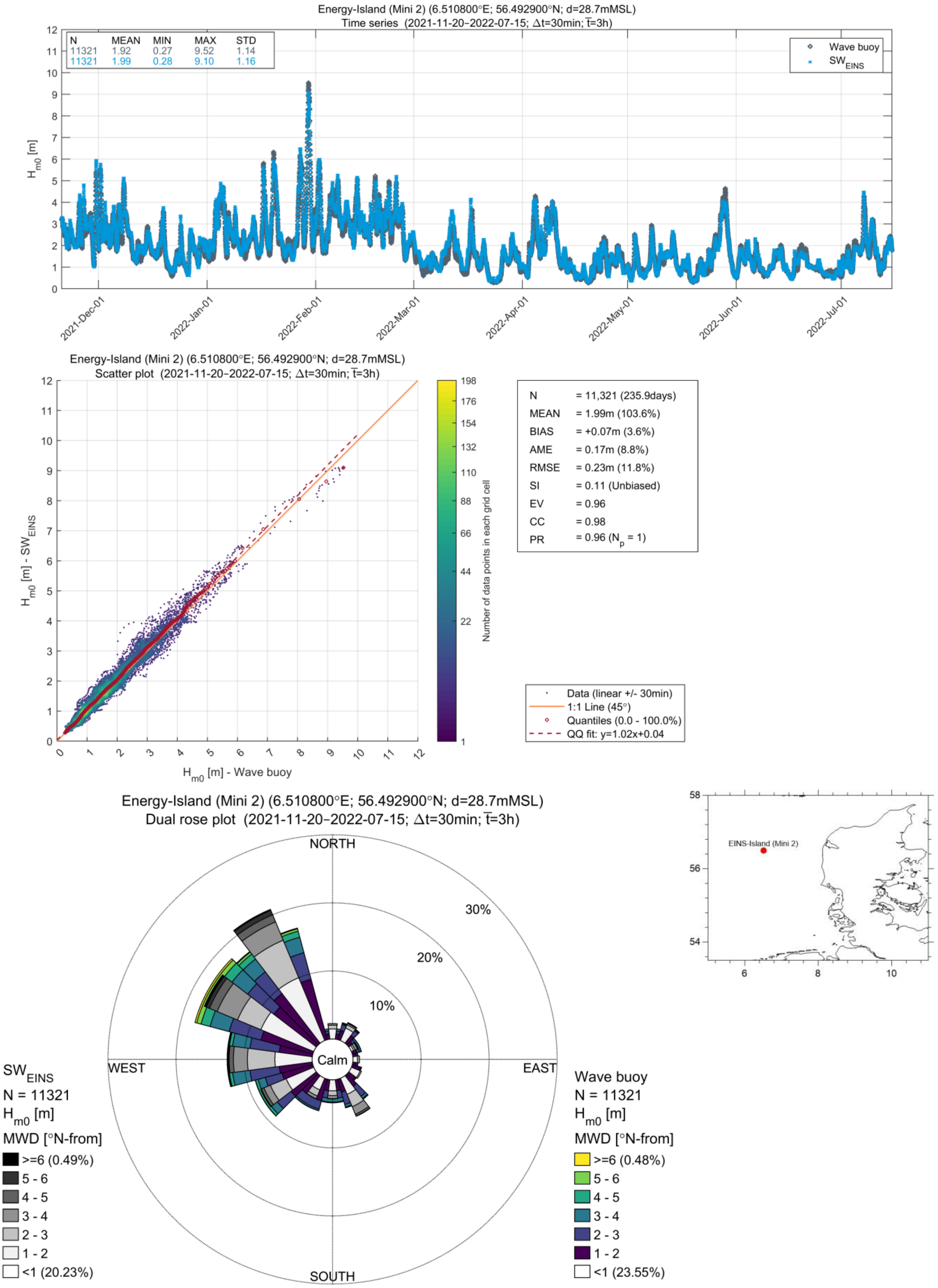

Figure 6.24 EINS-Island (Mini 2): Comparison of measured and modelled H_{m0}

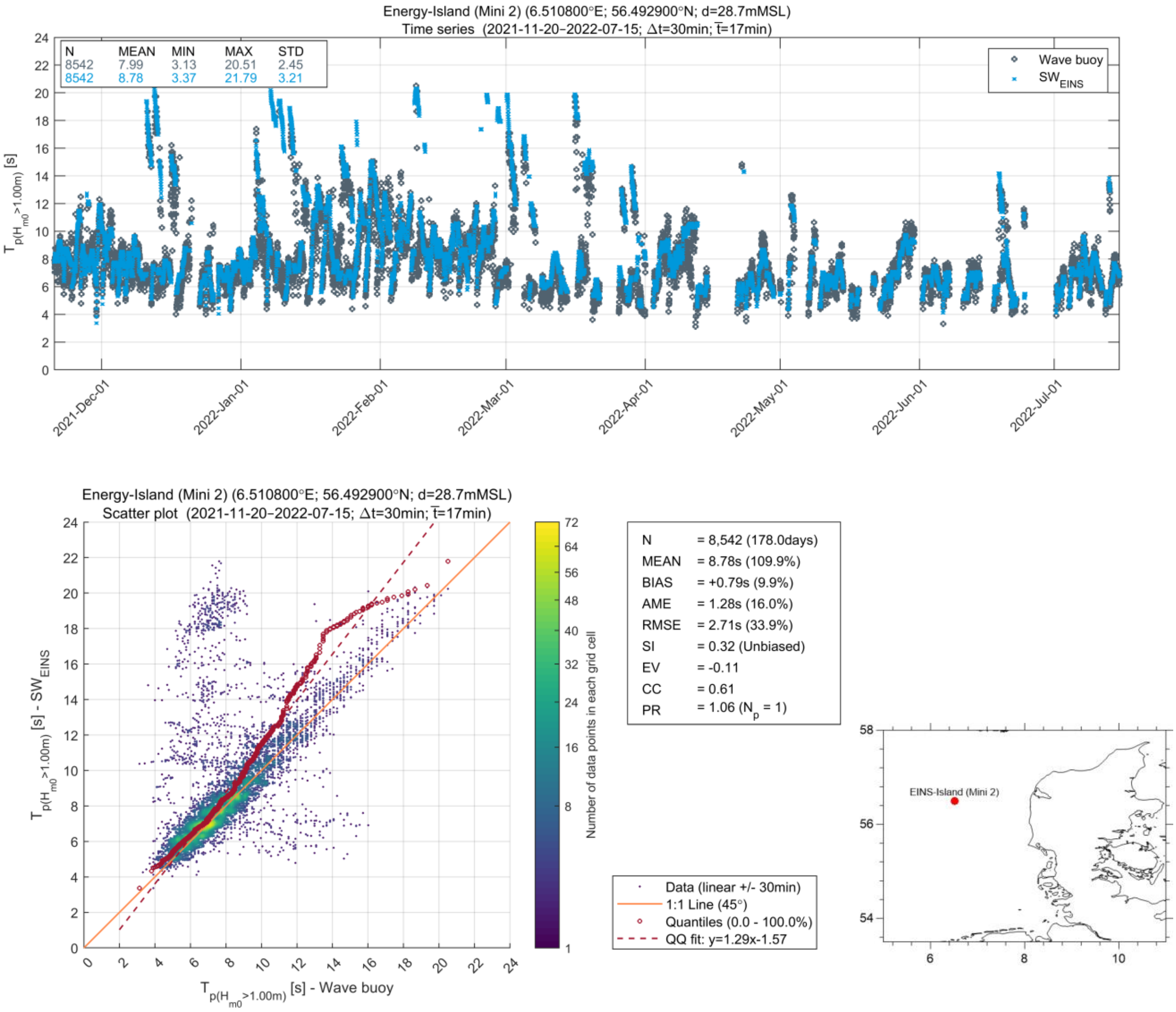

Figure 6.25 EINS-Island (Mini 2): Comparison of measured and modelled T_p

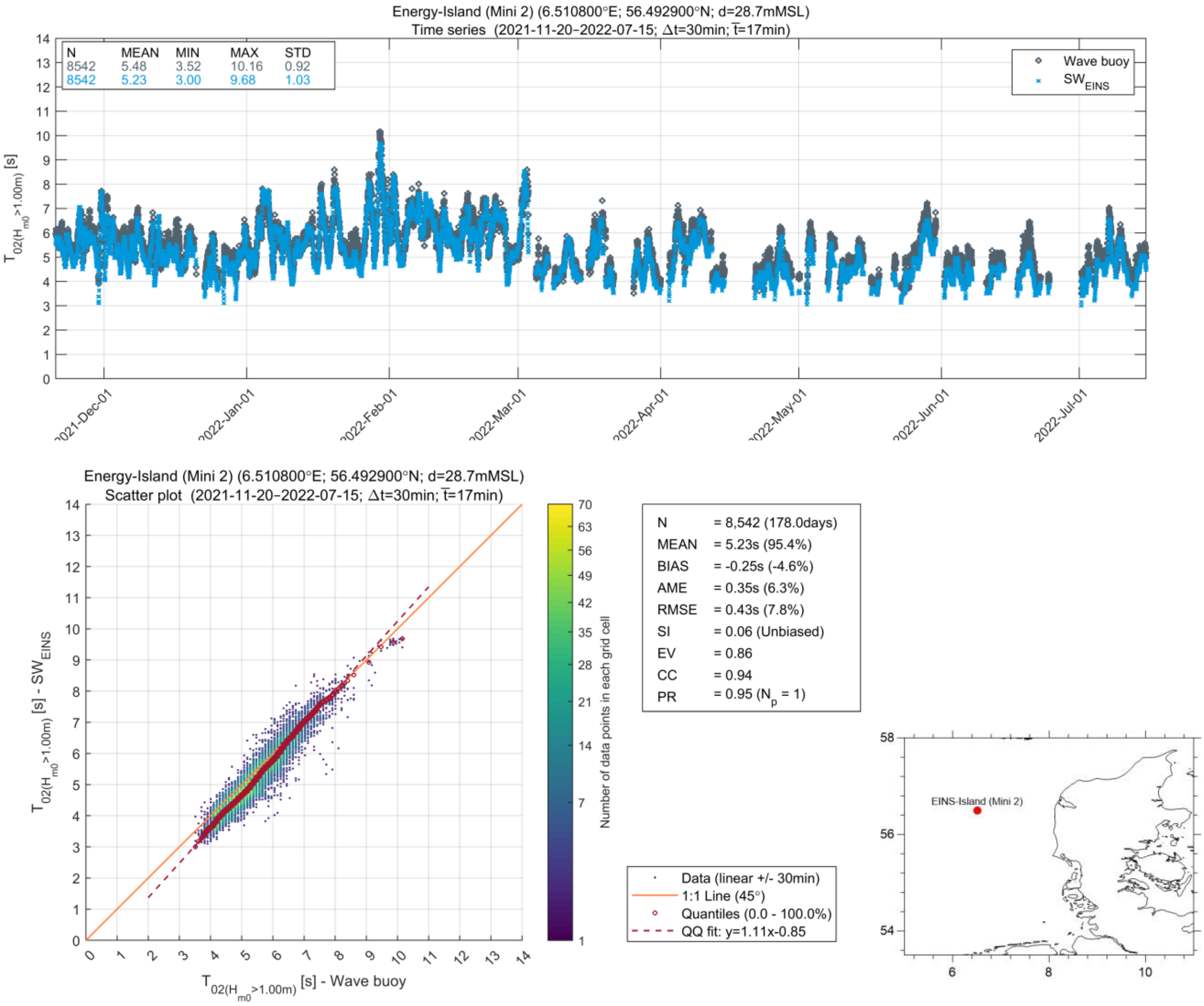

Figure 6.26 EINS-Island (Mini 2): Comparison of measured and modelled T_{02}

Harald

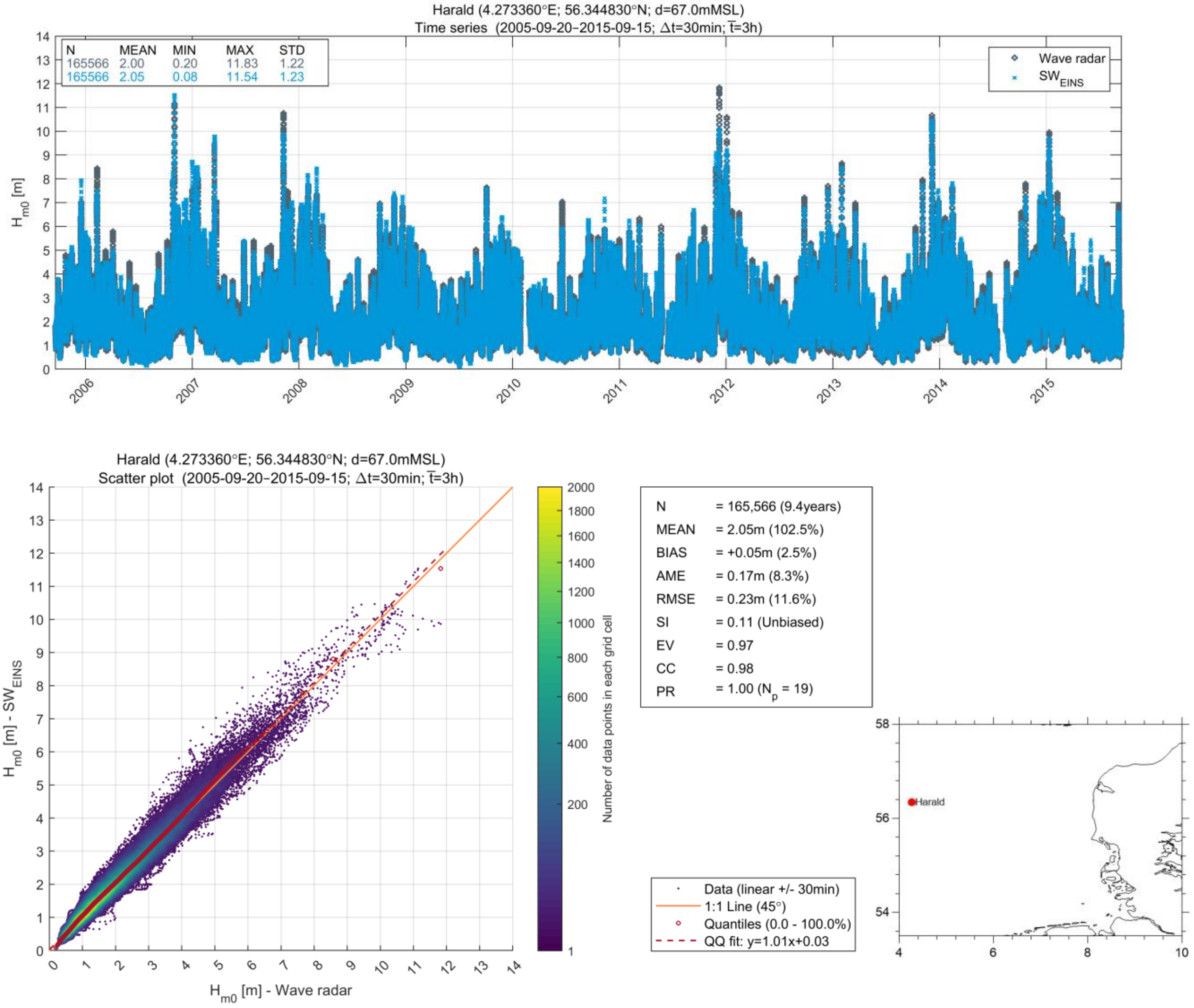

Harald (4.273360°E; 56.344830°N; d=67.0mMSL)
Time series (2005-09-20–2015-09-15; Δt=30min; t̄=3h)

Harald (4.273360°E; 56.344830°N; d=67.0mMSL)
Scatter plot (2005-09-20–2015-09-15; Δt=30min; t̄=3h)

Figure 6.27 Harald: Comparison of measured and modelled H_{m0}

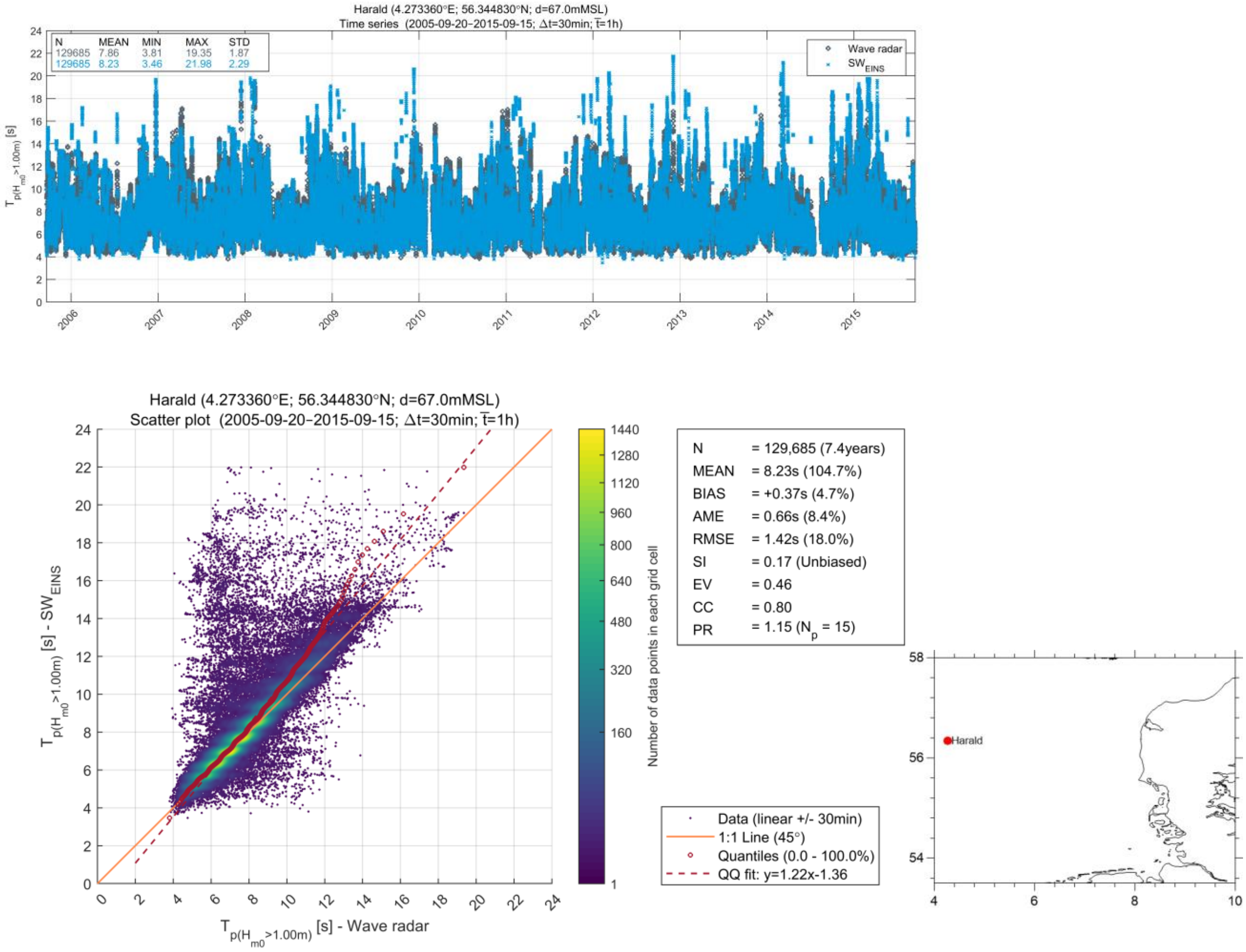

Figure 6.28 Harald: Comparison of measured and modelled T_p

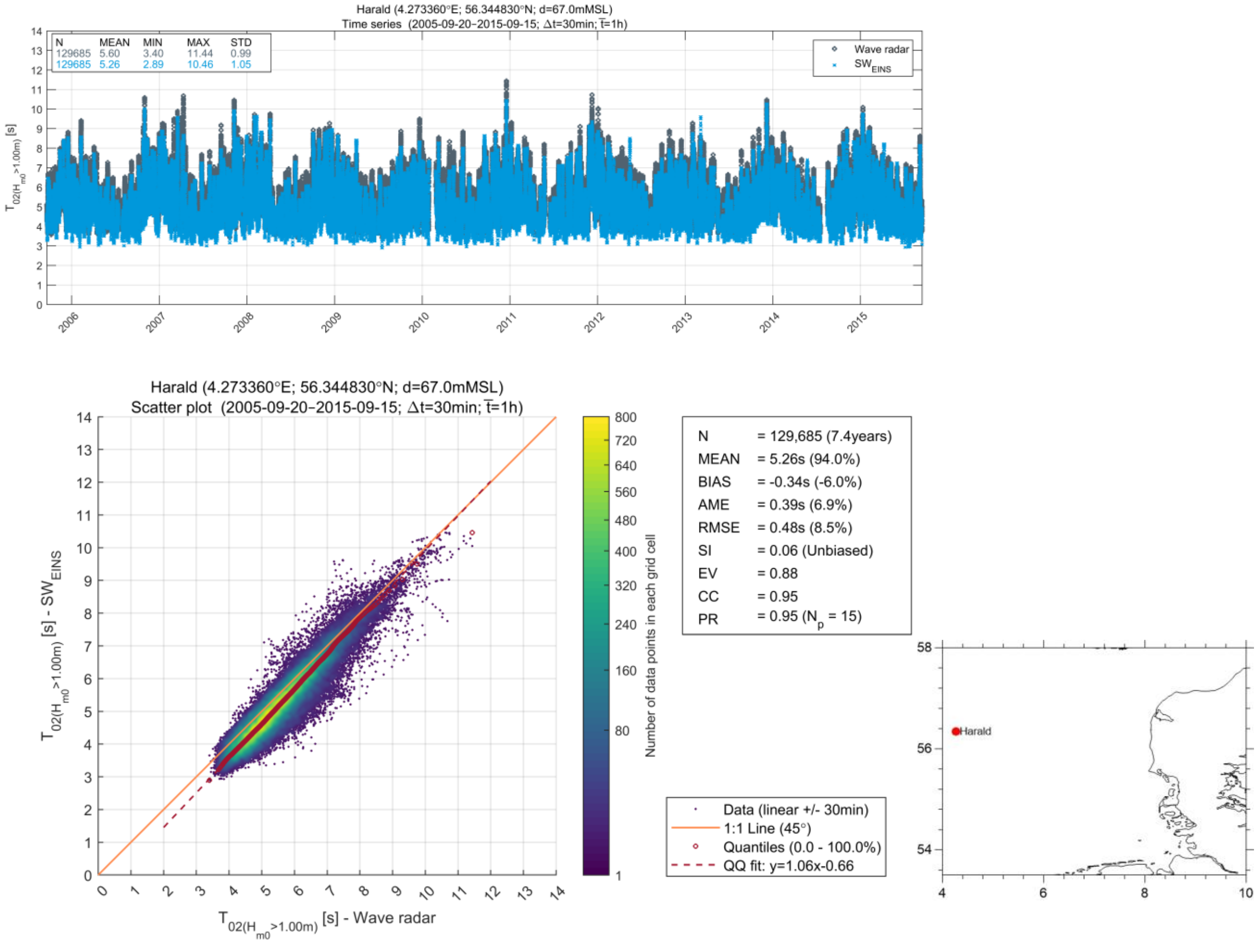

Figure 6.29 Harald: Comparison of measured and modelled T_{02}

Gorm

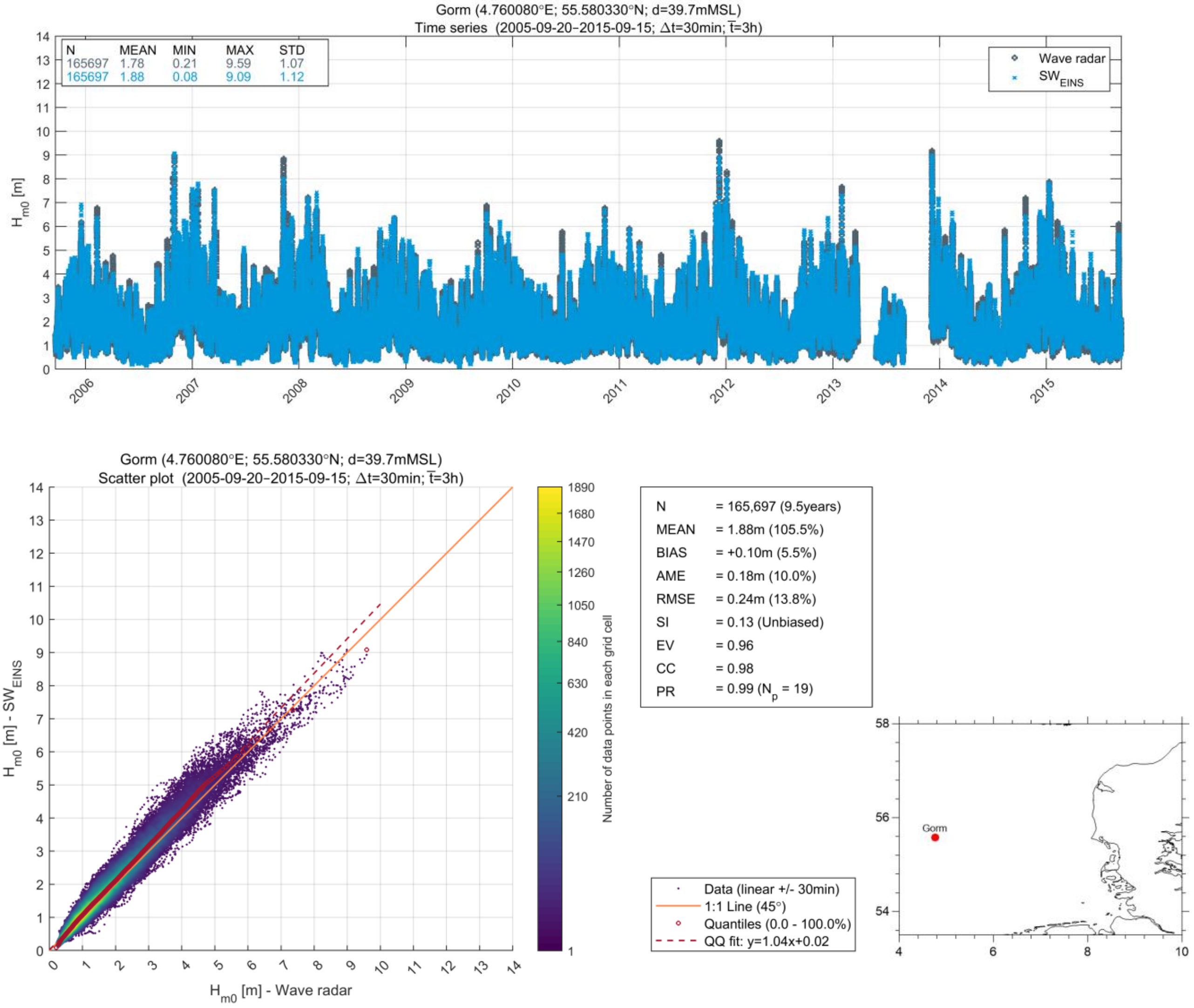

Figure 6.30 Gorm: Comparison of measured and modelled H_{m0}

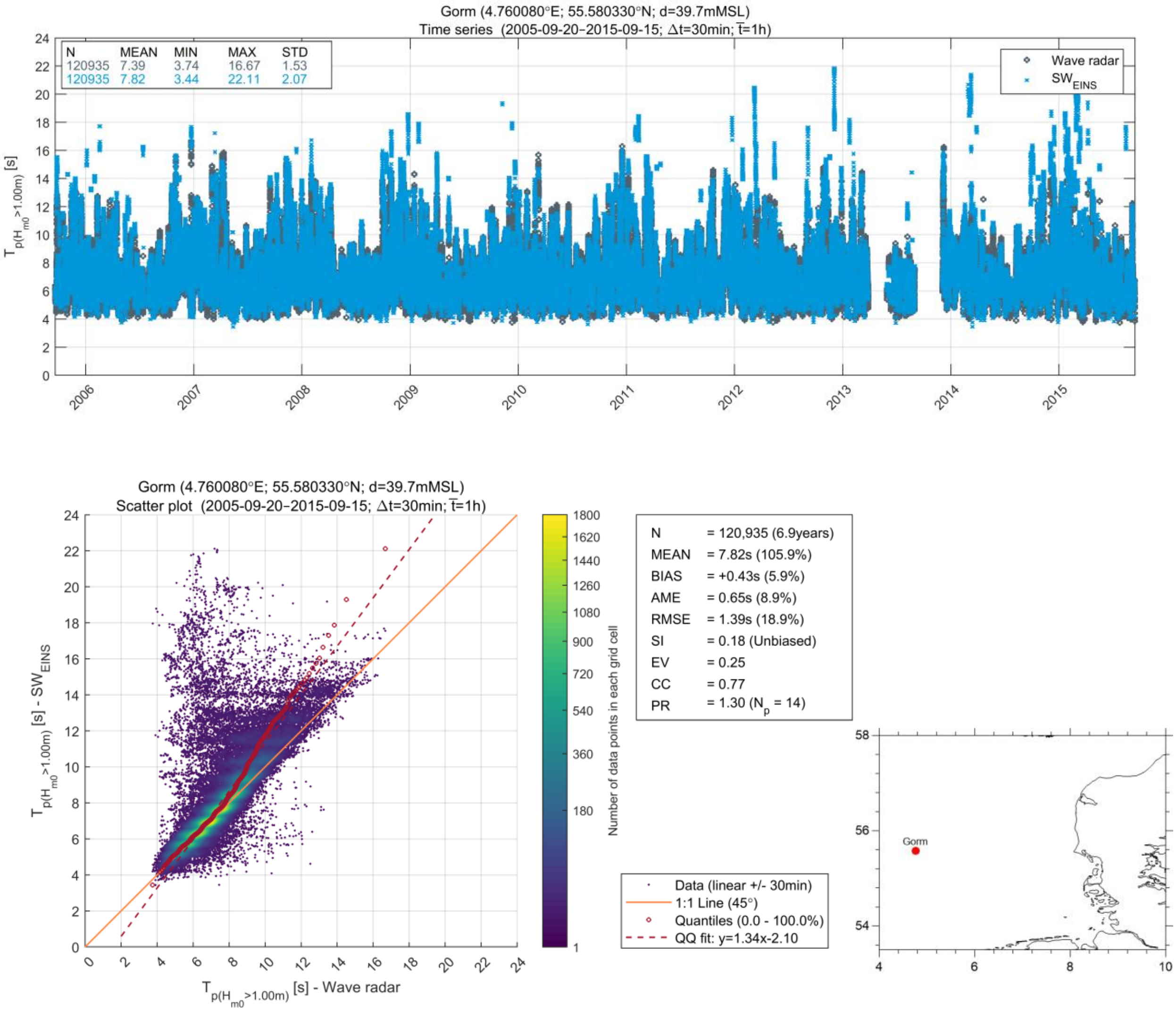

Figure 6.31 Gorm: Comparison of measured and modelled T_p

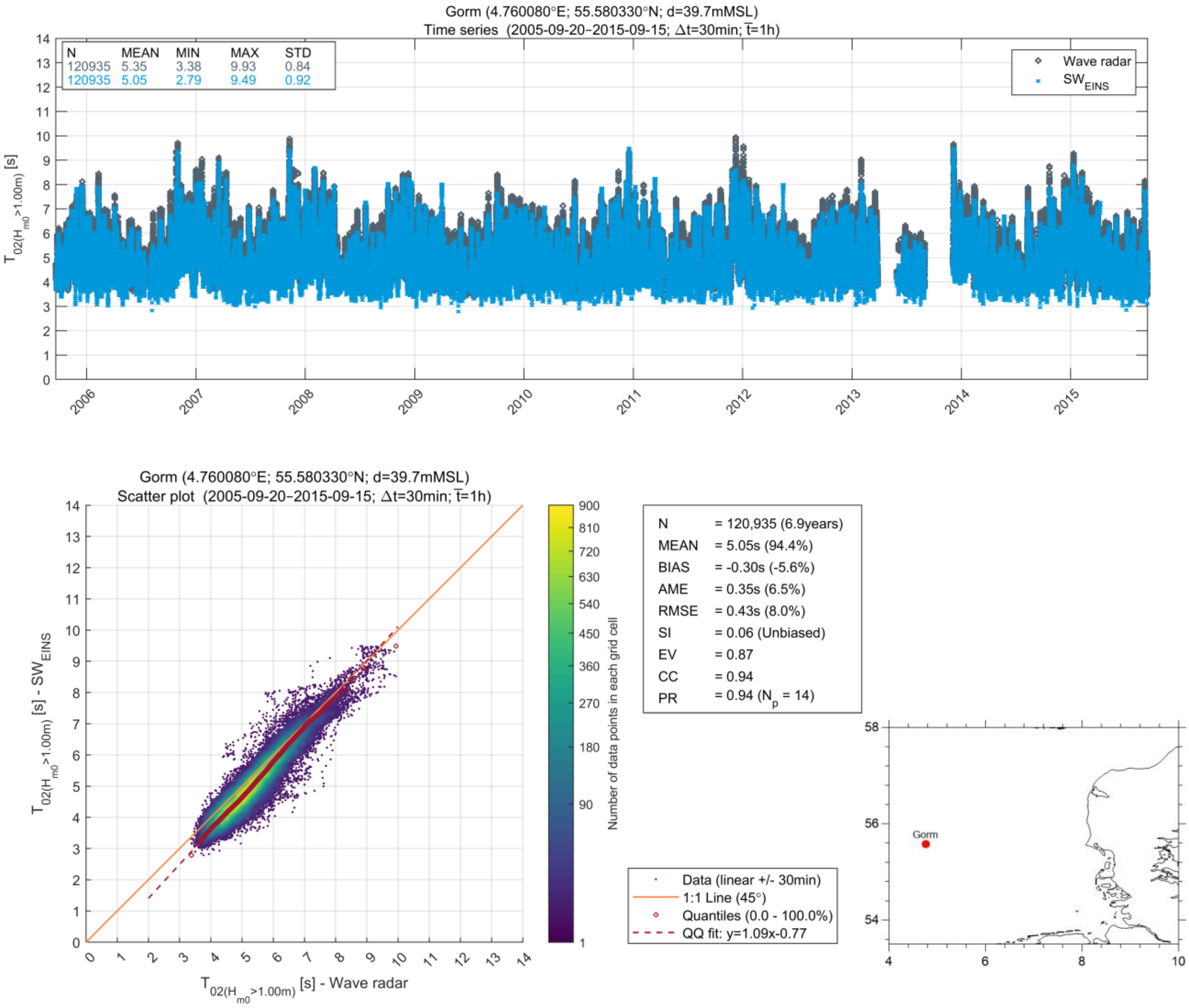

Figure 6.32 Gorm: Comparison of measured and modelled T_{02}

Ekofisk

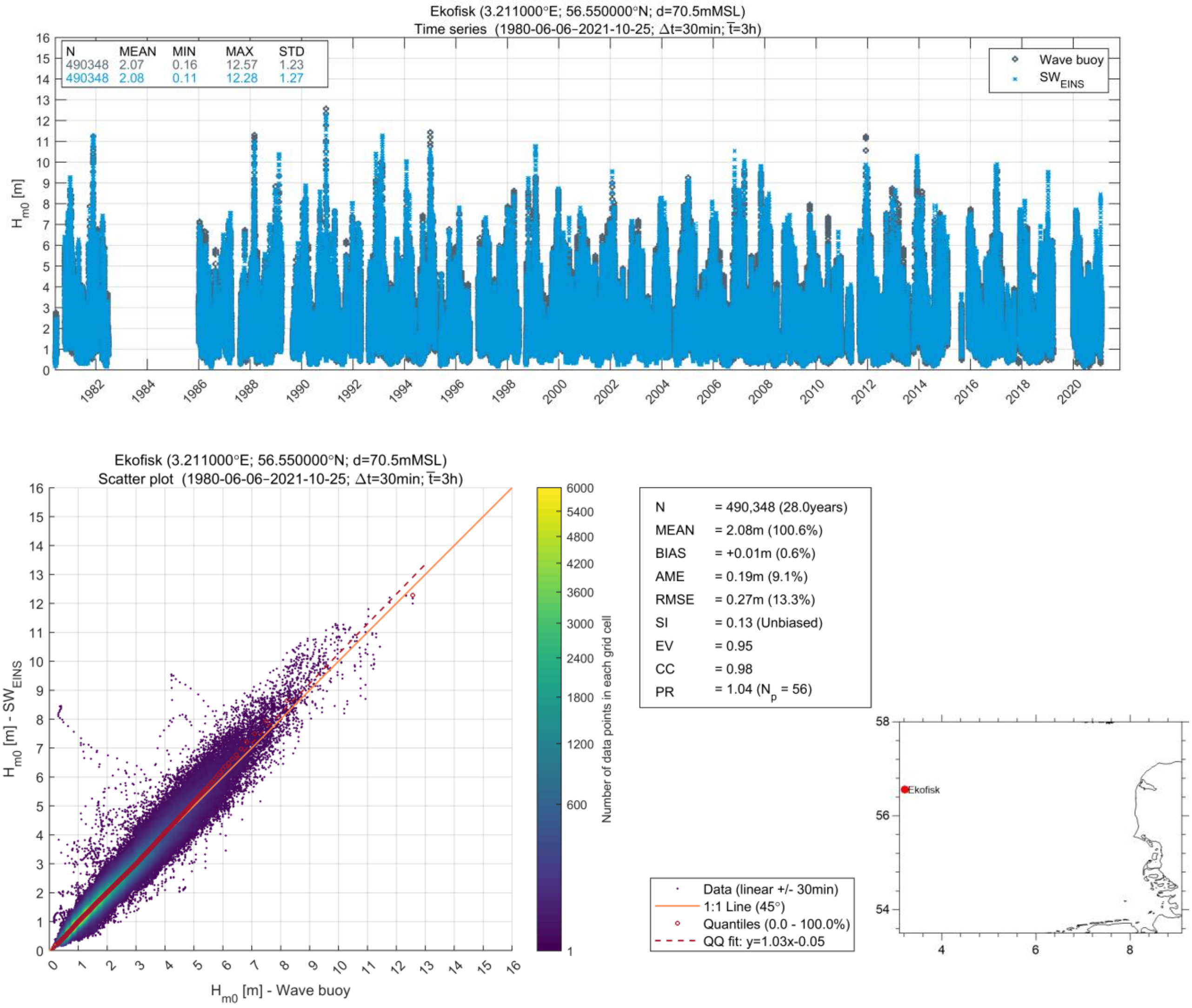

Figure 6.33 Ekofisk: Comparison of measured and modelled H_{m0}

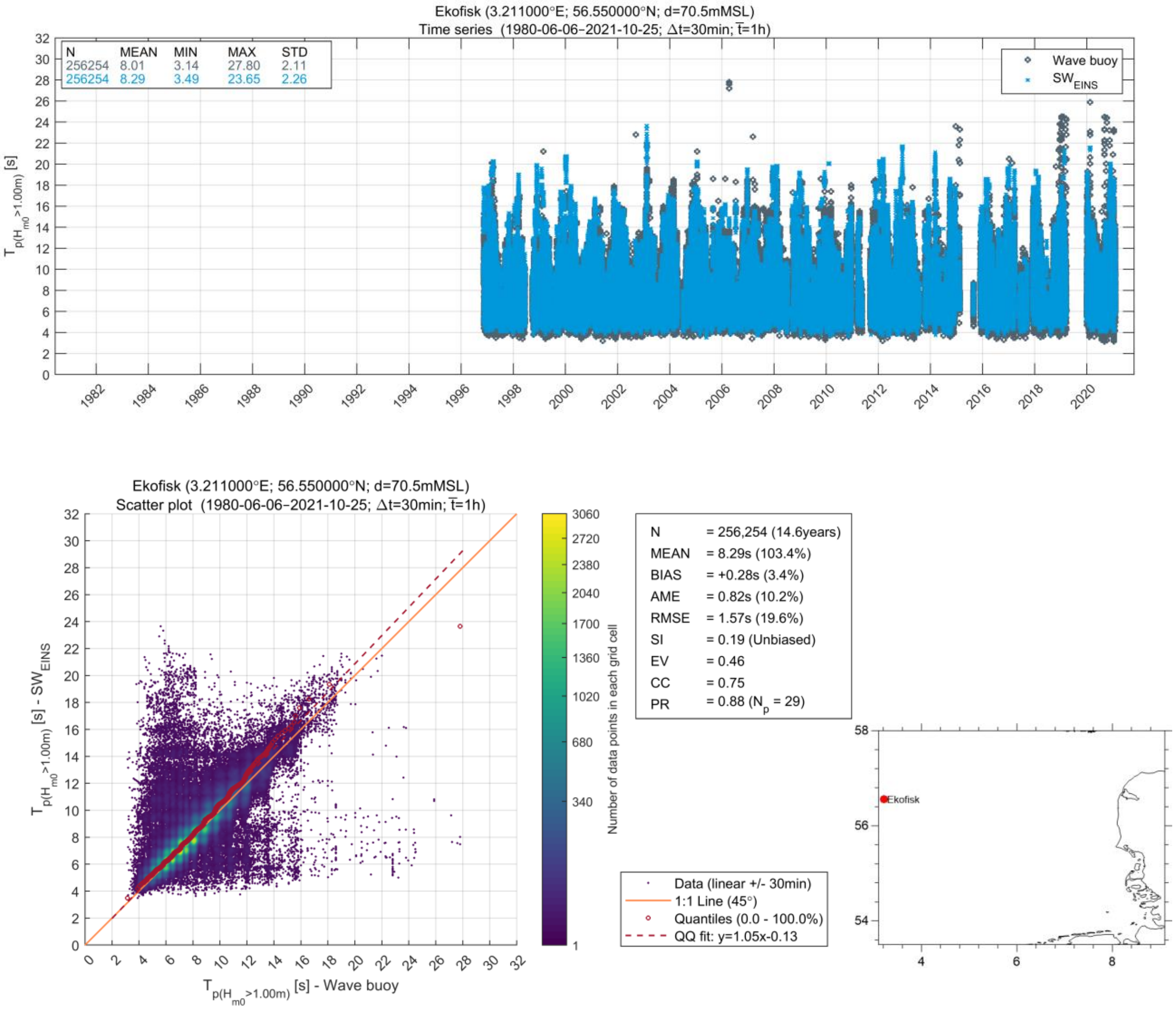

Figure 6.34 Ekofisk: Comparison of measured and modelled T_p

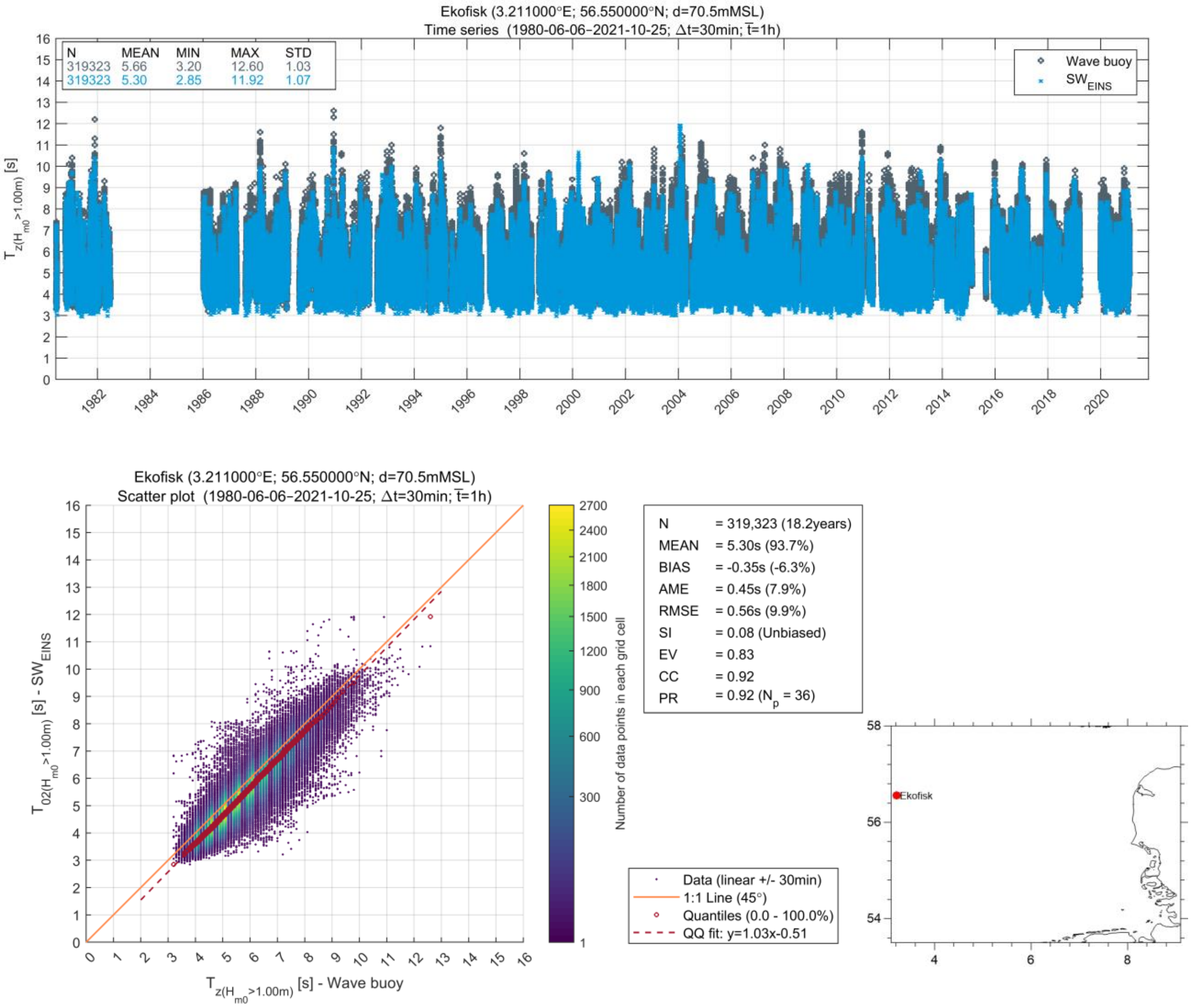

Figure 6.35 Ekofisk: Comparison of measured and modelled T_{02}

Thor

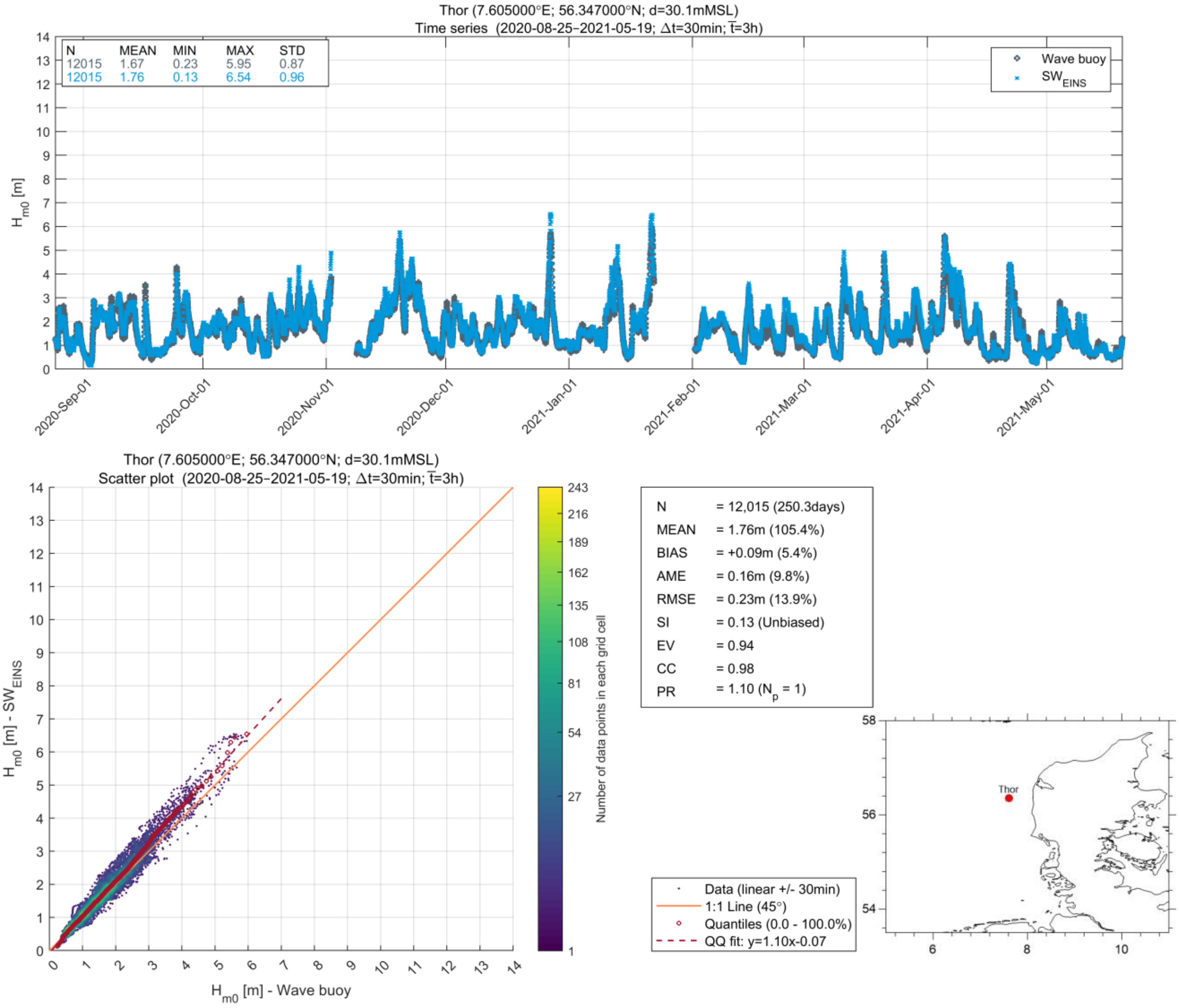

Figure 6.36 Thor: Comparison of measured and modelled H_{m0}

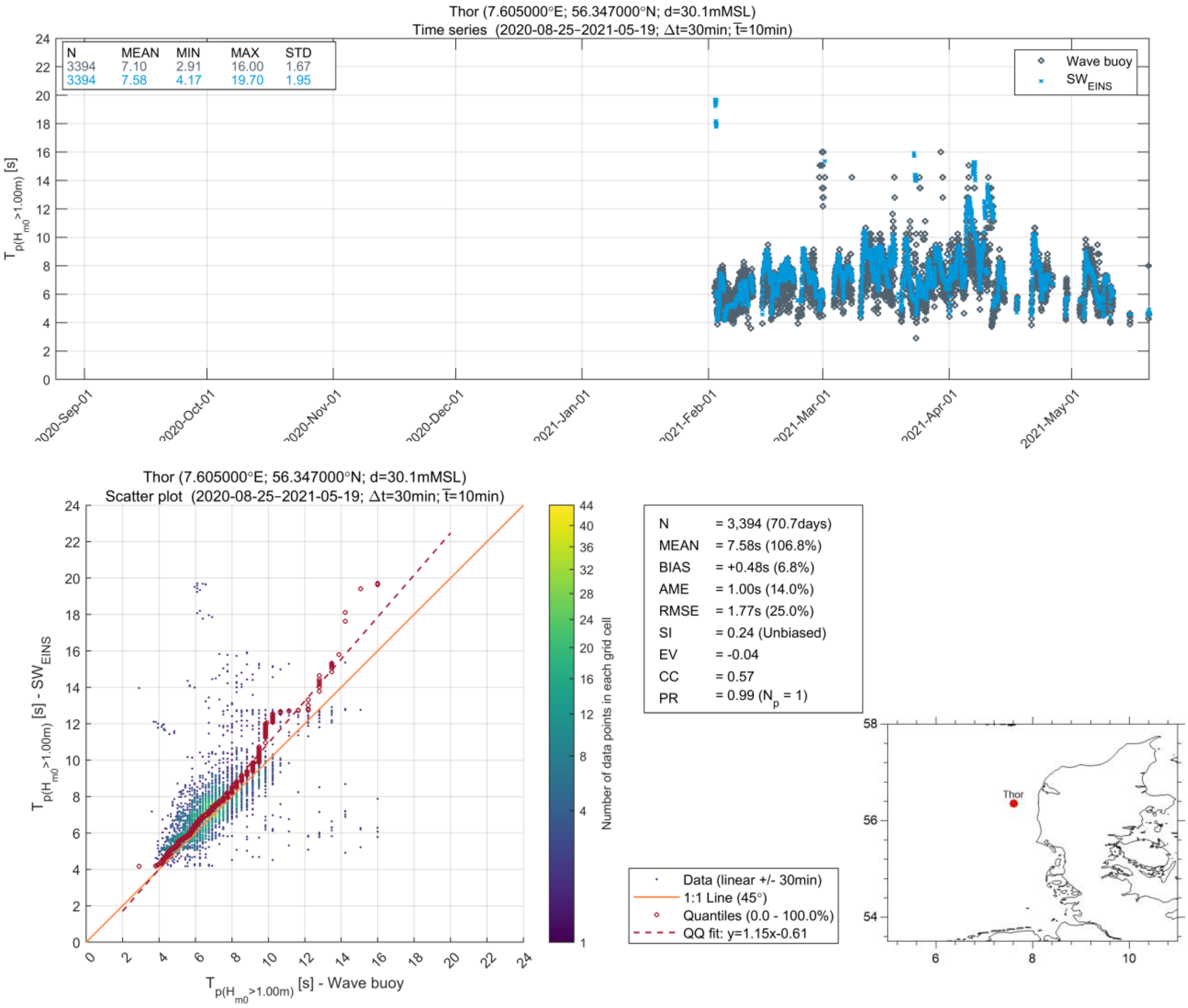

Figure 6.37 Thor: Comparison of measured and modelled T_p

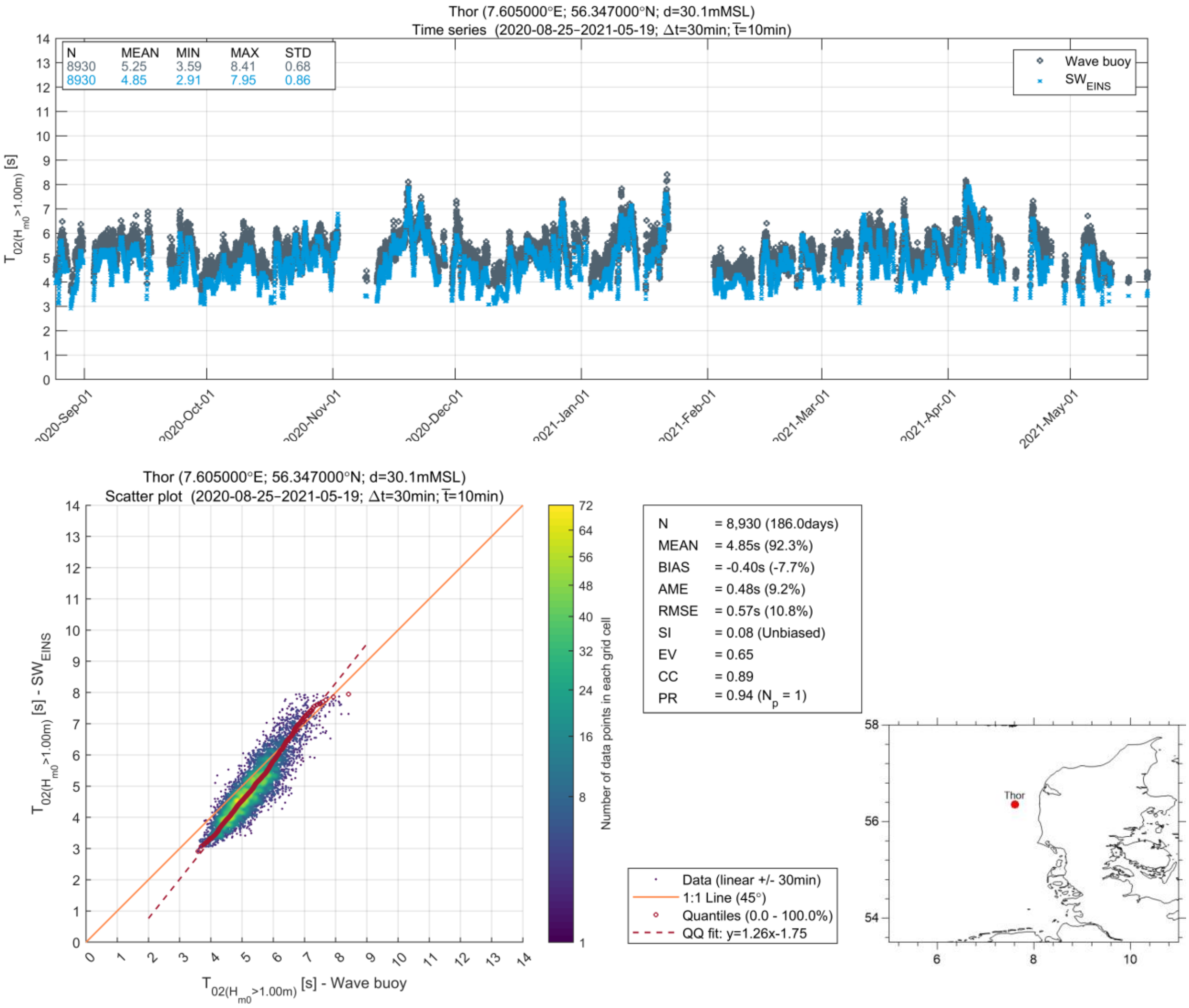

Figure 6.38 Thor: Comparison of measured and modelled T_{02}

6.3.7 Validation of extreme wave events

This section presents a validation of SW_{EINS} during storm events. Measured wave data from the stations presented in Section 6.2 was analysed to identify the largest storm events registered. A summary of the storm events and the stations used for validation are presented in Table 6.7.

Results of the comparisons are shown in Figure 6.39 to Figure 6.42, where time series of measured and modelled significant wave height are illustrated.

Table 6.7 presents the maximum significant wave height during each storm, both measured and modelled. The results demonstrate excellent capabilities of the SW_{EINS} to estimate significant wave heights during storm events. The largest difference obtained between measurements and model outputs is during the 2022 storm at EINS-North and EINS-Island (Mini 2) with an underestimation of 0.3-0.4 m, however, for the same event, the differences in wave height at the other two stations (EINS-Island (Mini 1) and EINS-South) are small and close to an exact match.

Table 6.7 Extreme events at several locations used for storm validation
The measurements are averaged across 3-hours.

Storm ID	Storm date	Station	H_{m0} measured [m]	H_{m0} from SW_{EINS} [m]
#1	1981-11-24	Ekofisk	11.23	11.26
#2	1990-12-12	Ekofisk	12.57	12.28
#3	2006-10-31	Harald	11.14	11.54
#4	2022-01-31	EINS-North	10.23	9.92
		EINS-Island (Mini 1)	9.06	9.06
		EINS-South	9.24	9.22
		EINS-Island (Mini 2)	9.52	9.10
		Average	**10.43**	**10.34**

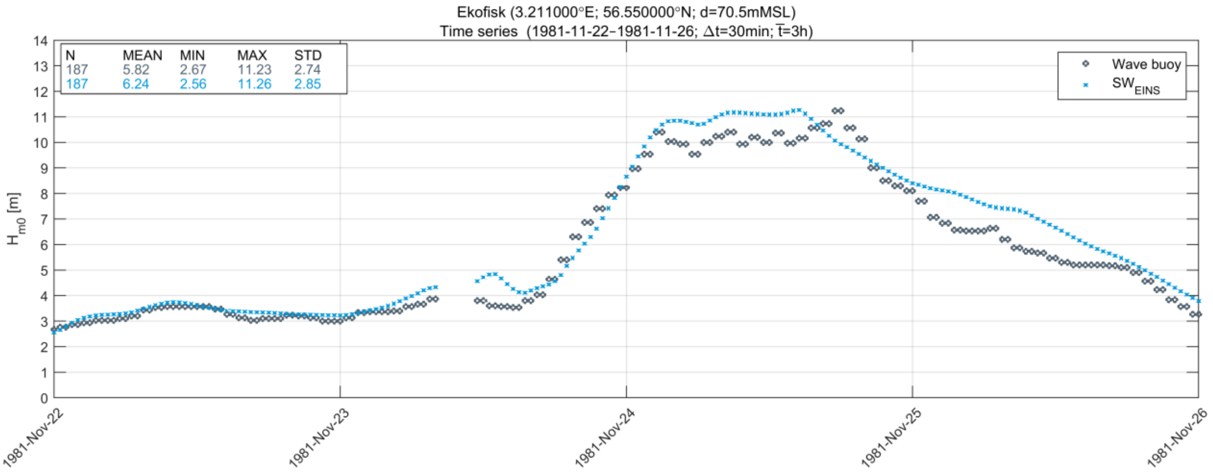

Figure 6.39 Comparison of H_{m0} at Ekofisk during storm event on 1981-11-24

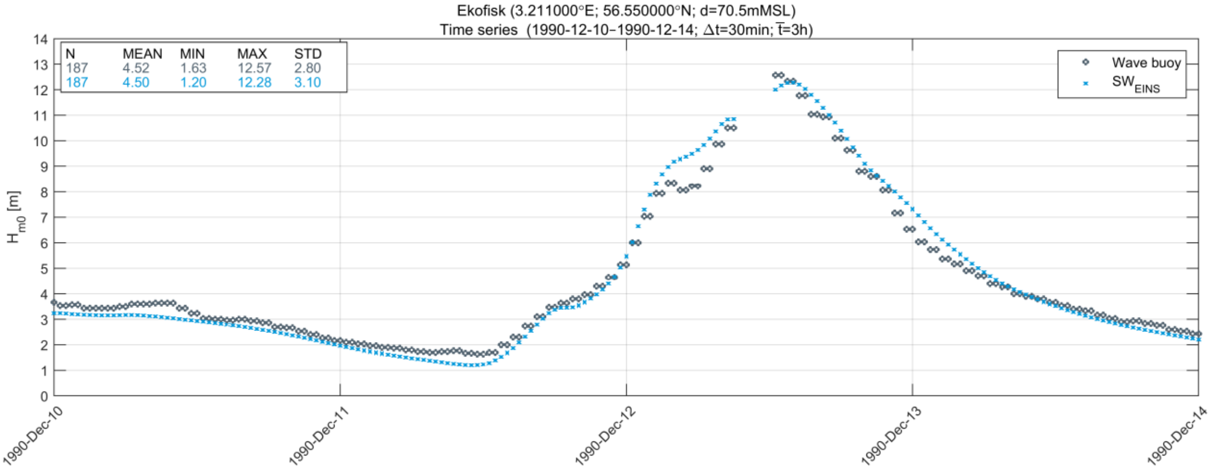

Figure 6.40 Comparison of H_{m0} at Ekofisk during storm event on 1990-12-12

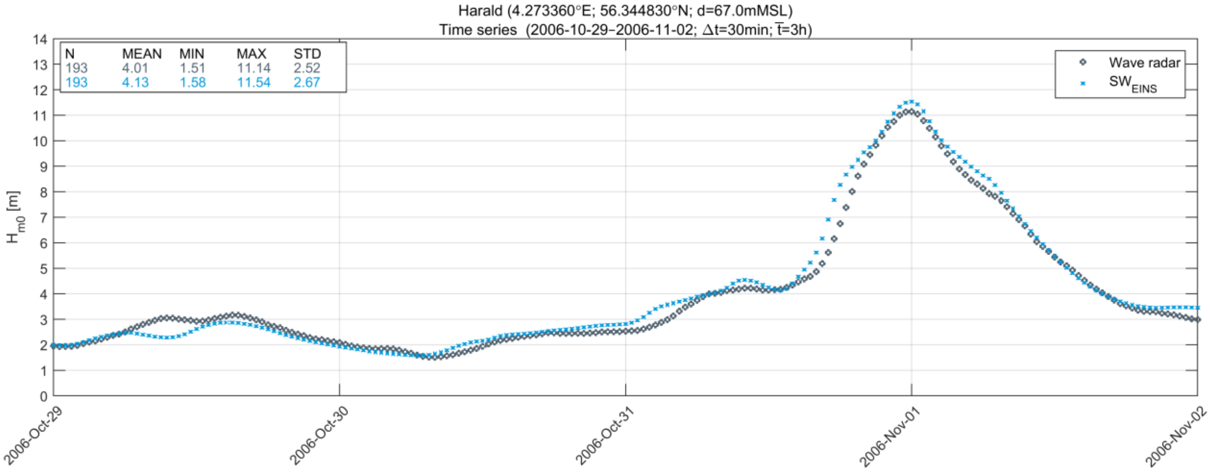

Figure 6.41 Comparison of H_{m0} at Harald during storm event on 2006-10-31

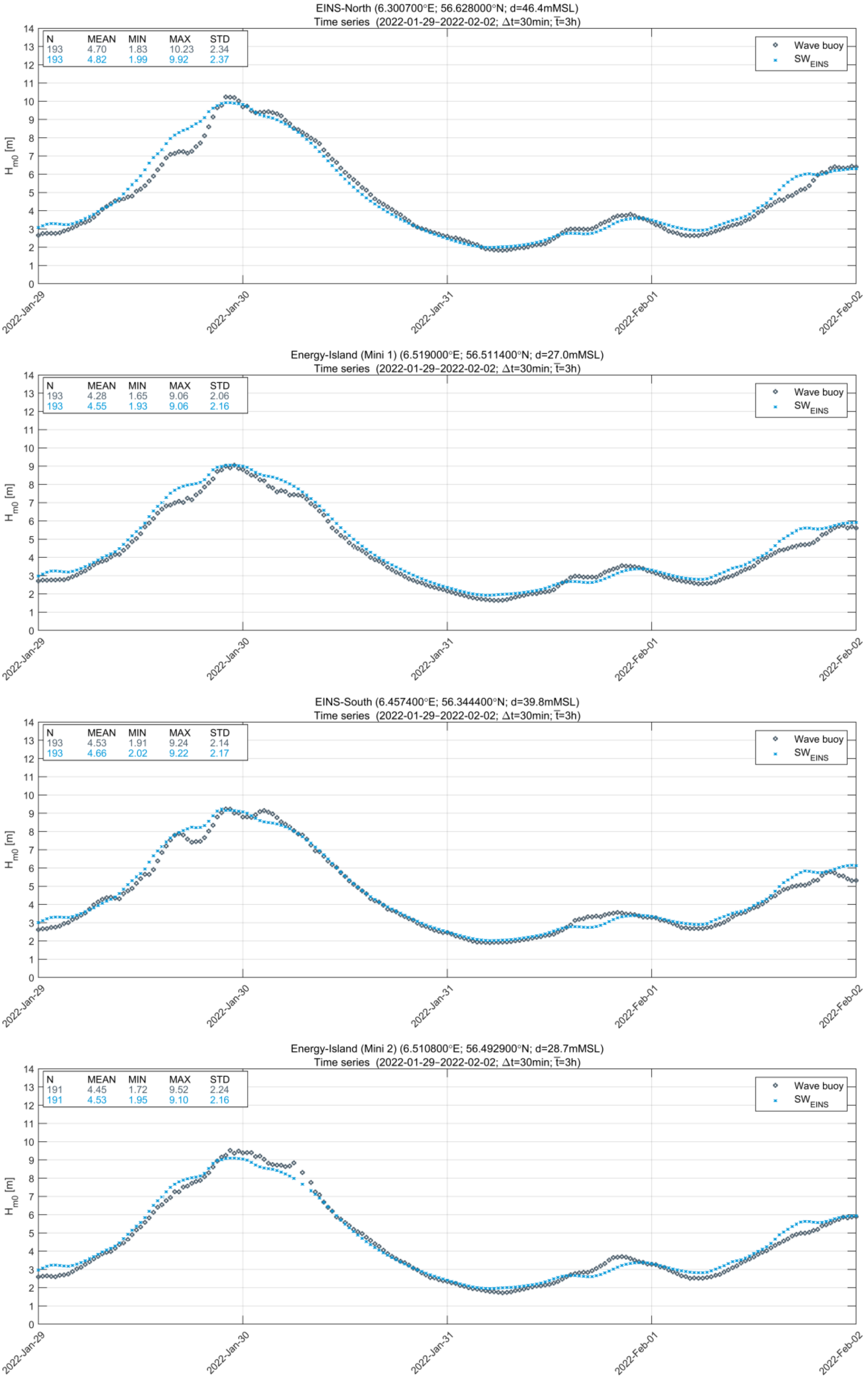

Figure 6.42 **Comparison of H_{m0} at EINS site during storm event on 2022-01-31**
From top to bottom: EINS-North, EINS-Island (Mini 1); EINS-South and EINS-Island (Mini 2)

6.3.8 Validation of frequency wave spectra

Measured wave energy spectra were available from the four Wavesense 3 devices deployed at the EINS site, and modelled wave spectra from SW_{EINS} were saved at the locations of the devices.

The measured spectral frequencies range from 0.04 to 1 Hz (1 – 25 s), whereas the modelled spectral frequencies range from 0.033-1.273 Hz (0.8 – 30 s). Therefore, the validation considers the overlapping frequency range.

Figure 6.43 presents four frequency spectra at EINS-South (normalized by the total energy of the spectra). Three of the spectra are dominated by a single (wind-sea) peak, and one (top right) has a bi-modal shape. The figures demonstrate a good ability of the model to replicate the measured spectral shapes. The spectra for 2022-01-29 (bottom right) is during storm Malik, which represent high and long waves (H_{m0} = 9.2 m and T_p = 14 s).

The figures also show the corresponding JONSWAP spectra with gamma estimated by Eq. (6.3), which demonstrate that the single-peaked spectra are well resembled by the JONSWAP spectra, while the bi-modal spectrum is not.

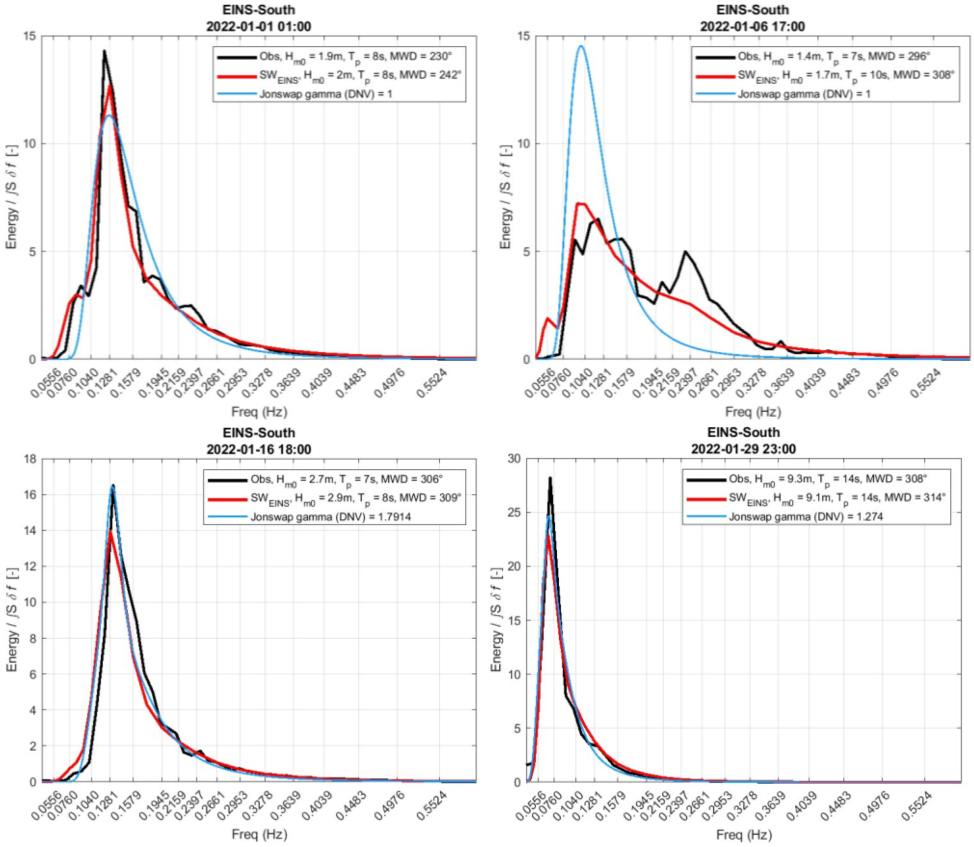

Figure 6.43 Comparisons of four frequency wave spectra at EINS-South
The spectra for 2022-01-29 (bottom right) is during storm Malik. The figures demonstrate a good ability of the model to replicate the measured spectral shapes, and that the single-peaked spectra are well resembled by the JONSWAP spectra.

6.4 Assessment of wave spectra

This section concerns an assessment of the applicability of theoretical spectra to describe the wave spectra for normal and extreme wave conditions. The assessment is based on the modelled frequency spectra which are validated against measurements in Section 6.3.8.

The wave conditions in the North Sea are dominated by local wind, but with some contribution of swell entering from the North Atlantic. Hence, the total sea state can in most cases be described adequately by a single-peaked spectrum (such as Pierson-Moskowitz or JONSWAP). Wave spectra with more than one peak may occur mainly during non-storm conditions, when there is a comparable amount of wave energy from wind-sea and from swells partitions.

The Pierson-Moskowitz spectrum

The Pierson-Moskowitz (PM) spectrum is given by Eq. (6.1), see e.g. Section 3.5.5.1 in DNV RP-C205, [42].

$$S_{PM}(\omega) = \frac{5}{16} \cdot H_s^2 \cdot \omega_p^4 \cdot \omega^{-5} \cdot \exp\left(-\frac{5}{4}\left(\frac{\omega}{\omega_p}\right)^{-4}\right)$$

$$where: \omega_p = \frac{2\pi}{T_p} is\ the\ angular\ frequency \tag{6.1}$$

The JONSWAP spectrum

The JONSWAP (J) spectrum is given by Eq. (6.2), see Section 3.5.5.2-5 in DNV RP-C205, [42].

$$S_J(\omega) = A_\gamma \cdot S_{PM}(\omega) \cdot \gamma^{\exp\left(-0.5\left(\frac{\omega-\omega_p}{\sigma \cdot \omega_p}\right)^2\right)}$$

$$\begin{aligned} &where: \\ &\gamma = non\ dimensional\ peak\ shape\ parameter \\ &\sigma = spectral\ width\ parameter \\ &\sigma = \sigma_a \text{ for } \omega \le \omega_p \\ &\sigma = \sigma_b \text{ for } \omega > \omega_p \\ &A\gamma = \frac{0.2}{0.065 \cdot \gamma^{0.803} + 0.135} \text{ is a normalizing factor} \end{aligned} \tag{6.2}$$

Average values are $\gamma = 3.3$, $\sigma_a = 0.07$, $\sigma_b = 0.09$. If no values are given, γ may be estimated by Eq. (6.3), i.e., defining γ for each sea state (timestep) using T_p and H_{m0}. For $\gamma = 1.0$, the JONSWAP spectrum reduces to the Pierson-Moskowitz spectrum.

$$\begin{aligned} &\gamma = 5\ for\ {}^{T_p}/_{\sqrt{H_{m0}}} \le 3.6 \\ &\gamma = exp\left(5.75 - 1.15 \cdot {}^{T_p}/_{\sqrt{H_{m0}}}\right)\ for\ 3.6 < {}^{T_p}/_{\sqrt{H_{m0}}} \le 5 \\ &\gamma = 1\ for\ 5 \le {}^{T_p}/_{\sqrt{H_{m0}}} \end{aligned} \tag{6.3}$$

Recommended spectrum

Figure 6.44 presents averaged modelled frequency spectra (during 2017-2022) of SW_{EINS} and the corresponding mean JONSWAP spectra for 0.5 m bins of H_{m0}. The figures show that the average modelled spectra match the average JONSWAP spectra well for moderate and high sea states, H_{m0} > 1.5 m. Hence, when there is considerable contribution of wind-sea, the spectrum is well represented by a single JONSWAP spectrum.

For low sea states, mainly H_{m0} < 1.5m, the spectra are bi-modal, due to the more comparable amount of wave energy in the wind-sea and the swells partitions. In such situations, there is less agreement between the averaged modelled and the JONSWAP spectra, and the spectrum should be represented by a JONSWAP fitted to each of the partitions separately, or by a proper two-peaked spectrum (such as e.g., the Torsethaugen or the Ochi-Hubble spectra).

In our experience (from the North Sea mainly), the modelled wave spectra are not expected to inform about the peak enhancement factor (gamma) of the JONSWAP spectrum. The modelled (wind-sea) spectra are generally a bit broader, and the fitting of JONSWAP spectra to modelled spectra usually results in somewhat lower gamma values compared to the mean value of 3.3 for wind-sea considered in the JONSWAP formulation following [43]. This concerns both total and the wind-sea (partitioned by wave-age) spectra. It is noted, though, that the value of gamma in [43] shows quite some spreading in the range of approximately 1 – 7 related to local conditions such as fetch and wind. The reason for the lower gamma values (compared to the mean value of 3.3) obtained by fitting of model spectra is not fully known, but it may be related to a combination of: a) generally broader/smoother spectra of spectral models (compared to measurements), b) too coarse discretisation of the model spectra, c) the partitioning not producing ‘pure’ wind-sea spectra, and d) the fitting process not being focused enough on the peak (but rather the bulk of the spectra). However, lower gamma values may also be due to local variations.

In conclusion, it is recommended to adopt JONSWAP spectra for normal and extreme wave conditions. For moderate and severe sea states, H_{m0} > 1.5 m, the spectrum is often well represented by a single JONSWAP spectrum, while for low sea states, H_{m0} < 1.5m, the spectra are often bi-modal, and should be represented by a JONSWAP fitted to each of the partitions separately. For information on gamma values, it is recommended to apply the guidelines in Section 3.5.5 of RP-C205 [42], i.e. defining γ based on T_p and H_{m0}, as given in Eq. (6.3). Table 6.8 presents JONSWAP peak shape factor, γ, per H_{m0} and T_p.

Table 6.8 JONSWAP peak shape factor, γ, per H_{m0} and T_p cf. Section 3.5.5.5 in DNV, [42]

γ	T_p [s]									
H_{m0} [m]	2	4	6	8	10	12	14	16	18	20
1	5.0	3.2	1.0	1.0	1.0	1.0	1.0	1.0	1.0	1.0
2	5.0	5.0	2.4	1.0	1.0	1.0	1.0	1.0	1.0	1.0
3	5.0	5.0	5.0	1.6	1.0	1.0	1.0	1.0	1.0	1.0
4	5.0	5.0	5.0	3.2	1.0	1.0	1.0	1.0	1.0	1.0
5	5.0	5.0	5.0	5.0	1.8	1.0	1.0	1.0	1.0	1.0
6	5.0	5.0	5.0	5.0	2.9	1.1	1.0	1.0	1.0	1.0
7	5.0	5.0	5.0	5.0	4.1	1.7	1.0	1.0	1.0	1.0
8	5.0	5.0	5.0	5.0	5.0	2.4	1.1	1.0	1.0	1.0
9	5.0	5.0	5.0	5.0	5.0	3.2	1.5	1.0	1.0	1.0
10	5.0	5.0	5.0	5.0	5.0	4.0	1.9	1.0	1.0	1.0

H_{m0} = [0.0 - 0.5] m

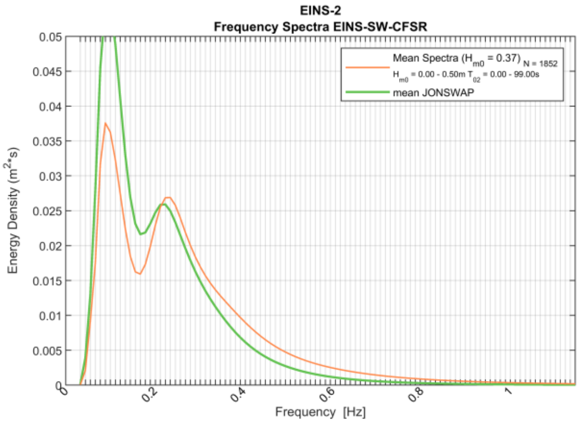

H_{m0} = [0.5 - 1.0] m

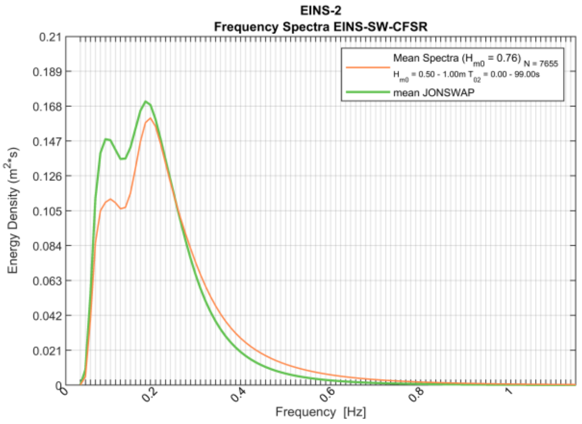

H_{m0} = [1.0 - 1.5] m

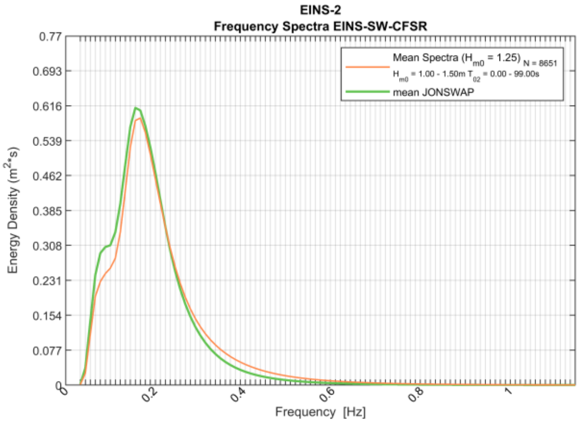

H_{m0} = [1.5 - 2.0] m

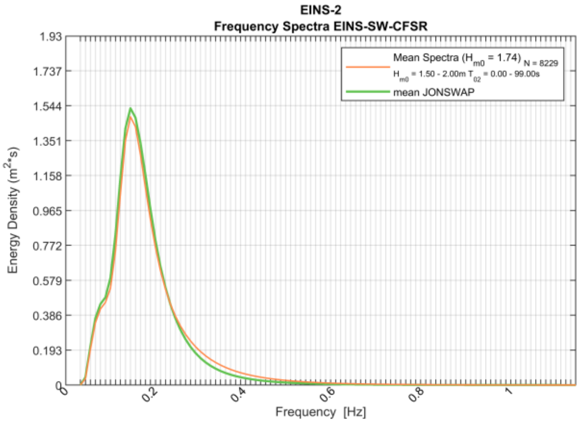

H_{m0} = [2.0 - 2.5] m

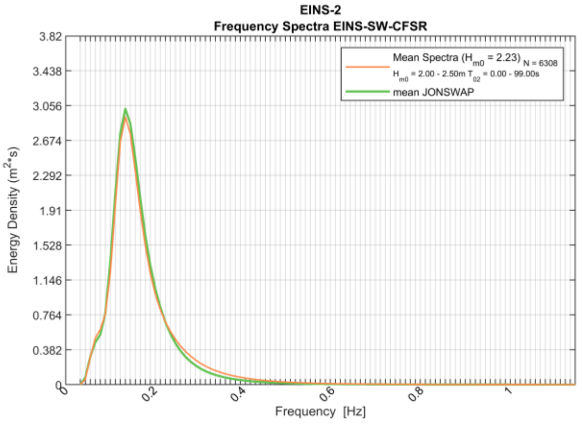

H_{m0} = [2.5 - 3.0] m

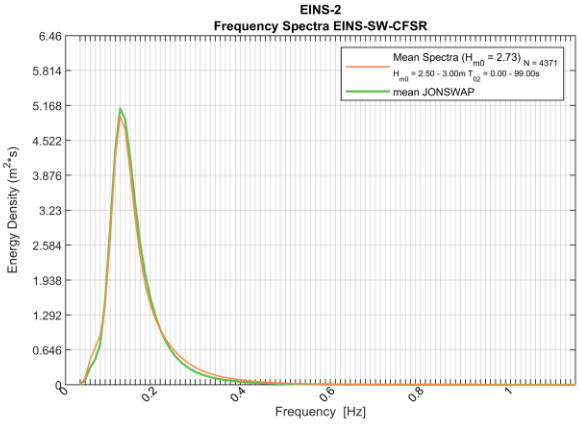

Figure continues next page.

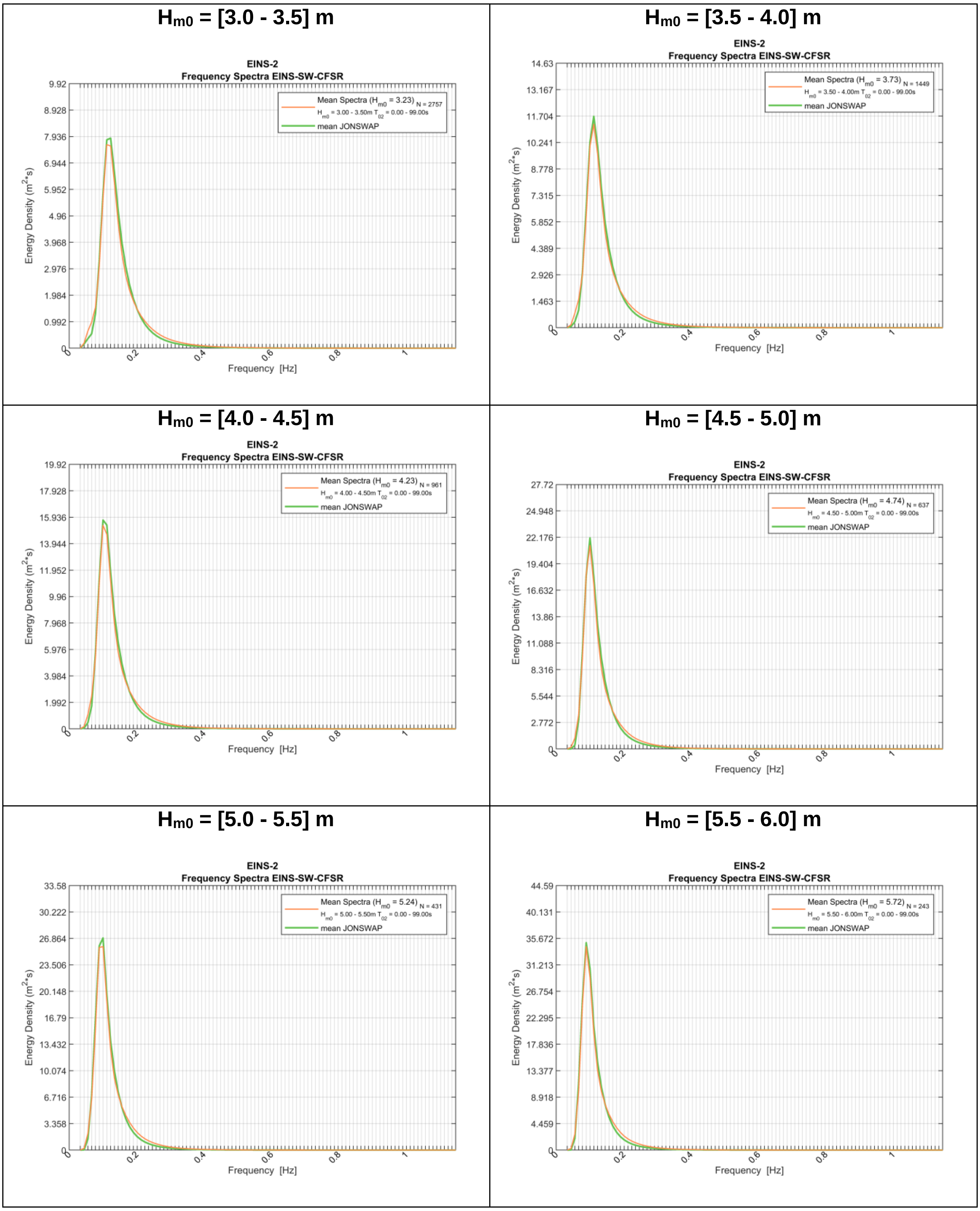

Figure 6.44 **Averaged frequency spectra (during 2017-2022) of SW_{EINS} and corresponding mean JONSWAP spectrum based on DNV [42], for 0.5 m bins (0 – 6 m) of H_{m0} at EINS-2**

7 Other Atmospheric Conditions

This section presents the data basis for assessing other atmospheric conditions.

Other atmospheric conditions concern rainfall, air temperature, humidity, solar radiation, lightning, and visibility.

7.1 Rainfall

Rainfall time series data were extracted from the ERA5 reanalysis product. The ERA5 data covers the period from 01-01-1979 to 01-01-2023 (44 years) with 1-hourly intervals and 30 km grid resolution. All of the five (5) EINS analysis points (see [10]) fall within the same ERA5 grid cell. Hence, only one rainfall time series is extracted and used in the analysis.

The ERA5 rainfall data were compared with measured rainfall data collected during the measurement campaign at EINS-North and EINS-South. These data cover a 6-month period from 15-11-2021 to 15-05-2022 with 10-min time resolution. Rainfall data collected after 15-05-2022 have large gaps and contain erroneous data and were not included in the analysis.

Accumulated precipitation of the three rainfall time series for the 6-month period are compared in Figure 7.1. The 6-month accumulated precipitation from ERA5 is larger than that of the in-situ measurements (8% compared to EINS-North and 27% compared to EINS-South). The difference between EINS-North and EINS-South is relatively constant in time.

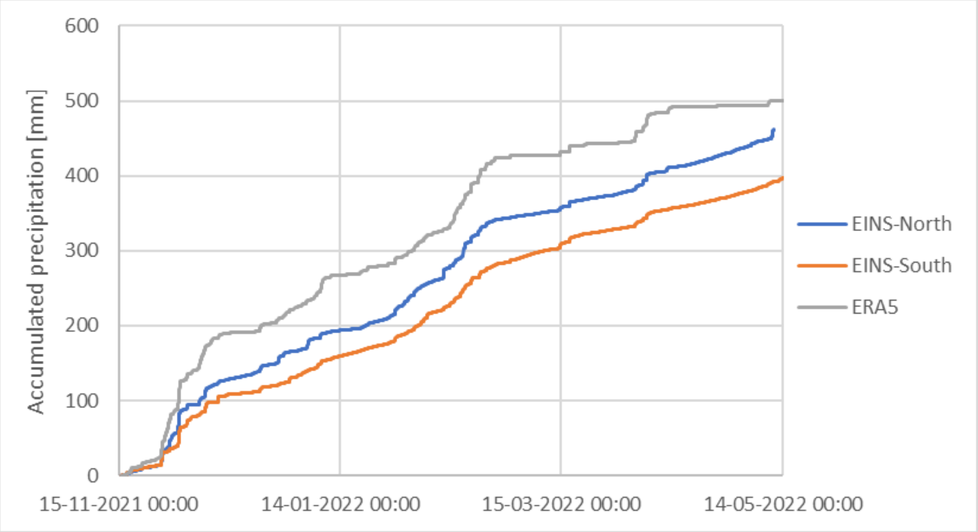

Figure 7.1 **Comparison of accumulated rainfall (15-11-2021 to 15-05-2022) from ERA5 and measurements at EINS-North and EINS-South**

Since only 6 months of in-situ measurements were available, it is difficult to assess the quality of ERA5 data, especially with respect to estimation of extreme rainfall statistics. A well-known problem with rain gauge measurements is the undercatch of rainfall, i.e. less rainfall than the "true" amount is being measured. The undercatch depends primarily on wind speed, rainfall intensity and precipitation type (rain or snow), with larger undercatch for high wind speed, low rainfall intensity and snow precipitation. The typical range for underestimation of rainfall is 10-25% (see e.g. [44], [45]) and maybe even larger in this case where the rain gauge is mounted on a buoy. Thus, the differences between ERA5 and the in-situ measurements are within the range of expected undercatch of the rain gauges. In conclusion, considering the measurement uncertainties (potential undercatch), the ERA5 data is applied as is (without any corrections) for the analyses of extreme rainfall.

7.2 Air temperature, humidity, and solar radiation

Time series data of air temperature, humidity, and solar radiation were extracted from CFSR (see Section 3.3.1) at EINS-North. The data covers 1979-01-01 – 2022-09-30 with 1-hourly intervals. Time series for these variables are shown in Figure 7.2. Time series comparisons against measurements are presented in Figure 7.3. The comparisons show a good agreement for temperature and relative humidity, while some scatter is seen for the downward solar radiation (DSWR). However, model results are in the same order of magnitude and follow a similar trend as the measurements.

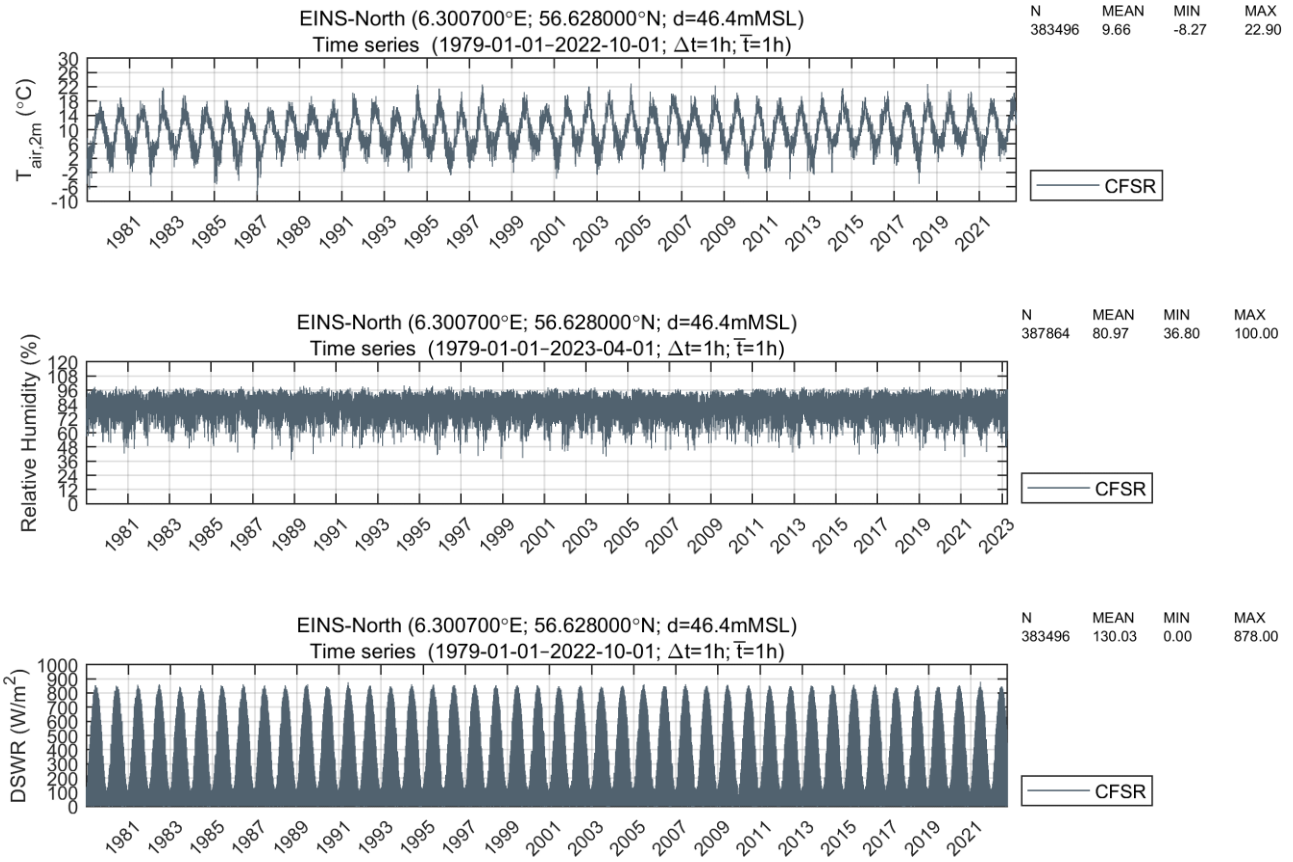

Figure 7.2 Time series of air temperature at 2 m, relative humidity, and downward solar radiation at EINS-North

Sensors are located at a height of 4.1 m

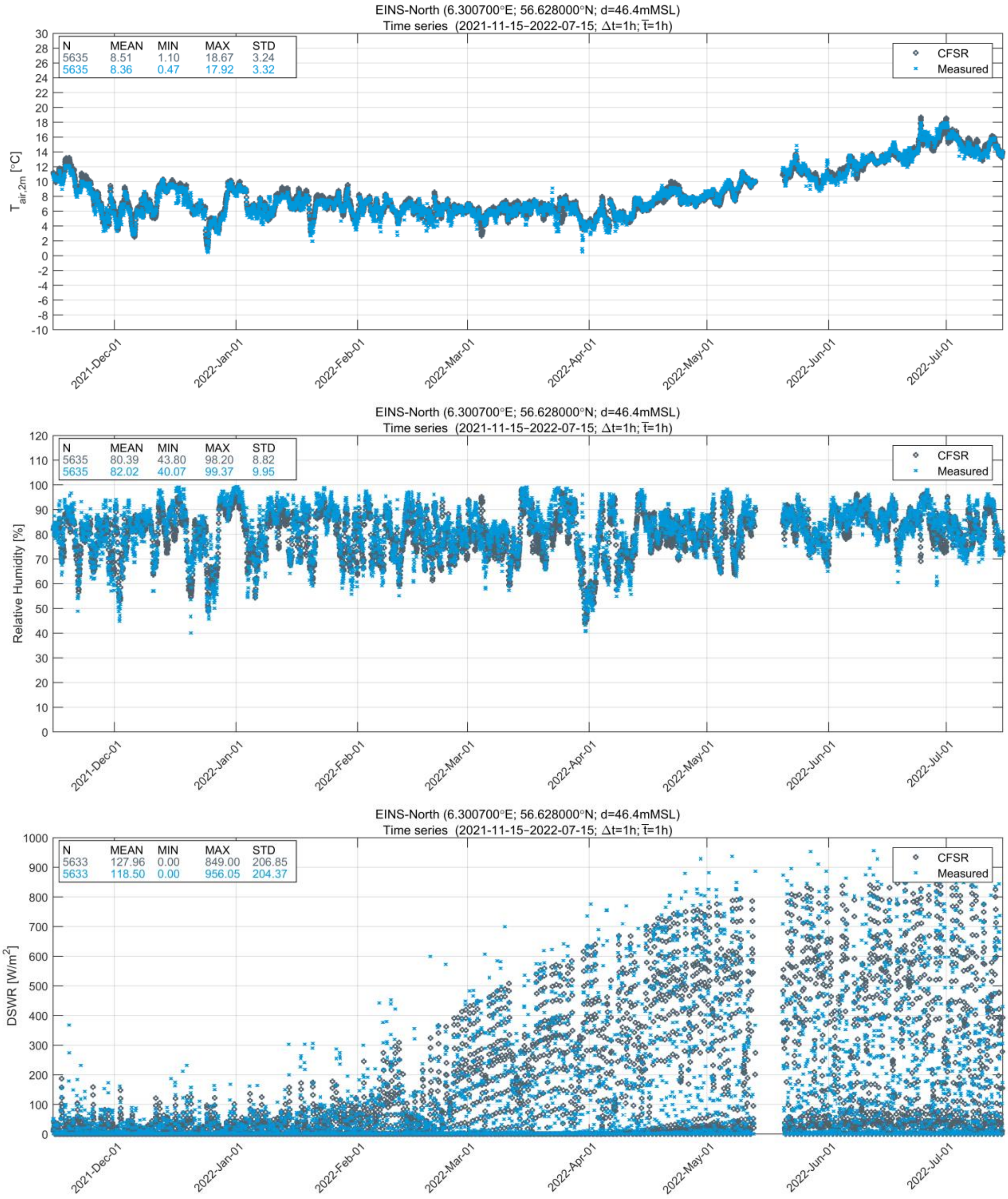

Figure 7.3 **Time series comparison of CFSR against measurements of air temperature at 2 m, relative humidity, and downward solar radiation at EINS-North**

Sensors are located at a height of 4.1 m. CFSR data corresponds to 2 m height

7.3 Lightning

Lightning data was obtained from the LIS/OTD Gridded Climatology dataset [3] from NASA's Global Hydrology Resource Center (GHRC). The data consists of gridded climatology of total lightning flash rates between 1995-05-04 to 2013-12-31, recorded by the Optical Transient Detector (OTD) and Lightning Imaging Sensor (LIS).

The climatology includes annual total lightning on a high resolution regular grid of 0.5° grid (HRFC), and at low resolution on a 2.5° grid (LRFC). Time series that shows the 30-day average of the flash rate density are also available. The description of the datasets can be found in [46]. Due to the positioning of the LIS (equatorward of about 38°), the tropic and subtopic records are the most robust, while the high latitude records are entirely from OTD. Figure 7.4 shows the global average flash rate density (fl/km^2/yr) based on high- and low-resolution data from the GHRC.

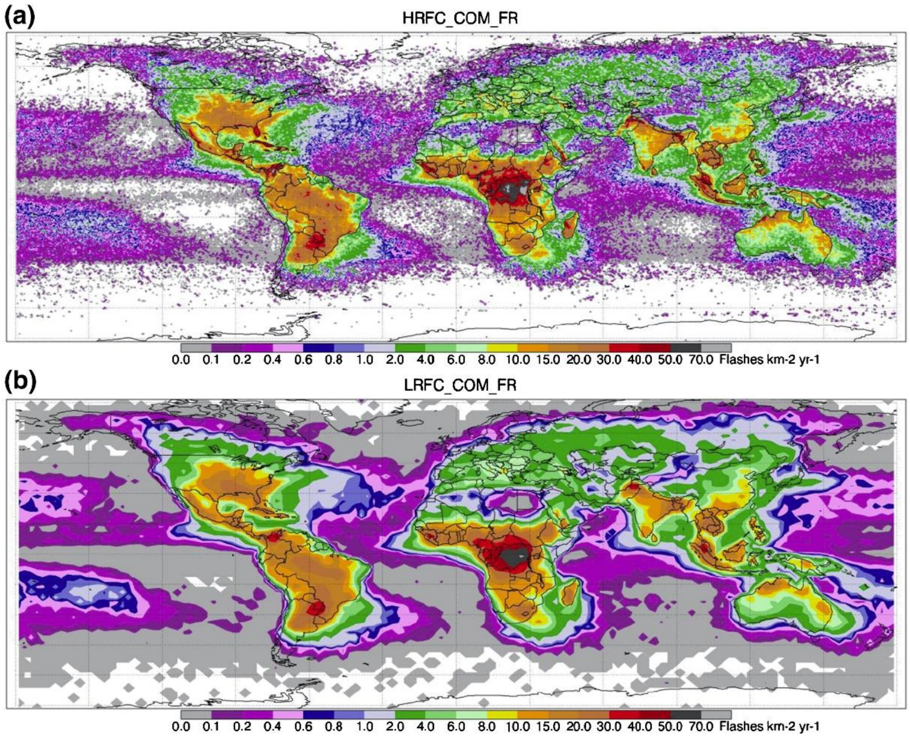

Figure 7.4 Global average flash rate density from GHRC data; (a) HRFC mean annual flash rate from combined LIS and OTD 0.5° grid and (b) LRFC mean annual flash rate from combined LIS and OTD 2.5°grid (from [46])

7.4 Visibility

The visibility was measured at EINS by a MiniPWS optical sensor. The sensor used an IR VCSEL laser and was heated to a few degrees above ambient temperature to keep moisture away from the lenses. To keep the electronics dry, a membrane ventilator kept the pressure inside at the same level as outside. The output was visibility in meters up to a max distance of 5 km.

Given the data available, the hindcast visibility was derived by applying an algorithm developed by the National Oceanic & Atmospheric Administration (NOAA)/Forecast Systems Laboratory (FSL) [47] that uses the air temperature at 2m height above sea surface, T_{2m}, and the relative humidity, RH, from CFSR as input (shown in Figure 7.2). There are more advanced approaches to derive visibility, like the one derived by Stoelinga and Warner [48]; however, it requires a larger number of input parameters not available in CFSR.

Figure 7.5 shows time series of visibility derived from CFSR variables (up to a max distance of 5 km to align with the recordings) at EINS-North for the full hindcast data period (1979 - 2022).

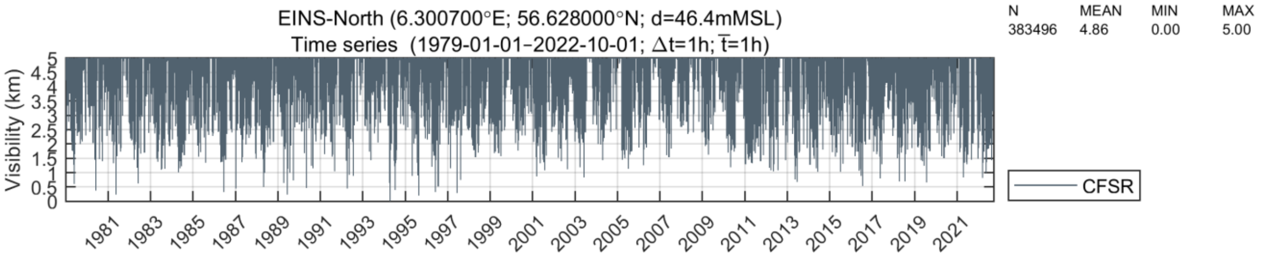

Figure 7.5 Time series of visibility derived from CFSR variables at EINS-North

Figure 7.6 shows the time series of the measured and hindcast visibility data for the extend of the measurements. This figure indicates that the hindcast visibility overestimates the number of short visibility events (the mean is lower). However, during those short visibility events, the hindcast visibility is slightly larger than the measured. Overall, one should consider substantial uncertainty in the definition/interpretation of the measured (and hindcast) range of visibility.

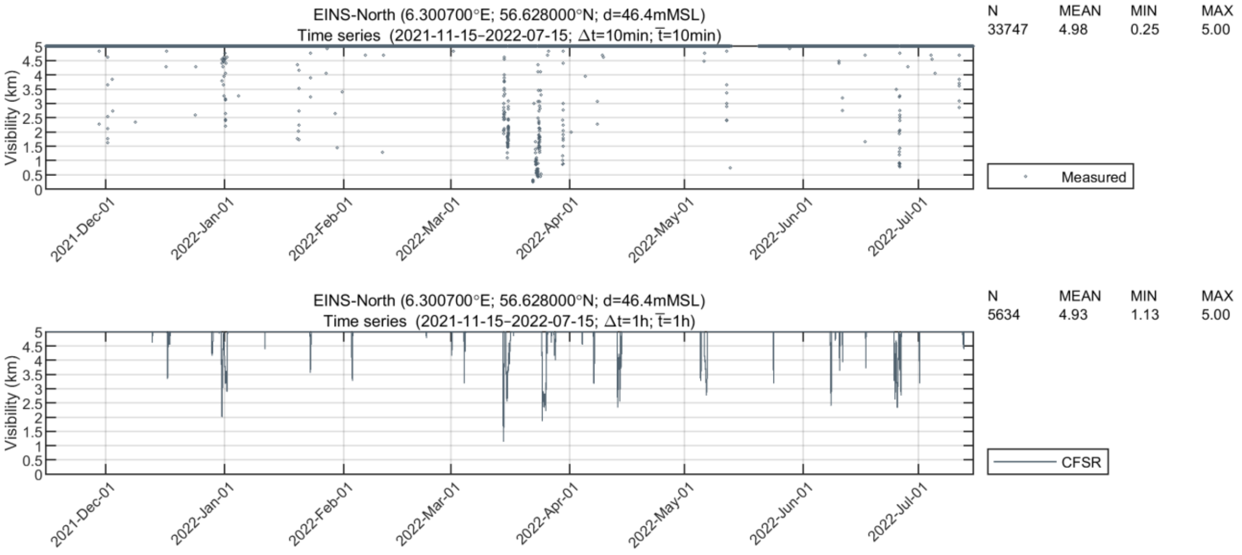

Figure 7.6 Time series of measured visibility (upper panel) and visibility derived from CFSR variables (lower panel) at EINS-North

8 Other Oceanographic Conditions

This section presents the data basis for the assessment of other ocean conditions.

Other ocean conditions concern water temperature, salinity, and density.

8.1 Water temperature, salinity, and density

Water temperature and salinity at the surface and bottom layers were adopted from the HD_{UKNS3D} model (see Section 5.4) at four locations (see Table 8.1).

Time series of the latter 10 years (2013-2022 incl.) were adopted for this study.

Table 8.1 Summary of data from HD_{UKNS3D} (2013-01-01 to 2023-01-01)

Name	Lon [°]	Lat [°]	Depth [mMSL]	Variables
EINS-1 (shallowest)	6.571	56.502	26.6	WL, CS, CD, Temp., Sal.
EINS-3 (max CS_{tot})	6.538	56.517	28.9	WL, CS, CD, Temp., Sal.
EINS-Island (Mini 2)	6.513	56.493	28.9	WL, CS, CD, Temp., Sal.
EINS-5 (South)	6.455	56.344	40.0	WL, CS, CD, Temp., Sal.

A comparison of the HD_{UKNS3D} salinity and temperature data was performed by comparing measurements from CTD Lot 2 against the model at 10 m and 34 m depths, see Figure 8.1 and Figure 8.2, demonstrating that HD_{UKNS3D} accurately describes the salinity and sea temperature.

Water density was calculated using the international one-atmosphere equation of state of seawater derived by Millero, F.J. and Poisson, A., [4].

Given the low spatial variability of these variables across the EINS site, time series for salinity, sea temperature and density are presented just for EINS-South (see location in Figure 4.2), see Figure 8.3.

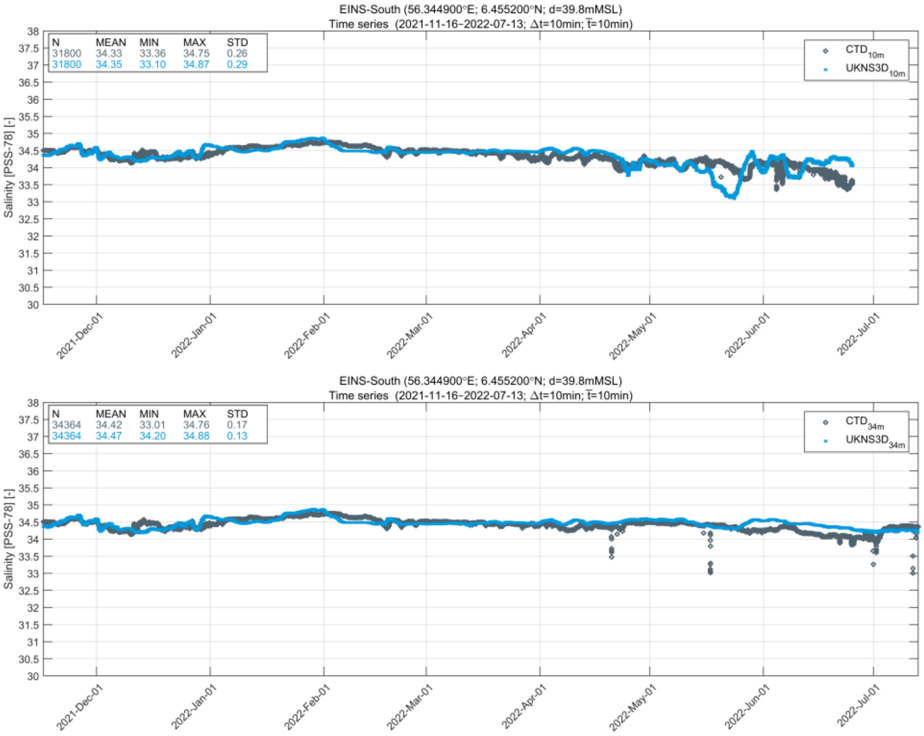

Figure 8.1 Salinity comparison at 10 m (top) and 34 m (bottom) depth between measurements and HD$_{UKNS3D}$ (2021-11-16 to 2022-07-13)

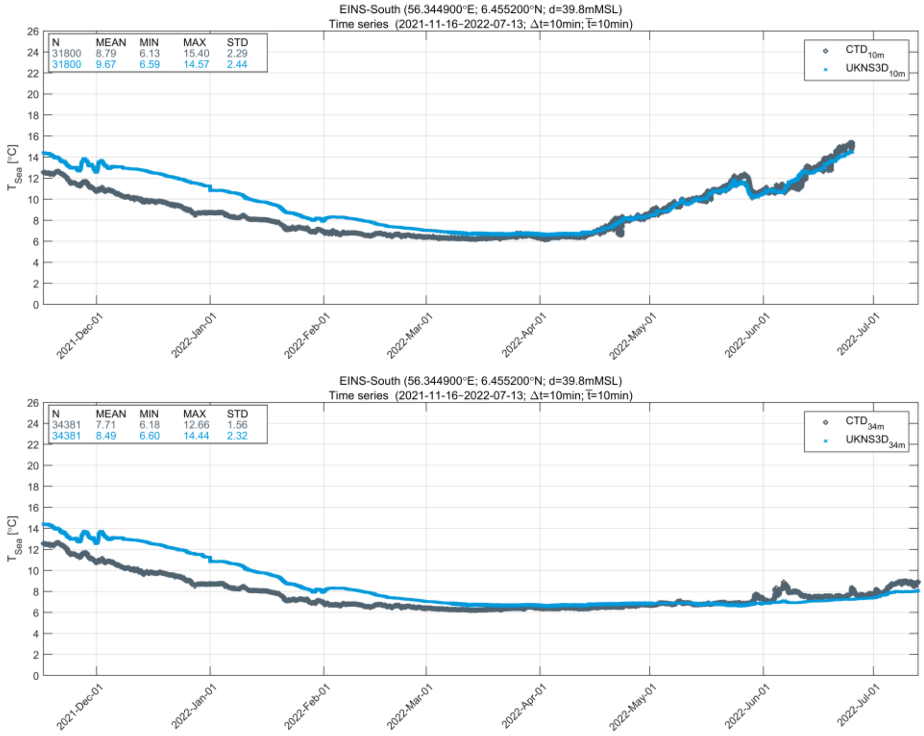

Figure 8.2 Temperature comparison at 10 m (top) and 34 m (bottom) depth between measurements and HD$_{UKNS3D}$ (2021-11-16 to 2022-07-13)

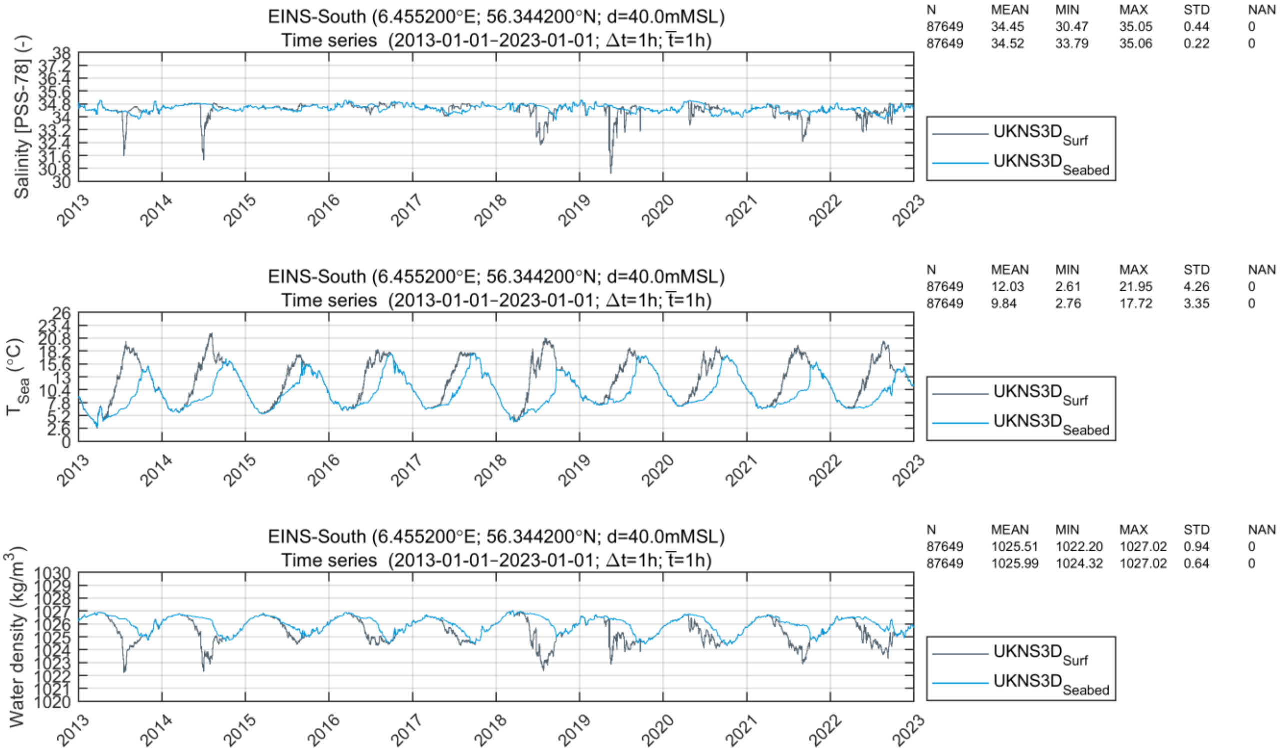

N	MEAN	MIN	MAX	STD	NAN
87649	34.45	30.47	35.05	0.44	0
87649	34.52	33.79	35.06	0.22	0

N	MEAN	MIN	MAX	STD	NAN
87649	12.03	2.61	21.95	4.26	0
87649	9.84	2.76	17.72	3.35	0

N	MEAN	MIN	MAX	STD	NAN
87649	1025.51	1022.20	1027.02	0.94	0
87649	1025.99	1024.32	1027.02	0.64	0

Figure 8.3 **Time series of salinity (top), water temperature (centre) and water density (bottom) at surface and seabed layers**

9 Climate Change

This section presents a literature review to assess the impact of climate change on the future wind conditions at the end of the expected 80-year lifetime of the Energy Island North Sea from expected construction completion in 2033, i.e., in year 2113. This is followed an assessment of the future sea level rise (SLR), general design guidelines (NORSOK), and a conclusion on the modelling approach for EINS.

9.1 Future wind conditions

The prediction of wind speed changes due to climate change in 2100 is very uncertain, and no conclusive statements have been made public. The Danish Meteorological Institute (DMI) has issued a climate atlas, [49], which includes the RCP4.5 and 8.5 scenarios and their regional footprint over Denmark. For Thisted municipality (the one closest to Danish North Sea conditions), the wind prediction is a slight decrease in mean wind speed (-1.1% for RCP4.5 and -0.3% for RCP8.5). The uncertainty is large within +/-2%, and no prediction for change in extreme wind speed is made.

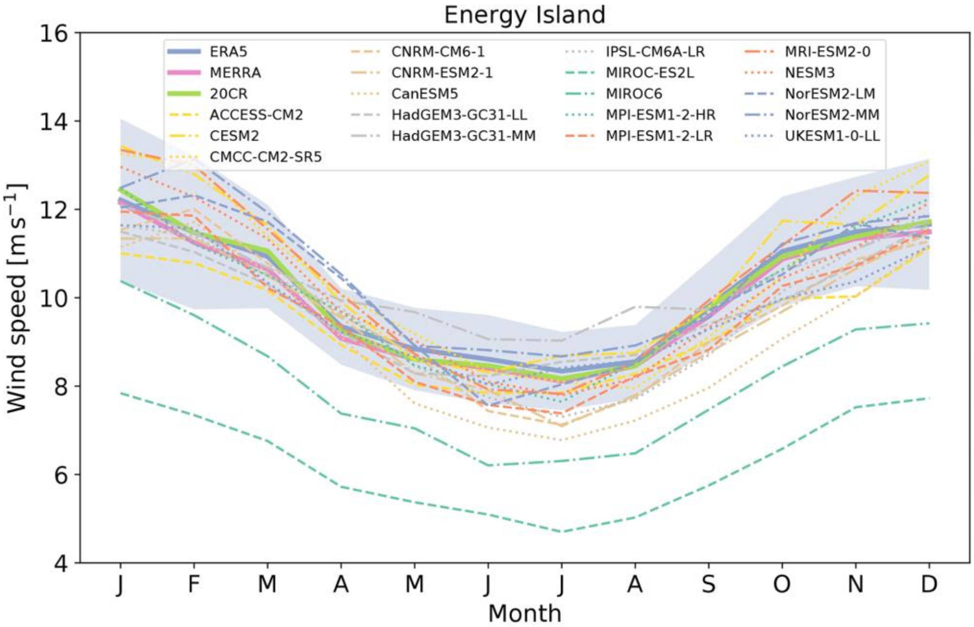

Figure 9.1 The annual cycle of mean monthly wind speed at 100 m a.g.l. simulated by the CMIP6 models and provided by the global reanalyses, during the full historical period (1980–2014), for the Energy Island location.

The shaded area is the ± 1 standard deviation of the monthly means for the ERA5 reanalysis [50]. Hence, most model predictions are within the ± 1 standard deviation.

A recent study from 2022, [50], based on a subset of 16 models in the CMIP6 collection show '*… that annual mean wind speed and wind resources in northern Europe are not particularly affected by climate change in 2031–2050 relative to 1995–2014.' However, the seasonal distribution of these resources is significantly altered. Most models agree on reductions in the future wind in summer in a band that extends from the British Isles to the Baltic Sea and on increases in winter in the southern Baltic Sea.*'. Figure 9.1 shows the annual cycle of mean monthly wind speed, at the Energy Island, for various CMIP6 models of this study. Most models are within ± 1 standard deviation of ERA5. I.e., seasonal changes are predicted, but the study does not address to what extent these changes affect extreme wind conditions (during winter).

In a study published in 2014 [51] by the Dutch Meteorological Office (Koninklijk Nederlands Meteorologisch Instituut, KNMI), similar conclusions were made for the mean wind speed, but for extreme wind speeds, a decrease of 0.4 m/s in the 100-year return period speed was found at the location of the Energy Island North Sea, by comparing the periods 2071-2100 with the past 30 years. This study also concluded that the uncertainty is very high.

Another recent study from 2022, [52], based on seven regional climate models in the EURO-Cordex project running the RCP8.5 scenario, predicts a slight increase in the 99th percentile of wind speed in the southeast corner of the North Sea, while the northwest corner displays a slight decrease. At the location of the Energy Island North Sea, the change is negligible.

Finally, a recent paper (currently in review) by DTU Wind, [53], also based on comparisons of various CMIP6 scenarios models, shows an increase of up to 0.008±0.78 m/s (i.e. +~0-1 m/s or ~0-3 %) of U_{50} (the 50-year extreme wind speed at 100 m) in the North Sea, for the near future period (2020–2049) compared to the historic period (1980–2009), see Table 9.1. If such (worst case) findings can be 'extrapolated' to 2100+, then the increase might double or triple, which would be rather dramatic. However, the paper does not address 2100+, and, as Table 9.1 demonstrates, the final number dependents strongly on which models (Group) is considered. Further, Figure 9.2 shows that the increase varies across the North Sea, i.e., not consistently high everywhere.

Table 9.1 Summary of the statistics of change in the extreme wind ∆U50 at 100 m (Fig. 5) over the entire domain

	Grouping of CMIP6 models		
Statistics	Group-I (all models)	Group-II (models 1, 5, 6, 9, 10, 18)	Group-III (models 1–7, 9, 10, 12, 13, 15–18)
mean $\pm\sigma$ (ms^{-1})	-0.23 ± 0.51	0.008 ± 0.78	-0.17 ± 0.50

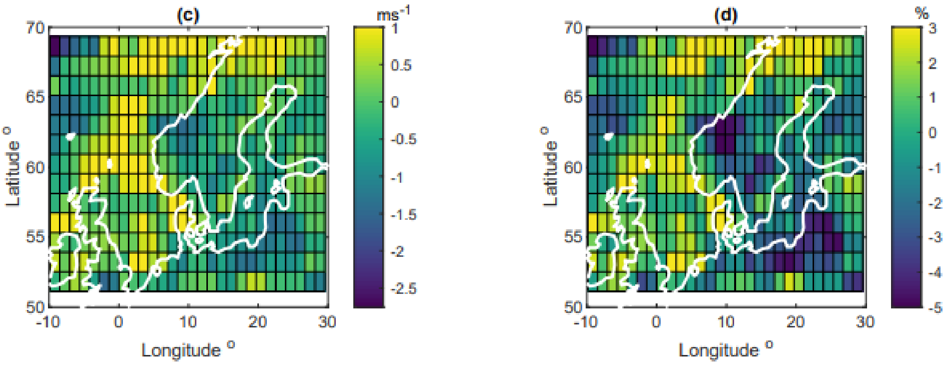

Figure 9.2 Spatial distribution of variation in wind speed (model Group-II)
Left: Model mean difference ∆U50; Right: Relative mean difference (∆U50/U50$_{\text{historical}}$)

9.2 Future sea level rise (SLR)

This section presents a quantitative assessment of future sea level rise due to climate changes within the expected lifetime of the EINS (year 2113).

The sixth assessment report (AR6) from the UN Intergovernmental Panel on Climate Change (IPCC) indicates a global mean SLR range between 0.3 and 1.6 m (5th-95th percentile) by year 2100 relative to 1995-2014 of the Representative Concentration Pathway (RCP) 8.5 scenario, see Figure 9.3, [54]. As a conservative choice, RCP 8.5 is adopted for this study.

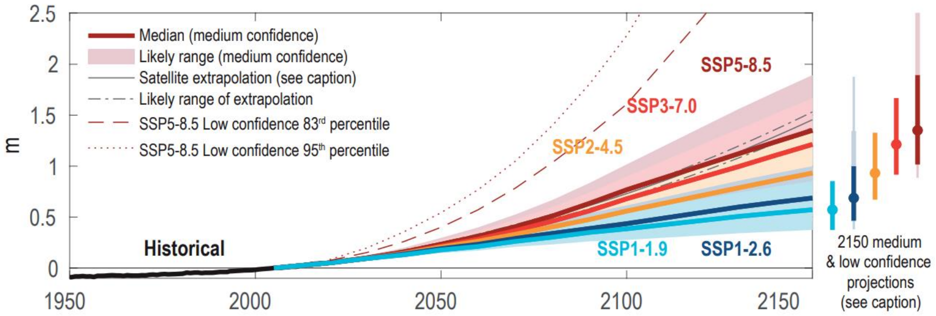

Figure 9.3 **Projected global mean sea level rise (SLR) under different Shared Socio-economic Pathway (SSP) scenarios (Figure 9.27 in [54])**

The SSP5-8.5 (RCP 8.5) median is adopted for this study.

The World Bank Group (WBG) has prepared a Climate Change Knowledge Portal (CCKP) for climate-related information and data, [55]. The CCKP provides SLR projections based on the RCP from the IPCC report per country. For Danish waters, the RCP 8.5 median SLR projection for the period between 2060-2079 is ~0.45 m with reference to the period (1986-2005), see Figure 9.4 (left). By 2100, the median projected SLR is 0.7 m. For this project, the projected SLR by 2113 is extrapolated to ~0.8 m, see Figure 9.4 (right). This agrees with the prediction given by DMI[8] of 82.8 cm by 2113 at Lemvig.

Sea level rise results in larger water depths and thus has the potential to influence current and waves, particularly during extreme events. This has been assessed by simulating the most severe historical storms during 1979-2022 with the anticipated 0.8 m sea level rise by year 2113 (ignoring expected/estimated land uplift of ~10-20 cm), see Sections 5.3.1 and 6.3.3.

---

[8] https://www.dmi.dk/index.php?id=3350 (Excel Regneark, Havniveaustigning (opdelt på kyststrækninger), Station: LF4 (Limfjorden ved Thisted), Scenarie: SSP5-8.5, 50-percentil, år: 2113).

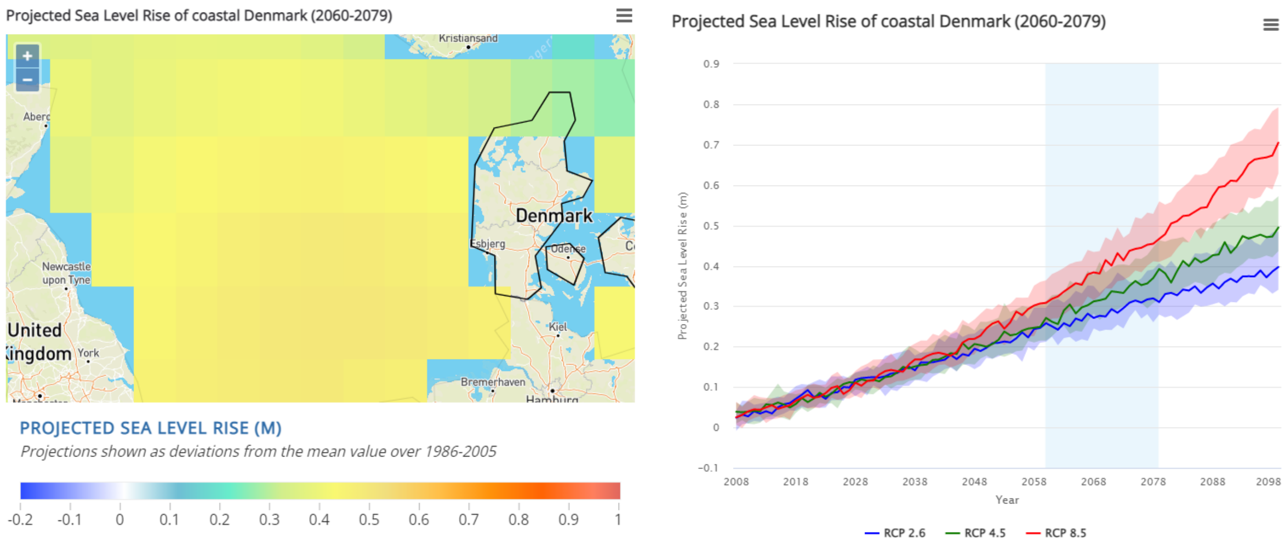

Figure 9.4 **Projected sea level rise of coastal Denmark (2060-2079), [54]**
Left: SLR from the CMIP5 collection presented at a 1° resolution. Right: Median projected SLR of coastal Denmark based on various RCP's. Shaded area indicates the 10-90% confidence range.

9.3 General design guidelines

Little information is available in general design guidelines. IEC, [9], and DNV, [8], do not (yet) address this, but NORSOK-003, (2016), [5], in Section "A.2 Comm. 6.1.2 *Possible consequences of climate changes*" states as follows:

- 'In lack of more detailed documentation the following increase in metocean values 50 years ahead may be used: extreme wind speeds: +4% on q-probability values.', and,

- 'The climate models predict an increase of about 6 – 8 % in extreme significant wave heights in the Eastern North Sea and Skagerrak through the 21st century.'

The NORSOK Standard does not give any recommendation on currents.

Of the various papers reviewed in Section 9.1, the NORSOK recommendations compares closest to the most conservative (worst case) scenarios, which would also be expected from the perspective of a certifying body.

9.4 Approach for EINS

Hence, the main conclusion is that global warming will not change the mean wind climate (intensity) over the North Sea beyond the large range of natural climate variability that has been experienced in the past, albeit seasonal variability may change somewhat depending on geographical location. From a modelling (hindcast) perspective it is essential that the wind intensity does not change, since this means that the atmospheric data forcing the hindcast (wave and hydrodynamic) models would not need adjustment to reflect a future scenario.

It is not fully clear from the above studies if the frequency of occurrence of storms may change, which would potentially affect the extreme statistics (return period values). But '*negligible change of the 99%-tile'* is some indication that any change in frequency is small. From this perspective, and by acknowledging the large uncertainties involved in predicting this, no further actions are taken to address (potential) climate change effect on wind.

Instead, it is recommended that the designer consults the project owner and any given design requirements on climate change, to decide on the safety policy with respect to possible climate change effects (e.g., NORSOK, [5]).

The effect of climate change on water level, i.e., sea level rise (SLR), is assessed in Section 9.2 to be ~0.1 m in 2033 and ~0.8 m in 2113. The derived effect of SLR on current and waves is assessed in Sections 5.3.1 and 6.3.3 to be negligible (~1%) compared to other uncertainties (wind) of climate change.

Therefore, the hindcast (wave and current) models are established and executed for present-day scenario only (no change in wind or water depth), and not for any future scenario. The present-day scenario will thus reflect the construction period (~2033) as well as the end-of-service period (~2113).

Extreme value analysis will be conducted on the data basis established for the present-day scenario, and results of variables referring to fixed vertical datums (high and low water level, and maximum wave crest, $C_{max,datum}$) are provided as two sets of results reflecting SLR (see Section 9.2), respectively:

1. Construction period (2033): Present-day scenario
2. End-of-service period (2113): SLR = +0.8 m

10 References

[1] Fugro, "SWLB measurements at Energy Islands, C75486_Project_Measurement_Plan_All_Lots 05, 6 April 2022," 2022.

[2] Fugro, "SWLB measurements at Energy Islands - Project Measurement Plan, All Lots," 2022.

[3] D. J. Cecil. *LIS/OTD Gridded Lightning Climatology Data Collection, Version 2.3.2015*, NASA EOSDIS Global Hydrology Resource Center Distributed Active Archive Center, Huntsville, Alabama, U.S.A., doi: http://dx.doi.org/10.5067/LIS/LIS-OTD/DATA311.

[4] F. J. Millero and A. Poisson, "International one-atmosphere equation of state of seawater," *Deep Sea Research Part A. Oceanographic Research Papers,* vol. 28, no. 6, pp. 625-629, 1981/06/01/ 1981, doi: https://doi.org/10.1016/0198-0149(81)90122-9.

[5] NORSOK, "Actions and action effects, N-003, Edition 3, April 2016," 2016.

[6] Energinet, "Scope of Services – North Sea Energy Island Metocean Conditions Assessment, document number: 2/05192-6, 2022-06-22," 2022.

[7] Energinet, "Scope of Services – Site Metocean Conditions Assessment for Offshore Wind Farms, North Sea, Document number: 22/08564-1, 2022-11-08," 2022.

[8] *Environmental Conditions and Environmental Loads*, DNV-RP-C205, DNV, 2021-09. [Online]. Available: http://rules.dnvgl.com/docs/pdf/DNV/codes/docs/2014-04/RP-C205.pdf

[9] *Wind energy generation systems – Part 3-1: Design Requirements for fixed offshore wind turbines. Ed. 1.0*, IEC-61400-3-1, 2019-04.

[10] DHI, "Energy Island North Sea, Metocean Site Conditions Assessment, Part B: Data Analyses – Energy Island, 2023-06-16," 2023.

[11] DHI, "Energy Island North Sea, Metocean Site Conditions Assessment, Part C: Data Analyses – Wind Farm Area, due 2023-06-28," 2023.

[12] DHI, "Energy Island North Sea, Metocean Site Conditions Assessment, Part D: Data Basis – Hindcast revalidation note, due Jan. 2024," 2024.

[13] MMT, "Geophysical survey for offshore wind farms and energy," 2021.

[14] J. W. Hurrell and H. Van Loon, "Decadal Variations In Climate Associated With The North Atlantic Oscillation," *Climatic Change,* vol. 36, no. 3, pp. 301-326, 1997/07/01 1997, doi: 10.1023/A:1005314315270.

[15] P. Yiou and M. Nogaj, "Extreme climatic events and weather regimes over the North Atlantic: When and where?," *Geophysical Research Letters,* vol. 31, no. 7, 2004, doi: https://doi.org/10.1029/2003GL019119.

[16] D. Panja and F. M. Selten, "Extreme associated functions: optimally linking local extremes to large-scale atmospheric circulation structures," *Atmos. Chem. Phys. Discuss.,* vol. 2007, pp. 14433-14460, 2007, doi: 10.5194/acpd-7-14433-2007.

[17] H. Lamb, *Historic storms of the North Sea, British Isles and Northern Europe*. 1991.

[18] *Petroleum and natural gas industries — Specific requirements for offshore structures — Part 1: Metocean design and operating considerations*, ISO 19901-1:2015, ISO, 2015.

[19] CEM, "Coastal Engineering Manual, Meteorology and Wave Climate," 2008. [Online]. Available: http://www1.frm.utn.edu.ar/laboratorio_hidraulica/Biblioteca_Virtual/Coastal%20Engineering%20Manual%20-%20Part%20II/Part_II-Chap_2.pdf

[20] *Guidelines for converting between various wind averaging periods in tropical cyclone conditions*, WMO/TD- No. 1555, WMO, 2010.

[21] S. M. a. H.-L. P. S. Saha, "The NCEP Climate Forecast System Reanalysis," *American Meteorological Society,* pp. 1015-1057, 2010.

[22] DHI, "MetOcean Study - Wind farm zone Hollandse Kust (zuid) & Hollandse Kust (noord) - V2.3," RVO.nl, Ultrecht, NL, 2017.

[23] DHI, "Metocean desk study and database for Dutch Wind Farm Zones, Hollandse Kust (Noord)," RVO, NL, Project Nr. 11822658, Final 2.4, 2019.

[24] E. P. Kvale, "Tides and tidal rhytmites," in *Encyclopedia of Sediments and Sedimentary Rocks*, G. V. Middleton, M. J. Church, M. Coniglio, L. A. Hardie, and F. J. Longstaffe Eds. Dordrecht: Springer Netherlands, 2003, pp. 741-744.

[25] DHI, "MIKE 21 Flow Model FM, Hydrodynamic Module, User Guide," 2022.

[26] OSPAR, "Quality status report 2000. Region II, the Greater North Sea," OSPAR Commissions, London, 2000.

[27] W. R. Turrell, "New hypotheses concerning the circulation of the northern North Sea and its relation to North Sea fish stock recruitment," *ICES Journal of Marine Science,* vol. 49, no. 1, pp. 107-123, 1992, doi: 10.1093/icesjms/49.1.107.

[28] "FLOATING LIDAR MEASUREMENTS THOR OFFSHORE WIND FARM," 2021.

[29] "M. Piano; P. E. Robins; A. G. Davies; S. P. Neill," *Energies,* vol. 11, no. 10, p. 2852, 2018.

[30] DHI, "MIKE 3 Flow Model FM - Hydrodynamic and Transport Module - Scientific Documentation ", 2023. [Online]. Available: https://manuals.mikepoweredbydhi.help//2023/Coast_and_Sea/MIKE_3_Flow_FM_Scientific_Doc.pdf

[31] Y. A. Cheng, O. B., "Improvement in global ocean tide model in shallow water regions. ," presented at the Altimetry for Oceans and Hydrology OST-ST Meeting, Lisbon, Lisbon, 2010, Poster, SV.1-68 45.

[32] DHI, "Hydrodynamic Model of North Sea and UK Waters (UKNS2) - Setup and Validation, version 2," 2018.

[33] I. Karmpadakis, "Wave Statistics in Intermediate and Shallow Water Depths," Doctor of Philosophy, Department of Civil and Environmental Engineering, Imperial College London, 2018.

[34] I. K. C. S. M. Christou, "A new wave height distribution for intermediate and shallow water depths," *Coastal Engineering,* vol. 175, 2022.

[35] G. Klopman, "Extreme wave heights in shallow water," *WL/Delft hydraulics,* 1996.

[36] G. Z. Forristall, "Wave Crest Distributions: Observations and Second-Order Theory," *Journal of Physical Oceanography,* vol. 30, no. 8, pp. 1931-1943, 2000, doi: dx.doi.org/10.1175/1520-0485(2000)030<1931:wcdoas>2.0.co;2.

[37] G. Z. Forristall, "Maximum Crest Heights over an Area. Laboratory Measurements Compared To Theory," in *Proceedings of the ASME 2015 34th International Conference on Ocean, Offshore and Arctic Engineering*, St. John's, Newfoundland, Canada, 2015, pp. OMAE2015-41061.

[38] J. P. D. Tychsen, Martin, "Wave kinematics and hydrodynamic loads on intermediate water depth structures inferred from systematic model testing and field observations – Tyra Field Extreme Wave Study 2013-15," in *The 3rd Offshore Structural Reliability Conference*, Stavanger, Norway, 2016.

[39] DHI, "Metocean assessment focused on normal and extreme currents and waves; Part A - Modelling Assessment," 2022.

[40] J. A. Battjes and a. J.P.F.M., "Energy loss and set-up due to breaking of random waves," in *16th Int. Conf. On Coastal Eng.*, NY, 1978: ASCE, pp. 569-587.

[41] DHI, "MIKE 21 Spectral Wave Module; Scientific Documentation," Danish Hydraulic Institute, 2013.

[42] *Loads and site conditions for wind turbines*, DNV-ST-0437, DNV, 2021-11.

[43] K. Hasselmann and D. Olbers, "Measurements of wind-wave growth and swell decay during the Joint North Sea Wave Project (JONSWAP)," *Ergänzung zur Deut. Hydrogr. Z., Reihe A (8),* vol. 12, pp. 1-95, 1973. [Online]. Available: https://epic.awi.de/id/eprint/10163/.

[44] P. Allerup, Madsen, H., and Vejen, F., "A comprehensive model for correcting point precipitation," *Nord. Hydrol., 28, 1–20,* 1997.

[45] S. Stisen, Sonnenborg, T. O., Hojberg, A. L., Troldborg, L., and Refsgaard, J. C., "Evaluation of Climate Input Biases and Water Balance Issues Using a Coupled Surface-Subsurface Model," *Vadose Zone J., 10, 37–53,* 2011.

[46] D. J. B. Cecil, D. E.; Blackeslee, R. J., "Gridded lightning climatology from TRMM-LIS and OTD: Dataset description," *Atmospheric Research,* vol. 135-136, pp. 404-414, 2014.

[47] J. A. R. Doran, P.J.; Beberwyk, D.J.; Brooks, G.R.; Gayno, G.A.; Williams, R.T.; Lewis, J.M.; Lefevre, R.J. , "The MM5 at the Air Force Weather Agency - New products to support military operations, ," presented at the The 8th Conference on Aviation,Range, and Aerospace Meteorology, Dallas, Texas, 1999.

[48] M. T. a. W. Stoelinga, T.T., "Nonhydrostatic, Mesobeta-Scale Model Simulations of Cloud Ceiling and Visibility for an East Coast Winter Precipitation Event," *Journal of Applied Meteorology and Climatology,* vol. 8, no. 4, pp. 385-404, 1999, doi: https://doi.org/10.1175/1520-0450(1999)038%3C0385:NMSMSO%3E2.0.CO;2.

[49] DMI. "https://www.dmi.dk/klimaatlas/." (accessed.

[50] A. N. Hahmann, O. García-Santiago, and A. Peña, "Current and future wind energy resources in the North Sea according to CMIP6," *Wind Energ. Sci.,* vol. 7, no. 6, pp. 2373-2391, 2022, doi: 10.5194/wes-7-2373-2022.

[51] KNMI, "Large-scale winds in the southern North Sea region: the wind part of the KNMI’14 climate change scenarios (iop.org): https://iopscience.iop.org/article/10.1088/1748-9326/10/3/035004/pdf," 2015.

[52] S. S. e. al, "Frontiers | Climate Change Impact on the Offshore Wind Energy Over the North Sea and the Irish Sea (frontiersin.org): https://www.frontiersin.org/articles/10.3389/fenrg.2022.881146/full " 2022.

[53] X. G. Larsén, M. Imberger, Á. Hannesdóttir, and A. N. Hahmann, "The Impact of Climate Change on Extreme Winds over Northern Europe According to CMIP6," *Wind Energ. Sci. Discuss.,* vol. 2023, pp. 1-25, 2023, doi: 10.5194/wes-2022-102.

[54] IPCC, "Climate Change 2021: The Physical Science Basis. Contribution of Working Group I to the Sixth," 2021.

[55] W. B. Group. "https://climateknowledgeportal.worldbank.org/country/denmark/impacts-sea-level-rise " (accessed.

11 Appendix A: Model Quality Indices

To obtain an objective and quantitative measure of how well the model data compared to the observed data, several statistical parameters, so-called quality indices (QI's), are calculated.

Prior to the comparisons, the model data is synchronised to the time stamps of the observations so that both time series had equal length and overlapping time stamps. For each valid observation, measured at time t, the corresponding model value is found using linear interpolation between the model time steps before and after t. Only observed values that had model values within ± the representative sampling or averaging period of the observations are included (e.g., for 10-min observed wind speeds measured every 10 min compared to modelled values every hour, only the observed value every hour is included in the comparison).

The comparisons of the synchronised observed and modelled data are illustrated in (some of) the following figures:

- Time series plot including general statistics
- Scatter plot including quantiles, QQ-fit and QI's (density-coloured dots)
- Histogram of occurrence vs. magnitude or direction
- Histogram of bias vs. magnitude
- Histogram of bias vs. direction
- Dual rose plot (overlapping roses)
- Peak event plot including joint (coinciding) individual peaks

The quality indices are described below, and their definitions are listed in Table 11.1. Most of the quality indices are based on the entire dataset, and hence the quality indices should be considered averaged measures and may not be representative of the accuracy during rare conditions.

The MEAN represents the mean of modelled data, while the bias is the mean difference between the modelled and observed data. AME is the mean of the absolute difference, and RMSE is the root-mean-square of the difference. The MEAN, BIAS, AME and RMSE are given as absolute values and relative to the average of the observed data in percent in the scatter plot.

The scatter index (SI) is a non-dimensional measure of the difference calculated as the unbiased root-mean-square difference relative to the mean absolute value of the observations. In open water, an SI below 0.2 is usually considered a small difference (excellent agreement) for significant wave heights. In confined areas or during calm conditions, where mean significant wave heights are generally lower, a slightly higher SI may be acceptable (the definition of SI implies that it is negatively biased (lower) for time series with high mean values compared to time series with lower mean values (and same scatter/spreading), although it is normalised).

EV is the explained variation and measures the proportion [0 - 1] to which the model accounts for the variation (dispersion) of the observations.

The correlation coefficient (CC) is a non-dimensional measure reflecting the degree to which the variation of the first variable is reflected linearly in the variation of the second variable. A value close to 0 indicates very limited or no (linear) correlation between the two data sets, while a value close to 1 indicates a very high or perfect correlation. Typically, a CC above 0.9 is considered a high correlation (good agreement) for wave heights. It is noted that CC is 1 (or -1) for any two fully linearly correlated variables, even if they are not 1:1. However, the slope and intercept of the linear relation may be different from 1 and 0, respectively, despite CC of 1 (or -1).

The QQ line slope and intercept are found from a linear fit to the data quantiles in a least-square sense. The lower and uppermost quantiles are not included on the fit. A regression line slope different from 1 may indicate a trend in the difference.

The peak ratio (PR) is the average of the Npeak highest model values divided by the average of the Npeak highest observations. The peaks are found individually for each dataset through the Peak-Over-Threshold (POT) method applying an average annual number of exceedances of 4 and an inter-event time of 36 hours. A general underestimation of the modelled peak events results in a PR below 1, while an overestimation results in a PR above 1.

An example of a peak plot is shown in Figure 11.1. ‘X’ represents the observed peaks (x-axis), while ‘Y’ represents the modelled peaks (y-axis), based on the POT methodology, both represented by circles (‘o’) in the plot. The joint (coinciding) peaks, defined as any X and Y peaks within ±36 hours[9] of each other (i.e., less than or equal to the number of individual peaks), are represented by crosses (‘x’). Hence, the joint peaks (‘x’) overlap with the individual peaks (‘o’) only if they occur at the same time exactly. Otherwise, the joint peaks (‘x’) represent an additional point in the plot, which may be associated with the observed and modelled individual peaks (‘o’) by searching in the respective X and Y-axis directions, see example with red lines in Figure 11.1. It is seen that the ‘X’ peaks are often underneath the 1:1 line, while the ‘Y’ peaks are often above the 1:1 line.

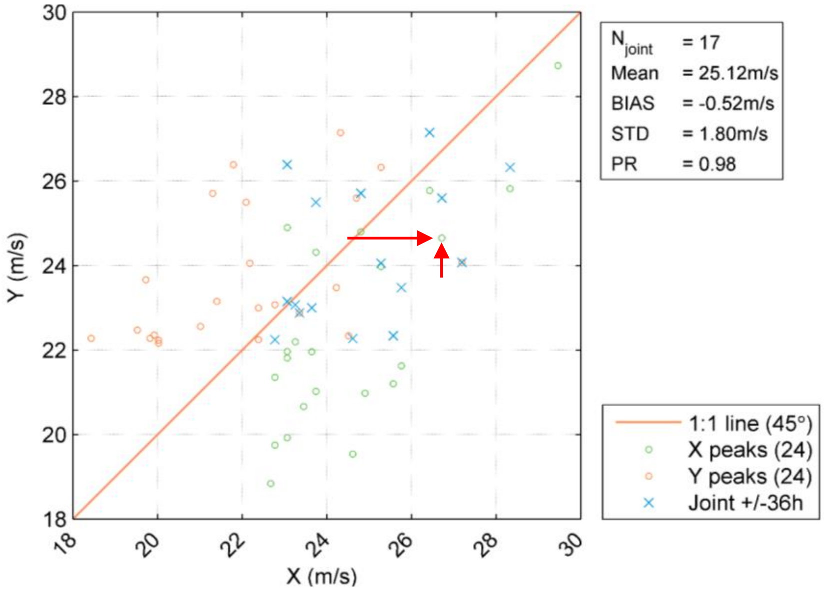

Figure 11.1 Example of peak event plot (wind speed)

---

[9] 36 hours is chosen arbitrarily as representative of an average storm duration. Often the measured and modelled peaks are within 1-2 hours of each other.

Table 11.1 Definitions of model quality indices (X = Observation, Y = Model)

Abbreviation	Description	Definition
N	Number of data (synchronised)	–
MEAN	Mean of Y data Mean of X data	$\frac{1}{\mathrm{N}}\sum_{\mathrm{i=1}}^{\mathrm{N}}\mathrm{Y_i} \equiv \overline{\mathrm{Y}}\ ,\ \frac{1}{\mathrm{N}}\sum_{\mathrm{i=1}}^{\mathrm{N}}\mathrm{X_i} \equiv \overline{\mathrm{X}}$
STD	Standard deviation of Y data Standard deviation of X data	$\sqrt{\frac{1}{\mathrm{N}-1}\sum_{\mathrm{i=1}}^{\mathrm{N}}(\mathrm{Y}-\overline{\mathrm{Y}})^2}\ ,\ \sqrt{\frac{1}{\mathrm{N}-1}\sum_{\mathrm{i=1}}^{\mathrm{N}}(\mathrm{X}-\overline{\mathrm{X}})^2}$
BIAS	Mean difference	$\frac{1}{\mathrm{N}}\sum_{\mathrm{i=1}}^{\mathrm{N}}(\mathrm{Y}-\mathrm{X})_{\mathrm{i}} = \overline{\mathrm{Y}}-\overline{\mathrm{X}}$
AME	Absolute mean difference	$\frac{1}{\mathrm{N}}\sum_{\mathrm{i=1}}^{\mathrm{N}}(\lvert\mathrm{Y}-\mathrm{X}\rvert)_{\mathrm{i}}$
RMSE	Root-mean-square difference	$\sqrt{\frac{1}{\mathrm{N}}\sum_{\mathrm{i=1}}^{\mathrm{N}}(\mathrm{Y}-\mathrm{X})_{\mathrm{i}}^{\ 2}}$
SI	Scatter index (unbiased)	$\frac{\sqrt{\frac{1}{\mathrm{N}}\sum_{\mathrm{i=1}}^{\mathrm{N}}(\mathrm{Y}-\mathrm{X}-\mathrm{BIAS})_{\mathrm{i}}^{\ 2}}}{\frac{1}{\mathrm{N}}\sum_{\mathrm{i=1}}^{\mathrm{N}}\lvert X_{\mathrm{i}}\rvert}$
EV	Explained variance	$\frac{\sum_{\mathrm{i=1}}^{\mathrm{N}}(X_{\mathrm{i}}-\overline{\mathrm{X}})^2-\sum_{\mathrm{i=1}}^{\mathrm{N}}[(X_{\mathrm{i}}-\overline{\mathrm{X}})-(\mathrm{Y_i}-\overline{\mathrm{Y}})]^2}{\sum_{\mathrm{i=1}}^{\mathrm{N}}(X_{\mathrm{i}}-\overline{\mathrm{X}})^2}$
CC	Correlation coefficient	$\frac{\sum_{\mathrm{i=1}}^{\mathrm{N}}(X_{\mathrm{i}}-\overline{\mathrm{X}})(\mathrm{Y_i}-\overline{\mathrm{Y}})}{\sqrt{\sum_{\mathrm{i=1}}^{\mathrm{N}}(X_{\mathrm{i}}-\overline{\mathrm{X}})^2\sum_{\mathrm{i=1}}^{\mathrm{N}}(Y_{\mathrm{i}}-\overline{\mathrm{Y}})^2}}$
QQ	Quantile-Quantile (line slope and intercept)	Linear least square fit to quantiles
PR	Peak ratio (of $\mathrm{N_{peak}}$ highest events)	$\mathrm{PR} = \frac{\sum_{\mathrm{i=1}}^{\mathrm{N_{peak}}}\mathrm{Y_i}}{\sum_{\mathrm{i=1}}^{\mathrm{N_{peak}}}X_{\mathrm{i}}}$

12 Appendix B: Validation Statistics

WS

Table 12.1 Validation statistics for all measurement locations for WS

Name	N	Mean [m]	Bias [m/s]	AME [m/s]	RMSE[m/s]	SI	EV	CC	PR	Plots
EINS-North	4,654	9.49	0.12	0.99	1.33	0.14	0.88	0.94	1.06	Figure 3.9
EINS-South	5,603	9.05	0.16	0.94	1.24	0.14	0.90	0.95	1.05	Figure 3.10
Thor	6,616	8.58	0.23	1.14	1.49	0.18	0.82	0.91	1.11	Figure 3.11

WL

Table 12.2 Validation statistics for all measurement locations for WL

Name	N	Mean [m]	Bias [m]	AME [m]	RMSE [m]	SI	EV	CC	PR	Plots
EINS-North (CP)	6,031	0.00	0.00	0.07	0.09	0.35	0.92	0.96	0.87	Figure 4.10
EINS-South (CP)	11,501	0.00	0.00	0.06	0.08	0.39	0.91	0.95	0.95	Figure 4.11
EINS-North (PS)	4,258	0.00	0.00	0.09	0.11	0.45	0.88	0.95	0.92	Figure 4.12
EINS-South (PS)	15,323	0.00	0.01	0.07	0.10	0.46	0.87	0.93	0.80	Figure 4.13
EINS-Island (Mini 2, CP)	8,922	0.00	0.00	0.07	0.07	0.39	0.91	0.95	0.76	Figure 4.14
Harald	164,097	0.01	0.01	0.06	0.07	0.42	0.89	0.94	1.05	Figure 4.15
Gorm	165,005	0.00	0.00	0.05	0.06	0.39	0.91	0.96	1.01	Figure 4.16
Ferring	369,184	0.00	0.00	0.10	0.13	0.43	0.89	0.95	0.97	Figure 4.17

CS

Table 12.3 Validation statistics for all measurement locations for CS

Name	N	Mean [m]	Bias [m/s]	AME [m/s]	RMSE[m/s]	SI	EV	CC	PR	Plots
EINS-North (CP seabed)	5,997	0.17	0.00	0.04	0.05	0.31	0.72	0.86	0.92	Figure 5.12
EINS-South (CP seabed)	11,501	0.13	-0.02	0.04	0.05	0.34	0.54	0.77	0.97	Figure 5.13
EINS-Island (Mini 2, CP seabed)	8,928	0.18	0.01	0.04	0.06	0.34	0.56	0.82	1.05	Figure 5.14
EINS-North (CP surface)	5,609	0.17	-0.02	0.06	0.08	0.40	0.42	0.71	0.83	Figure 5.15
EINS-South (CP surface)	5,761	0.15	-0.01	0.06	0.07	0.43	0.35	0.67	0.88	Figure 5.16
Valdemar	1,322	0.16	0.01	0.04	0.05	0.35	0.47	0.78	1.04	Figure 5.17
Thor	12,248	0.15	-0.02	0.05	0.06	0.35	0.69	0.84	1.07	Figure 5.18

H_{m0}

Table 12.4 Validation statistics for all measurement locations for H_{m0}

Name	N	Mean [m]	Bias [m]	AME [m]	RMSE [m]	SI	EV	CC	PR	Plots
EINS-North	10,924	2.09	0.07	0.18	0.24	0.11	0.96	0.98	0.97	Figure 6.15
EINS-South	11,363	2.01	0.09	0.18	0.24	0.11	0.96	0.98	0.11	Figure 6.18
EINS-Island (Mini 1)	17,191	1.89	0.08	0.17	0.23	0.12	0.96	0.98	1.02	Figure 6.21
EINS-Island (Mini 2)	11,321	1.99	0.07	0.17	0.23	0.11	0.96	0.98	0.96	Figure 6.24
Harald	165,566	2.05	0.05	0.17	0.23	0.11	0.97	0.98	1.00	Figure 6.27
Gorm	165,697	1.88	0.10	0.18	0.24	0.13	0.96	0.98	0.99	Figure 6.30
Ekofisk	490,348	2.08	0.01	0.19	0.27	0.13	0.95	0.98	1.04	Figure 6.33
Thor	12,015	1.76	0.09	0.16	0.23	0.13	0.94	0.98	1.10	Figure 6.36

T_p

Table 12.5 Validation statistics for all measurement locations for T_p (when H_{m0}>1 m)

Name	N	Mean [s]	Bias [s]	AME [s]	RMSE [s]	SI	EV	CC	PR	Plots
EINS-North	8,453	8.97	0.54	1.18	2.49	0.29	0.20	0.67	1.07	Figure 6.17
EINS-South	8,511	8.73	0.64	1.17	2.47	0.30	0.07	0.65	1.00	Figure 6.20
EINS-Island (Mini 1)	12,649	8.29	0.68	1.11	2.36	0.30	-0.19	0.62	1.06	Figure 6.23
EINS-Island (Mini 2)	8,542	8.78	0.79	1.28	2.71	0.32	-0.11	0.61	1.06	Figure 6.26
Harald	129,685	8.23	0.37	0.66	1.42	0.17	0.46	0.80	1.15	Figure 6.29
Gorm	120,935	7.82	0.43	0.65	1.39	0.18	0.25	0.77	1.30	Figure 6.32
Ekofisk	256,254	8.29	0.28	0.82	1.57	0.19	0.46	0.75	0.88	Figure 6.35
Thor	3,394	7.58	0.48	1.00	1.77	0.24	-0.04	0.57	0.99	Figure 6.38

T_{02}

Table 12.6 Validation statistics for all measurement locations for T_{02} (when H_{m0}>1 m)

Name	N	Mean [s]	Bias [s]	AME [s]	RMSE [s]	SI	EV	CC	PR	Plots
EINS-North	4,221	5.33	-0.36	0.41	0.51	0.06	0.86	0.94	0.91	Figure 6.17
EINS-South	4,255	5.26	-0.32	0.39	0.48	0.06	0.85	0.94	0.94	Figure 6.20
EINS-Island (Mini 1)	12,649	5.11	-0.26	0.37	0.45	0.07	0.81	0.93	0.95	Figure 6.23
EINS-Island (Mini 2)	8,542	5.23	-0.25	0.35	0.43	0.06	0.86	0.94	0.95	Figure 6.26
Harald	129,685	5.26	-0.34	0.39	0.48	0.06	0.88	0.95	0.95	Figure 6.29
Gorm	120,935	5.05	-0.30	0.35	0.43	0.06	0.87	0.94	0.94	Figure 6.32
Ekofisk	319,323	5.30	-0.35	0.45	0.56	0.08	0.83	0.92	0.92	Figure 6.35
Thor	8,930	4.85	-0.40	0.48	0.57	0.08	0.65	0.89	0.94	Figure 6.38